Helmholtz Institute Ulm
Electrochemical Energy Storage

Novel electrode materials for rechargeable batteries based on cationic and anionic shuttles

Dissertation zur Erlangung des Doktorgrades Dr. rer. nat.

der Fakultät für Naturwissenschaften an der Universität Ulm

vorgelegt von

Ping Gao

aus Hunan, China

ulm university universität ulm

Dekan der Fakultät für Naturwissenschaften: Prof. Dr. Peter Dürre

Erstgutachter: Prof. Dr. Maximilian Fichtner

Zweitgutachter: Prof. Dr. Rolf Jürgen Behm

Promotions datum: 18.11.2016

Abstract

Ever-growing energy needs and the environmental issues arising from the combustion of fossil fuels demand a stronger use of renewable energy sources and the development of sustainable storage technologies. Batteries are widely used in the various energy storage applications, but their storage capabilities are regarded as limited at the moment. Moreover, high costs and sustainability issues on the long term make the development of alternative systems based on sustainable resources more and more attractive.

The planned worldwide introduction of electric vehicles and grid-scale renewable energy storage raises grand challenges to develop systems with high energy density, long cycle life, high safety and low cost of the batteries. In this regard, novel electrode materials for rechargeable batteries based on different ionic shuttles have been investigated in this doctoral thesis. The experimental chapters concentrate on the following four parts: rechargeable batteries based on anionic shuttle, i.e., chloride ion batteries (in the first and second part); rechargeable batteries based on both cationic and anionic shuttles, i.e., organic-based batteries (in the third part); and rechargeable batteries based on cationic shuttle, i.e., Li-ion and Na-ion batteries (in the fourth part).

In the first part, a rechargeable chloride ion battery (CIBs) using vanadium oxychloride (VOCl) cathode, Li anode and chloride ion conducting liquid electrolyte was investigated. An initial discharge capacity of 189 mAh g^{-1} was observed at a current rate of 130 mA g^{-1}. A capacity of 113 mAh g^{-1} remained after 100 cycles at 2 C rate with a coulombic efficiency of 98 %. The reaction mechanism of the VOCl electrode was

studied in detail by electrochemical tests, *ex-situ* X-ray diffraction (XRD), X-ray photoelectron spectroscopy (XPS), infrared spectroscopy (IR), and transmission electron microscopy (TEM). It was revealed that the VOCl interlayers were expanded in the initial discharge, and the expanded structure facilitated the chloride ion exchange in the subsequent cycling.

In the second part, magnesium (Mg) based materials were introduced as anodes in the CIB, in which the VOCl material worked as a cathode. Composite of Mg powder with carbon black (MC) and a mixture of magnesium chloride, Mg and carbon black (MMC) were tested as anodes. The VOCl cathode can be charged while $VOCl_2$ is formed and discharged to VO when coupled with an MMC anode, delivering two discharge plateaus at around 1.9 and 1.3 V in the first cycle. The VOCl electrode delivered a reversible capacity of 101 mAh g^{-1} at a current density of 10 mA g^{-1} after initial 9 cycles.

The third part of the thesis deals with an organic-based rechargeable battery using a porphyrin complex of [5,15-Bis(ethynyl)-10,20-diphenylporphinato]copper(II) (CuDEPP) as a new electrode-active material. Due to the bipolar redox property of the CuDEPP, both cations and anions of the electrolyte shuttled during the reaction, enabling the transfer of four electrons per CuDEPP formula unit. The CuDEPP could be used as a cathode, as anode, or both cathode and anode in the organic cells. Using a lithium metal anode, the CuDEPP cathode delivered an initial discharge capacity of 210 mAh g^{-1} at a current density of 200 mA g^{-1} between 4.5 V and 1.8 V. When coupled with a graphite cathode, a high specific power density of 14.4 kW kg^{-1} was achieved for the CuDEPP anode at a high current density of 10 A g^{-1}. In a symmetric cell, it also demonstrated highly reversible charge and discharge behavior.

In the last part, a high performance electrode was developed for Li-ion (LIB) and Na-ion batteries (SIB) which are based on a multi-electron reaction. The layered VOCl electrode was investigated for both cells. The number of the transferred electrons varied when the working window was changed. The VOCl electrode in LIB delivered

first discharge and recharge capacities of 1228 mAh g^{-1} and 759 mAh g^{-1} at a current density of 100 mA g^{-1} in a voltage range of 3.0 - 0.05 V (vs Li/Li^+), respectively, which corresponds to 2.8 Li per VOCl formula unit. A discharge capacity of 120 mAh g^{-1} was obtained for SIB at a 0.5 C rate in a voltage range of 1.0 - 3.0 V (vs Na/Na^+). The reaction mechanism of the VOCl electrode for LIB and SIB was systematically investigated.

The results of this thesis suggest that the migration of chloride ions can be fast using a VOCl material as a cathode in chloride ion batteries, and both Li and Mg based materials can serve as the anode. High rate capability, and long-term cycle stability of energy storage devices could be built using organic based rechargeable batteries shuttling of both positive and negative ions. In addition, developing of conversion based materials for rechargeable batteries is also of great importance in order to increase the energy density.

Zusammenfassung

Der stetig wachsende Energiebedarf und die Umweltprobleme durch die Verbrennung von fossilen Brennstoffen erfordern eine zunehmende Nutzung erneuerbarer Energiequellen und nachhaltiger Speicherungstechnologien. Batterien werden in verschiedenen Anwendungsbereichen zur Energiespeicherung eingesetzt. Deren Speicherkapazitäten werden derzeit jedoch als begrenzt erachtet. Außerdem treiben hohe Kosten und Nachhaltigkeitsaspekte langfristig die Entwicklung alternativer Systeme (der Energiebereittellung), basierend auf nachhaltigen Ressourcen, voran. Die Herausforderung für den langfristigen Erfolg von Elektrofahrzeugen und der Speicherung von erneuerbaren Energien im Stromnetz liegt insbesondere in der Entwicklung von den Batterien mit hohen Energiedichten, langer Lebensdauer, hoher Sicherheit und niedrigen Kosten. In dieser Doktorarbeit wurden neuartige Elektrodenmaterialien für wiederaufladbare Batterien mit verschiedenen ionischen Transportsystemen untersucht. Der Experimentalteil ist in die vier folgenden Teile untergliedert: Die ersten beiden Teile befassen sich mit wiederaufladbaren Batterien, basierend auf einem anionischem Ladungstransportsystem (in diesem Fall: Chloridionen-Batterien). Im dritten Teil geht es um wiederaufladbare Batterien, basierend auf sowohl anionischem als auch kationischem Ladungstransportsystem (in diesem Fall: organisch basierten Batterien). Der letzte Teil befasst sich mit wiederaufladbaren Batterien, insbesondere auf Li- bzw. Na-Ionen-Basis, welche auf einem kationischen Transportsystem beruhen.

Im ersten Teil wurden Chlorid-Ionen-Batterien mit Vanadiumoxychlorid (VOCl) als Kathode und Lithium als Anode untersucht. Der zugehörige Elektrolyt ist flüssig und

gut chloridionenleitend bei Raumtemperatur. Bei einer Anfangskapazität von 189 mAh g^{-1} wurde beim Entladen eine Stromrate von 130 mAh g^{-1} erreicht. Nach 100 Zyklen bei 2 C betrug die Kapazität 113 $mAhg^{-1}$ mit einer Coulomb'schen-Effizienz von 98 %, der ex-situ Röntgendiffraktometrie (XRD), Röntgenphotoelektronenspektroskopie (XPS), Infrarotspektroskopie (IR) und Transmissionselektronenmikroskopie (TEM) untersucht. Es zeigte sich, dass die Zwischenschichten von VOCl während des ersten Entladens aufgeweitet wurden und dass dieser Vorgang den Chlorid-Ionenaustausch in den folgenden Zyklen erleichterte.

Im zweiten Teil dienten magnesiumbasierte Materialien als Anode und VOCl als Kathode für die CIB. Als Anodenmaterial wurden Komposite aus Mg-Pulver mit Kohlenstoffruß, engl. „carbon black" (MC) und ein Gemisch aus Magnesiumchlorid, Mg und carbon black (MMC) getestet. Mit einer MMC-Anode gekoppelt, bildete sich an der VOCl-Kathode beim Aufladen $VOCl_2$ und beim Entladen VO. Beim ersten Entladen zeigten sich zwei Spannungsplateaus bei 1.9 und 1.3 V. Bei einer Stromdichte von 10 mA g^{-1} lieferte die VOCl Kathode eine reversible Kapazität von 101 mAh g^{-1} für 9 Zyklen.

Der dritte Teil der Arbeit befasste sich mit auf organischen Elektroden basierenden Batterien, in denen neuartige Porphyrin-Komplexe [5,15-Bis(ethynyl)-10,20-diphenylporphinato]kupfer(II) (CuDEPP) als Elektrodenmaterialien verwendet werden. Aufgrund der bipolaren Redoxeigenschaften von DEPP können in den entsprechenden Elektrolyten sowohl Kationen als auch Anionen zwischen den beiden Elektroden frei wandern, wodurch vier Elektronen pro DEPP-Formeleinheit übertragen werden. Die CuDEPP-Komplexe konnten deshalb sowohl als Kathoden wie auch Anoden oder gleichzeitig, als Kathode und Anode, in einem Batteriesystem eingesetzt werden. Zusammen mit einer Li-Anode lieferte die CuDEPP-Kathode bei einer Stromdichte von 200 mA g^{-1} eine Anfangskapazität von 210 mAh g^{-1} bei Spannungswerten zwischen 4.5 V und 1.8 V. Eine Graphit-Kathode erreichte mit CuDEPP als Anode erreichte bei einer hohen Stromsichte von 10 A g^{-1} eine hohe spezifische Leistungsdichte von 14.4 kW kg^{-1}. In

einer symmetrischen Zelle zeigte sich auch nach einigen Tausend Zyklen die hohe Reversibilität beim Be- und Entladen.

Das Ziel im letzten Teil der Arbeit bestand in der Entwicklung von Li-Ionen- und Na-Ionen- Batterien mit hohen Leistungsfähigkeiten durch mehrfachen Elektronentransfer. Die VOCl-Elektrode mit seinem schichtartigen Aufbau des Materials wurde für beide Batteriesysteme untersucht. Die Anzahl übertragener Elektronen wurde durch die Wahl des Spanungsfensters beeinflusst. Die VOCl-Elektrode in der LIB lieferte bei einer Stromdichte von 100 mA g^{-1} und in einem Spannungsbereich zwischen 3.0 - 0.05 V (vs Li/Li^{+}) Kapazitäten um 1228 mAh g^{-1} für das erste Entladen und 759 mAh g^{-1} für das Wiederaufladen. Die Entladekapazität entspricht ca. 2.8 Li-Einheiten pro VOCl-Formeleinheit. Für Na-Ionen-Batterien wurde bei einer Stromrate von 0.5 C in einem Spannungsbereich zwischen 1.0 - 3.0 V eine Entladekapazität von 120 mAh g^{-1} erhalten. Desweiteren wurde in den Li- und Na-Ionen-Batteriesystemen der an der VOCl-Elektrode stattfindende Reaktionsmechanismus systematisch untersucht.

Die Ergebnisse dieser Arbeit legen nahe, dass eine schnelle Chloridionenwanderung in Chloridionenbatterien mit VOCl als Kathodenmaterial, zusammen mit Li- und Mg-basierten Anoden, zu bewerkstelligen ist. Mit organisch basierten, wiederaufladbaren Batterien, die imstande sind, sowohl positiv als auch negativ geladene Ionen zu transportieren, könnten Energiespeichersysteme aufgebaut werden, die eine hohe Leistungsfähigkeit als auch eine langanhaltende Zyklenstabilität aufweisen. Desweiteren ist zu sagen, dass die Entwicklung von Konversionsmaterialien für wiederaufladbare Batterien von großem Interesse ist, vor allem im Hinblick auf die Steigerung der Energiedichte.

Table of Content

Abstract I

Zusammenfassung V

Chapter 1 Introduction 1

Chapter 2 Fundamentals 5

2.1 Battery basics 5

2.1.1 Battery specification 6

2.1.2 Thermodynamics and kinetics 7

2.2 Rechargeable batteries based on cationic shuttle 9

2.2.1 Lithium ion batteries 9

2.2.2 Sodium ion batteries 16

2.3 Rechargeable batteries based on anionic shuttle 20

2.3.1 Working principle of chloride ion batteries 20

2.3.2 Solid state chloride ion conductors 22

2.3.3 Chloride ion batteries 24

2.4 Rechargeable batteries based on both cationic and anionic shuttles 29

2.4.1 Graphite electrode based dual-ion batteries 29

2.4.2 Organic electrode based dual-ion batteries 32

2.5 Aim of the thesis 36

Chapter 3 Experimental methods 39

3.1 X-ray diffraction 39

3.2 Scanning electron microscopy 40

3.3 Transmission electron microscopy 42

3.4 X-ray photoelectron spectroscopy 44

3.5 Infrared spectroscopy 45

3.6 Galvanostatic cycling 46

3.7 Cyclic voltammetry 47

Chapter 4 VOCl cathode and lithium anode for rechargeable chloride ion batteries 49

4.1 Introduction 49

4.2 Experimental section 50

4.2.1 Synthesis of VOCl 50
4.2.2 Material characterization 50
4.2.3 Electrode preparation 51
4.2.4 Electrochemical measurements 51
4.3 Results and discussion 52
Chapter 5 VOCl cathode and magnesium anode for rechargeable chloride ion batteries 67
5.1 Introduction 67
5.2 Experimental section 68
5.2.1 Electrode preparation 68
5.2.2 Material characterization 69
5.2.3 Electrochemical measurements 69
5.3 Results and discussion 69
Chapter 6 Porphyrin complex as electrode for rechargeable batteries 81
6.1 Introduction 81
6.2 Experimental section 82
6.2.1 Synthesis of [5,15-Bis(ethynyl)-10,20-diphenylporphinato]copper(II) 82
6.2.2 Materials characterization 84
6.2.3 Electrochemical measurements 85
6.3 Results and discussion 86
6.3.1 Porphyrin complex as cathode for rechargeable batteries 86
6.3.2 Porphyrin complex as anode for rechargeable batteries 96
6.3.3 Porphyrin complex as both cathode and anode for rechargeable batteries 100
Chapter 7 VOCl as a novel electrode for rechargeable Li-ion and Na-ion batteries 103
7.1 Introduction 103
7.2 Experimental section 104
7.2.1 Electrode preparation 104
7.2.2 Material characterization 104
7.2.3 Electrochemical measurements 105
7.3 Results and discussion 105
7.3.1 VOCl electrode for lithium ion batteries 105
7.3.2 VOCl electrode for sodium ion batteries 119

Chapter 8 Conclusions 125
Chapter 9 Outlook 133
Bibliography 135
Appendix 157
Abbreviations 163
Acknowledgements 167
Publications and conferences 169
Erklärung 173
Curriculum Vitae 175

Chapter 1 Introduction

The climate change, energy production and energy storage are among the most important topics in the global society nowadays. According to the Hubbert peak theory, the fossil-fuel under the ground in any region is finite and the rate of discovery has run over a maximum already. It is claimed that a double of our present rate of energy production is needed by 2050 up to 28 terawatt (TW). This equals to 130,000 TWh or the equivalent of 10^{10} tons of oil yearly (Figure 1.1).[1,2] Thus, it is not surprising that in the mid-term, one day the energy based on fossil-fuel will hardly meet the needs of humans. In addition, carbon dioxide emissions should be considered and effective efforts need to be done to alleviate the global warming. To cope with all these challenges, the development of both renewable energy sources and sustainable energy storage technologies are mandatory. There are several renewable energy sources, which have been used, such as wind, sunlight, tides, geothermal heat, and biomass. However, the use of these energies for all aspects of human society is not satisfactory yet. In particular, the technologies for capturing, storing and transporting of the renewable energy need to be further developed. To make best use of these energies, good energy storage systems are of great importance. Although great efforts have been made in the past decades, there is still only a limited capacity that can store around 1 % of the energy consumed worldwide only.[1,2] To secure the energy supply for next few decades and beyond, electrochemical storage devices such as rechargeable batteries can play an important role as the battery is a simple concept

that can efficiently store/release energy between the electric and the chemical form.

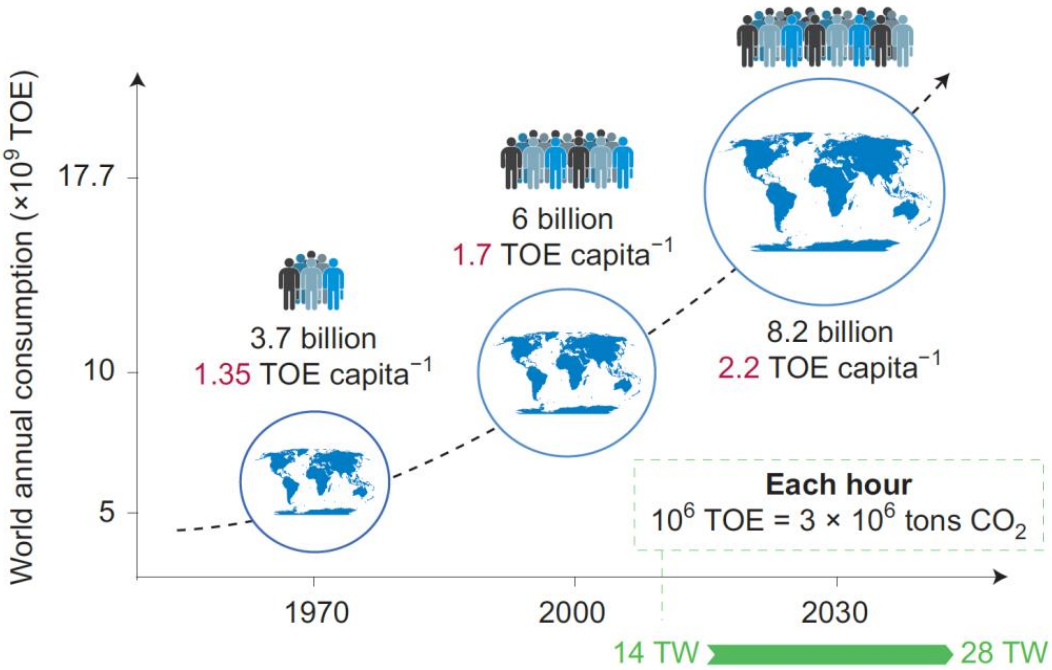

Figure 1.1: Past, present and forecast of the world's energy needs up to 2050. TOE is ton of oil equivalent. Reprinted by permission from Macmillan Publishers Ltd: Nature, ref.[3], copyright (2014).

The use of rechargeable batteries started since the invention of lead-acid battery in 1859. Subsequently, there was an impressive development and market-growth of nickel-cadmium batteries (1899), nickel-metal hydride batteries (1967), and lithium ion batteries (1985). However, the energy storage capability of the battery using traditional electrode material is still limited, which can hardly keep pace with the rate of ever-growing energy needs. For example, although lithium ion batteries have been widely applied in portable applications, entertainment, computing, electric vehicles, and even large grid storage fields, there are also arguments for developing "post-lithium chemistries" or "beyond-lithium ion batteries". Some advanced energy storage systems have been proposed recently as shown in Figure 1.2. For example, the lithium-air batteries have theoretical specific energy about 10 times higher than most batteries in the market today. Organic-based batteries are inspired by nature and the

electrode materials can be made from biomass. There are hardly limitations for developing "beyond-lithium ion batteries", new materials and new chemistries are always necessary for further progress. In this thesis, new electrode materials are developed for rechargeable batteries based on different ionic shuttles, e.g. batteries based on anionic shuttle (i.e. chloride ion batteries), both cationic and anionic shuttles (i.e. organic based batteries), and cationic shuttle (i.e. Li-ion and Na-ion batteries), aiming at broadening new ideas and strategies for the next generation energy storage.

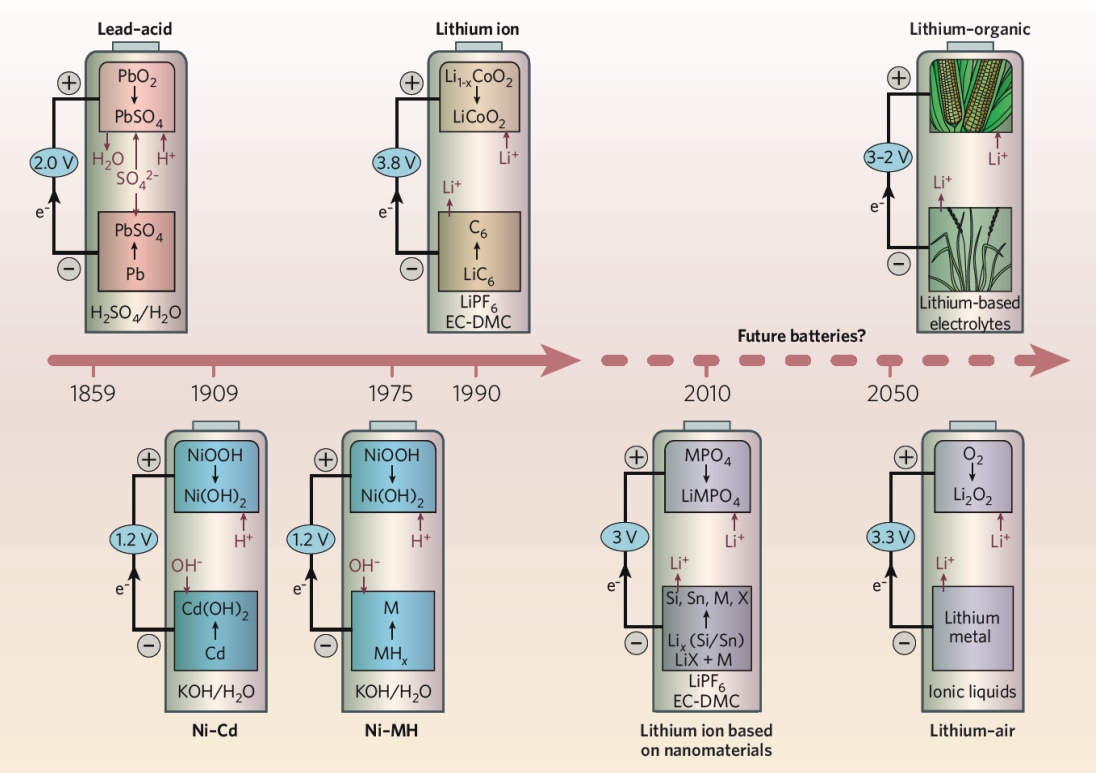

Figure 1.2: Battery systems over the years. Reprinted by permission from Macmillan Publisher Ltd: Nature, ref.[4], copyright (2008).

Chapter 2 Fundamentals

2.1 Battery basics

A battery is an energy storage device which consists of a group of electrochemical cells interconnected either in parallel or in series or both ways to provide the demanded voltage and capacity. Each cell is composed of a cathode (positive electrode) and an anode (negative electrode) for the energy storage units where the electrochemical reaction occurs. A porous electronic insulator separator is placed between the cathode and the anode to prevent short circuit but it allows ions to migrate freely. In addition, an electrolyte is needed to enable ionic conductivity between the electrodes during the electrochemical reaction, which normally contains metal salt (e.g. $LiPF_6$ for LIBs) and suitable solvents.

Two types of batteries exist, primary batteries and secondary batteries. The former delivers electrical energy into an electrical circuit until the battery is exhausted. The electrodes cannot be recovered after the discharge process. For example, zinc-manganese batteries and alkaline batteries are classic primary batteries which have widely been used in past few decades.[5] In contrast, secondary batteries are able to re-store electrical energy after being discharged through a recharge process and the chemical state of the electrode can be in principle recovered to its original condition. Lead-acid batteries, nickel-cadmium, nickel-metal hydride, and LIBs are commercialized rechargeable batteries at the moment.

During the discharge and recharge process, ions migrate between electrodes through the ionic conductor (electrolyte), meanwhile the electrons travel through the external electronic circuit to ensure the conservation of electric neutrality. For better understanding of rechargeable batteries, several general terms and definitions are summarized in the following section.

2.1.1 Battery specification

- **Cathode**: the positive electrode which accepts electrons from the external circuit during the cell discharge.
- **Anode**: the negative electrode which donates electrons into the external circuit during the cell discharge.
- **Electrolyte**: A salt dissolved in solvent(s) or an ionic conducting compound which has a high ionic conductivity but a low electronic conductivity.
- **Capacity**: The amount of charge that a battery (cell) contains, often expressed as mAh or Ah. It depends on the amount and the type of active materials in a battery cell. Specific capacity (C, mAh g^{-1} or Ah kg^{-1}) is the amount of charge per unit weight that an electrode material contains. It is defined for each active material, and can be given by Equation 2.1,

$$C = \frac{n \cdot F}{M} \qquad (2.1)$$

  Where n is the number of electrons transferred during the reaction, F is the Faraday constant (96485.3 C mol^{-1}), M is the molar weight of the active material. The capacity is a fundamental characteristic of the active material which is used for the battery, it depends on its redox chemistry and structure.
- **Energy density**: Energy per volume of an active material or a device. It is expressed as Wh L^{-1}. Energy density is a combination of the cell voltage and capacity in volume of an electrode material.

- **Specific energy**: Energy per unit weight of an active material or a device. It is expressed as Wh kg^{-1}. Specific energy is a combination of the cell voltage and capacity in weight of an electrode material.
- **Power density**: is expressed as W L^{-1}. Power density is the product of the cell operation voltage and the current per volume of an active material or a device.
- **Specific power**: is expressed as W kg^{-1}. Power density is the product of the cell operation voltage and the current per unit weight of an active material or a device.
- **C-rate:** In order to normalize against battery capacity, discharge (or charge) current density is often expressed as the C-rate. It is the measure of the rate at which a battery is discharged (or charged) relative to its maximum capacity. A 1 C rate means a discharge (or charge) of the entire battery to a maximum capacity in 1 hour. For n C rate, the discharge (charge) time will be in 1/n hours.
- **Coulombic efficiency**: is also called Faradaic efficiency. It is the ratio of number of charge output a battery to input of charge. A coulombic efficiency less than 100 % is primarily due to the loss of charge in unwanted irreversible side reactions.

2.1.2 Thermodynamics and kinetics

The basic thermodynamic equation for a reversible electrochemical reaction is given as:[6]

$$\Delta G = \Delta H - T\Delta S \qquad (2.2)$$

Where ΔG is the Gibbs free energy (unit: J), ΔH is the enthalpy (unit: J), ΔS is the entropy (J K^{-1}), and T is the absolute temperature (unit: K). ΔG, ΔH, and ΔS are state functions which only depend on the identity of material in the initial and final state of

the reaction. The direction of the spontaneous reaction can be estimated by ΔG. The reaction in a certain direction is spontaneous, if the value of ΔG is negative. In a rechargeable battery, the net useful energy available for the electrochemical reaction can be given as ΔG. Combined with electrical terms, the electromotive force (EMF, V) of the battery reaction at an equilibrium condition can be given as:

$$EMF = -\frac{\Delta G}{nF} \qquad (2.3)$$

Where *n* is transferred number of electrons in one mole of the reactant. F is the Faraday constant. As a negative Gibbs free energy is provided in a spontaneous process, a positive EMF can be obtained according to equation 2.3.

In practice, the discharge (charge) potential is always lower (higher) than the equilibrium potential when the current is flowing through the electrode. This is due to kinetic limitations and other factors including physical, chemical, and electrochemical steps upon charge-transfer and charge transport. Mainly three different kinetic effects need to be considered: (1) the activation polarization of the charge-transfer at electrode/electrolyte interfaces of electrodes, (2) the ohmic polarization of the resistance from the connection of individual cell components, (3) the concentration polarization of mass transport limitations. To build a high performance rechargeable battery, one must consider both thermodynamic and kinetic factors. Therefore, a deep understanding is necessary of the reaction mechanism, the electrode properties, and the system.

Building novel batteries with performance-oriented active materials is of great importance, as all breakthroughs for energy storage greatly depend on new materials and new chemistries. In the following, an overview of diverse active materials for rechargeable batteries will be addressed, including the state-of-art of rechargeable batteries based on

- cationic shuttle such as lithium ion batteries and sodium ion batteries,
- anionic shuttle based on the novel concept of chloride ion batteries, and
- both cationic and anionic shuttle such as graphite cathode based batteries and organic electrode based batteries.

2.2 Rechargeable batteries based on cationic shuttle

Several rechargeable batteries based on cationic shuttle have been proposed in past few decades, such as Li^+, Na^+, K^+, Mg^{2+}, Ca^{2+}, Al^{3+} etc.[7–20] Among them, the one based on lithium ions shuttle, i.e., LIBs, which was first commercialized by the Sony Corporation in 1991, dominates the majority of the market today. Recently, sodium ion batteries (SIBs) have been considered as an alternative energy storage system that has potential to partially replace LIBs in certain areas such as large stationary energy storage due to the much cheaper price and abundant sodium resources. Among the different battery chemistries, the performance of the active materials is of utmost importance, as this is a key factor for the performance of the battery. In this section, an overview will be given on the state-of-art of electrode materials for LIBs and SIBs.

2.2.1 Lithium ion batteries

The working principle of a LIB is based on lithium ions shuttling between a cathode and an anode. The schematic illustration of a LIB is shown in Figure 2.1.

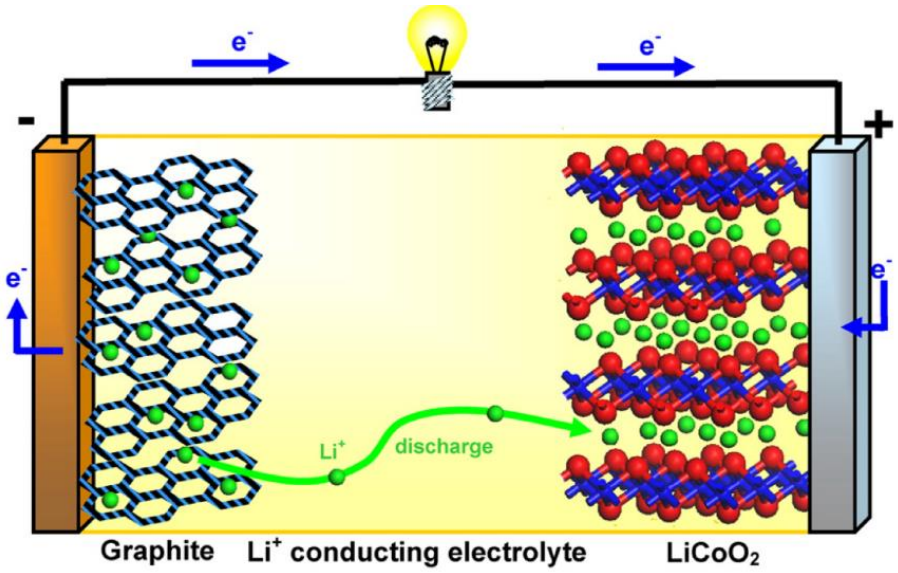

Figure 2.1: Schematic illustration of the LIB (anode: graphite, cathode: $LiCoO_2$). Reprinted from Ref.[21], copyright (2008), with permission from Elsevier.

During the charge, Li ions leave the $LiCoO_2$ cathode, travel through the electrolyte and are inserted into the graphite anode. At the same time, electrons are generated at the cathode and travel through the external circuit and reach at the graphite anode for neutralizing the charge. In the discharge, the Li ions and electrons are moving in an opposite direction. The electrode reactions during the charge process can be written as follows:

At the cathode: $\mathrm{LiCoO_2} \rightarrow \mathrm{Li_{1-x}CoO_2} + \mathrm{x\,Li^+} + \mathrm{x\,e^-}$ (2.4)

at the anode: $\mathrm{6C} + \mathrm{x\,Li^+} + \mathrm{x\,e^-} \rightarrow \mathrm{Li_xC_6}$ (2.5)

Cathode: Intercalation based compounds are commonly used as cathodes in LIBs as shown in Figure 2.2. They are divided into three types: i) layered transition metal material with a two-dimensional (2D) ion diffusion path (e.g. $LiMO_2$, M = Ni, Co, Mn), ii) spinel structural material with a three-dimensional (3D) ion diffusion path (e.g. $LiMn_2O_4$, $LiNi_{0.5}Mn_{1.5}O_4$), and iii) olivine structure material with a one-dimensional (1D) ion diffusion path (e.g. $LiMPO_4$, M = Fe, Mn, Co). Figure 2.3 shows the crystal structure of three common used cathode materials with different Li ion insertion channels.

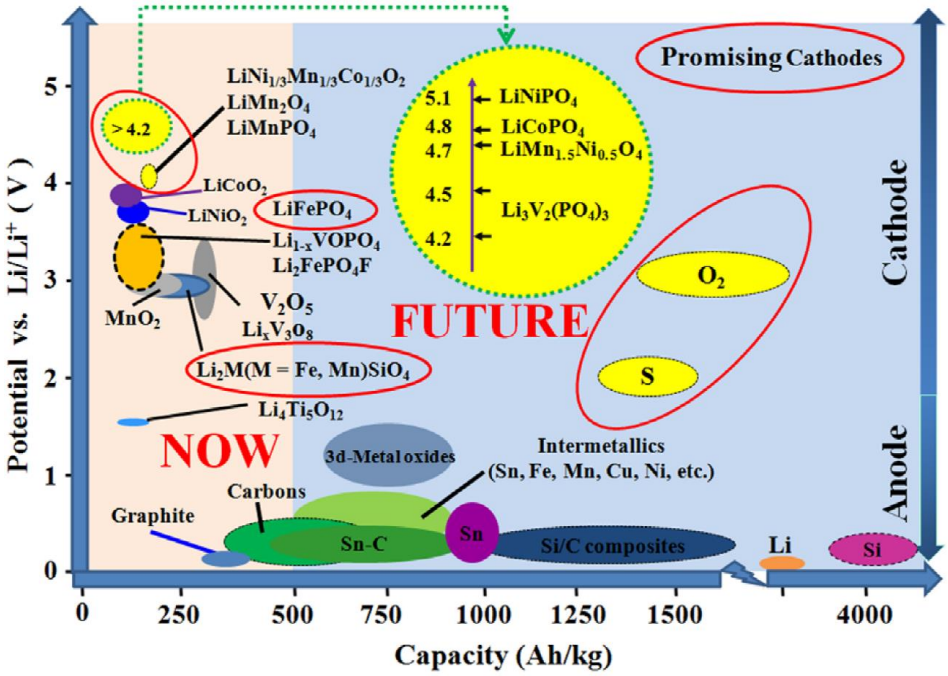

Figure 2.2: Electrode materials and corresponding electrochemical performance in current LIB technologies. Reprinted from Ref.[22], copyright (2013), with permission from Elsevier.

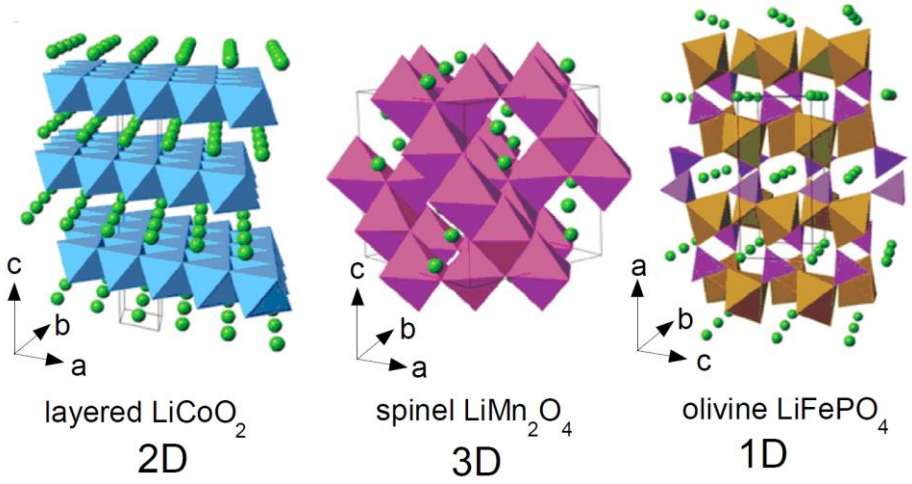

Figure 2.3: Crystal structure of three Li-insertion compounds in which Li^+ ions are mobile through the 1D, 2D, and 3D frameworks, respectively. Adapted from Ref.[23], open access under the CC BY-SA 3.0, https://creativecommons.org/licenses/by-nc-sa/3.0/.

Layered $LiCoO_2$ was firstly introduced by Goodenough in 1980.[24] It forms an α-$NaFeO_2$ distorted rock-salt structure where cations order in alternating (111) planes. It was originally commercialized by SONY in 1991. The specific capacity of the $LiCoO_2$

electrode is limited to around 150 mAh g^{-1} at room temperature. Around 0.5 mol Li^+ are reversibly intercalated per $LiCoO_2$ formula unit, although its theoretical capacity is 274 mAh g^{-1}.[25,26] The discharge curve of the $LiCoO_2$ electrode is shown in Figure 2.4. Increasing discharge capacity would be possible by extracting more lithium ions from the lattice by increasing the charge cutoff voltage (> 4.2 V), however this would lead to fast decrease in capacity retention upon cycles due to the instability of the structure.[27] Good power density can be maintained if the working potential is between 4.2 V and 3.0 V (vs. Li/Li^+). The major limitations of the $LiCoO_2$ material are its low thermal stability and the high cost. Partial replacement of Co by other metals in the lattice (Mn, Fe, Al, Cr) and coating of various metal oxides (Al_2O_3, ZrO_2, etc.) are effective ways to improve the electrode performance.[28–31] For example, $LiNi_xCo_yMn_zO_2$ and $LiNi_xCo_yAl_zO_2$ (x + y + z = 1) have been proposed as promising cathode materials for the next generation LIBs as the electrochemical performance can be comparable or even better than the $LiCoO_2$ depending on the content of the transition metal element. More importantly, these materials are much cheaper and safer than the $LiCoO_2$.[32,33]

Another cathode material, e.g. $LiMn_2O_4$, forms a spinel structure and crystallizes in the *Fd3m* space group with a cubic lattice parameter a = 8.239 Å.[34] At approximately 4 V (vs Li/Li^+) the discharge occurs in a two-stage process where Li^+ ions intercalate/de-intercalate in 3D Li ion diffusion paths upon the reaction. The theoretical capacity of the electrode is 147 mAh g^{-1}. The main challenge in the development of this material is the capacity fade during cycling, which is due to the following reasons: i) the dissolution of Mn^{2+} ($Mn^{3+} \rightarrow Mn^{4+} + Mn^{2+}$) in the electrolyte, ii) the instability of spinel structure in the delithiated state combined with the loss of oxygen, iii) Jahn-Teller distortion at the end of discharge. Here, a substitution was proposed of 25 % Ni for Mn in $LiMn_2O_4$ spinel to keep Mn in the 4+ valence state, i.e., $LiNi_{0.5}Mn_{1.5}O_4$ (see Figure 2.4), in order to improve the electrochemical performance of

the spinel electrode.[35,36]

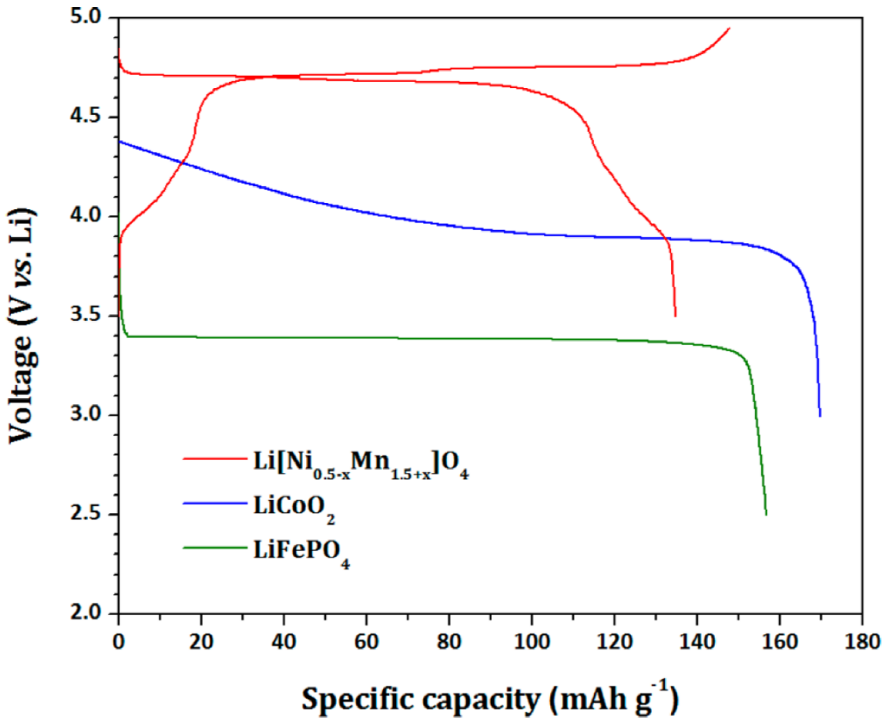

Figure 2.4: Comparison of charge and discharge curves of three different cathode materials in a half cell with lithium metal as an anode (blue curve for $LiCoO_2$, red curve for $LiNi_{0.5}Mn_{1.5}O_4$, and green curve for $LiFePO_4$). Reprinted with permission from Ref.[37]. Copyright (2013) American Chemical Society.

The olivine structure $LiFePO_4$, firstly presented by Goodenough in 1997, is used as a cathode material for LIBs due to its inexpensive and less-toxic element composition and excellent cycling stability. It has been tested for large-scale applications such as hybrid electric vehicles (HEV), and stationary energy storage. $LiFePO_4$ crystallizes in the orthorhombic system with *Pnma* space group. The crystal structure is shown in Figure 2.3, where FeO_6 octahedra are corner-shared and linked together in bc-planes, while LiO_6 octahedra are edge-shared along the b-axis and the PO_4 group connected neighboring FeO_6 octahedra by sharing a common edge.[38,39] The electrons are stored by the redox reaction between Fe^{2+} and Fe^{3+} with a redox potential of 3.4 V (vs Li/Li^+), at a theoretical specific capacity of 170 mAh g^{-1}. The inherent challenge of the $LiFePO_4$ electrode is the extremely low Li^+ diffusion coefficient ($\approx 10^{-14}$ cm^2 s^{-1}) and low

electronic conductivity (< 10^{-9} S cm^{-1}).[40,41] Reduced particle size and carbon coating are reported to be effective approaches to increase the electrochemical performance.[42–45] Although the $LiFePO_4$ electrode has been applied in HEVs and other applications, the energy density is regarded as being not high enough even though its theoretical capacity can be reached.

To further improve the energy density, one of the fundamental routes is to develop novel electrode materials with a multi-electron reaction. Several high performance battery systems have been proposed, for example i) sulfur cathode and lithium metal anode (Li-S) for rechargeable LIBs ($2Li + S \leftrightarrow Li_2S$), the theoretical capacity is 1675 mAh g^{-1} and the operating voltage is $\sim$ 2.1 V (vs Li/Li^+). The reported specific energy of Li-S battery is almost two or three times higher than that of conventional batteries,[46–48] ii) conversion type electrode materials (MF_x, M = Fe, Ni, Co, Mn, etc.), for example, the cathode material of FeF_3 has a high theoretical capacity of 712 mAh g^{-1},[49–51] and iii) novel electrode materials such as organic electrode materials, where the theoretical capacity can be tuned by designing the molecular structures. The state-of-art of organic based electrode for rechargeable lithium batteries will be discussed in section 2.4.

Anode: Lithium metal is an ideal anode material for LIBs due to its light weight, high theoretical capacity (3680 mAh g^{-1}), and the lowest redox potential of all elements (-3.04 vs Standard hydrogen electrode, SHE). However, the main challenge of using lithium metal in LIBs is the formation of dendrites upon Li plating during cycling, which may grow through the separator, reach the cathode, and cause short-circuit of the battery and possibly ignite flammable electrolyte. Since carbonaceous materials such as graphite, hard carbon, soft carbon have interlayer sites for lithium ions intercalation/de-intercalation at a low redox potential (< 1.0 V vs Li/Li^+), these carbon materials as anode are capable of avoiding the formation of dendrites, a development which significantly promoted the LIB technology. The commercialized graphite anode

has a theoretical capacity of 372 mAh g^{-1} based on the formation of LiC_6 upon insertion of lithium ions into graphene inter-layers.[52][53] The spinel $Li_4Ti_5O_{12}$ as an alternative anode material has a theoretical capacity of 175 mAh g^{-1}, and it can be cycled at very high current densities without changing the structure.[54] TiO_2 compound, a theoretical capacity of 335 mAh g^{-1} for one lithium intercalation/de-intercalation per formula unit, and has also been proposed as an anode due to its high reversible capacity and power density.[55] However, the redox potential (> 1.0 V vs Li/Li^+) is relatively high. This will compromise the energy density in the application.

To overcome the current limitation of the energy density, novel anode materials are needed. As can be seen in Figure 2.2, conversion-type anode materials and alloying-type anode materials are of importance for next generation LIBs because of their high specific capacities. Main-group IV (Si, Sn, Ge, *etc.*) and main-group V (P, Sb, *etc.*) elements and their composites as alloying-type materials have been proposed recently. The alloying reaction (Li + n X → Li_nX) refers to the formation of a new compound phase (Li_nX) by reaction of elements (X, Si, Ge, Sn, P, etc.) and Li. For example, the Si anode has a high theoretical capacity of 4200 mAh g^{-1} according to the reaction of 4.4 Li + Si ⟶ $Li_{4.4}Si$.[56,57] Another type of material, so-called conversion material, can also have high theoretical capacity, the reaction can be written as follows:

$$M_aX_b + (\mathrm{b} * \mathrm{n})\mathrm{Li} = \mathrm{a\ M} + \mathrm{b}\ Li_n\mathrm{X} \qquad (2.6)$$

Where M is transition metal, X = O, N, S, P, etc., and n is the formal oxidation state of X. New phases are formed in the M_aX_b electrode when it reacts with lithium. The reduced M metal embedded in a Li_nX matrix can be reversibly converted to its original state upon the recharge process. The transferred electrons greatly depend on the oxidation state of the transition metal such as Fe_2O_3 (6 electrons per formula unit, 1007 mAh g^{-1}), CoO (2 electrons, 715 mAh g^{-1}), FeS (2 electrons, 610 mAh g^{-1}), NiP_2 (6 electrons, 1333

mAh g^{-1}). Reversible capacities of ca. 600 to 1000 mAh g^{-1} were reported using conversion materials as anode.[58–60] However, these materials currently suffer from a large irreversible capacity in the first charge, and from a relatively poor cycling stability. Many strategies both on fundamental ways and engineering are proceeding to bring these high performance materials closer to the commercial implementation.

2.2.2 Sodium ion batteries

The sodium ion battery (SIB) has similar configurations and components as the LIB, i.e. cathode, anode, electrolyte, separator, and other batteries components. During the operation, sodium ions migrate between the cathode and the anode through a sodium ion conducting electrolyte while electrons are generated by a redox reaction at the respective electrode and are guided through the outer electrical circuit. The investigation on SIBs actually has been performed in parallel with lithium based systems in the 1980s.[61,62] However, due to the great successes of LIB chemistry, in particular, after the commercialization of LIBs in 1991, SIBs were regarded as less attractive. Undeniably, the widespread LIBs are promising candidates for power hybrid and electric vehicles. Nevertheless, in particular areas, for example the application of electric stationary storage such as grids, room temperature rechargeable SIBs could be an alternative to replace LIBs because the sodium element is much more abundant (2.64 wt %) than lithium (0.006 wt %) on earth. Moreover, since sodium and lithium are both in the first group of the periodic table, fundamental chemical properties of SIBs and LIBs are similar. There are still opportunities to develop high performance electrode materials and the development of SIB can be of great importance for sustainable energy storage in the future. In the next section, the state-of-art of cathode and anode materials for SIBs will be addressed.

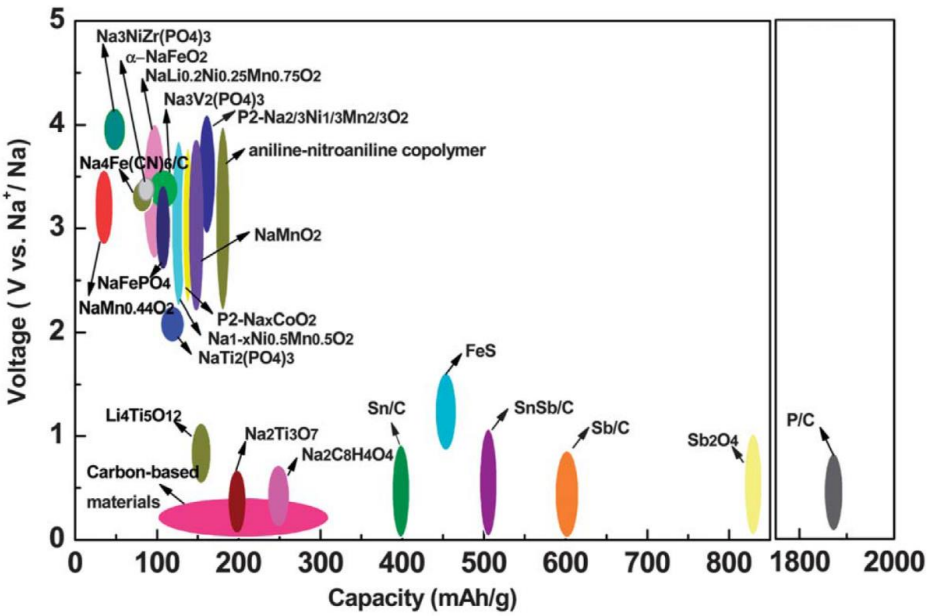

Figure 2.5: Electrode materials and the corresponding electrochemical performance for SIBs. Adapted from Ref.[63] with permission of The Royal Society of Chemistry.

Cathode: Layered materials of P2-Na_xCoO_2,[64] P2-Na_xMnO_2,[65] O3-$NaFeO_2$,[66] $NaCrO_2$,[67] $NaNiO_2$,[68] and solid solution layered oxides of O3-$NaNi_{1/3}Co_{1/3}Mn_{1/3}O_2$,[69] O3-$NaNi_{1/3}Mn_{1/3}Fe_{1/3}O_2$,[70] P2-$Na_{2/3}Ni_{1/3}Mn_{2/3}O_2$,[71] P2-$Na_{0.45}Ni_{0.22}Co_{0.11}Mn_{0.66}O_2$,[72] etc., have been proposed as candidate cathode materials for SIBs, as shown in Figure 2.5. Reversible discharge capacities of 80 - 160 mAh g^{-1} were reported depending on the type of cathode material. Among these metal oxide materials, the P2-type materials delivered higher reversible capacity and better cycle performance than the O3-type. In was suggested that the Na ion occupying a large trigonal prismatic site in P2 phase is kinetically favorable compared to in the octahedral site in O3 phase and that the phase transition from P2 phase to other phase is difficult.[73,74]

$Na_{0.44}MnO_2$ with an orthorhombic structure has two channels for sodium ion insertion/extraction, and can be a high power electrode. Cao *et al*. reported an excellent cycling stability of a SIB using $Na_{0.44}MnO_2$ nanowires as cathode, a capacity retention of 77% was achieved after 1000 cycles.[75] Phosphates and pyrophosphates

such as $NaFe_xMn_{1-x}PO_4$,[76] $Na_2MP_2O_7$ (M = Fe, Mn, Co),[77] were also proposed as cathode materials for SIBs due to their stable structure and high redox potential (3.0 V associated with Fe^{2+}/Fe^{3+} and 3.6 V associated with Mn^{2+}/Mn^{3+} vs Na/Na^+), with reversible capacities in the range of 60 - 120 mAh g^{-1}. NASICON type compounds are classic solid state Na^+ conductors due to the high Na^+ ion conductivity in their 3-D open structure. Zhu *et al*. reported a NASICON type of $Na_3V_2(PO_4)_3$ material embedded in a porous matrix carbon composite as cathode. A reversible capacity of 44 mAh g^{-1} was obtained within 7 seconds (200 C), capacity retention of 80 % was achieved after 1000 cycles at 10 C rate.[78] Other compounds such as $Na_{1.5}VOPO_4F_{0.5}$, Na_2MPO_4F (M= Fe, Mn, Co, Ni), FeF_3, $NaFeF_3$, and Prussian Blue have also been tested as cathodes due to their high redox potential and high reversible capacities.[79–82]

Anode: Sodium metal may not be suitable as anode for SIBs because the use of highly reactive sodium metal may cause safety issues. Graphite anodes, which are commonly used in LIBs, do not intercalate sodium to an appreciable extent and the intercalation of sodium rather proceeds in partially disordered environments such as hard carbon.[83,84] Several non-graphitic carbon materials were proposed as anode for SIBs, where reversible capacities of ca. 200 to 300 mAh g^{-1} were reported.[83,85,86] Charge and discharge curves of the hard carbon anode are shown in Figure 2.6. Two sloping profiles are often observed using hard carbon as anode in SIBs, implying two different processes upon the sodiation/de-sodiation. It was suggested that the intercalation/de-intercalation of Na ions into the graphene inter-layers of the hard carbon occurs in Region 1, and Na ions filling the pores of the carbon often occurs in Region II.

Non-carbon compounds were also investigated as anode. Similar to the concept in LIBs, intercalation, conversion, and alloying based materials have been proposed as non-carbon anode. Intercalation compounds such as $Na_2Ti_3O_7$,[87] TiO_2,[88] $Li_4Ti_5O_{12}$,[89] were reported to deliver high power density owing to the specific

channels for Na ions insertion/extraction, however, the reported specific capacity was low.

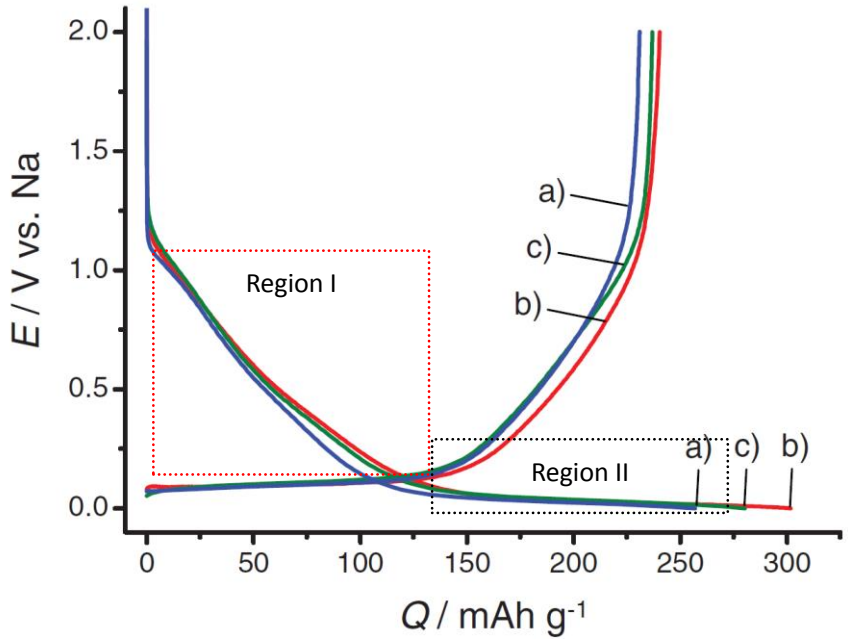

Figure 2.6: Charge and discharge curves of the hard carbon electrode, cycled in the electrolyte of $LiClO_4$ in (a) ethylene carbonate, (b) propylene carbonate, (c) butyl carbonate, respectively. Adapted from Ref.[83] with permission of The John Wiley & Sons, Inc.

Conversion compounds and alloying compounds provide opportunities to achieve higher capacity compared to intercalation compounds due to the multi-electron reaction. For example, conversion compounds of metal oxides (e.g. $CuO + 2\ Na \leftrightarrow Cu + Na_2O$, 674 mAh g^{-1}, theoretical capacity, the same below) and metal dichalcogenides (e.g. $MoS_2 + 4\ Na \leftrightarrow Mo + 2\ Na_2S$, 670 mAh g^{-1}) were investigated by several groups.[90,91] Alloying compounds such as Sn ($Sn + 4.4\ Na \leftrightarrow Na_{4.4}Sn$, 847 mAh g^{-1}), Pb ($Pb + 4.4\ Na \leftrightarrow Na_{4.4}Pb$, 485 mAh g^{-1}), Sb ($Sb + 3\ Na \leftrightarrow Na_3Sb$, 660 mAh g^{-1}) and P ($P + 3\ Na \leftrightarrow Na_3P$, 2596 mAh g^{-1}) were proposed as high performance anode materials for SIBs.[92–94] Despite all these efforts, the development of SIBs is still in an early stage. There may be more opportunities to reach high energy density, cyclic stability, and high rate capability of electrode materials for SIBs if new compounds and new chemistries are developed.

2.3 Rechargeable batteries based on anionic shuttle

The state-of-art of rechargeable batteries based on cationic shuttle, e.g. LIBs and SIBs have been discussed in previous sections. In principle, there are opportunities to build even higher energy density, safer and cheaper of novel battery systems than conventional Li or Na batteries, with rechargeable batteries based on anionic shuttle. Recently, two types of batteries based on anionic shuttle were proposed, i.e. fluoride ion battery (FIB) and chloride ion battery (CIB), where the charge transfer ions are fluoride ions and chloride ions, respectively. Of these two battery systems, FIBs might be suitable for the application of high temperature energy storage as several stable fluoride conductors are available for solid state electrolytes, while CIBs have potential to be used at room temperature.[95–98] This section mainly focuses on the CIB system where only a handful of research papers have been published so far. As mentioned, high theoretical capacities are possible as several electrons per formula unit can be transferred and several oxidation states of a transition metal can be used for storing the electrons. Selected redox couples for CIBs are shown in Table 2.1. Not only lithium anode, also other anode materials such as magnesium, calcium, sodium, etc. can be utilized in CIBs. Therefore, the investigation on a novel rechargeable battery based on chloride ions shuttle is of great interest and it initially provides opportunities to build better energy storage devices compared to some of the conventional batteries. In this section, the working principle of CIBs, solid state chloride ion conductors, and the investigation of CIBs are reviewed.

2.3.1 Working principle of chloride ion batteries

The working principle of the CIB is based on chloride ions shuttle between a cathode and an anode through an anion conducting electrolyte as shown in Figure 2.7. The cathodic and anodic reaction of the CIB during discharge process can be described as

follows:

At the cathode: $MCl_x + xe^- \leftrightarrow M + xCl^-$, (2.7)

at the anode: $M' + xCl^- \leftrightarrow M'Cl_x + xe^-$, (2.8)

where the cathode material and the anode material are MCl_x and M', respectively. M is a metal (e.g. Fe, Bi, Cu or V) or metal monoxide (FeO, VO or BiO), and M' is the low potential metal (e.g. Li, Na, Mg, Ca, or Ce). During the discharge, electrons are generated in a thermodynamically feasible, spontaneous redox reaction at the anode. These electrons travel through an external circuit to recombine with the cathode material (MCl_x), where the MCl_x is reduced to M and chloride ions are released. The released chloride ions leave the cathode, migrate through the electrolyte, and react with the M' at the anode, where $M'Cl_x$ is formed and electrons are generated. In the recharge, chloride ions and electrons move in the opposite direction, to the cathode and the anode, where the cathode and the anode recover back to their original state.

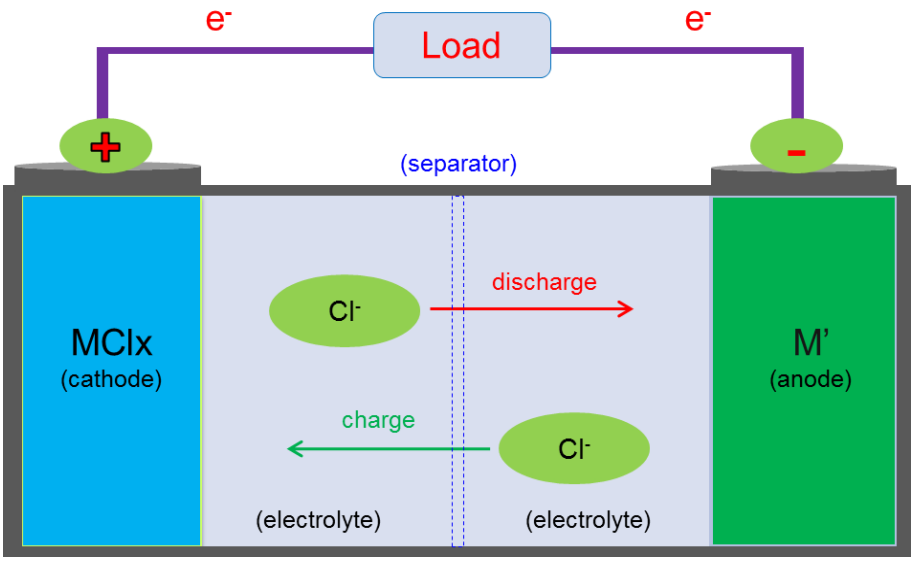

Figure 2.7: Sketch of the working principle of a CIB.

2.3.2 Solid state chloride ion conductors

Ion conductors are solids in which ions are highly mobile at certain conditions. These materials are important for the application of electrochemical devices and various sensors. The successful development on ion conductor for batteries is based on cationic mobility, e.g. lithium ion conductors. In addition, anion conductors, such as oxygen, fluoride, and chloride conducing compounds have also been studied.[99–102] In this section, an introduction will be given on solid state chloride ion conductors.

High chloride ionic conductivities at evaluated temperature have been achieved with cotunnite $PbCl_2$ structure compounds (space group *Pnma*), such as $PbCl_2$,[103] $SnCl_2$,[104] and $BaCl_2$.[105] Simkovich *et al*.[103] investigated the conductivity of the pure $PbCl_2$ and doped compounds, where an increased ionic conductivity was observed when $PbCl_2$ was doped by KCl, while the ionic conductivity decreased by introducing $LaCl_3$. At 573 K, a conductivity of 2.5×10^{-4} S cm^{-1} was observed for the pure $PbCl_2$. This value increased to 3.1×10^{-3} S cm^{-1} after doping 0.5 mol % of KCl in $PbCl_2$ and it decreased to 1.5×10^{-5} S cm^{-1} when 0.4 mol % of $LaCl_3$ were doped in the lattice at the same temperature. The migration of chloride ions through Schottky defects was proposed, as the concentration of chloride ion vacancies increases when the K atom takes the Pb site in a $PbCl_2$ lattice, while the concentration of chloride ion vacancies decreases when the La occupies the Pb sites.

Perovskite-type chlorides of $PbCl_2$·RbCl, $CsPbCl_3$, and $KMnCl_3$, were also proposed as chloride ion conductors.[106,107] The conduction mechanism in Perovskite-type chlorides was proposed to be similar to that of in cotunnite $PbCl_2$ structure compounds, where the chloride ion conductivity was caused by vacancy-hopping of chloride ions.

The Frenkel defect compound strontium dichloride ($SrCl_2$) was also proposed as chloride ion conductor.[108–111] G. M. Hood *et al*.,[108] studied the ionic conduction

and the ionic diffusion behavior in a single crystal of $SrCl_2$, revealing that the contribution of Sr^{2+} to the conductivity can be neglected. Hence, the conductivity of $SrCl_2$ was mainly attributed to the migration of chloride ions. The pure $SrCl_2$ crystal delivered conductivities of 1.5×10^{-5} and 1×10^{-2} S cm^{-1} at 373 K and 573 K, respectively. After doping with 0.01 wt % Na^+, the conductivity was increased to 3.9×10^{-2} (ohm^{-1} cm^{-1}) at 573 K. A further study on diffusion mechanism of $SrCl_2$ by M. Beniere *et al*.[109] suggested that the mobility of the cation can be negligible, and the motion of chloride ion in anion sub-lattice was partially due to the classic vacancy mechanism (80 %) and partially related to the exchange mechanism (20 %) where ions are occupied lattice and interstitial sites.

In addition, water-insoluble of lanthanum oxychloride (LaOCl) based solid electrolyte was also reported to be able to deliver a high chloride ion conductivity at high temperature.[112] By doping with 20 % Ca, i.e. $La_{0.8}Ca_{0.2}OCl_{0.8}$, the chloride ion conductivity increased significantly, up to 1.9×10^{-2} S cm^{-1} at 1073 K, which is about four orders of magnitude higher than that of the pure material. Hardy *et al.*[113] reported poly (diallydimethylammonium chloride) (DDAC) plasticized with poly (ethylene glycol) as a polymer chloride ion conductor. The reported anionic conductivity of the polymer was 1×10^{-5} S cm^{-1} at 299 K and 3×10^{-4} S cm^{-1} at 370 K, respectively. Further investigations on this system by Huang *et al.*[114] claimed that a maximum conductivity of 2.2×10^{-4} S cm^{-1} at 298 K was achieved by adding 8.8 wt % of a tetramethylammonium chloride salt in the polymer, a value that was 22 times greater than the value reported by Shriver. Although several chloride conductors were proposed and the conduction mechanisms were investigated years ago, there are no reports on using these chloride ion conductors as electrolytes in battery systems.

Table 2.1: Parameters of proposed electrochemical couples in CIBs.[a]

Battery reactions	ΔG/ KJ/mol	EMF/ V	Specific energy/ Wh/kg	Energy density/ Wh/L
$FeCl_3 + 3Li \rightarrow Fe + 3LiCl$	-819	2.83	1243	2392
$CuCl_2 + 2Li \rightarrow Cu + 2LiCl$	-593	3.07	1109	2506
$BiCl_3 + 3Li \rightarrow Bi + 3LiCl$	-838	2.89	691	2205
$2FeCl_3 + 3Mg \rightarrow 2Fe + 3MgCl_2$	-1107	1.91	773	1991
$CuCl_2 + Mg \rightarrow Cu + MgCl_2$	-416	2.15	725	2148
$2BiCl_3 + 3Mg \rightarrow 2Bi + 3MgCl_2$	-1145	1.97	452	1822
$CoCl_2 + 2Li \rightarrow Co + 2LiCl$	-499	2.58	962	2136
$CuCl + 2Li \rightarrow Cu + 2LiCl$	-264	2.74	693	1985
$VCl_3 + 3Li \rightarrow V + 3LiCl$	-642	2.21	997	1970
$NiCl_2 + 2Li \rightarrow Ni + 2LiCl$	-509	2.64	986	2264
$VOCl + Li \rightarrow VO + LiCl$	-232	2.41	590	1513
$2VOCl + Mg \rightarrow 2VO + MgCl_2$	-288	1.49	348	1088
$2VOCl_2 + Li \rightarrow 2VO + 2LiCl_2$	-537	2.78	982	2080
$VOCl_2 + Mg \rightarrow VO + MgCl_2$	-360	1.86	614	1672

[a] The calculation of the specific energy and energy density is based on the cathode and anode, excluding auxiliary components of a cell such as collector, electrolyte, separator etc. ΔG is Gibbs free energy, EMF is the electromotive force of a cell.

2.3.3 Chloride ion batteries

The proof-of-principle of CIBs was first proposed by Fichtner *et al.*[98] Several electrochemical couples were demonstrated as electrodes and ionic liquid electrolytes for chloride ion transfer in the first study. Composites of $CoCl_2$/C, VCl_3/C or $BiCl_3$/C (C denotes the carbon black) were used as a cathode, lithium foil was used as an anode, and an ionic liquid mixture of 1-methy-3-octylimidazolium chloride and 1-butyl-3-methylimidazolium tetrafluoroborate was used as an electrolyte in the first report. The ionic conductivity of the ionic liquid electrolyte was 9.1×10^{-4} S cm^{-1} at room temperature (298 K). The $CoCl_2$ electrode delivered a first discharge capacity of 80 mAh g^{-1} with a discharge plateau at around 2.5 V. *Ex-situ* XRD technique was

performed to identify the evolution of the electrode, where diffraction patterns related to Co metal in the cathode and LiCl phase in the anode were observed in the discharged state (Figure 2.8). This implies a reaction of $CoCl_2 + 2e^- \rightarrow Co + 2Cl^-$ in the cathode and the reaction of $Li + Cl^- \rightarrow LiCl + e^-$ in the anode, supporting the concept of a chloride ion shuttle.

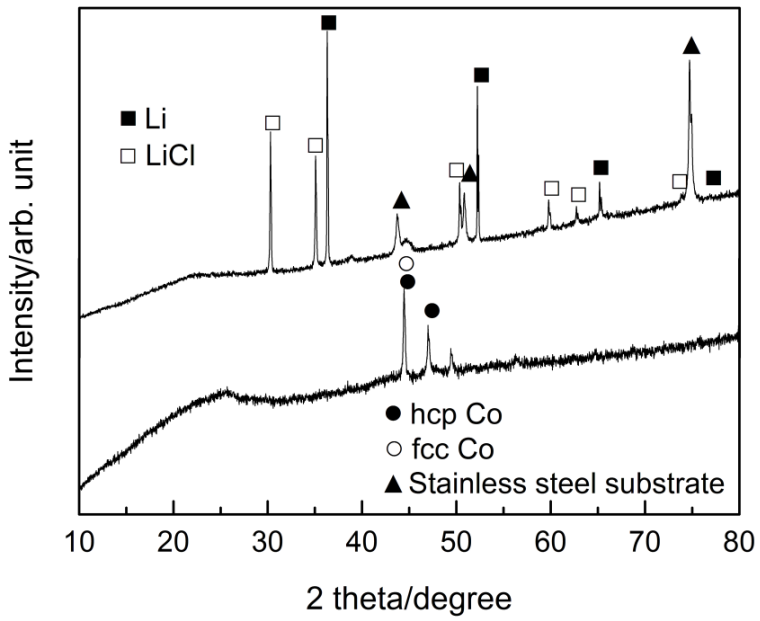

Figure 2.8: XRD patterns of lithium foil anode (up) and $CoCl_2$ cathode (bottom) in the first discharged state. Reprinted from Ref.[98], copyright (2014), with permission from Elsevier.

Several plateau regions were detected using VCl_3 or $BiCl_3$ as cathode, suggesting a multi-step reaction. Initial discharge capacities of 111 mAh g^{-1} and 176 mAh g^{-1} were obtained for the VCl_3 and $BiCl_3$ cathode, respectively (Figure 2.9). The electrochemical reaction mechanism was investigated by *ex-situ* XRD, XPS, and CV measurements. No diffraction peak was detected in the discharged state of the VCl_3 cathode, implying the formation of nano/amorphous phase. In the $BiCl_3$ electrode, sharp peaks ascribed to Bi metal were detected instead, indicating the dissociation of chloride ions from the cathode in the discharge. The reversible process was also evidenced by *ex-situ* XPS, where binding energies attributed to Bi metal in the discharged state and Bi^{3+} species were detected in the recharged state. However, a certain amount of cathode materials

was dissolved in the liquid electrolyte, leading to a poor cycling performance.

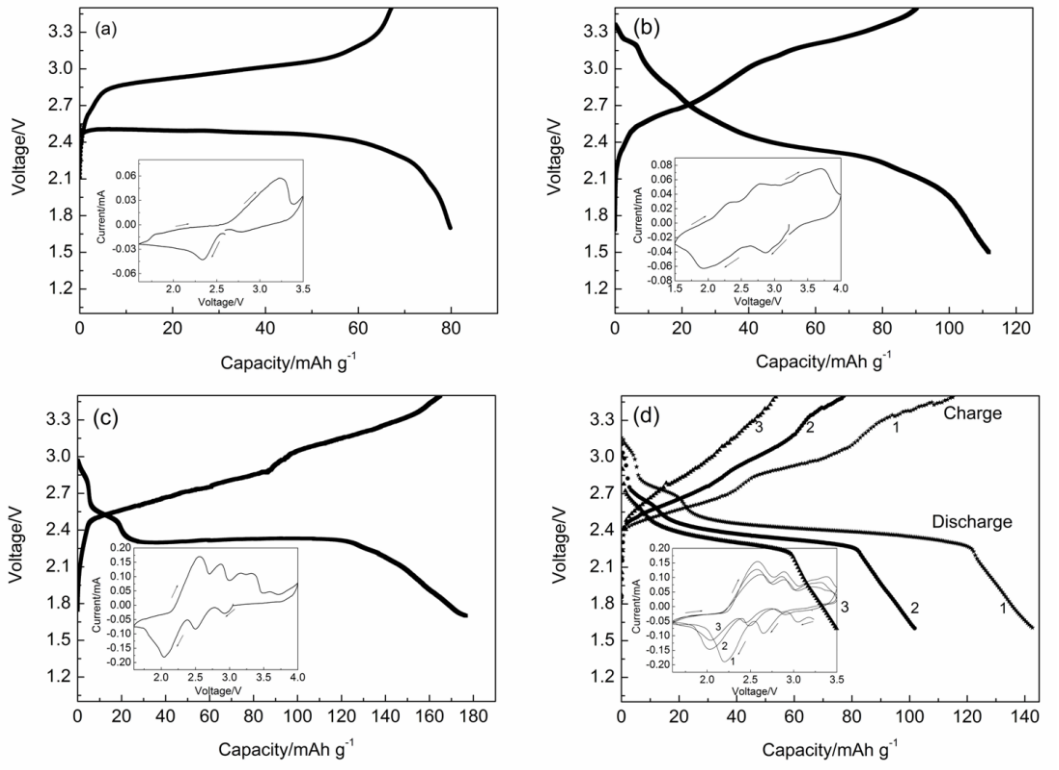

Figure 2.9: Charge and discharge curves of CIBs cycled at current densities of 1 or 3 mA g^{-1}. (a) $CoCl_2$-Li cell, (b) VCl_3-Li cell, (c) $BiCl_3$-Li cell and (d) $BiCl_3$-Li cell (cycled at 3 mA g^{-1}). Insets are the corresponding CV curves at a scan rate of 50 μV s^{-1}. Reprinted from Ref. [98], copyright (2014), with permission from Elsevier.

Metal oxychlorides (e.g. FeOCl, BiOCl) were also proposed as cathode for CIBs.[115] With strong metal-oxygen bonds in the compound, the metal oxychlorides are more stable than the metal chlorides in common liquid electrolyte. FeOCl or BiOCl were both tested as cathode with lithium foil as anode (FOCl-Li and BiOCl-Li cells). Two ionic liquid electrolytes of benzyldimethyltetradecylammonium chloride dissolved in butyltrimethylammonium bis(trifluoromethylsulfony)imide ($N_{116}Cl$) and 1-butyl-1-methylpiperidinium chloride dissolved in 1-butyl-1-methylpiperidinium bis(trifluoromethylsulfonyl)imide ($PP_{14}Cl$) were tested as the electrolyte. The concentration was 0.5 mol L^{-1}.

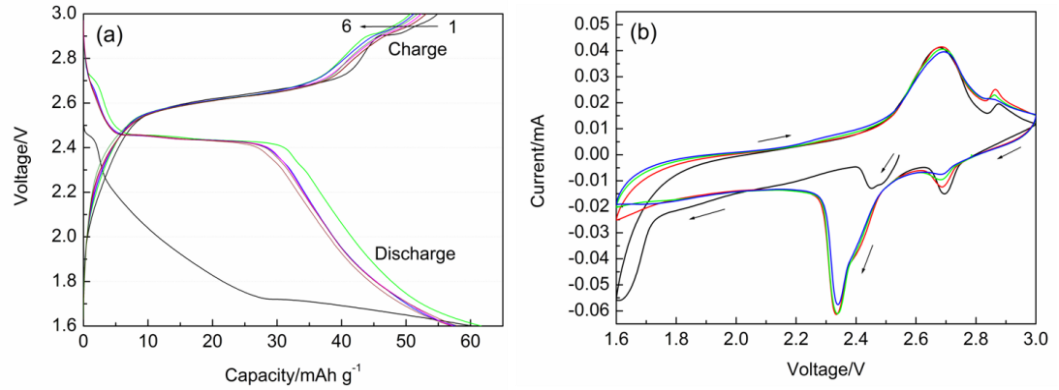

Figure 2.10: a) Charge and discharge curves (1st - 6th cycles with a current density of 5 mA g^{-1}) and CV curves (50 µV s^{-1}) of the BiOCl-Li battery cell using an electrolyte of 0.5 M $N_{116}Cl$ at 298 K. Adapted from Ref.[115] with permission of The John Wiley & Sons, Inc.

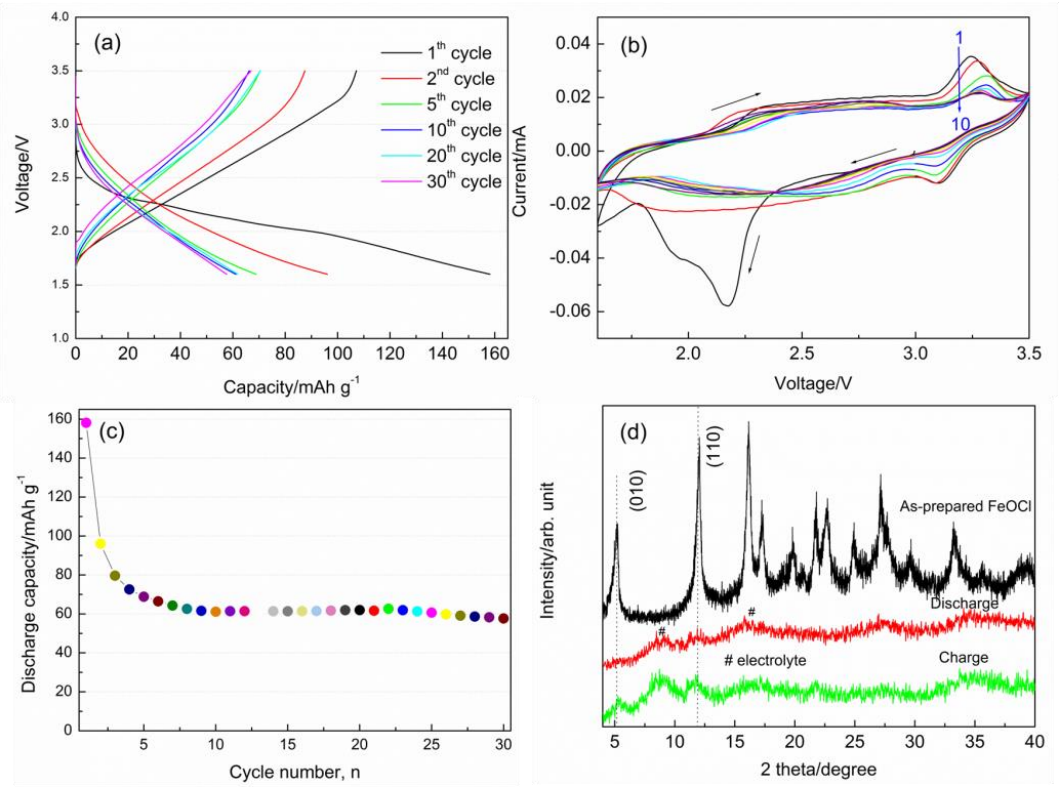

Figure 2.11: (a) Selected charge-discharge curves (10 mA g^{-1}), (b) CV curves (1st - 10th cycles at 60 µV s^{-1}) and (c) cycling performance of the FeOCl-Li battery cell, (d) XRD patterns of the FeOCl cathode in different states. Adapted from Ref.[115] with permission of The John Wiley & Sons, Inc.

Compared to the previously tested metal chlorides a better cycling stability was observed when using the metal oxychloride compounds. The BiOCl-Li battery cell

delivered a first discharge capacity of 60 mAh g^{-1} and only slight capacity fade was observed in the subsequent cycles (Figure 2.10). In FeOCl-Li battery cell, an initial discharge capacity of 160 mAh g^{-1} was reported and it decayed to 100 mAh g^{-1} in the second cycle at a current density of 10 mA g^{-1}. A reversible capacity of 60 mAh g^{-1} was maintained after 30 cycles (Figure 2.11). The reaction mechanism was characterized by *ex-situ* XRD and HRTEM, which evidenced that the chloride ion shuttled between the cathode and the anode during the charge and discharge process.

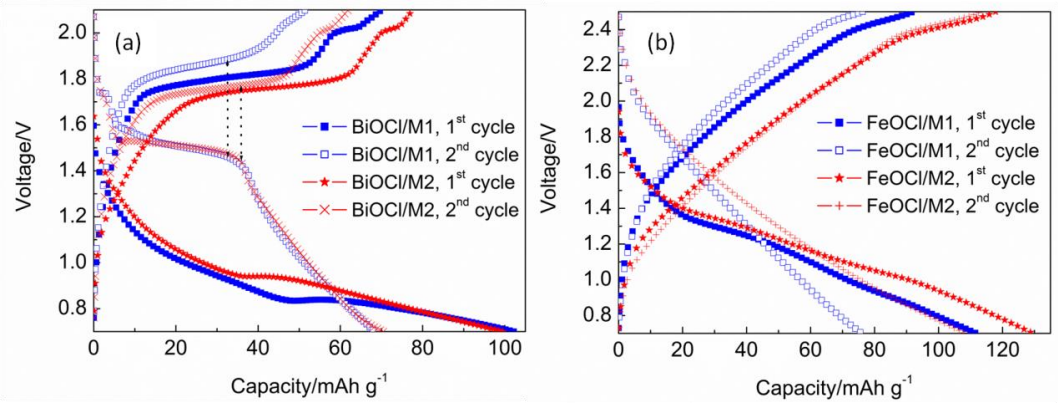

Figure 2.12: (a) Charge-discharge curves of BiOCl-Mg (5 mA g^{-1}), and (b) FeOCl-Mg (10 mA g^{-1}) battery cells using an electrolyte of 0.5 M $PP_{14}Cl$ at 298 K. Reprinted with permission from Ref.[116]. Copyright (2014) American Chemical Society.

Beneath lithium, magnesium was also tested as an anode for the CIB. Zhao *et al.* reported a lithium free CIB using FeOCl or BiOCl as the cathode, and Mg as the anode and an ionic liquid electrolyte of 0.5 M $PP_{14}Cl$ at room temperature.[116] The performance of the CIB cell using different Mg anodes was compared. It was shown that the cell can hardly be cycled if Mg foil was directly used as the anode. In contrast, relatively stable charge and discharge curves were achieved using a ball milled magnesium powder and carbon black composite (M1) or Mg/C composite (M2) prepared by decomposing a mixture of ball milled MgH_2 and carbon black. The hysteresis of the cell using M2 anode was smaller than using M1 as anode. Discharge capacity of 102 and 130 mAh g^{-1} were obtained in BiOCl-Mg (M2 as anode) battery cell and FeOCl-Mg (M2) battery cell, respectively (Figure 2.12). The $MgCl_2$ phase was

detected in the Mg anode after discharge using XRD and XPS techniques, indicating the migration of chloride ions.

There are challenges such as the dissolution of active material into the electrolyte leading to poor cycling stability. Novel chemistries and concepts for CIBs are needed to mitigate these deleterious effects.

2.4 Rechargeable batteries based on both cationic and anionic shuttles

In previous sections, the state-of-art of rechargeable batteries based on cation shuttle, e.g. LIBs or SIBs, and on anionic shuttle, e.g. CIBs were discussed. There is another concept under investigation, the so-called “dual-ion” batteries. Here, the shuttle ions are both cations and anions, and both are stored simultaneously at the electrodes. Currently, two “dual-ion” batteries were proposed, i.e. graphite electrode and organic electrode based batteries. Because of their fast reaction kinetics, high power densities can often be obtained of these batteries.

2.4.1 Graphite electrode based dual-ion batteries

Graphite intercalation compound (GIC) is a redox-amphoteric intercalation host, therefore cations (donor-type) or anions (acceptor-type) can in principle be electrochemically intercalated at different voltages.[117] Compared to the limited number of cationic intercalation guests (Li^+, Na^+), a variety of anions can intercalate into the graphite to form acceptor-type GICs, such as tetrafluoride species, e.g. PF_6^-, AsF_6^-, BF_6^-, oxide based guests including SO_4^-, NO_3^-, ClO_4^- and hexachloride compounds such as $AlCl_4^-$.[118–120] In addition, intercalation of large anions into graphite has also been reported, such as bis(trifluoromethanesulfonyl) imide ($(CF_3SO_2)_2N^-$), tris(trifluoromethanesulfonyl) methide ($(CF_3SO_2)_3C^-$), trifluoroacetate ($CFCOO^-$), or perfluorooctanesulfonate ($C_8F_{17}SO_3^-$).[121–123] A high redox potential (> 4.0 V vs Li/Li^+)

can be achieved if anions are intercalated into the graphite interlayer. Therefore, the commonly used graphite anode material for LIBs can also be used as a cathode material in rechargeable batteries. The concept of GICs intercalated by anions as cathode was suggested by Carlin *et al*.[124] The cell using a 1,2-dimethyl-3-propylimidazolium-tetrachloroaluminate [DMPI][$AlCl_4$] electrolyte achieved an open-circuit voltage of 3.5 V. The electrolyte did not only act as a charge carrier but also delivers the species for intercalation. Placke *et al.*[122,123] reported a highly reversible graphite cathode for intercalation/de-intercalation of bis (trifluoromethanesulfonyl)imide anions ($TFSI^-$) from an ionic liquid electrolyte, where lithium metal or insertion hosts (graphite, and $Li_4Ti_5O_{12}$) were used as anodes for intercalation/de-intercalation of Li^+ cations. This dual-ion battery delivered a stable cycling performance with a capacity retention of 99 % after 500 cycles. Typical charge and discharge curves of the dual-ion cell using a graphite cathode and a lithium metal anode are shown in Figure 2.13. One of the merits of using graphite as cathode is that a high discharge potential (~4.5 V vs Li/Li^+) can be provided, enabling a high energy density. In addition, high power density can be achieved as well, which is close to that of supercapacitors.

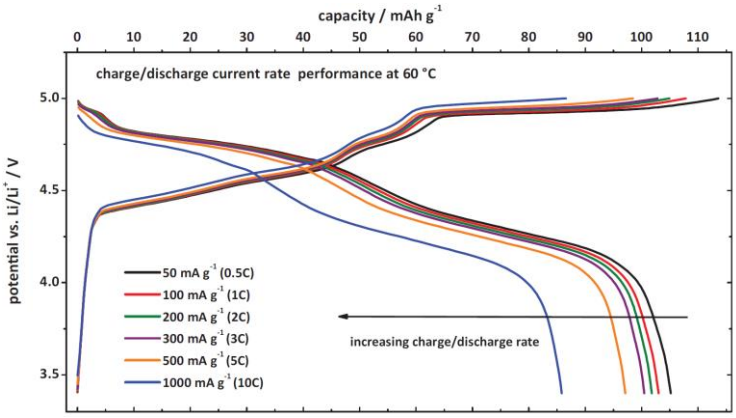

Figure 2.13: Charge and discharge curves of a dual-ion cell with a graphite cathode and a lithium anode at different current densities, operation temperature was at 333 K, the potential range was 3.4 - 5.0 V. Reproduced from Ref.[123] with permission of The Electrochemical Society.

A symmetric dual-ion cell, in which the graphite acted both as cathode and as anode in an electrolyte containg Li^+ cation and $TFSI^-$ anion, was also reported.[123] The reaction mechanism is proposed in Figure 2.14, where anions intercalate into the graphite cathode while cations intercalate into the graphite anode during the charge process. In the discharge process, both ions are returned back into the electrolyte. A reversible capacity of 120 mAh g^{-1} was reported at a cutoff potential of 5.2 V (vs Li/Li^+).

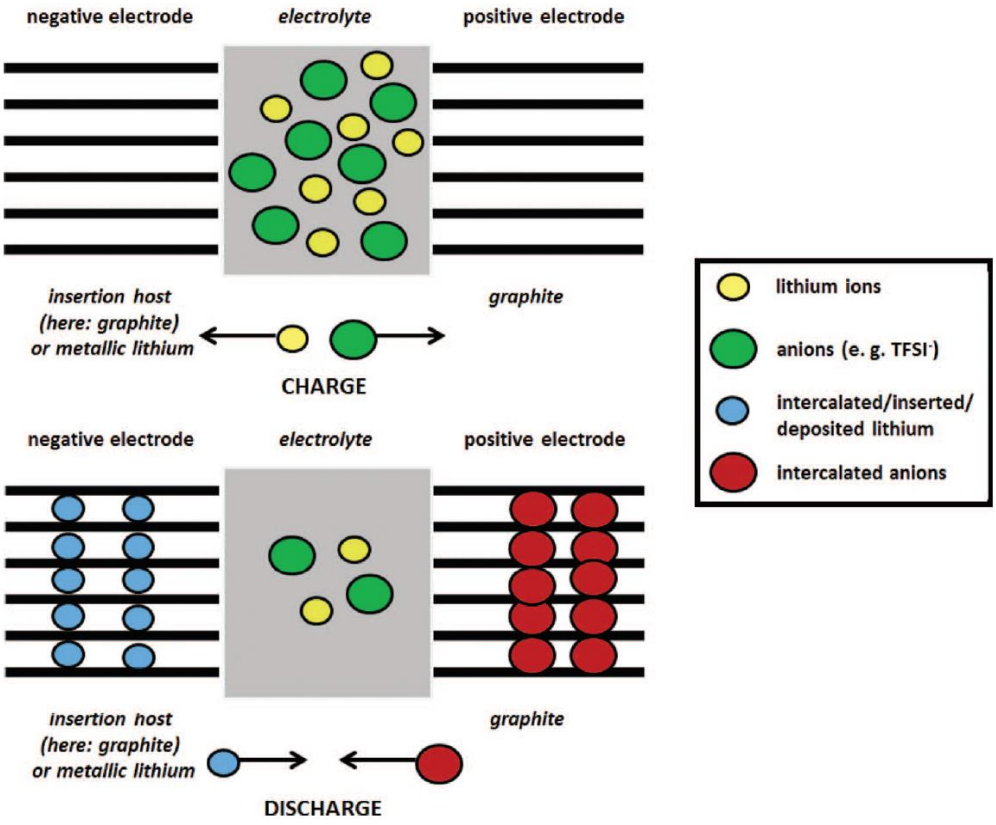

Figure 2.14: Working principle of a dual-ion cell with a graphite cathode and a Li metal or insertion host anode during the charge process (upper part) and discharge process (lower part). Reproduced from Ref.[123] with permission of The Electrochemical Society.

The concept of the dual-ion battery using graphite as both electrodes also attracted industry's interest and a disruptive carbon battery (carbon material for both cathode and anode) was announced in 2014 by Power Japan Company and Kyushu University.[125] They claimed that this battery not only had a high energy density, but

it was also economical, safe, reliable, and environmentally sustainable. Most importantly, it can charge 20 times faster than common used Li-ion batteries. Nevertheless, there are still challenges that need to be addressed, e.g., suitable anions with appropriate size and stable electrolytes with large electrochemical window (high cutoff potential > 5.0 V is preferred) are needed.

2.4.2 Organic electrode based dual-ion batteries

Organic electrode materials for energy storage have been considered as alternatives for conventional inorganic electrode materials due to their tunable properties, environmental friendliness, flexibility, good safety and sustainability.[126,127] Different from the redox reaction mechanism of the inorganic electrode which is related to the change of valence of the transition metal, for the organic electrode, the redox reaction is ascribed to the change of the charge state of the electroactive organic group or moiety. Organic electrode materials can be divided into the following three types: n-type organics, p-type organics, and bipolar-type organics. For n-type organics, such as organodisfulfide and conjugated carbonyl molecules, the electron transfer is between the neutral state (N) and the negatively charged state (N^-) of a molecule (Figure 2.15 a and b). In p-type organics, such as conjugated amine and conjugated thioether molecules, the reaction is between the neutral state (P) and the postively charged state (P^+) (Figure 2.15 c and d). In bipolar-type organics (B) (Figure 2.16), such as conjugated hydrocarbon and nitroxyl radical molecules, the reaction is either between the negatively charged state (B^-) and the neutral state (B), or between the positively charged state (B^+) and the neutral state (B), or even between the negatively charged state (B^-) and the positively charged state (B^+).

Several organic electrode materials and their redox mechanism are proposed as shown in Table 2.2. Most of organic electrode batteries are typically Li-organic batteries with p-type or bipolar-type organic electrode. They involve dual ions shuttle during the

electrochemical reaction. This means the anion (A^-) and cation (Li^+) of the electrolyte are transported between the electrolyte and the electrode during the electrochemical reaction.

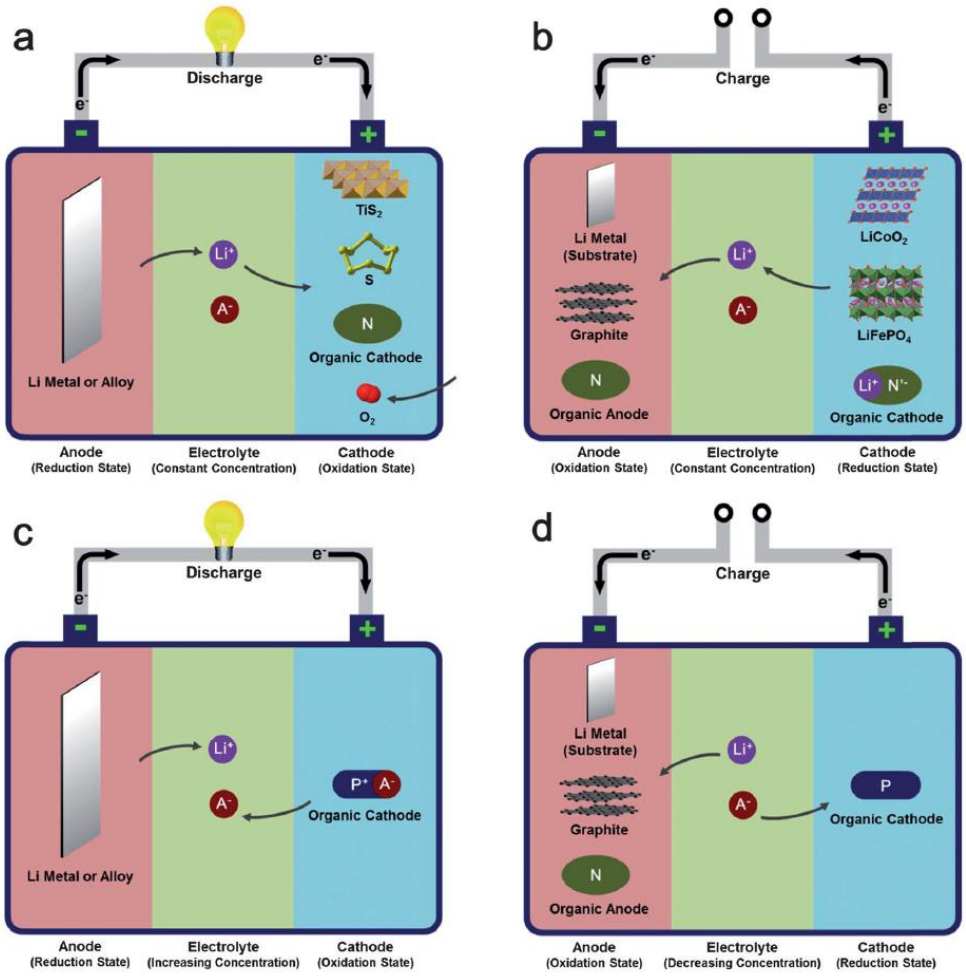

Figure 2.15: The cell configurations and charge transfer processes of various types of rechargeable batteries, (a and b) n-type organic material electrode, (c and d) p-type organic material electrode. Bipolar organic systems can be regarded as both n- and p- type in these configurations according to the real electron reaction. Adapted from Ref.[127] with permission of The Royal Society of Chemistry.

Compared to the relatively low redox potential of n-type organic electrode (< 2.5 V vs Li/Li^+), an average discharge potential more than 3.0 V (vs Li) can be obtained if p-type or bipolar-type organic electrode materials are used. For example, the bipolar-type of

nitroxide radical polymer, poly(2,2,6,6-tetramethylpiperidenyloxyl-4-yl methacrylate) (PTMA), delivered an average discharge potential of 3.5 V (vs Li/Li^+).[128–130] This compound also endures fast reaction kinetics and cycling stability. A capacity retention of 89 % of the PTMA electrode was obtained after 1000 cycles and the discharge profile was almost the same even at a high current density of 50 C rate.[131] The electron transfer process of nitroxide radical electrode is shown in Figure 2.16.

Table 2.2: The structure and redox mechanism of different type of organic electrode materials. Adapted from Ref.[127] with permission of The Royal Society of Chemistry.

Structure	Redox mechanism	Examples
Conjugated hydrocarbon	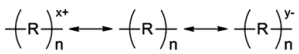	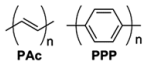 PAc PPP
Conjugated amine	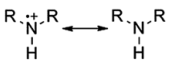	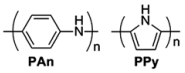 PAn PPy
Conjugated thioether	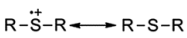	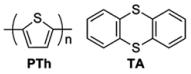 PTh TA
Organodisulfide	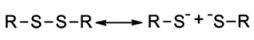	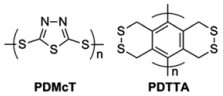 PDMcT PDTTA
Thioether (4e)	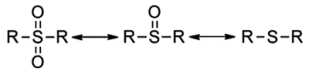	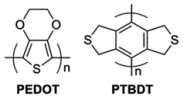 PEDOT PTBDT
Nitroxyl radical	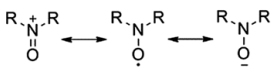	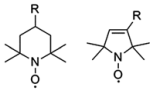
Conjugated carbonyl	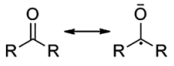	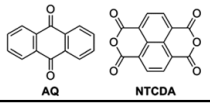 AQ NTCDA

The nitroxide radical is a typical oxygen-centered stable radical with spin-density localization on the oxygen atom, which displays two redox couples, i.e. it can either be oxidized to form the corresponding oxoammonium cation (p-type) or reduced to the aminoxy anion (n-type). This type of organic compound therefore has attracted remarkable interest as it can either be used as a cathode or as an anode, or even as both cathode and anode for an all organic battery. The schematic illustration of a dual-ion cell using nitroxide material as a cathode and a graphite anode is shown in

Figure 2.17, where cations and anions of the electrolyte diffuse into to the anode and the cathode during the charging, respectively.

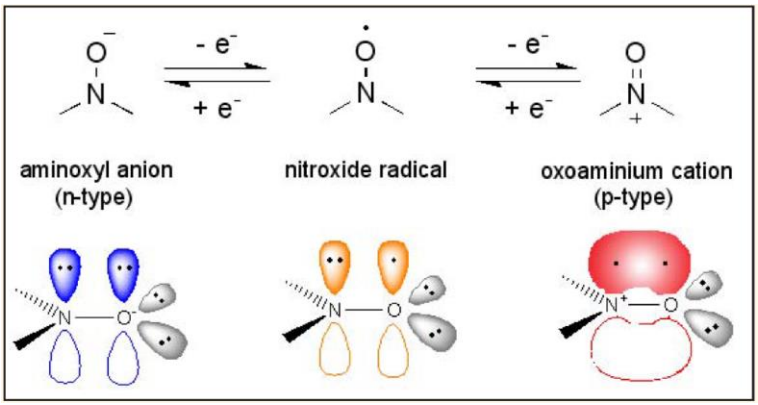

Figure 2.16: The redox processes involving a nitroxide radical (bipolar-type). Adapted from Ref.[132] with permission of The Electrochemical Society.

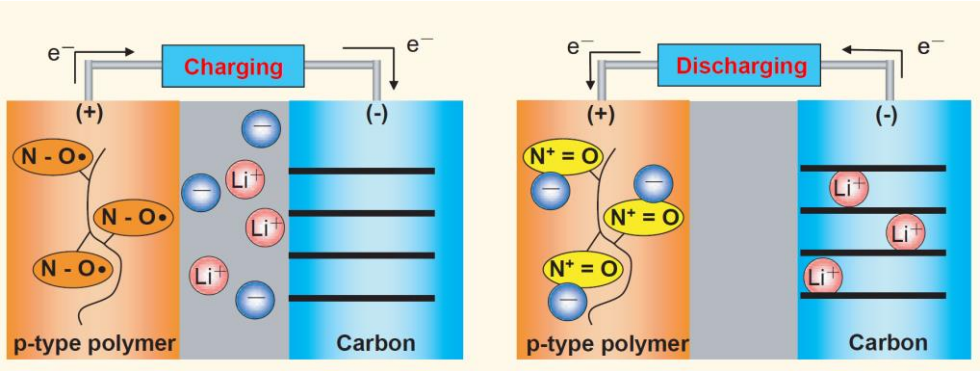

Figure 2.17: A rechargeable Li-organic battery based on the nitroxide electrode. Adapted from Ref.[132] with permission of The Electrochemical Society.

Suga *et al.* reported an all organic battery using a redox-active radical compound of poly[4-(nitronylnitroxyl)styrene] as both cathode and anode.[133] In the charging process, anions migrated to the cathode, while cations transferred to the anode (Figure 2.18 i). The cation and anion were returned back into the electrolyte in the discharging process (Figure 2.18 ii). In addition, further discharge is still possible due to the flexible change of the N-O charge state. For example, the cathode at i stage (p-type) can be further discharged in the formation of n-type at the stage of iii (as anode). The result showed that an extremely high current density (150 C rate) can also be endured.

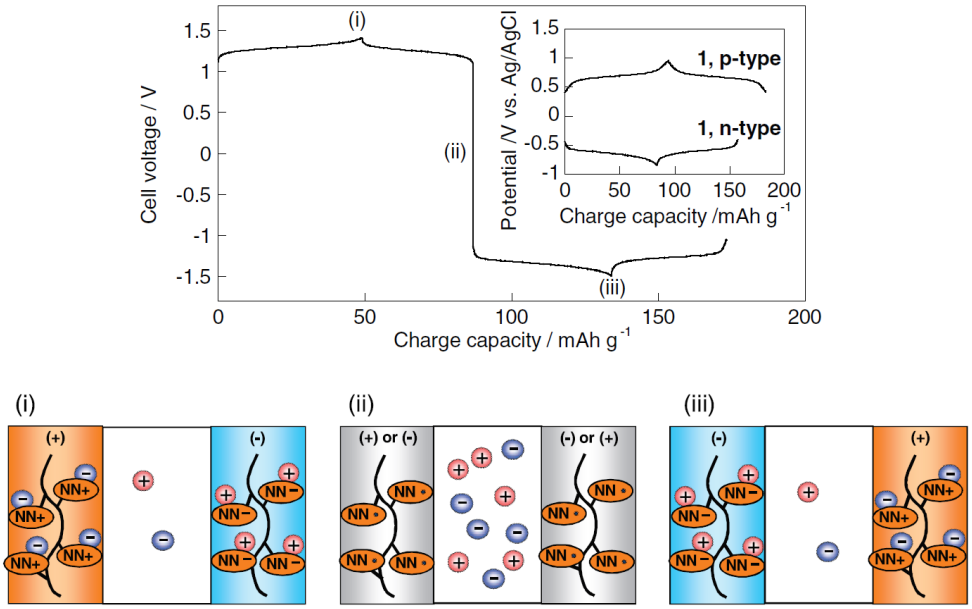

Figure 2.18: The working principle of the all organic battery cell using nitroxide radical compound as both cathode and anode. NN refers to the N-O group in the nitroxide radical compound. Adapted from Ref.[133] with permission of The John Wiley & Sons, Inc.

Rechargeable batteries based on dual-ion shuttle would provide many opportunities to build novel sustainable energy storage devices. First of all, these batteries are potentially more environmentally friendly than conventional LIBs because the organic electrodes do not need to contain any metals that may cause problem of the disposal. In addition, cheap and renewable organic resources can be used as electrode materials. Moreover, high power densities can be achieved due to the fast kinetics of the electrochemical reaction. It could be a suitable candidate for bridging supercapacitors and batteries for the next generation energy storage.

2.5 Aim of the thesis

The target of this thesis is to develop new electrode materials and new chemistries for rechargeable batteries, aiming at broadening the idea and offering more materials and opportunities for the future energy storage. Three different battery systems are designed, including batteries based on anionic (chloride ion batteries), both cationic

and anionic (organic based batteries), and cationic shuttle (Li-ion and Na-ion batteries).

In Chapter 4 and Chapter 5 of the thesis, a novel concept of rechargeable battery based on anionic (Cl^-) shuttle is tested, i.e. chloride ion battery (CIB). A layered vanadium oxychloride (VOCl) material is synthesized and used as a cathode in the CIB. Both lithium anode and magnesium anode are introduced in the CIB. These two chapters will assess the electrochemical performance and reaction mechanism of the CIB.

Chapter 6 aims at developing a new porphyrin complex as electrode for rechargeable batteries. Due to the bipolar redox property of the molecule, it is used as a cathode, as anode, and as both cathode and anode in the cells, enabling the shuttle of both cations and anions during the charge and discharge. Three cells are constructed with different components to investigate the reaction mechanism. The long-term cycling stability and high rate capability of the cells are explored.

Chapter 7 is aimed at developing high performance electrode for Li-ion and Na-ion batteries which are based on multi-electron reactions. The layered VOCl material is used as electrodes for both cells. The number of the transferred electrons is controlled by adjusting the working window. The electrochemical performance and the reaction mechanism of the electrode are investigated.

The use of new materials as electrode for rechargeable batteries could provide opportunities for developing sustainable energy storage systems. High performance of energy storage devices could also be made with rechargeable batteries based on different ionic shuttles during the electrochemical reaction.

Chapter 3 Experimental methods

3.1 X-ray diffraction

X-ray diffraction (XRD) is an analytical technique primarily used for identifying the structure of a crystal. The wavelength of the X-rays (0.01 - 10 nm) is in the same order of magnitude as the spacing (d) between atomic planes in the crystal, which is necessary in a diffraction experiment. X-ray diffractometers consist of three basic elements: an X-ray tube, a specimen holder, and an X-ray detector. The electrons are produced by heating a tungsten filament, and are accelerated towards an anode target (e.g. copper) by applying a high voltage (20 - 60 kV). When these electrons have sufficient energy to dislodge inner shell electrons of the target material, continuous spectra of X-rays are produced. Since only K_α radiations are required for XRD analysis, undesirable parts of the X-rays such as K_β radiations are removed by a monochromator. When the incident X-rays are collimated and directed onto the specimen, the scattered X-rays which are emitted by atoms interfere each with other and with different intensities. The constructive interference occurs only when the path length difference of diffracted X-rays is equal to an integer multiple of the wavelength (Figure 3.1). The mathematical condition for the constructive interference can be described by Bragg's law,[134]

$$n \cdot \lambda = 2 \cdot d \cdot \sin\theta \qquad (3.1)$$

where λ is the wavelength of the incident X-ray, d is the interplanar spacing, θ is the

diffraction angle, n is an integer. During the measurement, the specimen and the detector are rotated, and the intensity of diffracted X-rays is recorded. Because there are many individual crystals of random orientation in the powder sample, therefore all possible diffractions can be observed.

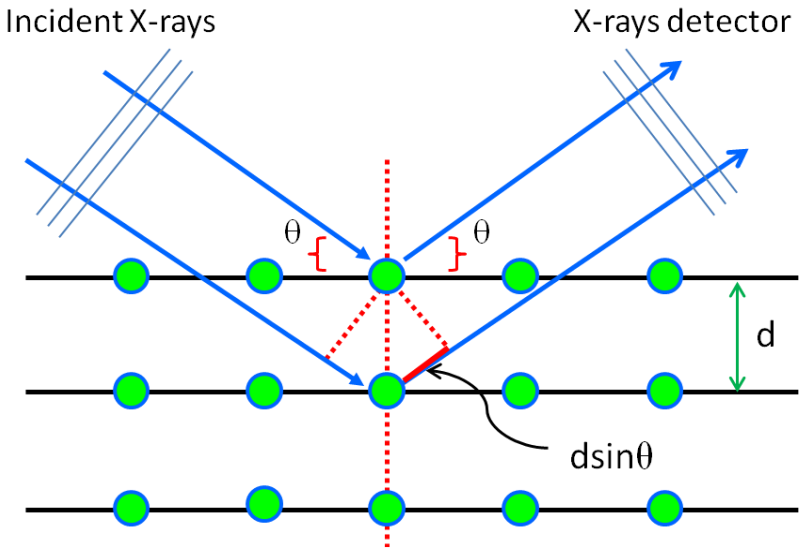

Figure 3.1: Geometry for interference of a wave scattered from two atoms.

In this work, powder XRD patterns were recorded on a STOE STADI P powder diffractometer with a Debye-Scherrer transmission geometry (operated at 40 kV, 40 mA) and a Bruker D8 Advance diffractometer (operated at 50 kV, 40 mA) with a Bragg-Brentano reflection geometry in Ulm and a Philips X'PERT diffractometer (operated at 40 kV, 40 mA) in Karlsruhe, respectively. The Cu $K\alpha_1$ radiation (λ = 0.154 nm) was used for the measurements.

3.2 Scanning electron microscopy

The scanning electron microscopy (SEM) is used to image the sample by scanning its surface with a high-energy beam of electrons, providing much higher magnification than in an optical microscopy, due to the shorter wavelength of the electron beam. The electron beam interacts with atoms at the surface of the sample, producing

several signals that can be used to obtain the information of the surface topography of the sample. There are three signals which are generated during the interaction, i.e. backscattered electrons (BSEs), secondary electrons (SEs), and characteristic X-rays.[135] The schematic setup of a SEM is shown in Figure 3.2.

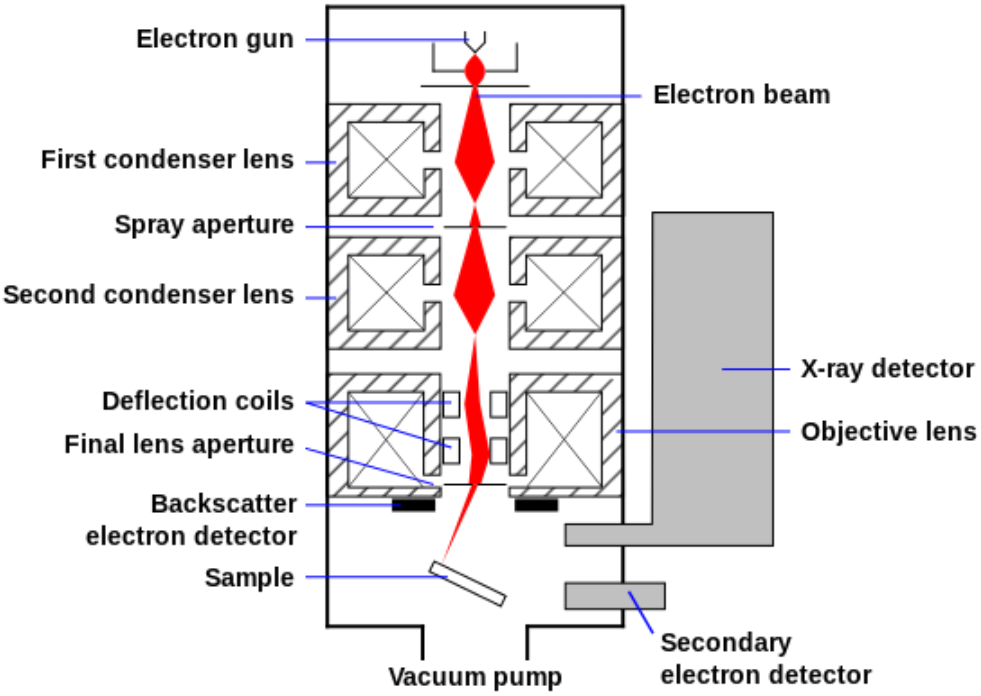

Figure 3.2: Schematic setup of a SEM. Adapted from free encyclopedia [136], open access under the CC BY-SA 3.0, https://creativecommons.org/licenses/by-nc-sa/3.0/.

The most common imaging mode in SEM is the collection of low-energy SEs. These electrons are ejected from the K-shell of the specimen atoms by the primary electron beam. Due to the low energy (< 50 eV), secondary electrons are emitted close to (a few nanometers) the sample surface. High-resolution images can therefore be produced by detecting these electrons with a secondary electron detector. BSEs are primary electrons which are backscattered by atoms of the specimen. Since heavy elements backscatter electrons more strongly than light elements, these electrons are useful to provide chemical contrast information of the materials.

Characteristic X-rays are emitted when the electron beam releases inner shell

electrons of the specimen, causing outer-shell electrons to fill the vacancy in the inner shell (Figure 3.3).[137] These characteristic X-rays are measured by an X-ray detector and used to identify the composition and the elements of the sample. This method is called energy dispersive X-ray spectroscopy (EDS or EDX).

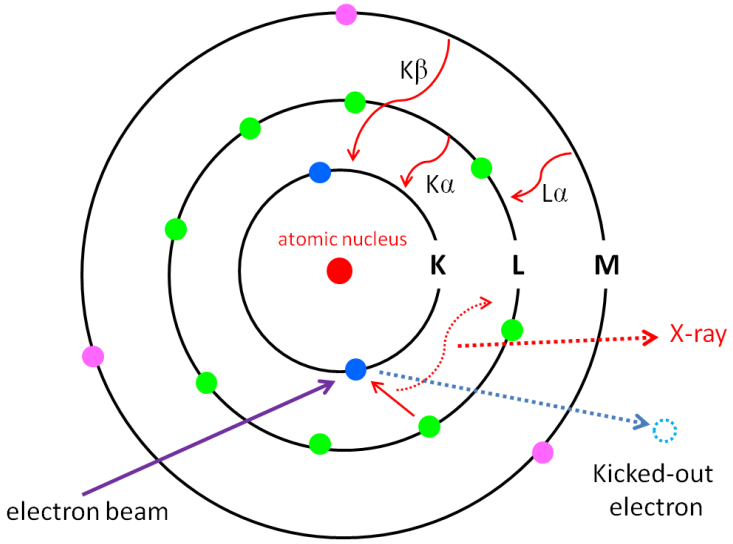

Figure 3.3: Principle of characteristic X-ray generation.

In this work, SEM images and EDX spectra were obtained using a ZEISS LEO 1550 VP Field Emission SEM with an X-Max Silicon Drift Detector.

3.3 Transmission electron microscopy

Transmission electron microscopy (TEM) is a microscopy technique which can provide very high resolution images down to a level of angstroms (1 Å = 0.1 nm). The schematic setup of a TEM is shown in Figure 3.4. Because electrons are needed to transmit the specimen, a high voltage (100 - 300 kV) is required in the TEM system. And the specimen should be thin enough (< 100 nm) to allow electrons to pass through. When an electrons beam passes through a specimen, electrons are scattered. A sophisticated system of electromagnetic lenses focuses the scattered electrons into an image, or a diffraction pattern, or a nano-analytical spectrum depending on the

mode of operation. Each of these modes offers a different insight about the specimen. For example, the bright field imaging mode, the common used mode for a TEM, provides a highly magnified view of the micro- and nanostructure. In the high resolution imaging mode a direct map of atomic arrangements of the specimen can be provided.

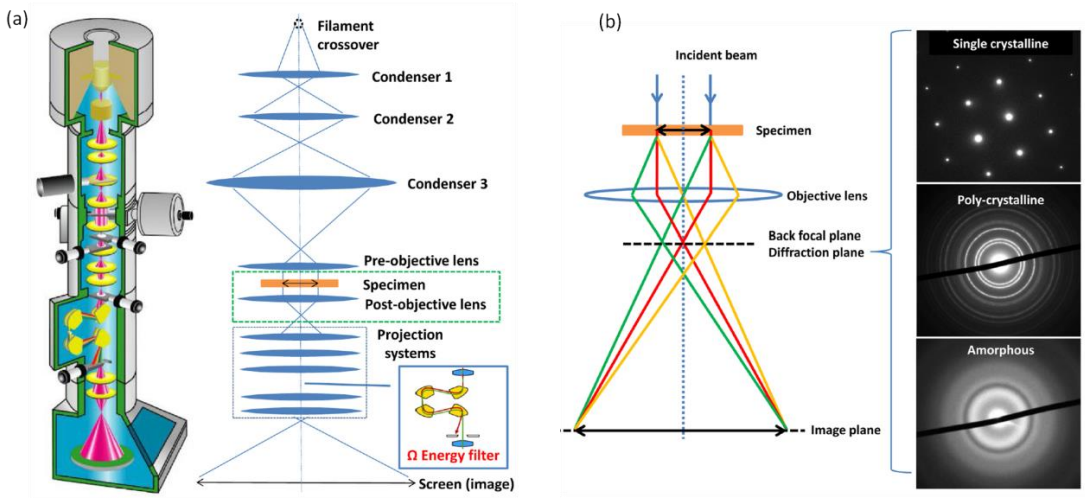

Figure 3.4: (a) Schematic setup of a TEM, (b) the detailed ray diagram near the objective with some examples of diffraction patterns. Based on Zeiss EM912 Ω operating manual [138].

The local crystal structure information can be provided using a diffraction mode, e.g. selected area diffraction (SAD) images. When the electrons pass through the sample, some fraction of electrons can be scattered to particular angles, resulting in diffraction patterns in an image. Single spots appear only if incident electrons are diffracted by a single crystal, while SAD of polycrystalline materials gives ring patterns, and the feature of concentric rings will disappear for amorphous materials (Figure 3.4b). In nanoanalytical modes, the inelastic interactions occur between incident electrons and specimen, the energy loss can be determined by an energy loss spectrometer, where the elements, chemical bonding information of the sample can be provided. This technique is called electron energy loss spectroscopy (EELS).

In this work, the transmission electron microscopy (TEM) measurement was performed using an aberration (image) corrected FEI Titan 80-300 operated at 300 kV

acceleration voltage, equipped with a Gatan US1000 CCD camera, a Gatan Tridem 863 energy filter and an EDAX S-UTW EDX detector at the Institute of Nanotechnology (INT), Karlsruhe Institute of Technology (KIT).

3.4 X-ray photoelectron spectroscopy

X-ray photoelectron spectroscopy (XPS), also known as Electron Spectroscopy for Chemical Analysis (ESCA), is a surface-sensitive semi-quantitative spectroscopic technique that measures the chemical information of specimen on the surface. The principle of an XPS measurement is shown in Figure 3.5. When the specimen is irradiated by incoming photons (such as an Al Kα primary radiation with energy of 1486.6 eV), core level electrons of atoms on the surface are emitted, and kinetic energies (E_k) of these electrons are measured by the detector (see Figure 3.5). Based on the conservation of energy, the characteristic binding energy (E_b) of respective elements can be calculated, giving the elemental composition information of the specimen on the surface.

$$E_b = h\upsilon - E_k - \phi \qquad (3.2)$$

Φ is a work function taking into account energy absorbed by the detector, h is Plank's constant, and υ is the frequency of the photon.

XP spectra were measured using a physical Electronics PHI 5800 ESCA System with mono-chromatic Al K_α radiation (13 kV, 250 W) and pass energies of 93.9 eV for survey scans over the whole binding energy range and 29.35 eV for detail scans, respectively. The measurement was carried out at the Institute of Surface Chemistry and Catalysis, Ulm University, Germany.

(a)

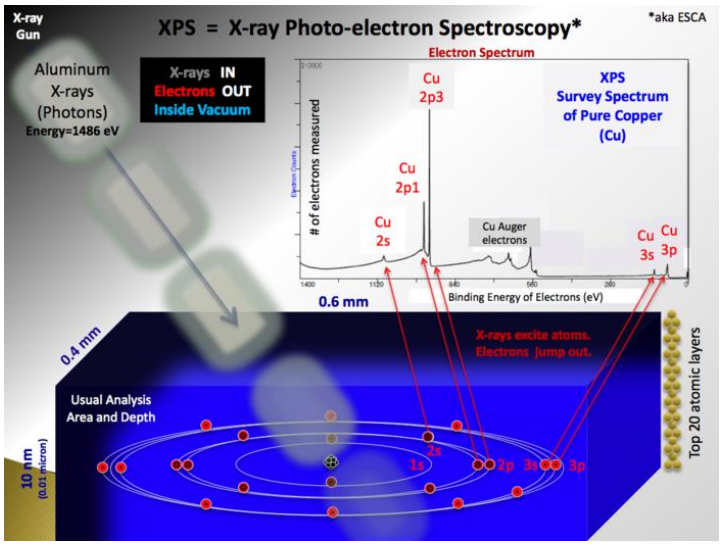

(b)

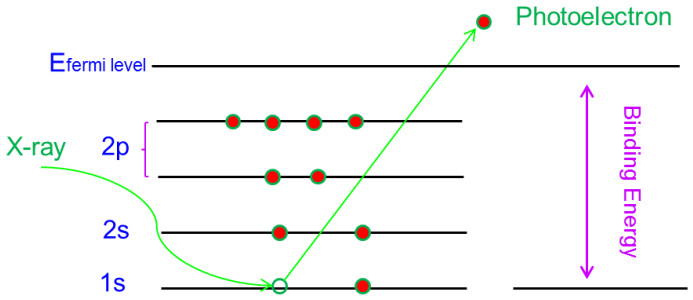

Figure 3.5: (a) Principle of an XPS measurement, and (b) schematic diagram of the photoemission process of a XPS. Adapted from free encyclopedia [139][140], open access under the CC BY-SA 3.0, https://creativecommons.org/licenses/by-nc-sa/3.0/.

3.5 Infrared spectroscopy

Infrared (IR) spectroscopy is an analytical technique used to indentify molecular components and structures of a sample. It has been widely used in the organic structure determination and verification. An infrared spectrum is commonly obtained by passing infrared radiation through the sample and determining what fraction of the incident radiation is absorbed at a particular energy. In a molecule, different functional groups bend, stretch, or wag at different frequencies, the molecule will absorb the infrared radiation only if the frequency of the incident radiation matches the

frequency of stretching, bending, or wagging of the functional group. Therefore, absorption bands in IR spectra enable to determine if certain functional groups are present in a molecule. A typical IR spectrum is a plot of the amount of transmitted infrared versus its wavenumber ($\bar{\nu}$). Wavenumber is inversely proportional to the wavelength ($\bar{\nu} = 1/\lambda$) with a unit in cm^{-1}. Most bonds in organic molecules absorb infrared radiation with wavenumbers between 4000 cm^{-1} and 400 cm^{-1}.

Fourier transform infrared spectroscopy was measured with a Perkin Elmer Infrared spectroscopy instrument (Spectrum Two L1600401) in an argon-filled glovebox at Helmholtz Institute Ulm.

3.6 Galvanostatic cycling

The galvanostatic cycling technique is widely used for characterization of energy storage devices. In galvanostatic mode, a fixed current is set and controlled between the working electrode (WE) and the counter electrode (CE), and the potential between the WE and reference electrode (RE) is monitored. In this investigation, a two-electrode setup is used, where CE and RE are shorted on one of the electrodes while the WE is on the opposite side as shown in Figure 3.6. In this setup, the potential across the complete cell is measured, which includes potential contributions from the CE/electrolyte interface and the electrolyte itself. Therefore, the electrochemical behavior of the whole cell is under investigation.

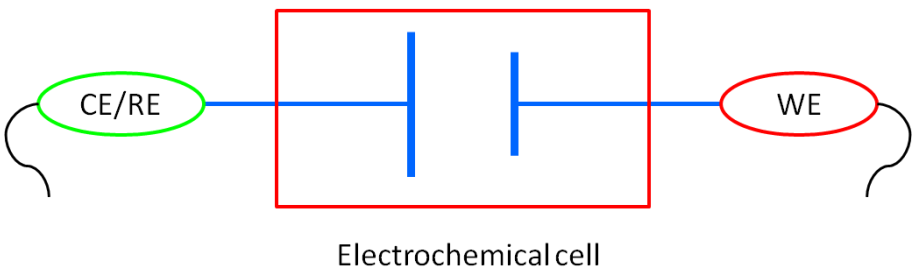

Figure 3.6: Schematic view of a two-electrode setup.

The capacity (Q_1) is an important factor to evaluate the performance of an electrode or a battery. It can be given as follows:

$$Q_1\ (mAh) = \int_0^t i(t)dt \qquad (3.3)$$

Where *i* is the set current, and *t* is the time of the measurement. The value is determined by the mass of the active material contained in the electrode or the battery. In order to evaluate the performance of an electrode, the specific capacity (Q_2) is used. The theoretical specific capacity (*C*, mAh g^{-1}) of the active material can be calculated according to the Faraday's law in equation 2.1 see section 2.1.

In this work, charge-discharge experiments were performed with an Arbin BT2000 battery system at 298 K with two-electrode setups of 2032-type coin cell or Swagelok cell.

3.7 Cyclic voltammetry

Cyclic voltammetry (CV) is a type of potentiodynamic electrochemical measurement. It is generally used to investigate the electrochemical properties of an electrode. In CV, the electrode potential ramps linearly versus time (scanning rate: mV s^{-1}) as shown in Figure 3.7a. The potential is applied between the working electrode and the reference electrode, while the current is measured between the working electrode and the counter electrode as shown in Figure 3.7b. The cathodic current (i_{pc}) and cathodic potential (E_{pc}) can be estimated when the scan goes towards negative direction, where a reduction reaction occurs ($A + e^- \rightarrow A^-$). In the reversible process, the anodic current (i_{pa}) and anodic potential (E_{pa}) will be provided, corresponding to the oxidation reaction of $A^- - e^- \rightarrow A$ (Figure 3.7b).

The difference between two peak potentials ($\Delta E = E_{pa} - E_{pc}$) gives important information about the redox system. In an ideal case of a reversible *n* e^- transferred

reaction, the difference (ΔE) should be 59/*n* mV. However, the typical value observed experimentally is often greater than that of the theoretical one, due to activation barriers of the charge transfer process and the diffusion of reactants at the electrode surface.

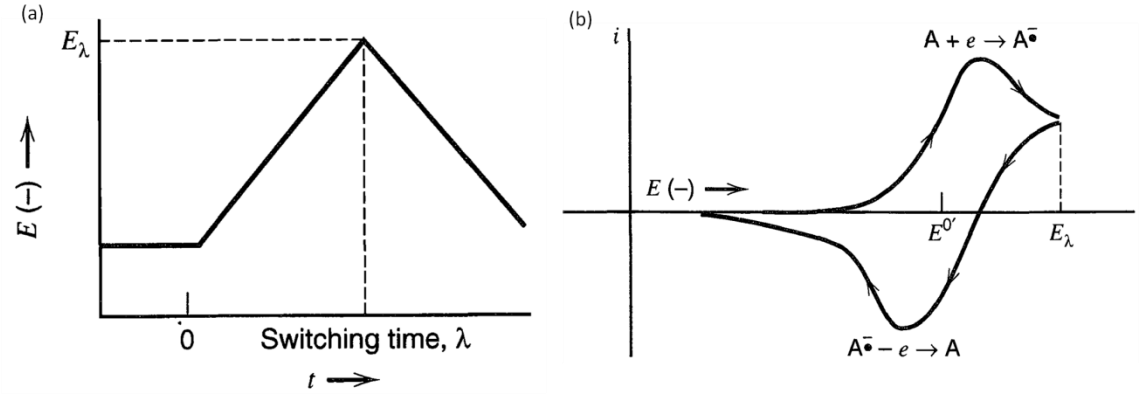

Figure 3.7: (a) the electrode potential ramps linearly versus time in cyclical phases, (b) typical cyclic voltammogram. Adapted from Ref.[141].

Linear sweep voltammetry (LSV) is similar to the cyclic voltammetry technique, which is also used to investigate the property of electrochemical systems. However, the scanning on the electrode is not inverted afterwards in LSV. It is often used to test the stability of the electrolyte in battery systems, giving the information of the electrochemical stability window of the electrolyte. CV and LSV data were collected using a Biologic VMP-3 electrochemical workstation in this work.

Chapter 4 VOCl cathode and lithium anode for rechargeable chloride ion batteries

4.1 Introduction

This chapter is based on the publication of *Angew. Chem. Int. Ed.,* 2016, 55, 4285-4290, titled "VOCl as a cathode for rechargeable chloride ion batteries", copyright (2016) John Wiley and Sons.

Recently, a novel rechargeable battery has been demonstrated based on chloride ion shuttle, i.e. chloride ion batteries (CIBs).[98] Multiple electron redox reactions have been realized in the first study of CIBs using active materials of $BiCl_3$, VCl_3 and $CoCl_2$ as cathodes, lithium metal as an anode and an ionic liquid electrolyte as transfer agent for chloride ions. However, the metal chloride compounds in this study were partly soluble in the liquid electrolyte, leading to poor cycling stability. More stable metal oxychlorides such as FeOCl, and BiOCl were proposed as potential cathode materials for CIBs due to their strong metal-oxygen bonds.[115] Investigation of CIBs currently focuses on exploring potential electrodes and electrode combinations with high reversibility, as well as the compatible electrolytes.

In this chapter, a novel room temperature chloride ion battery (Li/PP_{14}Cl-PC/VOCl) using layered VOCl material as a cathode, lithium metal as an anode, and a liquid chloride ion electrolyte was studied and the electrochemical reaction mechanism of the VOCl electrode was investigated in detail by various *ex situ* techniques.

4.2 Experimental section

4.2.1 Synthesis of VOCl

VOCl was synthesized by a solid-gas reaction.[142] Typical synthesis involved heating a mixture of 0.63 g V_2O_3 (98 %, Sigma Aldrich) and 1.2 g VCl_3 (97 %, Sigma Aldrich) in an evacuated and sealed quartz tube kept at 893 K for 120 hours with a heating rate of 1 K min^{-1}. The length, diameter and thickness of the quartz tube were 300 mm, 15 mm and 2 mm, respectively. A brown powder was obtained when the quartz tube was cooled down to room temperature naturally. The product was purified by washing with water and acetone to remove residual VCl_3 and it was further dried at 353 K under vacuum for 5 h.

4.2.2 Material characterization

Scanning electron microscopy (SEM) measurements were carried out using a ZEISS LEO 1530 instrument. Powder X-ray diffraction (XRD) patterns were recorded on a STOE STADI-P diffractometer with a Debye-Scherrer transmission geometry (operated at 40 kV, 40 mA) and a Bruker D8 Advance diffractometer (operated at 50 kV, 40 mA for lithium anode measurement), both equipped with a Cu Kα radiation source (λ = 0.154 nm**).** Fourier transform infrared spectroscopy (FTIR) was recorded between 4000 cm^{-1} and 400 cm^{-1} with a Perkin Elmer Infrared spectrometer instrument (Spectrum Two L1600401) in an argon-filled glovebox at room temperature. Transmission electron microscopy (TEM) was performed using an aberration (image) corrected FEI Titan 80 - 300 operated at 300 kV acceleration voltage, equipped with a Gatan US1000 CCD camera, a Gatan Tridem 863 energy filter and an EDAX S-UTW EDX detector. The sample was transferred under inert conditions (Argon) from the glove box to the microscope by using a Gatan vacuum transfer holder minimizing the possible reaction between the sample and the air. X-ray photoelectron spectroscopy (XPS) data were

recorded on a Physical Electronics PHI 5800 ESCA System using mono-chromatized Al K_α radiation (13 kV, 250 W) and pass energies of 93.9 eV for survey scans over the whole binding energy (BE) range and 29.35 eV for detail scans, respectively. Binding energy of XPS peaks were referenced to the C_{1s} signal of carbon black at 284.5 eV. The TEM and XPS measurements and evaluation of the data were performed by the respective operator of the instrument.

4.2.3 Electrode preparation

The cathode material was prepared by grinding a mixture of active material (VOCl, 56 mass %), polyvinylidene fluoride binder (PVDF, 10 mass %) and carbon black (34 mass %) with N-methyl-2-pyrrolidone (NMP) as solvent in a mortar for 30 minutes. The obtained slurry was then spread on stainless steel foils (SS, 16 mm in diameter) and dried at 373 K under vacuum overnight. The mass loading of the cathode material was 2.0-3.0 mg cm^{-2}. Lithium foil was used as the anode.

4.2.4 Electrochemical measurements

Electrochemical tests were conducted using 2032 type coin cells (Hohsen Corp., Japan). The glass fiber filter (GF/D, Whatman) was used as a separator. A solution of 0.5 M 1-butyl-1-methylpiperidinium chloride ($PP_{14}Cl$, 99 %, IoLiTech) in propylene carbonate solvent (PC, anhydrous, Sigma-Aldrich) was used as electrolyte. In addition, 1 M $LiPF_6$ dissolved in a mixture of ethylene carbonate (EC), dimethyl carbonate (DMC), and PC with a volume ratio of 1 : 3 : 1 was used as an electrolyte for testing the performance of the VOCl electrode in lithium ion battery. The charge and discharge measurements were performed using an Arbin BT2000 battery system at 298 K. Cyclic voltammetry (CV) and linear sweep voltammetry (LSV) data were collected with a Biologic VMP-3 electrochemical workstation. The CV was measured at a sweep rate of 0.1 mV s^{-1} in a potential range of 1.0 - 2.8 V.

4.3 Results and discussion

The XRD pattern of the as-synthesized VOCl and the VOCl/C composite is shown in Figure 4.1a. All peaks matched well with the VOCl reference pattern from Powder Diffraction File (PDF) card number 01-074-1274. In addition, small amounts of impurities of V_2O_3 (ca. 2 wt %), VCl_2 (ca. 1 wt %), and presumably an fcc metal were also found (see Figure A-1 in Appendix). Layered VOCl crystallizes in an orthorhombic structure with a space group of *Pmmn* (lattice parameters: a = 3.77 Å, b = 3.30 Å, c = 7.93 Å), which agrees well with the previous report.[143] The buckled V-O bilayer is sandwiched between chlorine layers that are weakly coupled along vector *c* by van der Waals forces. Each vanadium atom lies in the center of a distorted octahedron with two chloride atoms and four oxygen atoms as shown in the refined structure of VOCl (Figure 4.1b).

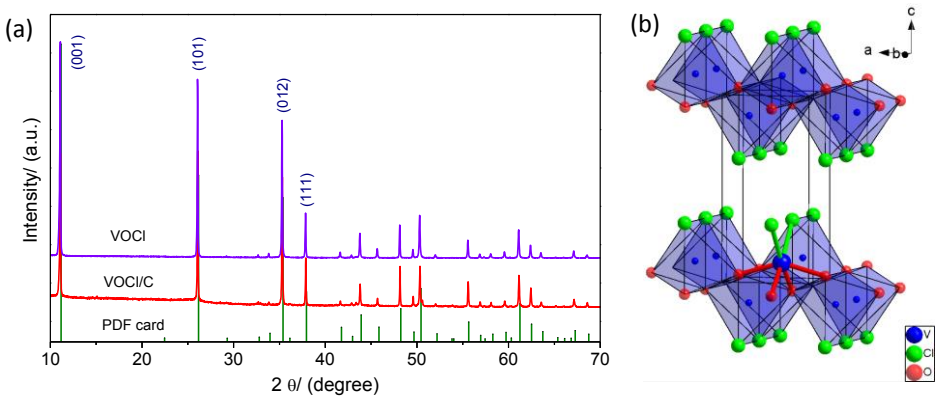

Figure 4.1: (a) XRD patterns of the VOCl and the VOCl/C composite, (b) crystal structure of the VOCl.

SEM images of the as-synthesized VOCl material and the VOCl/C composite are shown in Figure 4.2. They exhibit rod shape morphology with a length of 2 - 5 µm and approximately 300 nm in diameter (Figure 4.2a and Figure 4.2b). VOCl semiconductor was mixed with conducting additive of carbon black, thereby providing good electrical contact of VOCl in the electrode during the electrochemical reaction. The VOCl

particles in the composite retained the same morphology and particle size as the as-prepared VOCl, and were homogenously dispersed in carbon black as shown in Figure 4.2 c and Figure 4.2d.

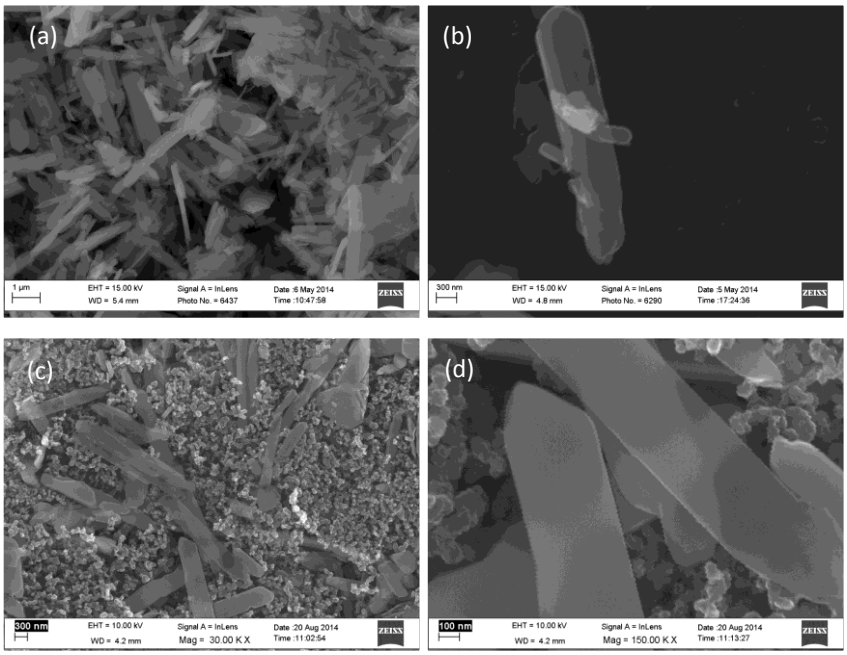

Figure 4.2: (a, b) SEM images of the VOCl, and (c, d) the VOCl/C composite.

The liquid electrolyte of the $PP_{14}Cl$-PC (0.5 mol L^{-1}) prepared in the study has a high ionic conductivity of 4.4 mS cm^{-1}, with an electrochemical window of 3.2 V (vs Li) measured at room-temperature, thus providing a stable environment for the electrochemical reaction (Figure A-2 in Appendix). The initial CV curve of the Li/$PP_{14}Cl$-PC/VOCl cell scanned in a voltage range of 1.0 - 2.8 V at 0.1 mV s^{-1} is shown in Figure 4.3a. Three main redox couples were observed at 1.57/1.67 V, 1.42/1.56 V, 1.2/1.26 V, which indicate a reversible multiple-step reaction proceeding during the discharge and recharge processes. In the subsequent cycles, the CV curves were similar to that of the first cycle. In addition, an irreversible anodic peak at around 2.5 V was only observed in the first cycle, the origin of this peak will be discussed below. Figure 4.3b shows the charge-discharge curves of the Li/$PP_{14}Cl$-PC/VOCl cell for the first 10 cycles obtained at a current density of 0.5 C (1 C = 261 mA g^{-1}). A small plateau

was observed at round 2.5 V, followed by a monotonic voltage drop to 1.7 V, and three discharge plateaus were observed at around 1.6, 1.5 and 1.2 V. A total discharge capacity of 189 mAh g^{-1} was obtained in the 1st discharge, corresponding to 0.72 electrons per VOCl unit participating in the reaction. A capacity of 180 mAh g^{-1} was recovered in the 1st recharge process with an irreversible capacity loss (ICL) of 9 mAh g^{-1} at 0.5 C.

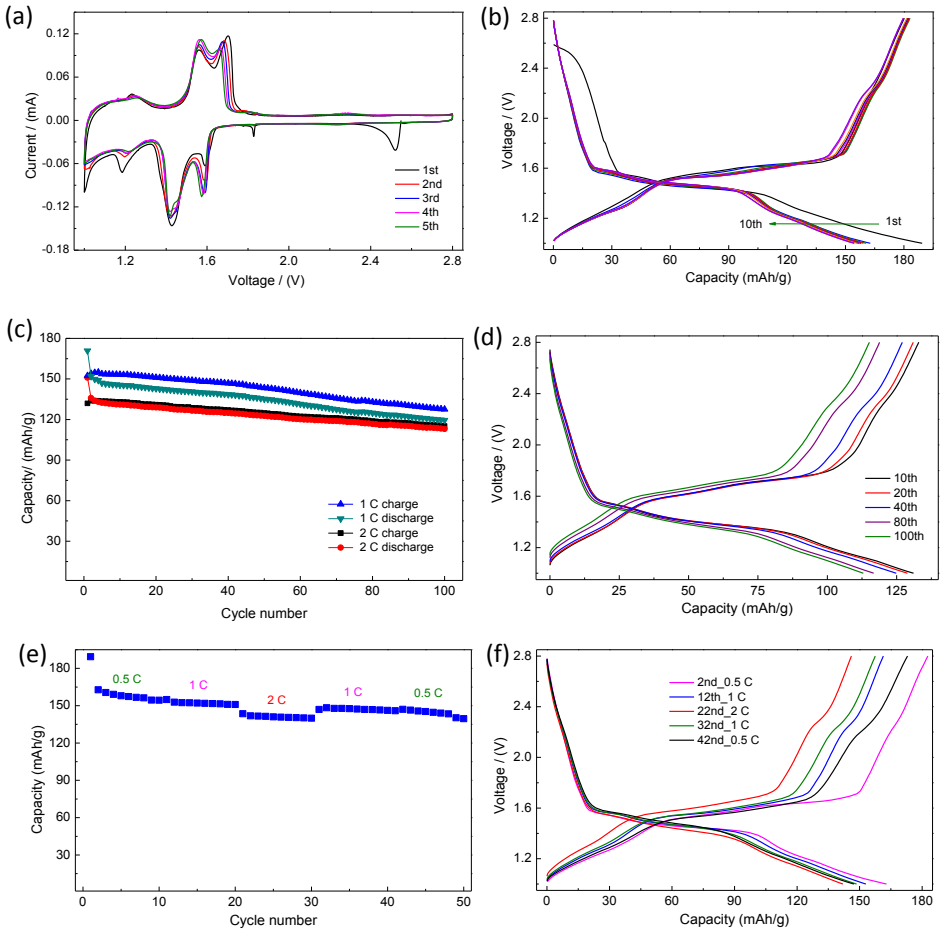

Figure 4.3: (a) CV curves of a Li/PP_{14}Cl-PC/VOCl cell at a scan rate of 0.1 mV s^{-1}, (b) initial charge-discharge curves of the cell at a current density of 0.5 C in the voltage range of 1.0 - 2.8 V, (c) cycling performance at 1 C and 2 C, (d) selected charge-discharge curves of the cell at 2 C, (e, f) rate performance of the cell, 1 C = 261 mA g^{-1}.

In the subsequent cycles, charge-discharge curves are very similar to that of the first cycle, which suggest a high reversibility of the VOCl electrode in this cell. The extension

of the small plateau at 2.5 V corresponds to a capacity of 20 mAh g^{-1}, which is equivalent to a 0.07 mole electron transfer. This step is attributed to the intercalation of 1-butyl-1-methypiperidinium ions (PP_{14}^{+}) from the electrolyte into the VOCl electrode. Previous reports have indicated that large organic cations can be intercalated into the interlayer of metal oxychlorides.[144–149] The intercalated molecule was detected by combined XRD, FTIR and XPS measurements, which will be discussed later.

The cycling performance of the Li/PP_{14}Cl-PC/VOCl cell recorded at current densities of 1 C (261 mA g^{-1}) and 2 C (522 mA g^{-1}) are shown in Figure 4.3c. Initial discharge capacities of 170 mAh g^{-1} and 151 mAh g^{-1} were obtained in a voltage range of 1.0-2.8 V at 1 C and 2 C, respectively. Capacities reduced to 151 mAh g^{-1} (1 C) and 135 mAh g^{-1} (2 C) in the second cycle. A capacity of 113 mAh g^{-1} was obtained at 2 C after 100 cycles with a coulombic efficiency of 98 %. The polarization increased slightly during the cycling, as shown Figure 4.3d. The rate performance of the Li/PP_{14}Cl-PC/VOCl cell is shown in Figure 4.3e. Discharge capacities of 189 mAh g^{-1}, 154 mAh g^{-1} and 143 mAh g^{-1} were obtained at 0.5 C (the 1st cycle), 1 C (the 11th cycle) and 2 C (the 21th cycle), respectively. After 10 cycles at 2 C, discharge capacities of 148 mAh g^{-1} (1 C in the 32nd cycle) and 147 mAh g^{-1} (0.5 C in the 42nd cycle) were recovered in the subsequent cycling. These results demonstrate that the cell is capable of delivering a high rate capacity and decent cycling stability. The charge-discharge curves of the VOCl electrode cycled at different current densities are presented in Figure 4.3f, where a similar curve with slightly increased polarization was observed at a high current density.

To understand the reaction mechanism of the Li/PP_{14}Cl-PC/VOCl cell, *ex situ* XRD measurements of the VOCl electrode and lithium anode were performed at different electrochemical states in the 1st and 10th cycle to probe the phase evolution during electrochemical reaction (Figure 4.4). Figure 4.4a shows the charge-discharge curve of

the VOCl electrode for the 1st cycle at 1 C with seven different discharged and charged states where *ex situ* XRD measurements were made. In the 1st cycle, points 1-7 represent the VOCl electrode in various electrochemical states: as-prepared (1), discharged 1.53 V (2), discharged 1.33 V (3), discharged 1.0 V (4), recharged 1.62 V (5), recharged 1.75 V (6), and recharged 2.8 V (7). Point 8 and point 9 shown in Figure 4.4b and Figure 4.4c, displays the discharged state (1.0 V) and the recharged state (2.8 V) of the VOCl electrode in the 10th cycle. Figure 4.4b shows the full XRD pattern, and Figure 4.4c displays the selected XRD patterns at low angles. After discharging to 1.53 V (point 2), the XRD pattern was significantly different from that of the as-prepared VOCl electrode, in particular in the low-angle region (Figure 4.4b and Figure 4.4c). A new strong diffraction evolved at $2\theta = 6.5°$, which corresponds to a d spacing value of 13.38 Å. In comparison with the original VOCl with a *c* axis spacing of 7.91 Å, a 5.47 Å expansion took place, which could indicate intercalation of PP_{14}^+ between the VOCl interlayers during the initial stage of discharge. Expansion of MOCl layers upon intercalation of large organic species have already been found in other metal oxychlorides.[145] All further reflections at higher angles strongly decreased in intensity, which is indicative of substantial disorder. This is potentially due to the relative torsion of neighboring layers or buckling of layers as the relative reorientation of neighboring layers is a well-known phenomenon of this structure type.[150,151] Upon further discharge to point 3 and point 4, reflections assigned to the VOCl-type phase show increased broadening. Interestingly, upon recharging to 2.8 V (point 7), the initial width is gradually recovered to its original state, demonstrating the topotactic nature of the electrochemical reaction. In the discharged VOCl after 10 cycles (point 8), (001)-type reflections were strongly broadened, while remaining parts of the pattern were similar to previous states. However, in the subsequent recharge (point 9), all peaks were recovered, and the XRD pattern was in good agreement with the pattern recorded in the first cycle, implying strong influences on the crystallinity/disorder

within the compound by increasing the cycle number.

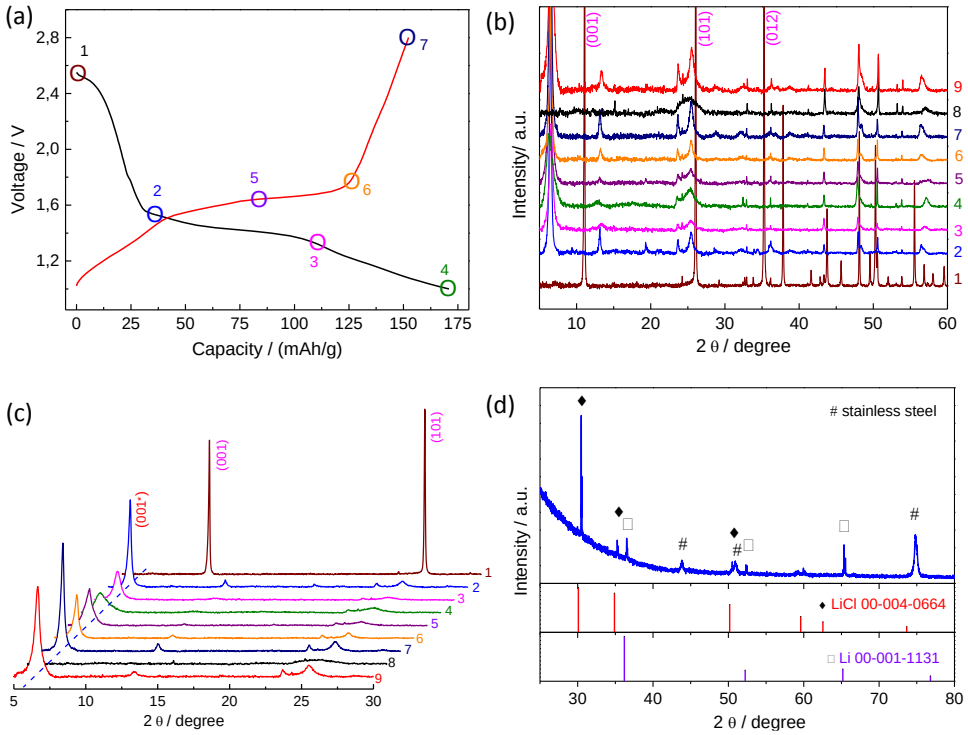

Figure 4.4: (a) Charge-discharge curves of the VOCl electrode at 1 C in the first cycle. The different electrochemical states at which *ex situ* XRD measurements were performed are marked. (b and c) *ex situ* XRD patterns of the VOCl electrode at different charge-discharge states in the 1st (1 → 7) and the 10th cycle (8 and 9), (d) XRD patterns of the lithium anode after the first discharge.

Analysis of the patterns in the charged and discharged electrodes demonstrate that the impurity phases V_2O_3, VCl_2 as well as the fcc metal were still present in the sample without showing a significant change in their relative intensities and/or peak positions (Figure A-3 in Appendix). This suggests that these compounds were electrochemically inactive and did not contribute to the charging/discharging process. The most obvious change was found in the fact that the c-axis increased strongly, supported by the following considerations: the first two reflections can be identified to be a (001) as well as a (002) reflection. The d-spacing of those reflections are ~13.38 Å and ~6.68 Å. The relationship of those d-spacing could be well explained by the intercalation of some larger molecular species in between the neutral VOCl layers terminated by Cl^-

ions.[145,150,152]

The structure of lithium anode was also investigated by *ex situ* XRD to further understand the reaction and associated phase evolution, data is shown in Figure 4.4d. Reflections at 2θ = 30.4°, 35.2° and 50.3° related to LiCl (PDF card no.00-004-0664) were detected as well as the lithium phase (2θ = 36.2°, 52.1° and 65.2°; PDF card no. 00-001-1131) and the stainless steel current collector (2θ = 43.8°, 50.9° and 74.9°). These results demonstrate that the lithium anode was oxidized into LiCl by chloride ions transported through the electrolyte during the discharge. This is supported by the Cl:V ratio on the cathode side. SEM-EDX spectra measured at several particles on the VOCl electrodes after the first cycle (see Figure A-4 in Appendix), evidenced a loss and gain of chloride in the discharge and recharge processes, respectively.

Figure 4.5a shows a STEM-HAADF overview image of the rod-shape morphology in the as-synthesized sample. The HRTEM micrograph (Figure 4.5b) reveals the layered structure corresponding to the Van-der-Waals bonded $(001)_{VOCl}$ planes. In the discharged state, the HRTEM micrograph (Figure 4.5d) shows layered features, too. The corresponding fast Fourier transformation (FFT, Figure 4.5e) exhibits broad peaks with a 1.2 nm lattice distance, corresponding to a distorted $(001)_{VOCl}$ lattice, which is in agreement with the XRD results in Figure 4.4. It was also found that the discharged sample is sensitive to electron beam damage. Under the electron beam irradiation (approximately 5×10^7 electrons nm^{-2}), vanadium (III) oxide crystallites (2 - 3 nm) were formed with a space group of *Fm3m* (225). This result could indicate a meta-stability of the layered structure in the discharged sample compared to the as-prepared and recharged samples. The d-values determined from the STEM-HAADF and the HRTEM micrographs of the recharged sample (approximately 1.2 nm, Figure 4.5 g-i) correspond to the distorted reflection of the $(001)_{VOCl}$ lattice plane.

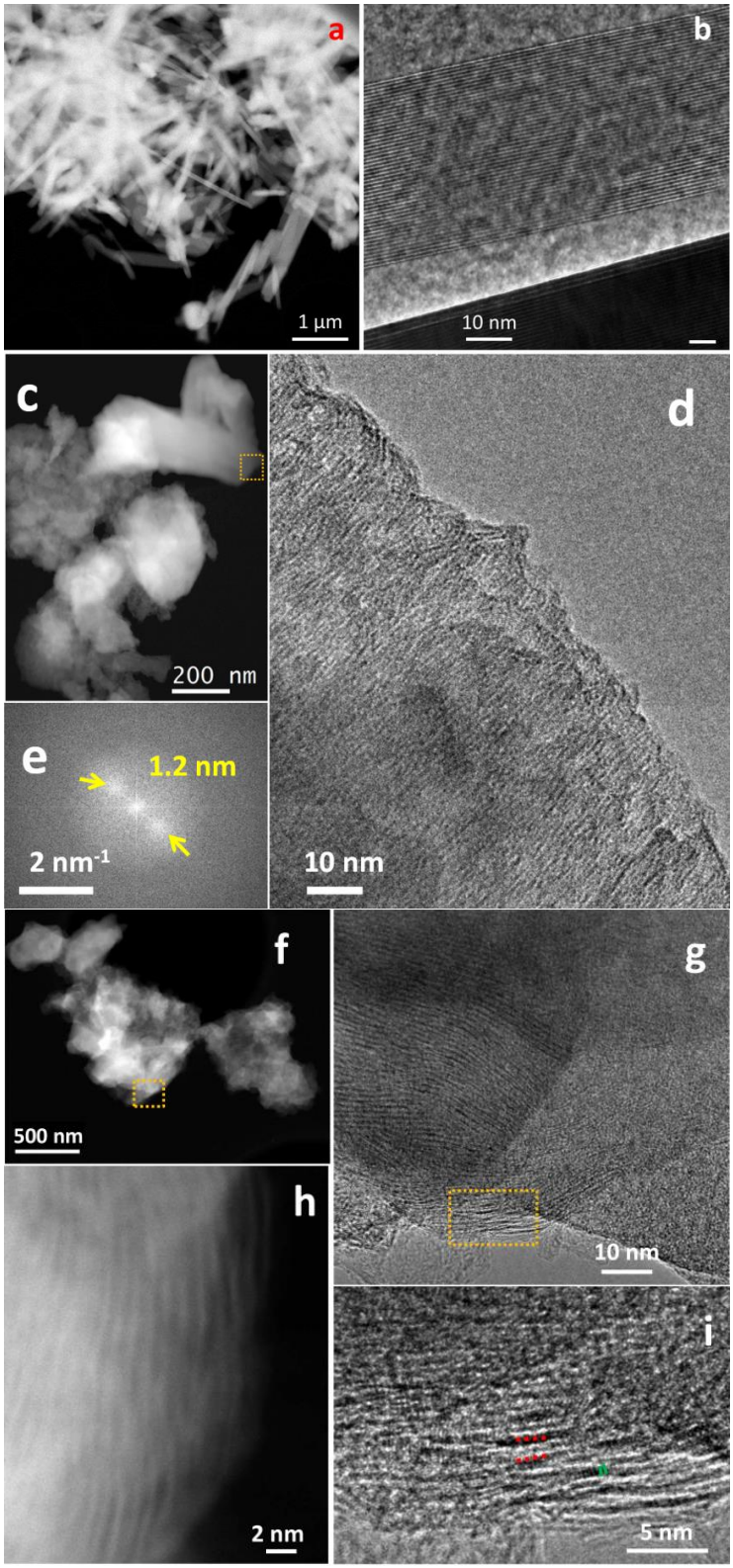

Figure 4.5: (a) STEM-HAADF large-area image, (b) enlarged HRTEM micrograph of the as-prepared VOCl, (c) STEM-HAADF overview image of the discharged sample, (d) low-dose

HRTEM micrograph from the area indicated in c, (e) fast Fourier transform of the HRTEM image in c, where the yellow arrows highlight the reflections corresponding to $(001)_{VOCl}$, (f) STEM-HAADF overview image of the recharged sample, (g) HRTEM micrograph from the area indicated in f, (i) magnified image of marked area in g, where the red dot-lines highlight distorted (001) lattices with a d-value of 1.2 nm, (h) STEM-HAADF image is from the same area as i, showing the distorted (001) lattices.

Figure 4.6 shows EEL spectra recorded on the same area of the TEM for the as-prepared (solid, black), discharged (dash-dotted, red) and recharged (dotted, blue) VOCl electrode, including the Cl-L edge at 200 eV and the V-L edge at 512 eV. The three background corrected spectra are aligned with respect to the vanadium signal. The area under the Cl-L edge directly relates to the relative amount of Cl in three samples, which implies a loss and gain of chloride ions in the VOCl electrode during the discharge and recharge processes, respectively.

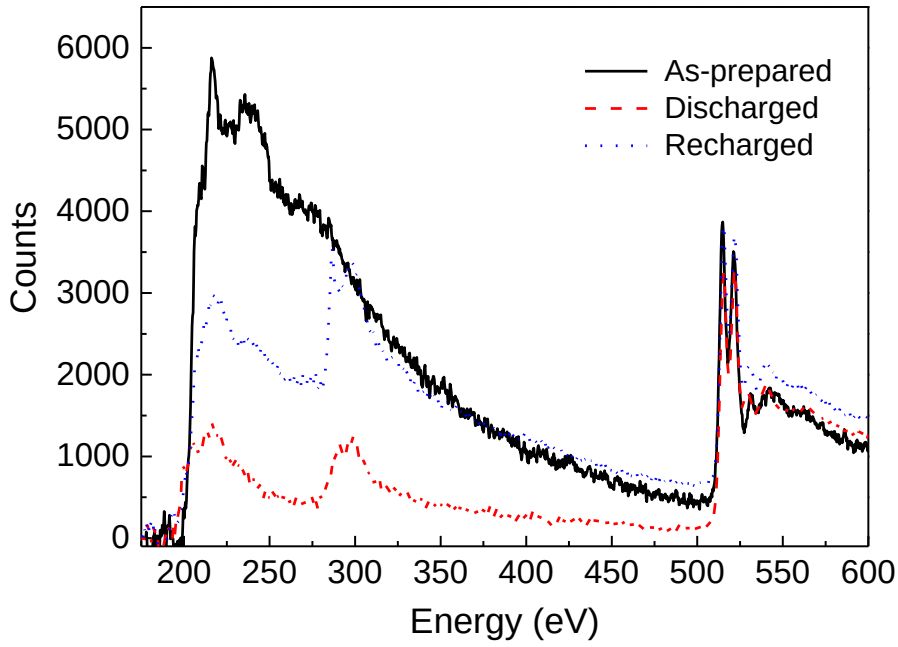

Figure 4.6: EEL spectra of the as-prepared (black, solid line), discharged (red, dashed line) and recharged (blue, dotted line) VOCl electrodes, features at 285 eV correspond to the carbon K-edge of the binder.

The oxidation state of vanadium in different electrochemical states was investigated by *ex situ* XPS measurement to further understand the reaction mechanism of the

Li/PP_{14}Cl-PC/VOCl cell. The survey spectra of the VOCl electrode in the as-prepared (a), discharged (b) and recharged (c) states are shown in Figure A-5 in the Appentix. Elements of C and F can be attributed to the carbon black and PDVF binder, respectively. No other impurity elements were detected in the VOCl electrode. Figure 4.7 shows the XP spectra of $V_{2p3/2}$ region in the as-prepared, discharged (1.8 V, 1.33 V, 1.0 V) and recharged (1.62 V, 1.75 V, 2.8 V) states of the VOCl electrode for the 1st cycle. In the as-prepared VOCl electrode, a single peak was observed in the $V_{2p3/2}$ region with a binding energy of 516.3 eV, which can be ascribed to the trivalent vanadium in VOCl.[153] Upon discharging to 1.8 V, a new peak with a binding energy at 513.7 eV appeared which is attributed to the $V_{2p3/2}$ state in V^{2+}.[154] And the $V_{2p3/2}$ peak at 516.3 eV, which is attributed to the V^{3+}, was also detected. The peak area attributed to V^{2+} was not large, which may be due to partial oxidation of V^{2+} on the surface, it generally increased upon discharge and decreased during the recharge process again. For XP spectra corresponding to the recharged VOCl (2.8 V), the lower binding energy peak at 513.7 eV disappeared and only the peak at 516.4 eV remained, which suggests that the V^{2+} was transformed back into V^{3+} in the recharge process. The observation of vanadium in a lower chemical valence can be ascribed to the partial reduction of V^{3+} to V^{2+}, in accordance to the dissociation of chloride ions from the VOCl in the discharge process. Upon recharging, the V^{3+} was re-acquired in the VOCl electrode, which demonstrates a reversible oxidation-reduction process.

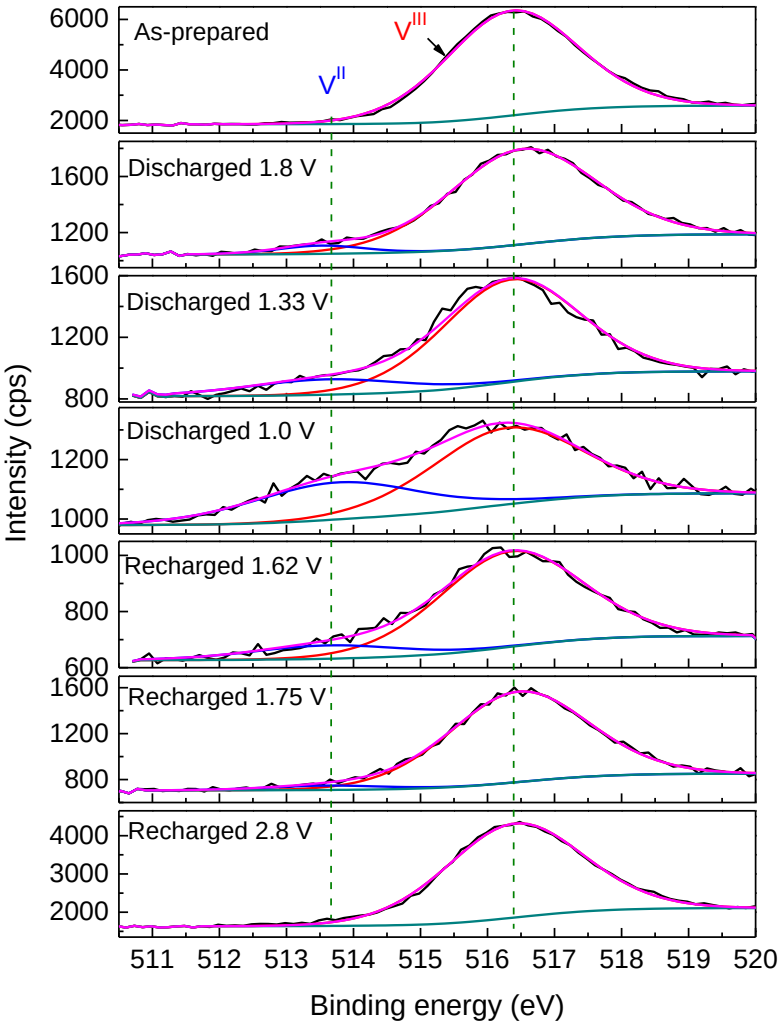

Figure 4.7: XP spectra in the $V_{2p3/2}$ region of the VOCl electrode in various electrochemical states, experimental data (black), fitted signals (light blue and red), fitted background (green).

To gain further insight into the potential intercalation of the organic cation from $PP_{14}Cl$ into the VOCl, additional IR and XPS measurements were performed. Figure 4.8 shows the FTIR spectra of the PVDF, the discharged VOCl (1.33 V) and the pure $PP_{14}Cl$ compound. Bands have been assigned at 944 cm^{-1} (N-C stretching and the rocking of H-C-H in the piperidinium ring), 2872 cm^{-1} (the symmetric C-H stretching in the butyl group) and 2938 cm^{-1} (symmetric and asymmetric C-H stretching in the piperidinium ring).[152,155] A shift of the bands to lower frequencies at 921, 2866 and 2920 cm^{-1} was observed in the cycled samples, which is found when organic guest molecules are intercalated in layered material.[150] The intercalation of PP_{14}^{+} into VOCl interlayers is

in the present case.

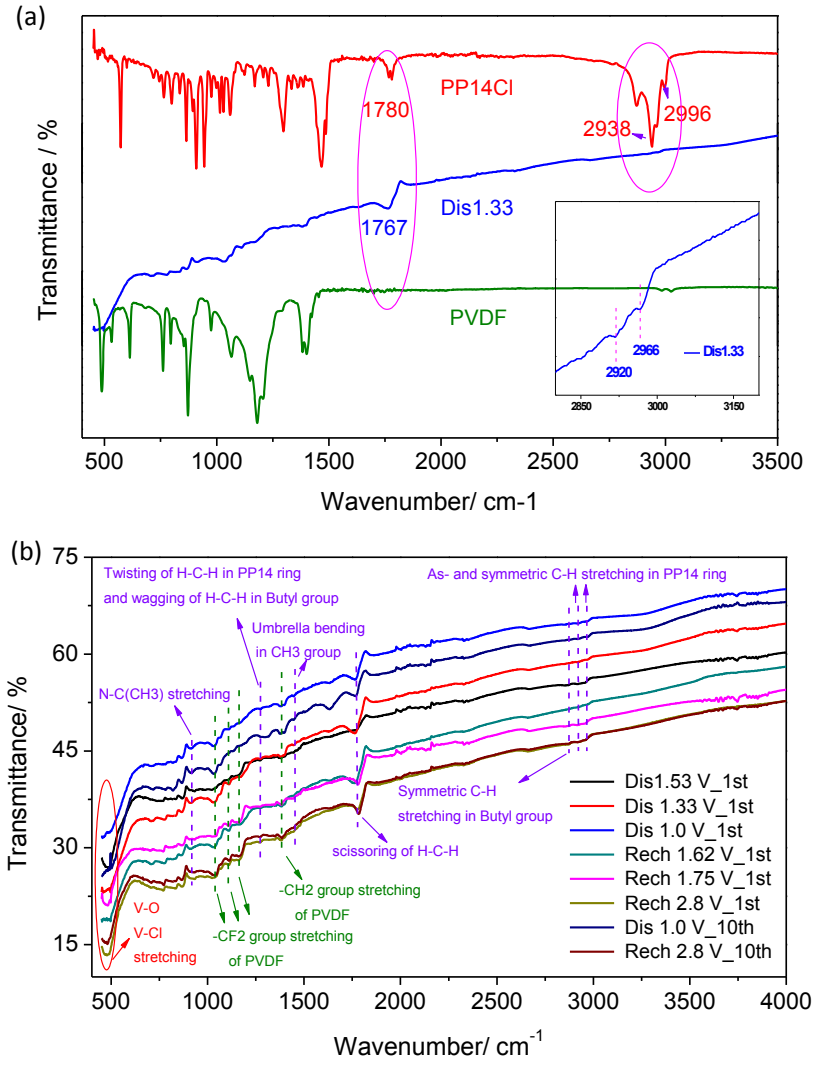

Figure 4.8: (a) IR spectra of the pure $PP_{14}Cl$ (red), the PVDF (green) and the discharged VOCl (1.33 V, blue), (b) IR spectra of the VOCl electrode in various charged and discharged states.

Figure 4.8b shows the IR spectra of the discharged (1.53, 1.33, 1.0 V in the 1st cycle and 1.0 V in the 10th cycle) and recharged (1.62, 1.75, and 2.8 V in the 1st cyle and 2.8 V in the 10th cycle) VOCl electrode. IR bands of the VOCl electrode in different states were at the same frequencies in the 1st and 10th cycles, which indicate that the PP_{14}^{+} cation remained in the VOCl interlayers during the cycling. IR spectra data of the pure $PP_{14}Cl$, IR data of the pure VOCl and cycled VOCl samples are shown in Table 4.1.

Table 4.1: IR data of the pure $PP_{14}Cl$, pure VOCl and the charged/discharged VOCl samples (C/D_{VOCl}).

$PP_{14}Cl$ (ν, cm^{-1})	VOCl (ν, cm^{-1})	C/D_{VOCl} (ν, cm^{-1})	Bands assignment
	526		V-O stretching
	606		V-Cl stretching
944		921	N-C stretching and rocking of H-C-H
		1039-1163	CF_2 group stretching of PVDF
1297		1278	Twisting of H-C-H in piperidinium ring and wagging of H-C-H in butyl group
		1387	$-CH_2$ group stretching of PVDF
1467		1453	H-C-H wagging and umbrella bending in CH_3 group
1780		1767	Scissoring of H-C-H
2872		2866	Symmetric C-H stretching in Butyl group
2938,2996		2920,2966	Symmetric and asymmetric C-H stretching in piperidinium ring

To further study the potential intercalation of the piperdinyl cation in the host, XP spectra were taken in the N_{1s} region of the carefully washed VOCl electrode in the as-prepared state, discharged states (a, 1.8 V and b, 1.33 V), and recharged states (c, 1.62 V and d, 1.75 V), see Figure 4.9. The binding energy of N_{1s} at 403 eV can be ascribed to the $PP_{14}Cl$, it appeared when the VOCl electrode was discharged to 1.8 V. This peak persisted during the recharging, which suggests the intercalation of the PP_{14}^+ into the VOCl electrode. In addition, binding energy of N_{1s} at 400 eV was also observed in the cycled sample, which might be ascribed to the decomposition products of the $PP_{14}Cl$ containing reduced N during the reaction. Based on these results and analysis the XRD pattern of the cycled electrode, it can be conclude that PP_{14}^+ is intercalated into the layered VOCl material during the initial stage of the first discharge and it remains in the interlayers during further cycles.

Based on the electrochemical measurement, *ex situ* XRD, TEM, FT-IR, XPS and SEM/EDX analysis we postulate the following reaction mechanism for the

Li/PP_{14}Cl-PC/VOCl battery cell. During the initial discharge at 2.5 V, 0.07 mol of the PP_{14}^{+} is intercalated irreversibly into the VOCl electrode, leading to an expansion of the interlayers. For charge balancing, an equal amount of Cl^{-} ions reacts with the anode and forms LiCl. Upon further discharge, chloride ions are deintercalated from VOCl, transported through the electrolyte, and react with Li to form LiCl.

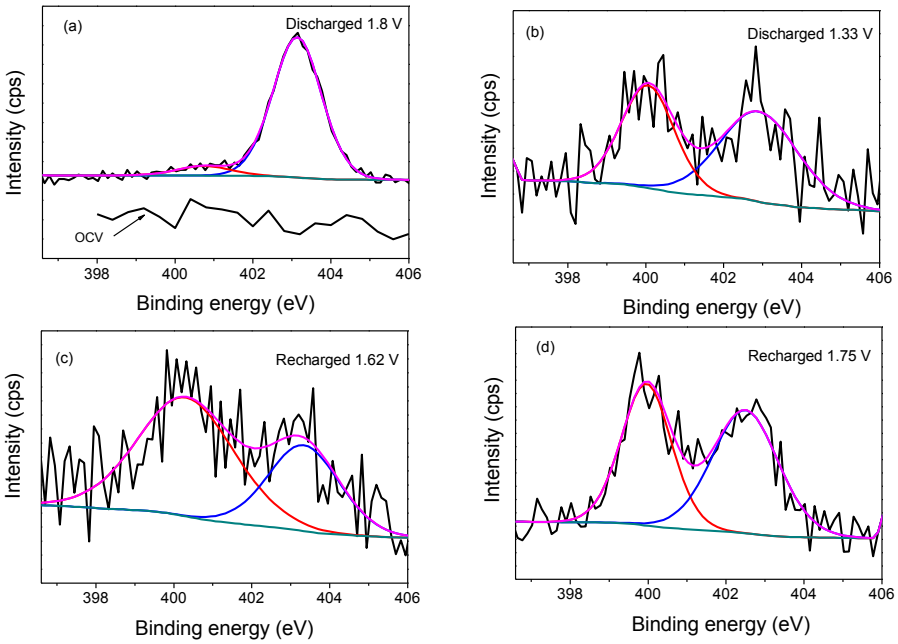

Figure 4.9: XP spectra in the N_{1s} region of the VOCl electrode in, (a) the as-prepared (OCV) and discharged to 1.8 V, (b) the discharged to 1.33 V, (c) the recharged to 1.62 V, and (d) the recharged to 1.75 V state.

During the recharge process chloride ions are intercalated into the VOCl electrode. The intercalated PP_{14}^{+} remains and facilitates the chloride ions deintercalation/intercalation processes by keeping layers widely spaced and intact, which is indicated by the reversible change of width of the remaining peak at $2\theta = 6.5°$ during charging and discharging. This could be a reason for the good reversible capacity of the electrode, which is also observed for high current densities.

It is interesting to compare the charge-discharge profiles of the Li/PP_{14}Cl-PC/VOCl cell and Li/$LiPF_6$-EC-DMC-PC/VOCl cell, the former one is based on chloride ion transport

and the later one is based on lithium-ion transport as shown in Figure 4.10. These two batteries used the same cathode (VOCl) and anode (Li), but different electrolytes. The charge-discharge profile of the VOCl electrode based on chloride ion migration is completely different in comparison to the Li/$LiPF_6$-EC-DMC-PC/VOCl cell, which further evidences that the Li/$PP_{14}Cl$-PC/VOCl cell works with a different mechanism. It should be mentioned that in the CIB cell, the discharge product of LiCl may dissolve to a certain extent in PC solvent. Therefore, the interference of lithium intercalation into VOCl electrode cannot be ignored during long cycling.

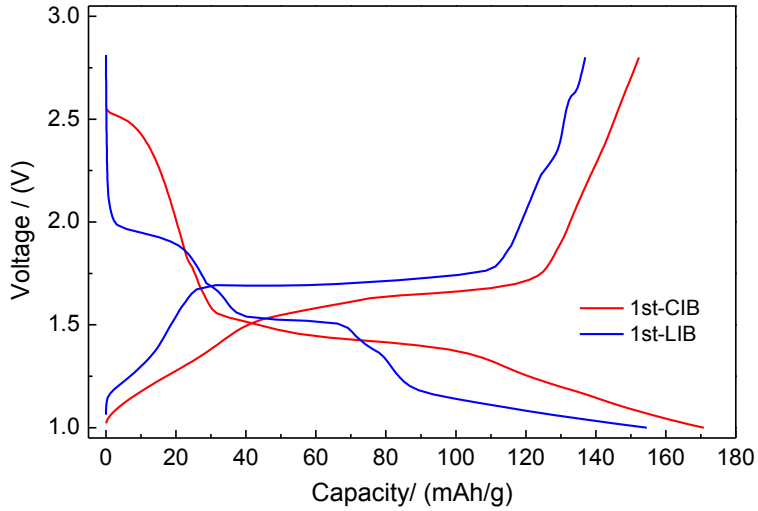

Figure 4.10: Charge-discharge curves of the VOCl electrode for the Li/$LiPF_6$-EC-DMC-PC/VOCl cell (blue) and Li/$PP_{14}Cl$-PC/VOCl cell (red) in the voltage range of 1.0 - 2.8 V at a current density of 260 mA g^{-1} in the first cycle.

In this chapter, we have presented a novel CIB using VOCl as cathode, lithium foil as anode and a liquid chloride ion electrolyte (Li/$PP_{14}Cl$-PC/VOCl). The reversible behavior of the CIB was characterized by CV and galvanostatic measurements. The results show that the battery can be well discharged and recharged even at a high current density. The reaction mechanism of the Li/$PP_{14}Cl$-PC/VOCl cell was validated by *ex situ* XRD, TEM, FTIR and XPS measurements. The results indicated that the chloride ion indeed shuttles between the cathode and anode and that the cation of the ionic liquid intercalates the host VOCl, this facilitates the chloride ion exchange.

Chapter 5 VOCl cathode and magnesium anode for rechargeable chloride ion batteries

5.1 Introduction

This chapter is based on the publication of *ACS Appl. Mater. Interfaces,* 2014, 6, 22430-22435, entitled "Vanadium oxychloride/magnesium electrode systems for chloride ion batteries", copyright (2014) American Chemical Society.

In the previous chapter, layered VOCl material as a cathode and lithium metal have been tested as an anode for CIBs. Highly reversible capability and cycling stability have been observed. In particular, the cell delivered a reversible capacity of 112 mAh g^{-1} after 100 cycles even at a high current density of 2 C rate. In principle, lithium-free materials such as sodium (Na), magnesium (Mg), calcium (Ca), etc. could be used as anode for the CIBs. Compared to Li anode, Mg electrode has a higher theoretical specific volumetric capacity (3833 mAh cm^{-3} for the Mg anode and 2046 mAh cm^{-3} for the Li anode) but lower electrochemical potential (-2.37 V for Mg/Mg^{2+} and -3.04 V for Li/Li^{+} vs Standard hydrogen electrode). In this chapter, a new rechargeable chloride ion battery using VOCl material as a cathode and a lithium-free anode composed of Mg based composite was investigated. The VOCl electrode is stable in the liquid electrolyte and it could be oxidized to vanadium oxydichloride ($VOCl_2$) during the charging, which has a high theoretical capacity of 388 mAh g^{-1} based on the reaction of $VO/VOCl_2$. Moreover, a large Gibbs free energy generated between $VOCl_2$ and Mg would yield a

still high EMF of 1.86 V.

5.2 Experimental section

5.2.1 Electrode preparation

The VOCl was prepared by a solid-gas reaction as described in the previous chapter. The VOCl/C composite was prepared by ball milling a mixture of 80 mass % VOCl and 20 mass % carbon black (Sigma Aldrich) using a silicon nitride vial and balls (10 mm in diameter) for 1 h at a speed of 200 rpm. The ball to powder ratio was 22 : 1. The $MgCl_2$/Mg/C composite (MMC) was prepared by milling of 50 mass % anhydrous $MgCl_2$ (98 %, Sigma Aldrich), 40 mass % Mg powder (99.8 %, Alfa Aesar), and 10 mass % carbon black using a tungsten carbide vial and tungsten carbide balls for 10 h at 300 rpm. The Mg/C composite (MC) was prepared by milling of Mg powder (80 mass %) with carbon black (20 mass %) using the same procedure as for the MMC composite. The ball to powder ratio was 30 : 1. Ionic liquids of 1-butyl-1-methylpiperidinium bis(trifluoromethylsulfonyl)imide ($PP_{14}TFSI$, 99 %, IoLiTech) and 1-butyl-1-methylpiperidinium chloride ($PP_{14}Cl$, 99 %, IoLiTech) were further dried at 358 K for 72 h under vacuum.

The cathode electrodes were prepared by grinding a mixture of active material (VOCl/C, 80 mass %), poly(vinylidene difluoride) binder (PVDF, 10 mass %) and carbon black (10 mass %) with N-methylpyrrolidone (NMP) as solvent for 30 minutes in a mortar. The slurry was then spread on stainless steel foils with 12 mm in diameter. The electrodes were further dried at 353 K overnight under vacuum. The mass loading of the electrode was 1.0 - 1.5 mg cm^{-2}. The MC and MMC anodes were prepared by pressing the composite into a pellet with 20 mg in mass and 11 mm in diameter, thickness approximately 1 mm. The electrolyte was prepared by stirring the mixture of $PP_{14}Cl$ and $PP_{14}TFSI$ for 10 h at room temperature. The concentration of the electrolyte

was 0.5 mol L^{-1}.

5.2.2 Material characterization

Powder X-ray diffraction patterns were obtained with a Philips X'PERT diffractometer equipped with Cu Kα radiation source (operated at 40 kV, 40 mA). Scanning electron microscope (SEM) and energy-dispersive X-ray spectroscopy (EDX) were carried out using a ZEISS LEO 1530 instrument. X-ray photoelectron spectroscopy (XPS) data was recorded on a physical electronics PHI 5800 ESCA System using mono-chromatized Al Kα radiation (13 kV, 250 W) and a pass energy of 29.35 eV for the detail scan in the vanadium (2p) binding energy (BE) region. For BE calibration, the main C_{1s} peak was set to 284.8 eV. XPS measurements and data evaluation were performed by the operator of the instrument.

5.2.3 Electrochemical measurements

Electrochemical tests were conducted using Swagelok-type cells with a two-electrode configuration. The cells were assembled in an argon-filled glove box using VOCl/C as cathode, glass fiber filter (GF/D, Whatman) as separator, and MMC or MC as anode. A mixture of 0.5 M $PP_{14}Cl$ in $PP_{14}TFSI$ was used as electrolyte. Galvanostatic charge and discharge measurements were performed with an Arbin BT2000 battery system at 298 K. The voltage ranges were 0.6 - 2.5 V and 0.6 - 2.2 V for the VOCl-MMC and VOCl-MC cell, respectively. Cyclic voltammetry (CV) was collected using a Biologic VMP-3 electrochemical workstation. In CV measurement, the scanning rate was 0.05 mV s^{-1} in the voltage range between 2.5 V and 0.6 V.

5.3 Results and discussion

The as-prepared VOCl material consisted of rod-like particles with a size of 100 - 500 nm in width and 2 - 5 µm in length, as in the previous chapter (Figure 5.1a). The EDX

spectrum of the as-prepared VOCl presented in Figure 5.1b indicates the elemental of Vanadium, Oxygen and Chlorine. After ball milling, the morphology of the VOCl particles was destroyed and the particles were surrounded with well-distributed carbon black (Figure 5.1c). The EDX elemental mapping of the VOCl/C composite shown in Figure 5.1d indicates a uniform elemental distribution. XRD patterns of the as-prepared VOCl material and the VOCl/C composite are shown in Figure 5.1e. All reflections can be indexed and assigned to the orthorhombic VOCl phase with the space group of *Pmmn* (VOCl PDF card no. 01-085-0353) except for minor impurity of V_2O_3. The peaks attributed to the VOCl phase broadened after ball milling, which indicates a reduction of the crystalline size.

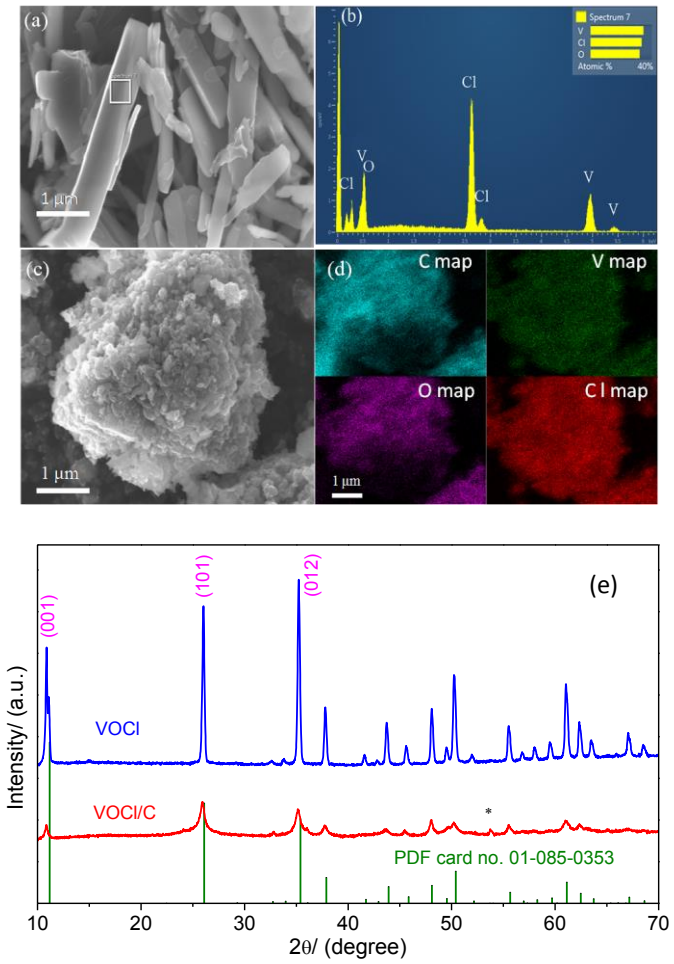

Figure 5.1: (a) SEM images of the as-prepared VOCl, (b) corresponding EDX spectrum from the

marked area in a, (c) SEM image of the VOCl/C composite, (d) corresponding elemental mapping of Carbon, Vanadium, Oxygen and Chlorine, (e) XRD patterns of the as-prepared VOCl (blue) and the VOCl/C composite (red), the * denotes the impurity of V_2O_3 (PDF no. 34-0187).

The electrochemical behavior of the VOCl cathode was investigated by galvanostatic charge-discharge test. Two cells of VOCl-MC (MC as anode) and VOCl-MMC (MMC as anode) were constructed. Figure 5.2a shows the cycling performance of the VOCl-MC cell at 5 mA g^{-1} in the voltage range of 0.6 - 2.2 V. A reversible discharge capacity of 40 mAh g^{-1} was obtained in the first cycle (the capacity is based on the active material of the VOCl cathode), which is close to 15 % of the theoretical capacity (260 mAh g^{-1}). The discharge capacity increased to 44 mAh g^{-1} in the 3rd cycle, and the coulombic efficiency increased from 83 % in the first cycle to 99 % in the 3rd cycle. Subsequently, the discharge capacity faded upon the cycling, and a capacity of 30 mAh g^{-1} remained in the 15th cycle. The selected charge/discharge curves of the VOCl-MC cell cycled at 5 mA g^{-1} are shown in Figure 5.2b, where an initial discharge plateau at 1.3 V was observed. A slope discharge profile was observed in the second cycle, and the hysteresis voltage increased significantly in the following cycles, which implies an increase of kinetic barriers in Mg electrode and/or the volume change in cathode and anode during the reaction.

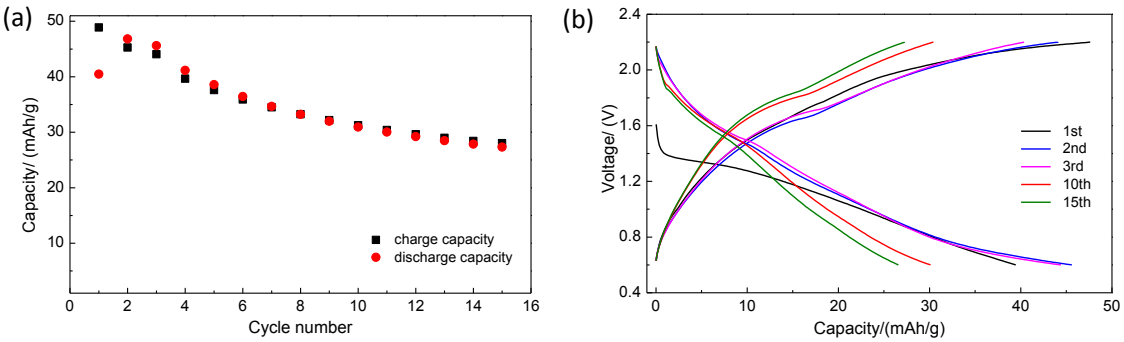

Figure 5.2: (a) Cycling performance, and (b) selected charge/discharge curves the VOCl-MC cell in a voltage range of 0.6 - 2.2 V at 5 mA g^{-1}.

A low reversible capacity has been observed in the VOCl-MC cell, which was based on transferring of 1 Cl per VOCl formula unit. As the VOCl cathode could be oxidized to

$VOCl_2$ by reacting with Cl ions, and these Cl ions could be dissociated from the $MgCl_2$ in the anode during the charge. In this case, two Cl can be provided in the $VOCl_2$ electrode, leading to a high theoretical capacity. In order to further investigate and improve the electrochemical performance of the VOCl electrode, MMC anode was used (VOCl-MMC). The battery performance of the VOCl-MMC cell is shown in Figure 5.3, where the VOCl-MMC cell was charged to 2.5 V firstly, aiming at the formation of $VOCl_2$. This process is different from that of the VOCl-MC cell, in which the cell was discharged to 0.6 V firstly. Figure 5.3a and b show the initial charge/discharge curves of the VOCl-MMC cell at current densities of 5 mA g^{-1} and 10 mA g^{-1}, respectively. The charge capacities of 259 mAh g^{-1} (at 5 mA g^{-1}) and 198 mAh g^{-1} (at 10 mA g^{-1}) were obtained in the first cycle with a charge plateau at around 2.1 V, which can be related to the transformation of VOCl to $VOCl_2$, details will be discussed below. The VOCl electrode delivered discharge capacities of 80 (at 5 mA g^{-1}) and 66 mAh g^{-1} (at 10 mA g^{-1}) with two distinct discharge plateaus at around 1.9 V and 1.3 V in the first cycle. However, in the VOCl-MC cell, only single plateau at 1.3 V can be observed in the first discharge, which indicates the different electrochemical reaction mechanism of these two cells.

The formation of interface layers on the electrode and partially reversible reaction of the electrode could lead to a low coulombic efficiency in the VOCl-MMC cell particularly in the first cycle. Nevertheless, the coulombic efficiency increased significantly in the subsequent cycling, which indicates the activation process in initial cycles. In comparison with the discharge curve of the VOCl-MC cell and VOCl-MMC cell in the first cycle (Figure 5.3c), the discharge plateau at about 1.9 V in the VOCl-MMC cell can be attributed to the redox reaction of $VOCl_2 + e^- \rightarrow VOCl + Cl^-$ (EMF = 2.24 V). A low discharge plateau at around 1.3 V was observed for both cells, suggesting the reaction of $VOCl + e^- \rightarrow VO + Cl^-$ (EMF = 1.49 V)**.** The cycling performance of the VOCl-MMC cell in 0.6 - 2.5 V at a current density of 10 mA g^{-1} is shown in Figure 5.3d,

where the capacity increased in the first few cycles and a maximum discharge capacity of 101 mAh g^{-1} was observed in the 9th cycle. Then the cell retained a discharge capacity of 87 mAh g^{-1} in 30 cycles. Subsequently, the capacity faded generally in the next 20 cycles and a capacity retention of 59 % was obtained after 53 cycles.

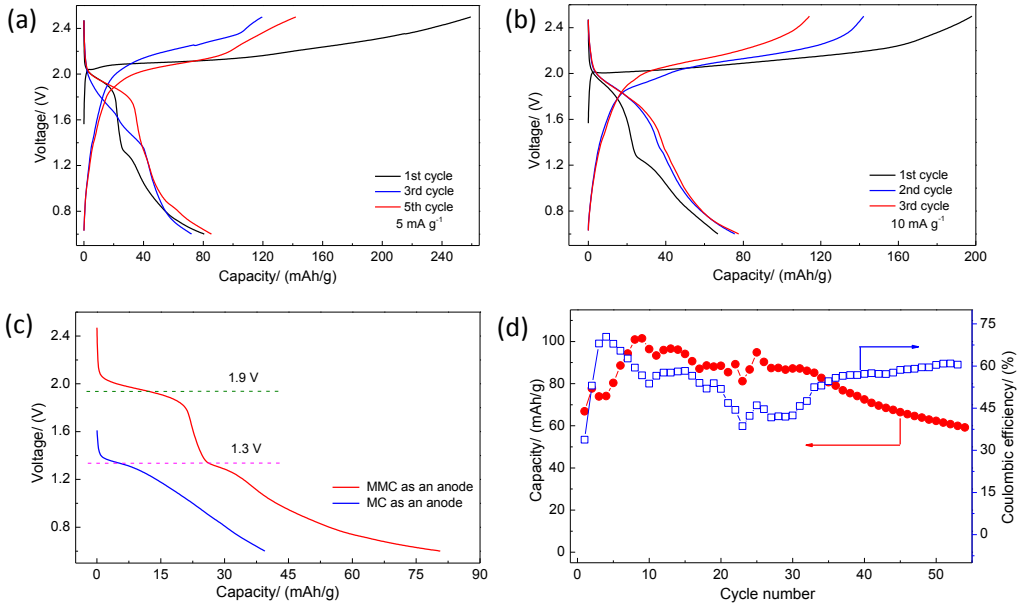

Figure 5.3: Initial charge/discharge curves of the VOCl-MMC cell (a) at 5 mA g^{-1}, and (b) 10 mA g^{-1}, (c) the discharge curve of the VOCl-MC cell and VOCl-MMC cell in the first cycle at 5 mA g^{-1}, (d) the cycling performance of the VOCl-MMC cell at 10 mA g^{-1}.

Figure 5.4 shows the CV curves of the VOCl-MMC cell in the potential range between 2.5 V and 0.6 V at a scan rate of 0.05 mV s^{-1}. In the CV measurement, it was initially swept from the open circuit voltage (OCV = 1.65 V) to 2.5 V. A broad anodic peak located at 2.4 V was observed in the first anodic scan from OCV to 2.5 V, which can be assigned to the reaction of $VOCl + Cl^- \rightarrow VOCl_2 + e^-$. Two cathodic peaks appeared at 2.0 V and 1.3 V in the first cycle, which can be attributed to a two-step reduction reaction of $VOCl_2 + e^- \rightarrow VOCl + Cl^-$ (EMF = 2.24 V) and $VOCl + e^- \rightarrow VO + Cl^-$ (EMF = 1.49 V), respectively. In the second cycle, the anodic peak shifted to a lower potential (2.3 V) and its intensity decreased. Meanwhile, the intensity of the cathodic peak at around 1.9 V increased upon cycling. This result is consistent with the increase of capacity in

the initial cycles shown in Figure 5.3. A pair of cathodic/anodic peaks at 1.3/1.5 V corresponding to the reaction of V^{3+}/V^{2+} was more stable. Two distinct redox couples of 2.3/1.9 V and 1.5/1.3 V were observed in the subsequent cycling, which suggests a two-step reaction upon cycling.

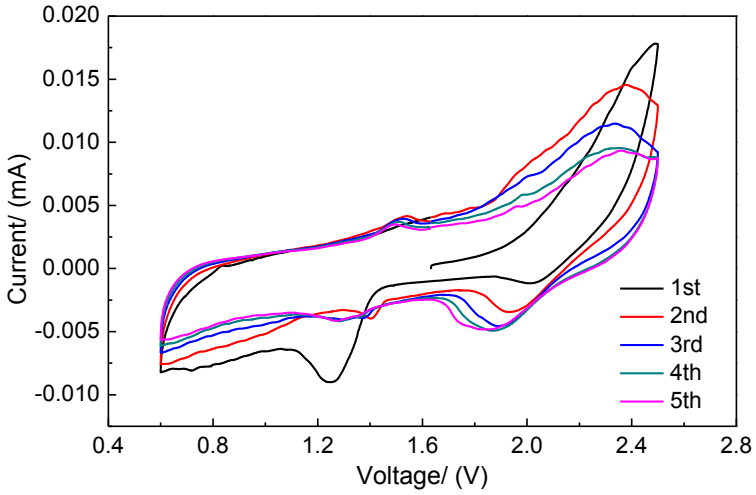

Figure 5.4: CV curves of the VOCl-MMC cell in initial cycles at a scan rate of 0.05 mV s^{-1}, the voltage range was 2.5 - 0.6 V.

In order to understand the reaction mechanism of the VOCl-MMC cell, the VOCl electrodes were stopped at various charge and discharge states for the *ex situ* XRD and XPS measurements. The first charge/discharge curve of the VOCl electrode is shown in Figure 5.5a, in which the electrode at the as-prepared (ϕ1), charged (2.5 V, ϕ2) and discharged (0.6 V, ϕ2) state were used for the XRD measurements. For the as-prepared VOCl/C electrode, the pattern can be indexed and assigned to the orthorhombic VOCl phase. And a small amount of V_2O_3 was detected however (Figure 5.5b line ϕ1). This may be caused by partial decomposition of VOCl during ball milling. When the VOCl/C electrode was charged to 2.5 V (line ϕ2), the intensity of the pattern related to the VOCl phase was decreased drastically. Nevertheless, the $VOCl_2$ phase was not detected, which is supposed to be formed by electrochemical oxidation of VOCl. This could be due to the formation of nanosized and/or amorphous phase. Upon discharging the

electrode to 0.6 V in the first cycle (line ϕ3), the diffraction peaks related to VO phase (PDF card no. 00-038-0974), V_2O_3 phase (PDF card no. 34-0187), and the VOCl phase were detected. One diffraction peak at 2θ = 13.5° was not identified. The formation of VO phase in the cathode demonstrates that the chloride ions were dissociated from the VOCl in the discharge process. In addition, the discharged state (0.6 V, ϕ4) of the electrode in the 10th cycle was also characterized by XRD, where the dominant phases of V_2O_3 with contribution of VOCl were detected. The VO phase was not detected.

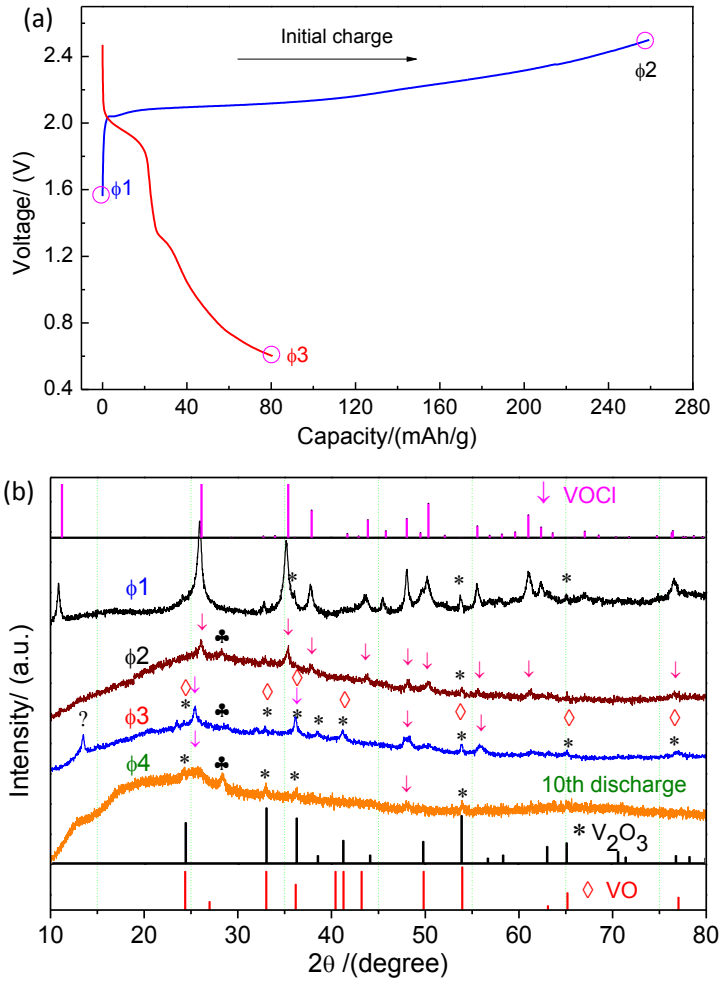

Figure 5.5: (a) Initial charge/discharge profiles of the VOCl-MMC cell, (b) XRD patterns of the VOCl electrode at different states.

Conversion reactions refine the active material particles and therefore lead to the formation of large fresh and active surfaces, which has been observed for a number of

conversion systems. However, VO of the discharged product was gradually oxidized to V_2O_3 during the XRD measurement (about 5 h), even though a protected XRD holder assembled in the glove box was used. A diffraction peak at $2\theta = 28.4°$ was observed in the 10th discharge state, and its intensity increased compared to the intensity of the electrodes (line $\phi 2$ and $\phi 3$) in the first cycle. This may be related to the formation of VO_2 phase (PDF no. 43-1051), which was formed by the oxidation of vanadium oxide with lower vanadium valence during the XRD measurement.

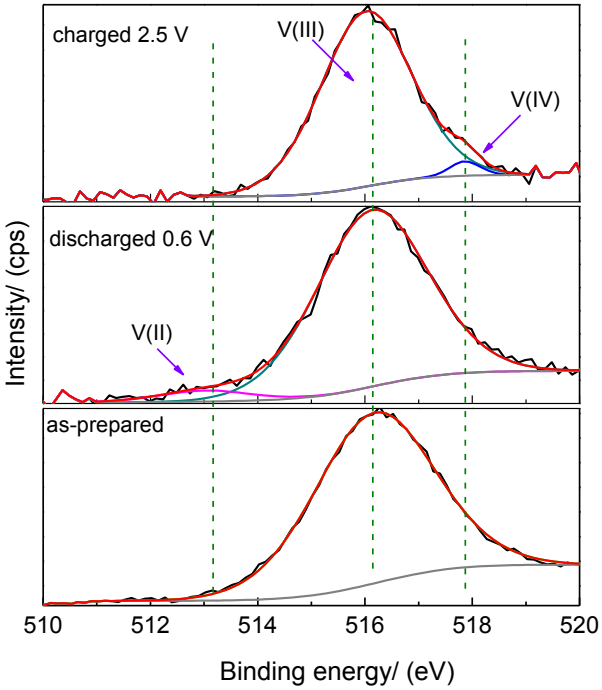

Figure 5.6: XP spectra of the $V_{2p3/2}$ region of the VOCl electrode in the as-prepared, charged, and discharge states.

The conclusion in this investigation could not be drawn on the basis of XRD data alone, because there were difficulties to detect some of the phases, possibly due to their nanoscale size and amorphous phase. Hence, XPS was used as an additional method, in order to detect the oxidation states of the vanadium in different charge and discharge states. Figure 5.6 shows the XP spectra in the $V_{2p3/2}$ region of the VOCl electrode in the as-prepared, charged (2.5 V) and discharged (0.6 V) states in the first cycle. The binding energy at 516.3 eV was observed for the as-prepared VOCl

electrode, which is consistent with V^{3+} oxidation state.[154,156] When the VOCl electrode was charged to 2.5 V, $V_{2p3/2}$ peaks at 516.3 eV and 517.8 eV were detected, which can be assigned to the vanadium oxidation states of V^{3+} (VOCl) and V^{4+} ($VOCl_2$), respectively.[157] The peak area at 517.8 eV corresponding to V^{4+} species was smaller than that of the main peak at 516.3 eV, suggesting that only partial electrochemical oxidation of VOCl to $VOCl_2$ in the first charge process took place.

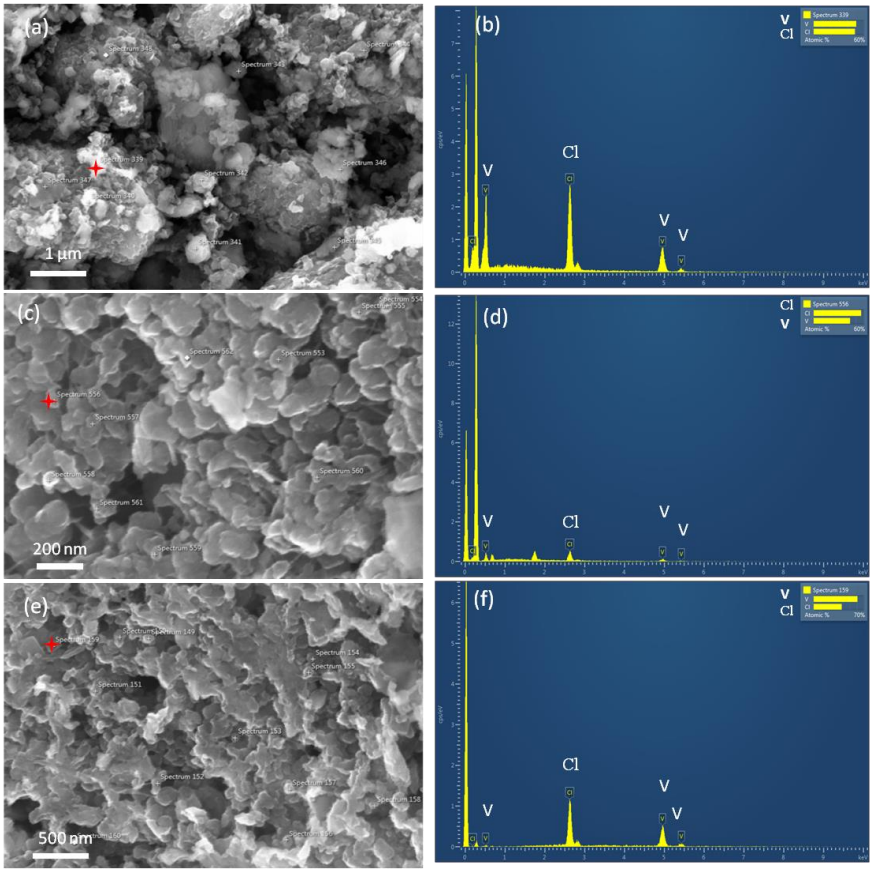

Figure 5.7: SEM images and the corresponding EDX spectra of the VOCl electrode (a, b) in the as-prepared state, (c, d) charged state, and (e, f) discharged state.

In the discharged (0.6 V) sample, a new $V_{2p3/2}$ peak with a binding energy of 513.2 eV appeared, which can be ascribed to VO. [154,156] The peak at 516.3 eV assigned to the V^{3+} species was still detected in the discharged electrode, indicating that the VOCl electrode was not fully transformed in the reduction reaction. The observed V^{4+} in the charged state and V^{2+} in discharged state indicate that the VOCl electrode can be

oxidized in the first charge process in the formation of $VOCl_2$ and be reduced to VO in the discharge, indicating the migration of chloride ions during the cycling.

EDX spectra of the VOCl electrode in the as-prepared state, charged state (2.5 V) and discharged state (0.6 V) further support the migration of chloride ion as shown in Figure 5.7. The atomic ratio of Cl/V varied depending on the electrochemical state of the VOCl electrode. It increased from Cl/V ≈ 1 in the as-prepared state (Figure 5.7b) to Cl/V > 1 in the 1st charged state (Figure 5.7d), and decreased to Cl/V < 1 in the discharged state (Figure 5.7f), which further indicates that the Cl ions migrated to the cathode during the charge and dissociated from the cathode in the discharge.

Based on the electrochemical and structural information above, it is concluded that the electrochemical reaction in the VOCl-MC cell and VOCl-MMC cell during cycling is reversible. The electrochemical reaction process of the cell is therefore proposed as shown in Figure 5.8. The cathodic and anodic reactions of the VOCl-MMC cell can be described as follows:

In the first charge,

$$2\ \mathrm{VOCl} + \mathrm{MgCl_2} \rightarrow 2\ \mathrm{VOCl_2} + \mathrm{Mg} \qquad \mathrm{EMF} = 2.24\ \mathrm{V} \qquad (5.1)$$

in the first discharge,

$$2\ \mathrm{VOCl_2} + \mathrm{Mg} \rightarrow 2\ \mathrm{VOCl} + \mathrm{MgCl_2} \qquad \mathrm{EMF} = 2.24\ \mathrm{V} \qquad (5.2)$$

$$2\ \mathrm{VOCl} + \mathrm{Mg} \rightarrow 2\ \mathrm{VO} + \mathrm{MgCl_2} \qquad \mathrm{EMF} = 1.49\ \mathrm{V} \qquad (5.3)$$

In the VOCl-MC cell (Figure 5.8a), the VOCl cathode is reduced to VO when the chloride ions are dissociated from the VOCl electrode in the first discharge. Meanwhile, the Mg anode is oxidized to $MgCl_2$ by reacting with chloride ions transferred from the electrolyte. The EMF of this reaction is 1.49 V as shown in equation 5.3. The chloride ions are therefore shuttled between the VOCl cathode and the MC anode.

In the VOCl-MMC cell (Figure 5.8b), the chloride ions are dissociated from the MMC anode ($MgCl_2 + 2\ e^- \rightarrow Mg + 2\ Cl^-$) and migrate to the VOCl cathode in the first charge,

which results in the formation of $VOCl_2$ in the cathode (EMF = 2.24 V, equation 5.1). In the subsequent discharge, both $VOCl_2$ and the residual VOCl are partially reduced to VO and the chloride ions move back to the anode (equation 5.2 and 5.3). Thus, the chloride ions are shuttled between the $VOCl_2$ cathode and the MMC anode for the VOCl-MMC cell.

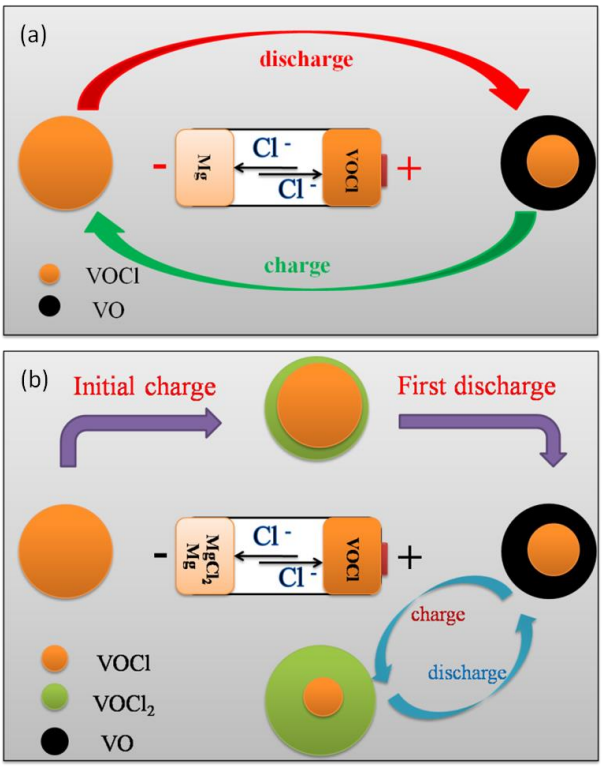

Figure 5.8: Schematic illustration of the phase evolution for the VOCl-MC cell (a), and the VOCl-MMC cell (b).

In this chapter, a rechargeable chloride on battery was demonstrated using VOCl cathode and Mg based anode in a liquid electrolyte, operating at room temperature. The VOCl electrode can be either oxidized to $VOCl_2$ in the first charge process, or be reduced to VO in a discharge process. The electrochemical performance and the reaction mechanism the cells were investigated by galvanostatic cycling, CV, XRD, XPS, EDX.

Chapter 6 Porphyrin complex as electrode for rechargeable batteries

6.1 Introduction

This chapter is based on the submitted version for an EU patent application (EP16000312.5), entitled “High performance organic electrodes for secondary batteries”, 2016.

Rechargeable batteries based on organic electrode materials are potential alternative to conventional lithium-ion batteries due to their tunable properties, environmental friendliness, flexibility, good safety, sustainability and relative low cost.[158–162] Porphyrins have an aromatic 18 π conjugated system delocalized over 24 core atoms which satisfy Hückel's (4n+2) π-electron rule. Many porphyrins and metalloporphyrins exist naturally and have a wide range of applications, e.g. in light harvesting, as a catalyst, etc.[163–166] Porphyrins and their derivatives with highly conjugated π-systems are suitable for efficient electron transfer processes due to the minimal structural change of the molecules during the removal or uptake of an electron. 16 π-electron and 20 π-electron “antiaromatic” porphyrins are accessible by the oxidation or reduction of the 18 π-electron systems of aromatic porphyrins and in some cases can be successfully isolated and structurally determined.[167–172]

In this chapter, [5,15-Bis(ethynyl)-10,20-diphenylporphinato]copper(II) (CuDEPP), is proposed as a new electrode-active material for rechargeable batteries, which is based

on the shuttling of both cations and anions during the electrochemical reaction. Excellent rate performance and long-term cycling stability have observed with the CuDEPP material either as a cathode or an anode, or as both cathode and anode in a symmetric organic battery.

6.2 Experimental section

6.2.1 Synthesis of [5,15-Bis(ethynyl)-10,20-diphenylporphinato]copper(II)

The synthesis and characterization of the CuDEPP material was done by Zhi Chen, from the group of Prof. Mario Ruben, at the Institute of Nanotechnology (INT), Karlsruhe Institute of Technology (KIT), Germany.

6.2.1.1 Synthesis of 5,15-Bis(trimethylsilanylethynyl)-10,20-diphenyl-21*H*, 23*H*-porphyrin (3)

Reactions requiring an inert gas atmosphere were conducted under argon, and the glassware was dried at 140 °C in an oven. THF was further distilled from sodium prior to use. Et_3N was distilled over CaH_2 and stored under argon. Commercially available chemicals were used as received.

5, 15-dibromo-10,20-diphenyl-21*H*,23*H*-porphyrin (0.620 g, 1 mmol), $Pd(PPh_3)_2Cl_2$ (0.035 g, 0.05 mmol), CuI (0.010 g, 0.05 mmol) and ethynyltrimethylsilane (0.206 g, 2.2 mmol) were added into the mixture of THF (35 mL) and triethylamine (15 mL) under an argon atmosphere. The reaction mixture was stirred at room temperature for 12 hours, then the solution was poured into 150 mL water and extracted by CH_2Cl_2 (3 * 50 mL). Solvents were removed in vacuum and the residue was purified by column chromatography on silica gel (hexane: CH_2Cl_2 = 1:1) affording brown purple solid of **3** (0.344 g, yield 52%).

^{1}H NMR (500 MHz, $CDCl_3$) δ ppm 9.63 (d, *J* = 4.68 Hz, 4H, pyrrole-*H*), 8.85 (d, *J* = 4.65 Hz, 4H, pyrrole-*H*), 8.20 (d, *J* = 6.14 Hz, 4H, Ph-*H*), 7.94-7.73 (m, 6H, Ph-*H*), 0.63 (s, 18H,

-Si(C*H*$_3$)$_3$), -2.16 (s, 2H, pyrrole -N*H*). ^{13}C NMR (126 MHz, $CDCl_3$) δ ppm 141.35, 134.55, 128.01, 126.94, 121.81, 106.87, 102.75, 100.88, 0.336. ^{1}H UV-vis (CH_2Cl_2, nm) 434, 508, 541, 582, 678. NIR (KBr cm^{-1}) 3428, 3319, 2956, 2924(Si(C-H$_3$)$_3$), 2853, 2141(C≡C), 1597, 1558, 1441, 1467, 1441, 1398, 1337, 1247, 1194, 1138, 1069, 1002, 974, 964, 844, 797, 704, 657, 418. ESI ToF Calc. for $C_{42}H_{39}N_4Si_2$: [MH$^+$], 655.3; Found: m/z 655.2.

6.2.1.2 Synthesis of [5,15-Bis(trimethylsilylethynl)-10,20-dipheny)porphinato] copper(II) (4)

$Cu(OAc)_2{\cdot}H_2O$ (0.400 g, 2 mmol) was added to a solution of **3** (0.332 g, 0.6 mmol) in a mixture of 50 mL THF, 50 mL CH_2Cl_2 and 5 mL Et_3N. The reaction was stirred at room temperature for 12 hours, then poured into 150 mL water and extracted by CH_2Cl_2 (3 *50 mL). The CH_2Cl_2 solution was concentrated under reduced pressure and the residue was passed through a short column chromatography on silica gel (hexane: CH_2Cl_2 = 1:1). After removed solvents, a dark purple solid 3 (0.343 g, 80 %) was obtained.

UV-vis (CH_2Cl_2, nm) 432, 564, 606. NIR (KBr cm^{-1}) 2917(Si(C-H$_3$)$_3$), 2849, 2134(C≡C), 1523, 1462, 1443, 1344, 1246, 1209, 1166, 1067, 1004, 993, 840, 794, 755, 706, 666, 620, 566. ESI ToF Calc. for $C_{42}H_{36}N_4Si_2$: [M$^+$], 715.2; Found: m/z 715.2.

6.2.1.3 Synthesis of [5,15-Bis(ethynyl)-10,20-diphenylporphinato]copper(II) (1)

4 (0.322 g, 0.45 mmol) was dissolved in THF (50 mL) under an argon atmosphere at 0 °C. Then tetrabutylammonium fluoride (0.252 g, 0.8 mmol) was added. After 30 min, the reaction was poured into 50 mL MeOH. The precipitate was filtered and washed by 100 mL MeOH. The product was collected to yield a dark purple solid **1** (0.244 g, 95 %).

UV-vis (CH_2Cl_2, nm) 425, 558, 598. NIR (KBr cm^{-1}) 3264 (CC-H), 2096 (C≡C), 1596, 1521, 1443, 1347, 1211, 1174, 1070, 1004, 936, 796, 751, 737, 711, 701, 676, 666, 646, 614, 503. MALDI ToF calc. for $C_{36}H_{20}N_4Cu$: [M$^-$], 571.1; Found: m/z 571.0.

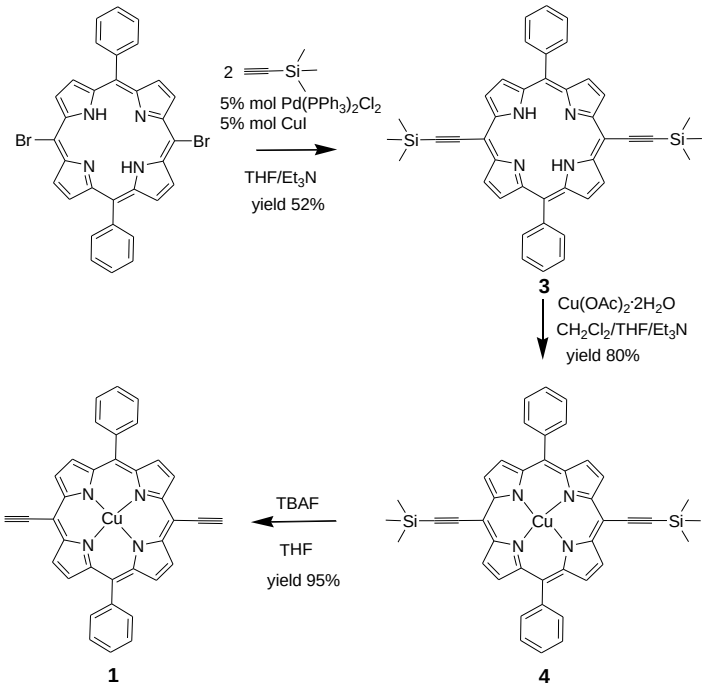

Figure 6.1: Synthetic route of CuDEPP (**1**).

6.2.2 Materials characterization

Thin-layer chromatography was performed on aluminum plates pre-coated with Merck 5735 silica gel 60 F_{254}. Column chromatography was performed with Merck silica gel 60 (230 - 400 mesh). ^{1}H NMR and ^{13}C NMR spectra were recorded on a Bruker DRX 500 spectrometer, chemical shifts are given in ppm, referenced to residual proton resonances of the solvents. UV-vis spectra were measured on a Varian Cary 500 Scan UV/vis/NIR spectrophotometer. The matrix-assisted laser desorption ionization time-of-flight (MALDI-ToF) mass spectroscopy measurements were carried out on a Synapt G2-S HDMS spectrometry workstation. IR spectra were measured in KBr pellets on MAGNA FTIR 750, Nicolet.

Scanning electron microscope (SEM) measurements were carried out using a ZEISS LEO 1530 instrument. Powder X-ray diffraction (XRD) patterns were recorded in transmission geometry using a STOE STADI-P diffractometer (operated at 40 kV, 40 mA). The thermogravimetric analysis (TGA) was conducted by a SETARAM SENSYS Evo

thermal analyzer under air flow (20 mL min^{-1}) with a heating rate of 5 ^{o}C min^{-1}.

6.2.3 Electrochemical measurements

[5,10,15,20-tetraphenylporphinato]copper(II) (**CuTPP**) and graphite material were purchased from Sigma-Aldrich. The graphite was dried before use at 473 K for 12 h under vacuum. The CuDEPP and CuTPP electrode were fabricated by mixing of the (CuDEPP or CuTPP) active material (50 mass %), carbon black (40 mass %), and polyvinylinde fluoride (PVDF, 10 mass %) in N-methylpyrrolidone (NMP) in a mortar for 30 min. The graphite electrode was prepared by mixing of graphite material (90 mass %) and PVDF (10 mass %) in NMP with the same procedure as for the CuDEPP electrode. The slurry was pasted on a stainless steel foil (16 mm in diameter). The electrodes were dried at 373 K under vacuum for 10 h. The mass loading of the CuDEPP (CuTPP) electrode and the graphite electrode were around 1.0 mg cm^{-2} and 3.0 mg cm^{-2}, respectively.

Electrochemical measurements were performed using a 2032 coin-type cell. A glass fiber filter was used as a separator. 1 M lithium hexafluorophosphate ($LiPF_6$) in a solvent mixture of ethylene carbonate (EC), propylene carbonate (PC), dimethyl carbonate (DMC) (EC : PC : MC = 1 : 1 : 3 by volume ratio) was used as an electrolyte for the Li/$LiPF_6$/CuDEPP cell and CuDEPP/$LiPF_6$/CuDEPP cell. The ionic liquid of 1-butyl-1-methylpiperidinium bis(trifluoromethylsulfonyl)imide ($PP_{14}TFSI$, 99 %, IoLiTech) was used as an electrolyte for the CuDEPP/$PP_{14}TFSI$/graphite cell. The cells were assembled in an argon filled glove box (MBRAUN) with water and oxygen concentrations below 0.1 ppm. Galvanostatic charge-discharge measurements were performed using an Arbin battery tester at 298 K. Cyclic voltammetry (CV) measurements were conducted using a Biologic VMP-3 potentiostat.

6.3 Results and discussion

6.3.1 Porphyrin complex as cathode for rechargeable batteries

[5,15-Bis(ethynyl)-10,20-diphenylporphinato]copper(II) (CuDEPP) bearing two *meso* ethynyl groups was successfully synthesized in three steps as shown in Figure 6.1. The obtained powder was characterized by means of matrix-assisted laser desorption ionization time-of-flight mass spectroscopy (MALDI-ToF-MS, Figure 6.2a), ultraviolet-visible spectroscopy (UV-vis, Figure 6.2b) and Infrared spectroscopy (IR) (Figure 6.2c), which evidence the characteristics of the CuDEPP molecule. Notably, the CuDEPP molecule is thermally stable up to 250 °C in air measured by the thermogravimetric-differential scanning calorimetric analysis (TGA-DSC) as shown in Figure 6.2d, which may be attributed to its highly π conjugated structure and aromatic character.

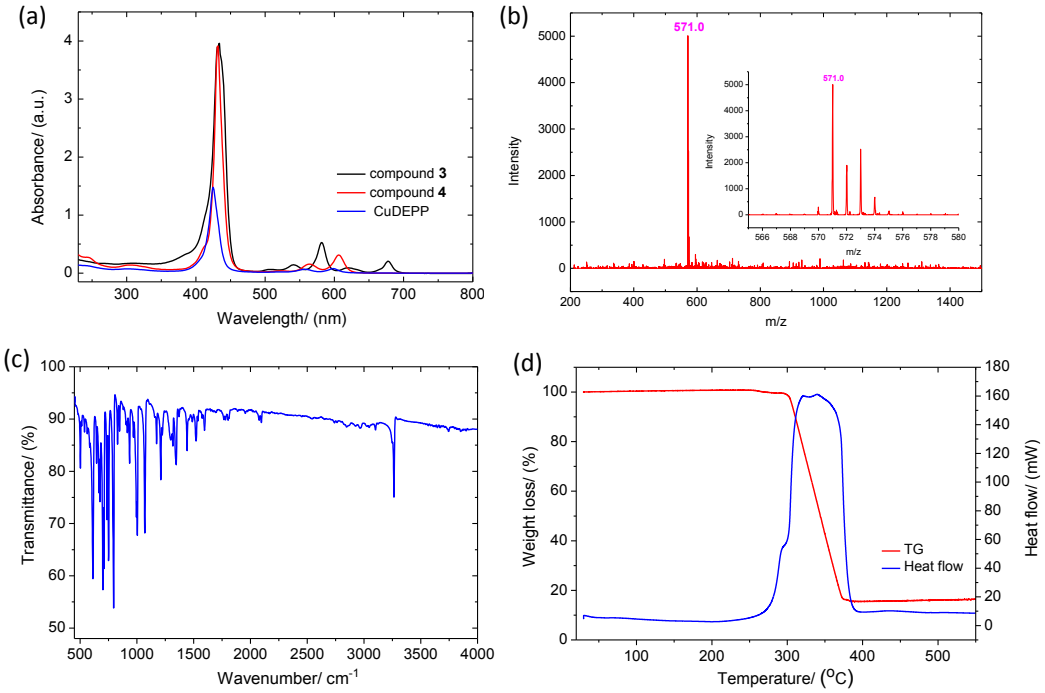

Figure 6.2: (a) UV-vis spectra of the compound **1**, **3** and **4**, (b) MALDI-ToF mass spectra, (c) IR spectra, and (d) the TG-DSC curve of the CuDEPP compound.

Based on the intrinsic properties of the aromatic 18 π conjugated system and the reported redox chemistry of the analogue compound CuTPP as well,[173] a reversible two-electron oxidation and a two-electron reduction are proposed for the CuDEPP molecule bearing 18 π-electrons, forming a dicationic species ($CuDEPP^{2+}$, 16 π-electron) and a dianionic species ($CuDEPP^{2-}$, 20 π-electron) as shown in Figure 6.3.

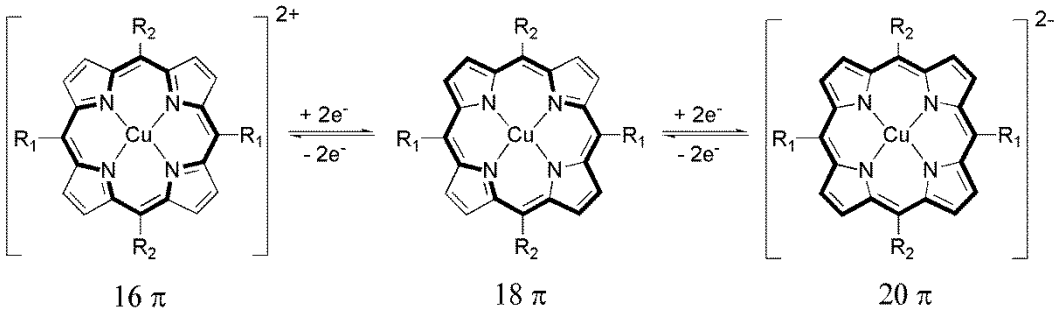

Figure 6.3: Schematic diagram of the electron transformation among 16, 18, 20 π-electron of the porphyrin core. The bold line denotes each π-conjugation circuit. R_1 = ethynyl, R_2 = phenyl (**CuDEPP**).

To verify the intriguing donor-acceptor chemistry and versatile redox relativity of the CuDEPP, three different battery cells were constructed according to the corresponding redox mechanism as illustrated in Figure 6.4. In **cell 1** ($Li/LiPF_6/CuDEPP$), the CuDEPP was used as a cathode, and lithium foil is used as an anode with an electrolyte of 1 M $LiPF_6$ in EC/DMC/PC.

In **cell 2**, i.e., $CuDEPP/PP_{14}TFSI$/graphite, the CuDEPP was used as an anode by coupling with the graphite cathode in an anhydrous ionic liquid electrolyte ($PP_{14}TFSI$).

Cell 3 ($CuDEPP/LiPF_6/CuDEPP$) was a symmetric organic battery system employing the CuDEPP as both cathode and anode, 1 M $LiPF_6$ in EC/DMC/PC was used as the electrolyte.

In these three cells, both cations and anions of the electrolyte act as the charge carriers during the charge and discharge, which is totally different from that of the conventional batteries where only single type of ion (either cations or anions) shuttles

between the cathode and the anode during the cycling.

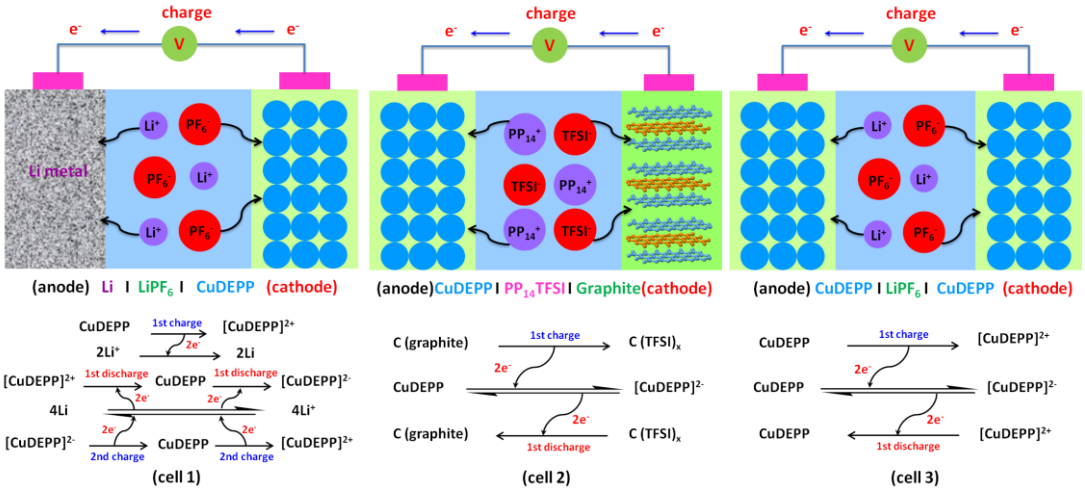

Figure 6.4: Operation schemes for **cell 1** wherein the CuDEPP is used as a cathode (left), **cell 2** system wherein the CuDEPP is used as an anode (middle), and **cell 3** system wherein the CuDEPP is used as a cathode as well as an anode (right).

[5,10,15,20-tetraphenylporphinato]copper(II) (CuTPP), a commercially available porphyrin complex, was initially tested as cathode with a construction of **cell 1**. However, the performance was unsatisfying as shown in Figure 6.5a. A discharge capacity of only 17 mAh g^{-1} (based on the mass of the active material) was observed in the first cycle at a current density of 100 mA g^{-1}, which is almost an order of magnitude lower than that of the CuDEPP electrode (198 mAh g^{-1}) in the voltage range of 4.5 - 1.8 V at 200 mA g^{-1}. This may originate from the high solubility of CuTPP active material in the liquid electrolyte and/or intrinsic limitations of the electrochemical kinetics of the CuTPP electrode. The molecular structure of the CuTPP and CuDEPP are presented in Figure 6.5c and d. Considering the ethynyl moities showing exceptional influence on the spectroscopic and electrochemical properties of the porphyrins,[174–178] I assume that the altered battery performance of the electrode was attributed to the decoration of ethynyl substituents onto the porphyrin molecular structure.

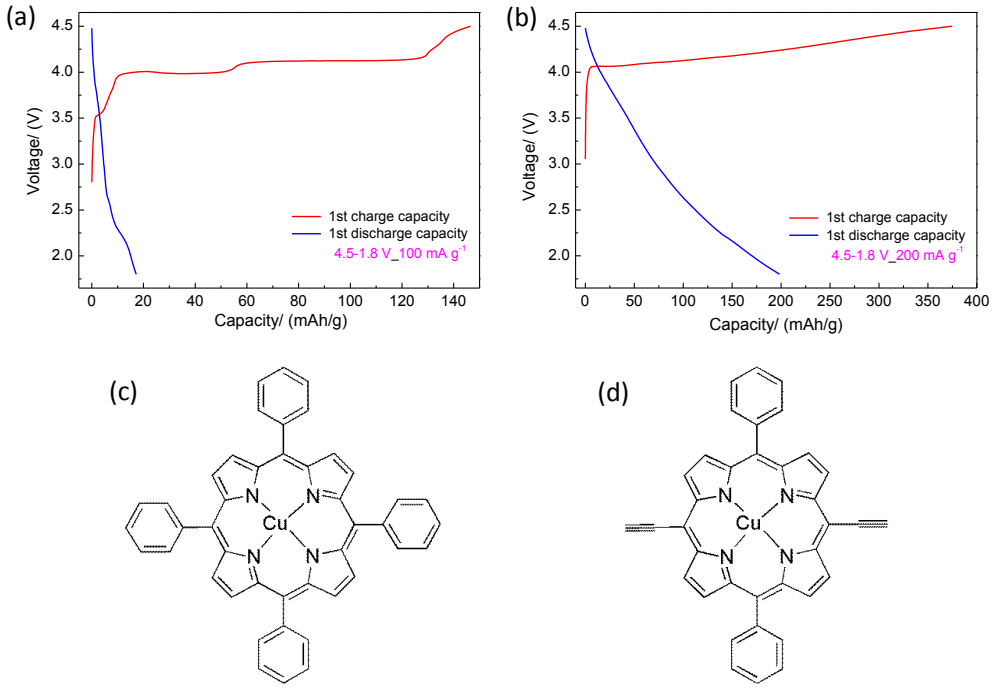

Figure 6.5: (a) Initial charge/discharge profiles of the CuTPP electrode, (b) the CuDEPP electrode in the voltage range of 4.5 - 1.8 V, (c, d) molecular structure of the CuTPP and CuDEPP.

To determine the working potential window for the Cell 1, the cyclic voltammograms with a two-electrode cell system were applied using the CuDEPP electrode as working electrode and a Li foil as the counter electrode in a voltage range of 4.5 - 0.05 V and 4.5 - 1.8 V, respectively. As shown in Figure 6.6a, a strong oxidative peak at 4.2 V is assigned to the oxidation of CuDEPP to $CuDEPP^{2+}$ and a possible polymerization of the ethynyl units. The cathodic peaks at 3.62 V and 2.34 V correspond to the reduction reaction at the porphyrin core, e.g. $CuDEPP^{2+}$ to $CuDEPP^{2-}$. The lowest irreversible reductive peaks at about 1.27 and 0.78 V are likely associated with the reduction of the center Cu(II) to Cu(I) and/or other side reactions. In the voltage range of 4.5 - 1.8 V (Figure 6.6b), reversible redox couples at 2.22/2.95 V and 3.55/3.68 V were observed from the second cycle, which are correlated to the redox reaction of the CuDEPP electrode. The weak intensity of the redox peaks may be caused by the fast electron

transfer process among the CuDEPP electrode, which is also reflected in the sloping discharge/charge profiles as discussed later.

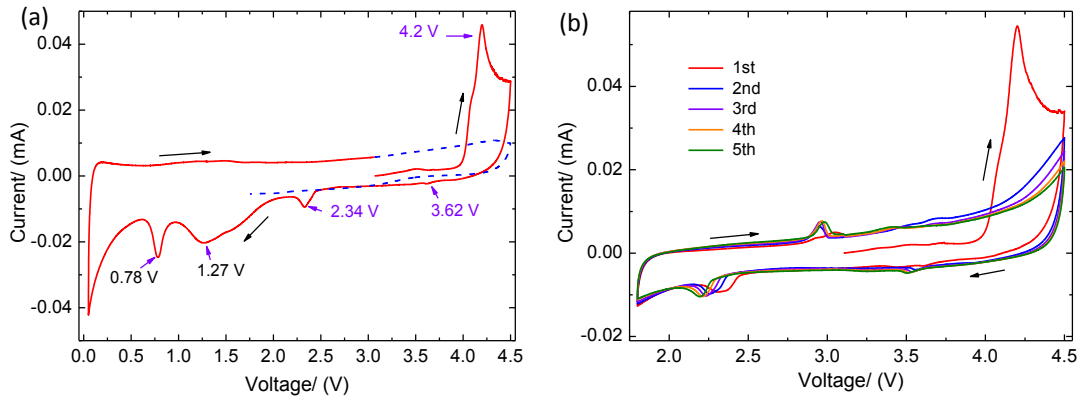

Figure 6.6: (a) Initial CV curves of the Li/$LiPF_6$/CuDEPP cell at a scan rate of 0.1 mV s^{-1} in a voltage range of 4.5 - 0.05 V, and (b) repeated CV scans in a 4.5 - 1.8 V window.

Two voltage ranges were applied (4.5 - 1.0 V and 4.5 - 1.8 V) to investigate the performance of the CuDEPP electrode as shown in Figure 6.7. A first discharge capacity of around 450 mAh g^{-1} was obtained in a voltage range of 4.5 - 1.0 V, which is almost two times higher than the electrode cycled between 4.5 V and 1.8 V (Figure 6.7a and c). However, the reversible capacity faded significantly in 4.5 - 1.0 V. Better capacity retention was observed when the cell cycled in 4.5 - 1.8 V compared to that of in 4.5 - 1.0 V. The CuDEPP cathode delivered a discharge capacity of 138 mAh g^{-1} (2 A g^{-1}, Figure 6.7c and d) in the 200th cycle in 4.5 - 1.8 V, while much lower capacity of 109 mAh g^{-1} (2 A g^{-1}, 200th, Figure 6.7a and b) was obtained in the 4.5 - 1.0 V window. In addition, the potential hysteresis increased significantly when the cell was cycled in between 4.5 and 1.0 V compared to that in the 4.5 - 1.8 V window (Figure 6.7b and d). This may be related to the unstable structure of the CuDEPP molecule in the low voltage range. Hence, the voltage range of 4.5 - 1.8 V was chosen for cell 1 in the further investigations.

The first charge capacity was approximately 400 mAh g^{-1} at a current density of 200 mA g^{-1} (Figure 6.7e), which is higher than the value estimated by a two-electron

oxidation from the CuDEPP to $CuDEPP^{2+}$ (theoretical capacity of the CuDEPP electrode is 47 mAh g^{-1} for one-electron transfer). The 1st discharge capacity was about 210 mAh g^{-1} and gradually decreased to 182 mAh g^{-1} in the 3rd cycle, which is close to the theoretical value of 187 mAh g^{-1} based on a four-electron reaction of $CuDEPP^{2+}$ → $CuDEPP^{2-}$ (*vice versa* for the recharge process).

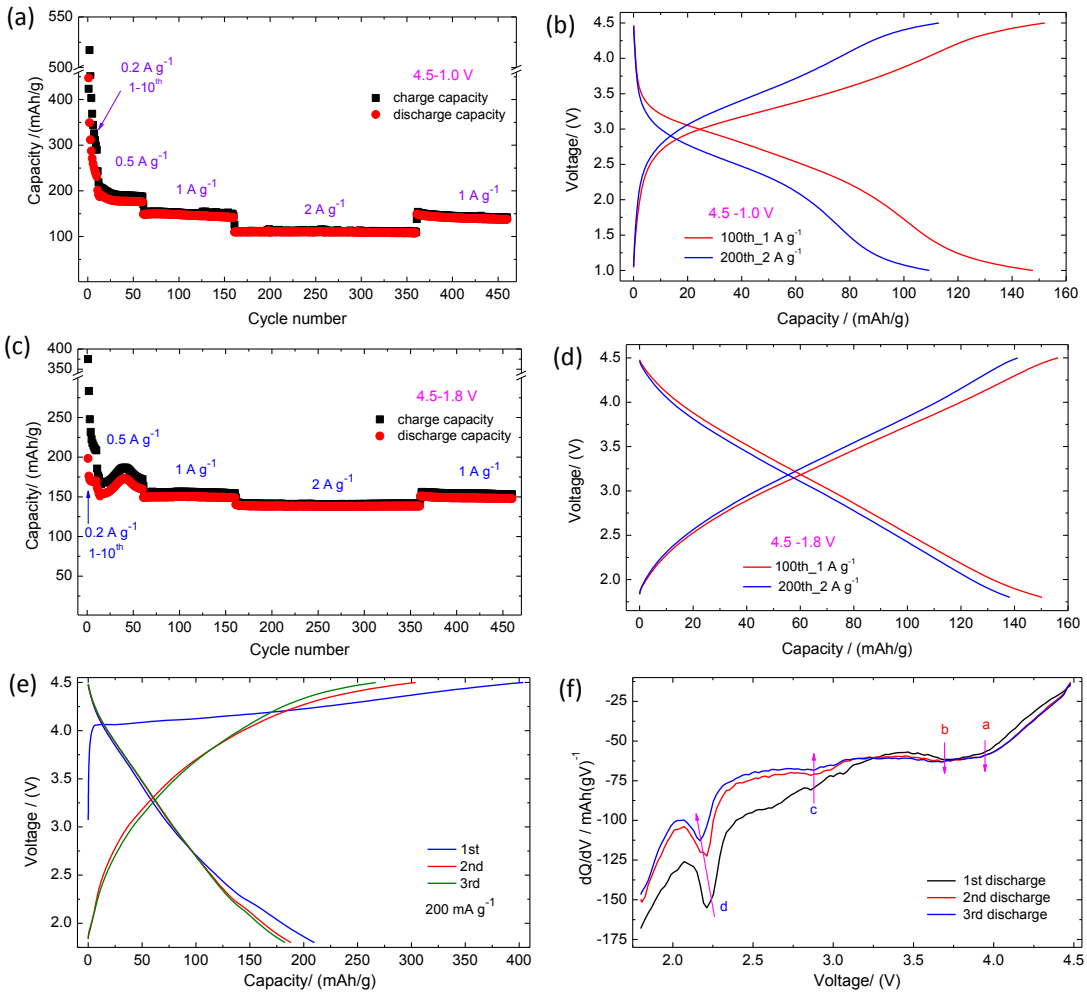

Figure 6.7: Cycling performance of the Li/$LiPF_6$/CuDEPP cell and the corresponding charge/discharge profiles: (a, b) in a voltage range of 4.5 - 1.0 V, (c, d) in a voltage range of 4.5 - 1.8 V. (e) Initial charge/discharge profiles of the CuDEPP electrode in the voltage range of 4.5 - 1.8 V, (f) dQ/dV plot of the discharge curve in e.

Considering the long and flat voltage plateau and the corresponding intense CV signal at about 4.2 V during the first anodic sweep, we suspect a side reaction as origin, probably occurring between the porphyrin molecule and liquid electrolyte and/or the

polymerization of ethynyl group of the initial CuDEPP molecule during the first charge process. No well-defined voltage plateaus were observed in the subsequent cycles, which suggest a fast electron transfer process through a solid solution reaction mechanism rather than a two-phase transition mechanism. In addition, the subtle discharge behaviors were illustrated in a dQ/dV plot of the initial cycles as shown in Figure 6.7e, in which four potential peaks at 3.9, 3.7, 2.9, and 2.2 V were revealed, implying a four-electron transfer process.

The rate performance of the Li/$LiPF_6$/CuDEPP cell was further evaluated. As shown in Figure 6.8a, the cell maintained a discharge capacity of 185 mAh g^{-1} with a coulombic efficiency of 84 % after the initial 20 cycles at a current density of 200 mA g^{-1}. Subsequently, the cell was cycled by employing increased current rates from 1 A g^{-1} to 10 A g^{-1}. The discharge capacities of 163, 143, 132, 125 mAh g^{-1} were observed at current densities of 1, 2, 4 and 6 A g^{-1} within a period of 100 cycles, respectively. Moreover, the discharge capacities can be mostly retrieved by stepwise tuning the current densities from 10 to 1 A g^{-1}. An average discharge potential about 3.0 V (vs Li) was observed for the CuDEPP electrode. The selected discharge profiles of the CuDEPP electrode at different current densities are shown in Figure 6.8b, in which the potential slightly decreased with increasing discharge rate. Remarkably, even at a high current density of 10 A g^{-1} (53 C), the CuDEPP electrode still delivered a stable reversible discharge capacity of 115 mAh g^{-1}, with a coulombic efficiency of 99.5 %. Here on discharge was finished within 42 seconds. This value corresponds to a specific energy density of 345 Wh kg^{-1} (based on the cathode active material) and a specific power of 29.5 kW kg^{-1}, which is in the range of supercapacitors.[179,180] The overlapped charge/discharge profiles were observed as shown in Figure 6.8c, which demonstrate that the voltage-fading can hardly be observed even at an extremely high current density of 10 A g^{-1} up to 100 cycles, implying excellent rate capability.

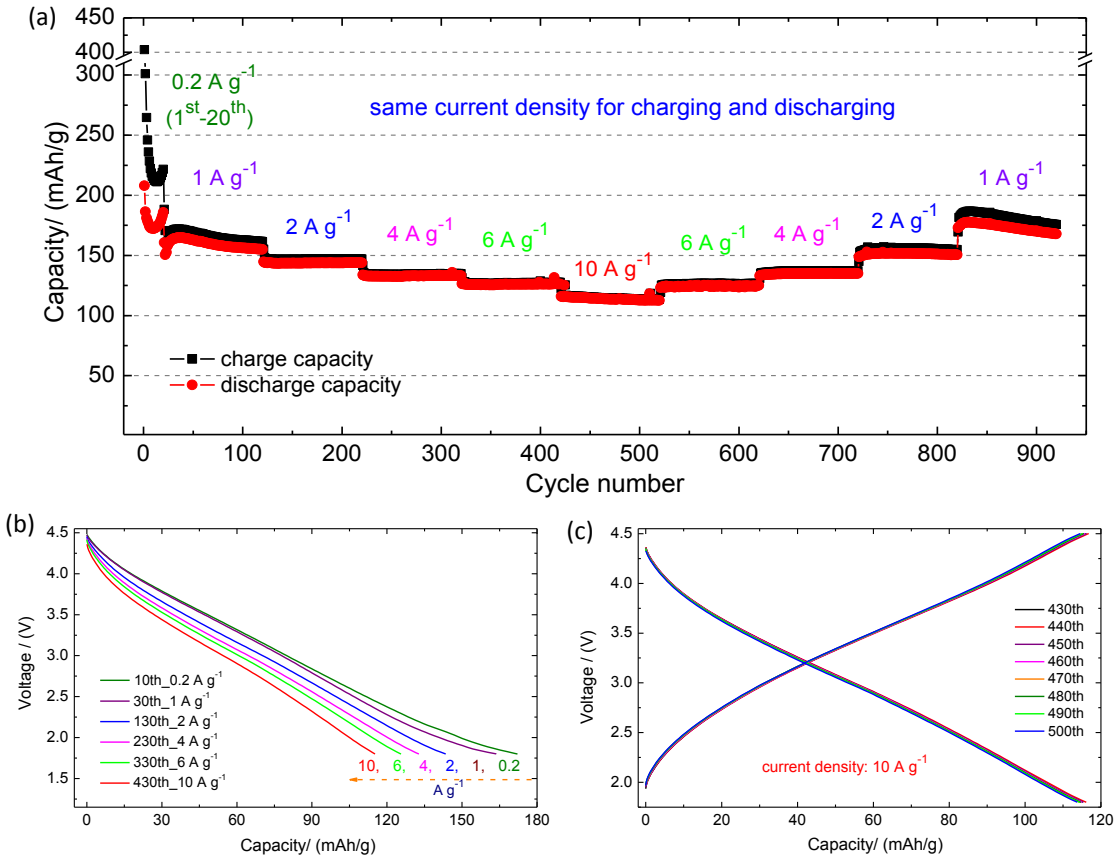

Figure 6.8: Electrochemical performance of the Li/$LiPF_6$/CuDEPP cell in a voltage range of 4.5-1.8 V. (a) rate performance, (b) selected discharge profiles at current densities from 0.2 to 10 A g^{-1}, (c) selected charge/discharge profiles at a current density of 10 A g^{-1}.

Due to the bipolar redox reactivity of CuDEPP electrode, the electrochemical behavior of the Li/$LiPF_6$/CuDEPP cell was also tested by starting with discharge process based on the reaction of CuDEPP + $2e^-$ → $CuDEPP^{2-}$ (Figure 6.9). The discharge voltage decreased steeply from the OCV (3.1 V) to 2.0 V, followed by a plateau at around 1.5 V, resulting in a capacity of 172 mAh g^{-1} at a current density of 200 mA g^{-1} (Figure 6.9a). In the subsequent cycling, the cell was operated between 4.5 V and 1.5 V. A reversible capacity of around 150 mAh g^{-1} was obtained in the 2nd cycle and the charge/discharge profiles were similar to that of the cell 1 as shown in Figure 6.9b.

For the cycling performance of the CuDEPP electrode, the Li/$LiPF_6$/CuDEPP cell was tested at a high current density of 4 A g^{-1} (21 C) for an extremely long-term cycling (8100 cycles in total). As shown in Figure 6.10, the cell was initially operated at a

current density of 200 mA g^{-1} for 20 cycles to activate the CuDEPP cathode. The maximal capacity of 150 mAh g^{-1} was obtained in the 226th cycle and the capacity retention was approximately 85 % for the first 2000 cycles and gradually decreased to 60 % after 8000 cycles with a high coulombic efficiency (> 99 %). The selected charge/discharge profiles of the cell are shown in Figure 6.10b and c, where the potential hysteresis was slightly increased upon the long term cycling.

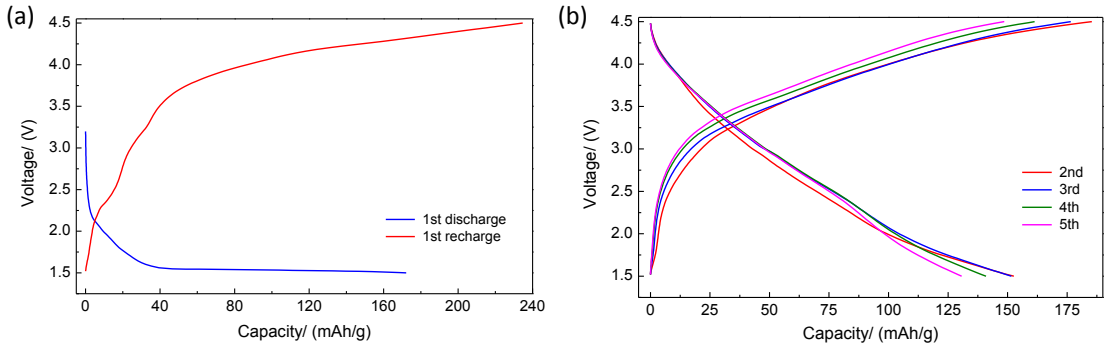

Figure 6.9: (a) Initial charge-discharge profiles, (b) the profiles in the 2nd - 5th cycle of the Li/$LiPF_6$/CuDEPP cell. The cell was discharged firstly from OCV to 1.5 V in a voltage range of 4.5 - 1.5 V.

Additional cyclic voltammograms were further captured after cycling the Li/$LiPF_6$/CuDEPP cell for 2000 cycles. As shown in Fig. 6.10d, a reversible well-defined redox peak at approximately 3 V was presented at a sweeping rate of 10 mV s^{-1}. In particular, CV curves over 10 cycles were almost identical even at a high scan rate of 100 mV s^{-1} as shown in Figure 6.10e, which indicates the highly reversible process and excellent rate capability of the CuDEPP cathode. The stability of the Li/$LiPF_6$/CuDEPP cell can be attributed to the good compatibility of the CuDEPP electrode and the liquid electrolyte, and the good stability of the CuDEPP molecule as well.

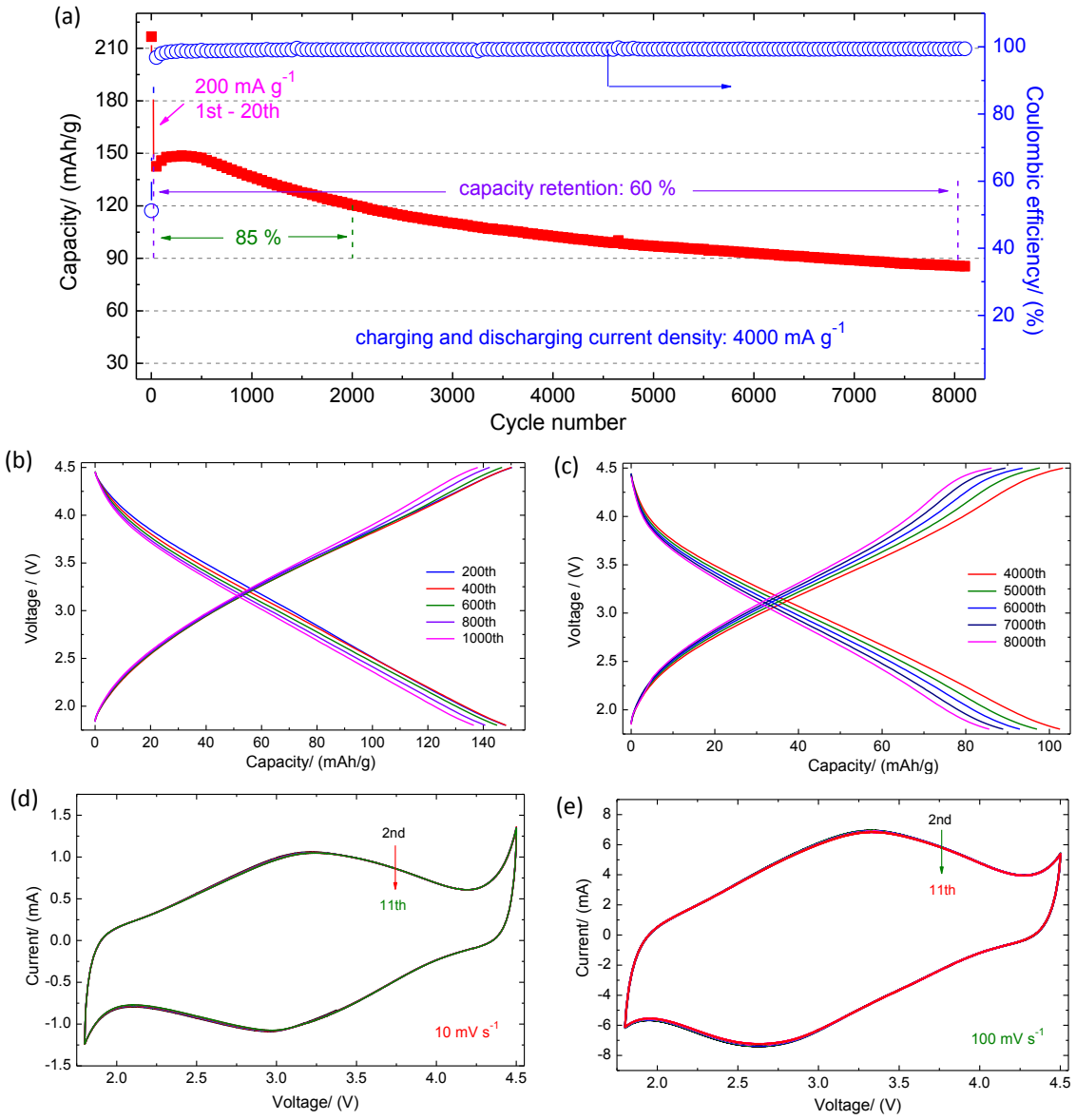

Figure 6.10: Long-term cycling of the Li/$LiPF_6$/CuDEPP cell: (a) Cycling performance, (b, c) selected charge/discharge profiles at a current density of 4 A g^{-1}. (d) CV curves of the cell obtained after 2000 cycles in a battery test at the scan rates of: (a) 10 mV s^{-1}, (b) 100 mV s^{-1}.

The morphology and crystallinity of the CuDEPP electrode material was analyzed by SEM and *ex situ* XRD in different states, respectively. Rod-like crystalline morphology with about 4 µm in length and 200 - 400 nm in width for the pristine CuDEPP was obtained as shown in Figure 6.11a and b. The morphology of the CuDEPP particle was unchanged after the first cycle (Figure 6.11 c and e). Some small particles were

observed on the surface of the CuDEPP particles, which can be due to the formation of the new phases (Figure 6.11d and f). The intensity of the XRD peaks of the CuDEPP crystal was weakened in the charged and further reduced in the discharged state. This indicates the loss of crystallinity of the CuDEPP material, which can be related to the formation of amorphous and/or nanosized crystalline when the PF_6^- and Li^+ react with the CuDEPP molecule during the charge and discharge process. It can also not be excluded that the order in the stacking of the porphyrin molecules was reduced.

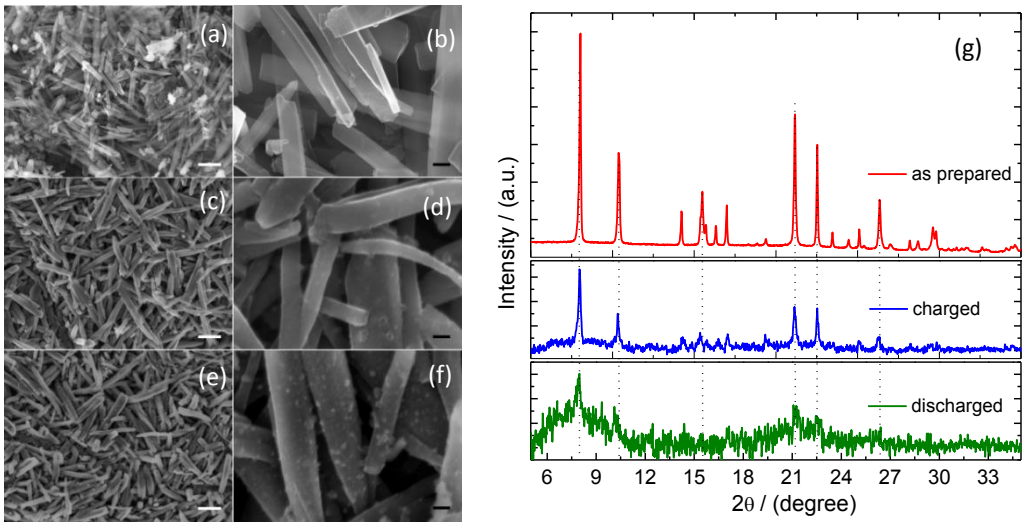

Figure 6.11: Morphology and XRD of the CuDEPP electrode at different states: (a, b) SEM images of the as-prepared, (c, d) charged to 4.5 V, and (e, f) discharged to 1.8 V states, (g) corresponding XRD patterns in the mentioned states of the CuDEPP electrode. White and black scale bar in SEM images represent 2 µm and 200 nm, respectively.

6.3.2 Porphyrin complex as anode for rechargeable batteries

In the previous section, the CuDEPP was tested as a cathode in the Li/$LiPF_6$/CuDEPP cell and excellent performance has been achieved either by charging or discharging the cell in the first cycle. In this section, another rechargeable battery cell is proposed using the CuDEPP as an anode and the graphite as a cathode, i.e. the cell 2 (CuDEPP/PP_{14}TFSI/graphite), as shown in Figure 6.4.

The CV measurements of the CuDEPP/PP_{14}TFSI/graphite cell were performed in a

voltage range of 4.0 - 0.0 V at scan rate of 5 mV s^{-1}. A couple of sharp oxidation/reduction peak was observed at 3.51/3.14 V, which is ascribed to the intercalation/de-intercalation of $TFSI^-$ into/from the graphite interlayers.[120–122] In addition, three reduction peaks at 2.57, 1.73 and 0.66 V were observed in the following anodic sweep, which suggests a multi-stage process for de-intercalation of $TFSI^-$ from the graphite. The peak intensity was significantly reduced in the second scan and the CV curves stabilized after the 2nd cycle (Figure 6.12a). In particular, overlapping CV curves were observed in the subsequent scans at a scan rate of 20 mV s^{-1} (Figure 6.12b), which implies the fast electron-transfer kinetics and the highly reversibility of the electrode.

Galvanostatic charge-discharge tests for the CuDEPP/PP_{14}TFSI/graphite cell were carried out in a voltage range of 4.0 - 0.0 V. The OCV of the cell was around 24 mV. A first discharge capacity of 94 mAh g^{-1} was observed (based on the mass of the CuDEPP material) at a current density of 1 A g^{-1} (Figure 6.12c). This value is close to the theoretical capacity of 93.5 mAh g^{-1} (CuDEPP $\rightarrow$ $CuDEPP^{2-}$). Excellent rate capability was achieved at current densities from 1 to 10 A g^{-1} (Figure 6.12d). Notably, a reversible discharge capacity of 32 mAh g^{-1} was obtained within 12 seconds at a current density of 10 A g^{-1} (106 C), corresponding to a high specific power of 14.4 kW kg^{-1}, suggesting that the power performance of the electrode is comparable to that of supercapacitors.

The cycling performance of the CuDEPP/PP_{14}TFSI/graphite cell was tested at a high current density of 5 A g^{-1} (53 C) as shown in Figure 6.12e. The capacity increased in initial cycles, stabilized in the following 100 cycles, and decreased slightly upon subsequent cycles. A reversible discharge capacity of 44 mAh g^{-1} was obtained in the 200th cycle. Selected charge/discharge profiles of the cell in the 50th, 100th, and 150th cycle are shown in Figure 6.12f, where the voltage fading was not significant during the cycling, which implies a highly reversible of the electrode at a high current rate.

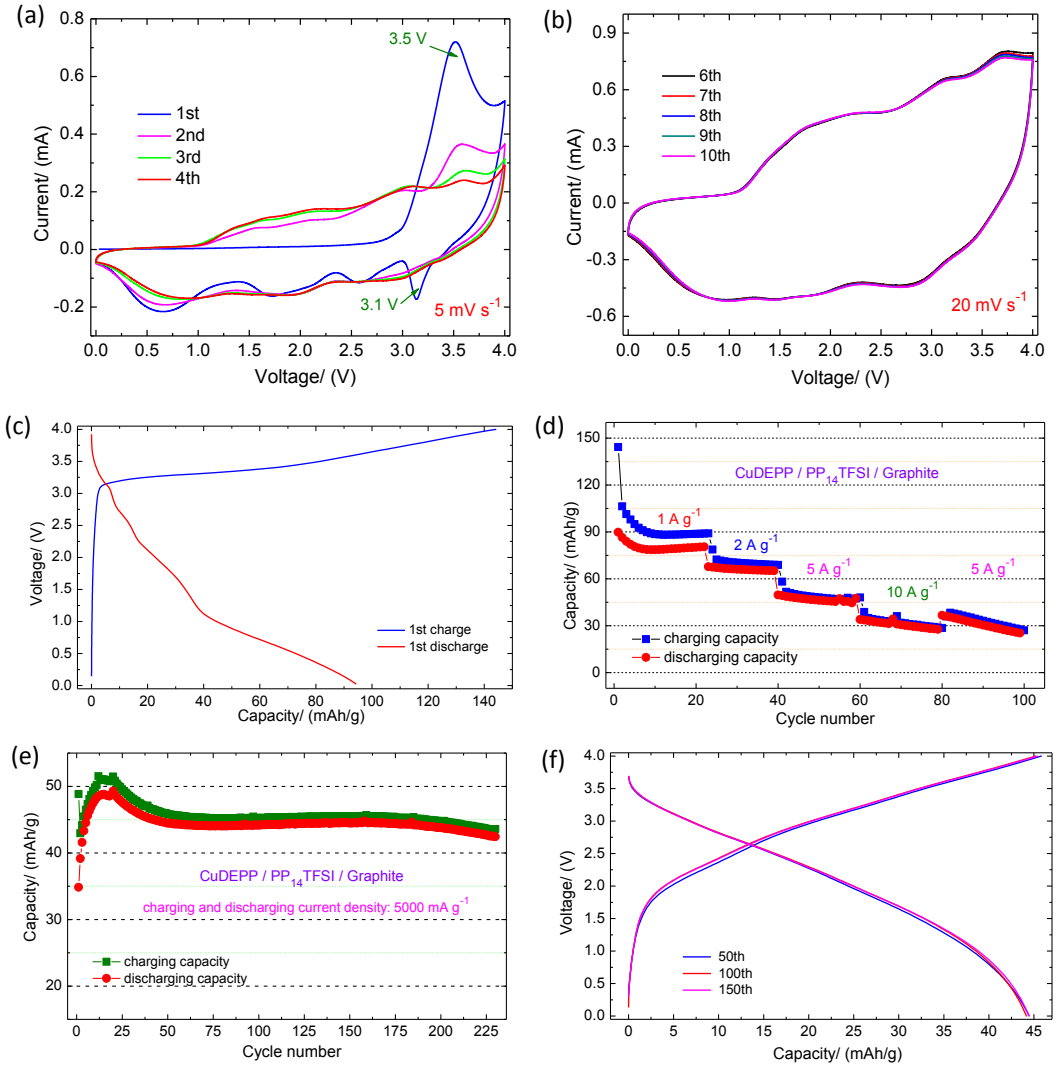

Figure 6.12: (a) Initial CV curves of the CuDEPP/PP_{14}TFSI/graphite cell at 5 mV s^{-1}, and (b) at 20 mV s^{-1}. (c) Initial charge-discharge profiles of the cell at 1 A g^{-1}, (d) rate performance of the cell for 100 cycles in total, (e) cycling performance of the cell at 5 A g^{-1} for 225 cycles, (f) selected charge-discharge profiles of the cell at the 50th, 100th and 150th cycle. The voltage range between 4.0 V and 0.0 V was applied.

The intercalation of $TFSI^-$ anions into graphite interlayers was verified by XRD, SEM, and EDX measurements. The graphite electrodes were stopped at 4.0 V in the first charged state, and at 0.0 V in the first discharged state. The (002) peak of the pristine graphite at 2θ = 26.4° shifted to a lower diffraction angle (2θ = 25.3°) in the charged state (4.0 V), which suggests that the lattice along of the graphite was expanded along c-axis by intercalating the $TFSI^-$ anion in the charge process (Figure 6.13a.). Upon

discharging, the expanded (002) peak was almost recovered (2θ = 26.3°), implying the shrinkage of the c-axis lattice upon de-intercalating of the $TFSI^-$. Compared to the pattern in pristine graphite, the XRD peaks were broadened both in the charged and discharged states, which indicates the reduction of the crystallite size of the graphite upon the intercalation/deintercalation of $TFSI^-$.

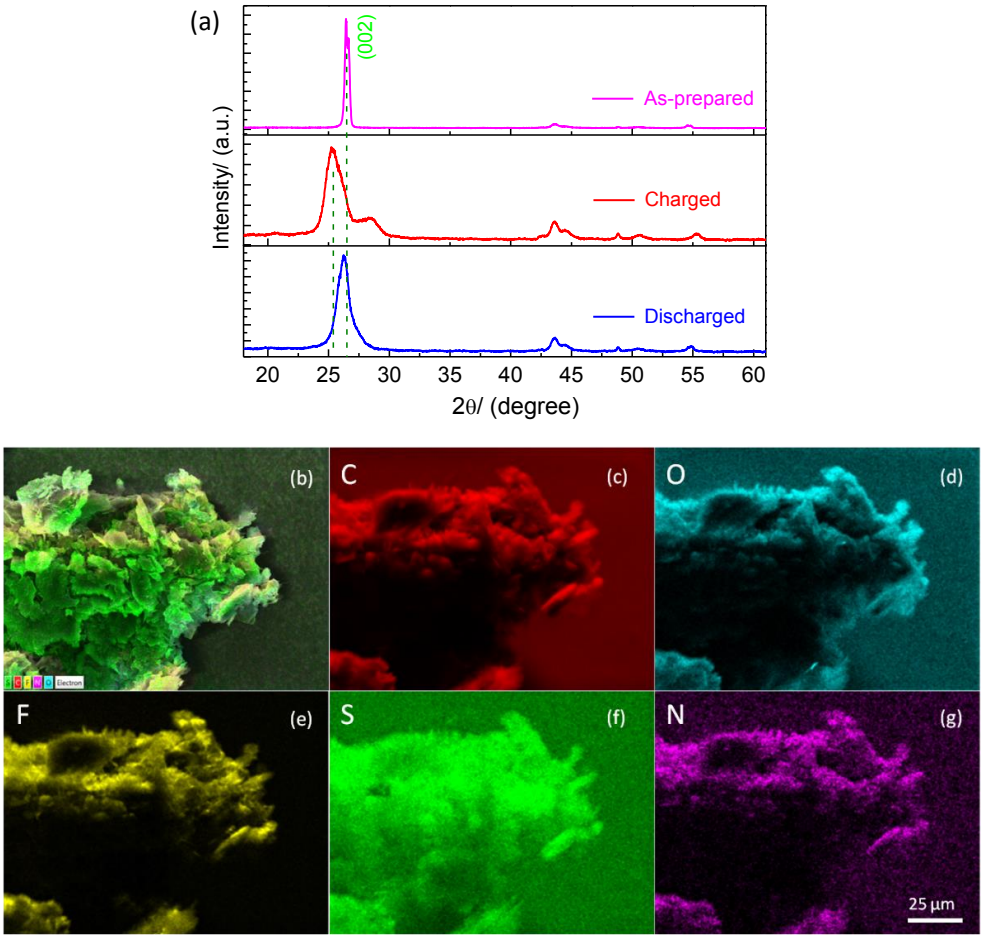

Figure 6.13: (a) XRD patterns of the graphite cathode in the as-prepared (upper), charged (middle) and discharged state (lower), (b) SEM image of the charged graphite cathode, (b → f) the corresponding elemental mapping of Carbon (c), Oxygen (d), Fluorine (e), Nitrogen (f), and Sulfur (g), respectively.

The intercalated $TFSI^-$ in the graphite cathode was further indicated by the EDX spectra and the elemental mapping (Figure 6.13b and Figure 6.14d). As shown in Figure 6.13b-f, the elemental mapping of carbon (C), oxygen (O), fluorine (F), nitrogen (N) and sulfur

(S) were uniformly distributed in the charged graphite electrode. In addition, the EDX spectrum further confirms the presence of the $TFSI^-$ species in the charged graphite cathode (see Figure A-6 in the Appendix). However, after discharging, the F, O, S, and N elements were still detected, which indicate that the de-intercalation of the $TFSI^-$ from the graphite electrode was not complete. The remaining partial $TFSI^-$ anions in the cathode kept expanding the graphite interlayers, which may facilitate the intercalation/de-intercalation processes.

6.3.3 Porphyrin complex as both cathode and anode for rechargeable batteries

In the previous sections, the CuDEPP was used as a cathode in the cell 1 and as an anode in the cell 2, both cells demonstrated highly reversible performance. In this section, the CuDEPP was used as both the cathode and the anode in a symmetric organic battery system to further probe the bipolar redox-activity (**cell 3**, CuDEPP/$LiPF_6$/CuDEPP), the schematic of the cell 3 is shown in Figure 6.4.

An initial discharge capacity of 72 mAh g^{-1} (based on the mass of active material in the cathode) was achieved in a voltage range of 0.0 - 2.8 V at 200 mA g^{-1}. Due to the bipolar redox-activity of the CuDEPP electrode, it can be oxidized to the $CuDEPP^{2+}$ species during the charge (the CuDEPP as a cathode indicated in the Chapter 6.3.1) and it can also be reduced to the $CuDEPP^{2-}$ species in the discharge (the CuDEPP as an anode indicated in the Chapter 6.3.2). Hence, in the symmetric cell, a two-electron redox process can be taken place in both CuDEPP cathode and CuDEPP anode in a voltage range of 0.0 - 2.8 V. In the cathode, the redox reaction involved between CuDEPP and $CuDEPP^{2+}$ species, i.e. CuDEPP + $2PF_6^-$ $\leftrightarrow$ CuDEPP$(PF_6)_2$ + $2e^-$. Meanwhile, in the anode, the redox reaction occurred between the CuDEPP and $CuDEPP^{2-}$ species, i.e. CuDEPP + $2Li^+$ $\leftrightarrow$ Li_2CuDEPP - $2e^-$. The capacity decreased upon cycling, discharge capacity of 59 mAh g^{-1} was obtained in the 5th cycle as shown in Figure 6.14a. However, large irreversible capacities were observed, which are probably related to the side

reaction of the electrolyte and/or the asymmetric kinetics in the cathode and the anode.

In order to further probe the bipolar redox-activity of the CuDEPP molecule (i.e. $CuDEPP^{2+} \leftrightarrow CuDEPP^{2-}$), the symmetric cell was also operated in a large voltage range of 2.6 - (-1.8) V. Four electrons can therefore be transferred between the $CuDEPP^{2+}$ and $CuDEPP^{2-}$ species in total. The voltage at 0.0 V (CuDEPP cathode vs CuDEPP anode) shown in the dotted line suggests that the symmetric cell has returned to its original state as shown in Figure 6.14b. A negative potential was observed in the profiles, meaning the formation of the $CuDEPP^{2-}$ species in the cathode and the formation of $CuDEPP^{2+}$ species in the anode in the discharge process (*vice versa* for the charge process). Reversible capacities of 138, 136, 134 mAh g^{-1} were obtained in the 10th, 20th, 30th cycle, respectively.

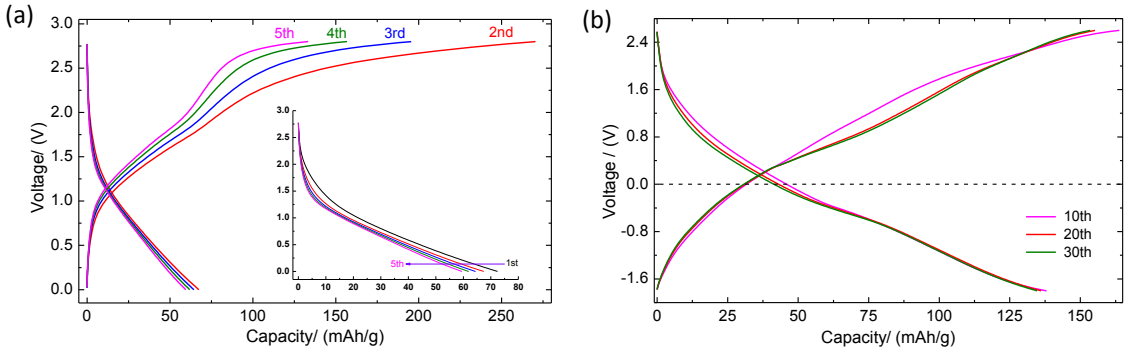

Figure 6.14: Charge/discharge profiles of the CuDEPP/$LiPF_6$/CuDEPP cell: (a) Initial cycles in 2.8-0.0 V, (b) profiles of the 10th, 20th, 30th cycle in the 2.6 - (-1.8) V window.

Figure 6.15 shows the Regone plots for various energy storage systems. In contrast to the comparably slow lithium insertion process in oxide host materials of Li-ion batteries, higher rate capability can be achieved with the CuDEPP electrode. In particular, the observed specific power density of the CuDEPP electrode was close to that of the supercapacitors without sacrificing its high specific energy density (same order of magnitude as Li-ion battery). Therefore, an energy storage device using CuDEPP molecule as electrode-active material has the potential for bridging the gap

between batteries and supercapacitors.

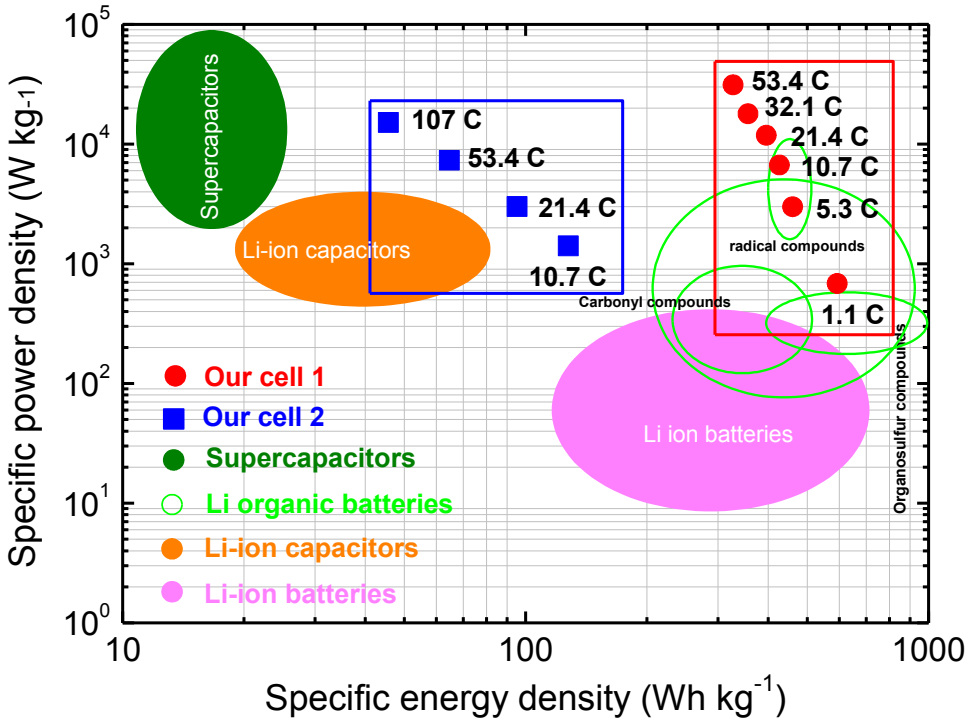

Figure 6.15: Ragone plots of the energy density and power density for various energy storage systems. Data refer to the Ref.[32,181–188]

In this chapter, we have developed a novel bipolar redox organic material of [5,15-Bis(ethynyl)-10,20-diphenylporphinato]copper(II) as electrode for rechargeable batteries. Three different battery cells have been constructed for investigating the electrochemical performance and the reaction mechanism of the CuDEPP electrode. During the cycling, both cations and anions of the electrolyte migrate between the cathode and anode. Excellent cycling stability and high rate capability have been achieved for the CuDEPP electrode either as a cathode or as an anode in the cells. Both high specific energy and high power density of the CuDEPP electrode have been observed, which would bridge the gap between the conventional rechargeable batteries and the supercapacitors for energy storage.

Chapter 7 VOCl as a novel electrode for rechargeable Li-ion and Na-ion batteries

7.1 Introduction

This chapter is based on the publication of *Electrochem. Commun.,* 2015, 60, 180-184, entitled “Vanadium oxychloride as electrode material for sodium ion batteries”, copyright (2015) Elsevier, and the publication of *Journal of The Electrochemistry of Society,* 2016, 163 (10) A2326-A2332, entitled “Electrochemical behavior of layered vanadium oxychloride in rechargeable lithium ion batteries” Copyright 2016 The Electrochemical Society.

Much progress has been achieved with the intercalation materials for rechargeable batteries, e.g. Li-ion batteries (LIBs) and Na-ion batteries (SIBs), because of their good cycle performance and rate capability.[189–191] However, the theoretical specific capacities are relatively low due to the limited number of vacant sites for Li (Na) ions intercalation/de-intercalation. Novel electrode materials capable of transferring more electrons per formula unit are therefore desirable. The number of electrons involved in an alloying/de-alloying reaction or in a conversion reaction can be more than one per formula unit, which enables high theoretical capacities, in principle.

In this chapter, a new layered VOCl material as electrodes is investigated for rechargeable Li-ion and Na-ion batteries. In chapter 4 and 5, the VOCl has been tested as electrode-active material in rechargeable chloride ion batteries, showing good

electrochemical performance. It has been found that the VOCl is air-stable and it is insoluble in the electrolytes so far. A high theoretical capacity of 260 mAh g^{-1} would be obtained in case of a full reaction of 1 VOCl with 1 Li (Na). Moreover, if a conversion reaction mechanism works with this compound as well, e.g. VOCl + 3 Li^+ + 3 e^- ↔ Li_2O + V + LiCl, the theoretical capacity of the VOCl electrode can be up to 788 mAh g^{-1}. In this chapter, the electrochemical performance and the reaction mechanism of the VOCl electrode for Li-ion and Na-ion batteries has been studied.

7.2 Experimental section

7.2.1 Electrode preparation

The preparation of the VOCl electrode for LIBs and SIBs is described in chapter 4.2.3 and chapter 5.2.1, respectively.

7.2.2 Material characterization

Scanning electron microscopy (SEM) was carried out in a ZEISS LEO 1530 instrument. Fourier transform infrared spectroscopy (FTIR) measurements were performed using a Perkin Elmer infrared spectrometer (Spectrum Two L1600401) in an argon-filled glove box. Powder X-ray diffraction (XRD) patterns were recorded in transmission geometry using a STOE STADI-P diffractometer with a Cu Kα radiation source (λ = 0.154 nm, operated at 40 kV and 40 mA). For *ex-situ* XRD measurements, the cycled VOCl electrode was carefully disassembled in the argon-filled glove box, washed with DMC and then dried at 353 K under vacuum overnight. X-ray photoelectron spectroscopy (XPS) data were recorded on a Physical Electronics PHI 5800 ESCA System using monochromatized Al K_α radiation (13 kV, 250 W) and a pass energy of 29.35 eV for detail scans and of 93.9 eV for survey scans, respectively. The binding energies (BEs) of the XPS peaks were referenced to the C(1s) signal of adventitious carbon at 284.8 eV.

Ex situ V K-edge XANES experiments were performed at the KMC-2 beamline at the BESSY II synchrotron in the transmission mode in Berlin, Germany. Powder samples were prepared and sealed in plastic bags in an argon-filled glovebox. Two argon-filled ionization chambers were used to detect the incident intensity and the transmitted intensity. Energy calibration was done by using V reference foils. The XPS and XANES measurements and data evaluation were performed by the operator of the instrument.

7.2.3 Electrochemical measurements

1 M $LiPF_6$ dissolved in a mixture of EC/DMC/PC was used as an electrolyte for LIBs (EC : DMC : PC = 1 : 3 : 1, volume ratio). 1 M sodium perchlorate ($NaClO_4$) dissolved in PC was used as the SIB electrolyte. Glass fiber filters (GF/D, Whatman) served as separators for both LIBs and SIBs. All electrodes and cells were fabricated in an argon-filled glove box with water and oxygen contents below 0.1 ppm. 2032-type coin cells were used for measuring the electrochemical performance of the VOCl electrode. The lithium foil and sodium foil were used as reference electrodes in LIBs and SIBs, respectively. The charge and discharge measurements were performed with an Arbin BT2000 battery system at 298 K. The cyclic voltammetry (CV) and electrochemical impedance spectroscopy (EIS) data were collected with a Biologic VMP-3 electrochemical workstation.

7.3 Results and discussion

7.3.1 VOCl electrode for lithium ion batteries

The electrochemical redox behavior of the VOCl electrode was characterized by CV measurements in a voltage range of 0.05 - 3.0 V (vs Li) at a scan rate of 0.1 mV s^{-1}. Initial CV curves of the VOCl electrode are shown in Figures 7.1. Four cathodic peaks of

2.08 V, 1.82 V, 1.63 V and 1.48 V were observed in the first cathodic scan down to 1.2 V, which implies a multi-step reaction involving sequential intercalation of lithium ions into the layered VOCl structure. Subsequently, an intense cathodic peak at 0.42 V was observed, which is ascribed to a conversion reaction during the further lithiation process. Few small peaks at 1.07 V, 0.95 V, 0.18 V, 0.12 V, which were only detected in the first cycle, may be related to an SEI formation and/or minor side reaction of the electrolyte in the initial discharge. From the 2nd cycle to the 4th cycle, two stable redox couples at 2.1/2.2 V and 1.0/1.2 V were observed (Figure 7.1b), which suggests a similar reaction path in these cycles.

The electrochemical performance of the VOCl electrode was tested in LIBs in a voltage range of 0.05 - 3.0 V (Figures 7.1c and d). Current density of 100 mA g^{-1} was applied for both charge and discharge processes. Two plateaus at 2.07 V and 1.61 V were observed in the first discharge down to 1.5 V (Figure 7.1c). Subsequently, a plateau-like region at 1.2 V appeared which is related to the intercalation of lithium ions into the VOCl material. Further lithiation led to a long slope from 0.85 to 0.3 V with a capacity contribution of about 756 mAh g^{-1}, which corresponds to the conversion reaction of the electrode with Li and will be discussed later. A total discharge capacity of 1228 mAh g^{-1} was obtained in the first cycle, which is higher than the theoretical capacity of 788 mAh g^{-1} based on the reaction of VOCl + 3 Li^+ + 3 e^- $\leftrightarrow$ Li_2O + V + LiCl. This excess capacity can be ascribed to initial side reactions of the electrode, probably with the electrolyte and/or the formation of solid electrolyte interface (SEI). A capacity of 759 mAh g^{-1} (corresponding to 2.8 Li per VOCl) was recovered in the first recharge (Figure 7.1c). In the 2nd cycle (Figure 7.1d), discharge capacity of 666 mAh g^{-1} (corresponding to 2.5 Li per VOCl) was obtained with a recharge capacity of 675 mAh g^{-1}, giving a coulombic efficiency of 98.6%.

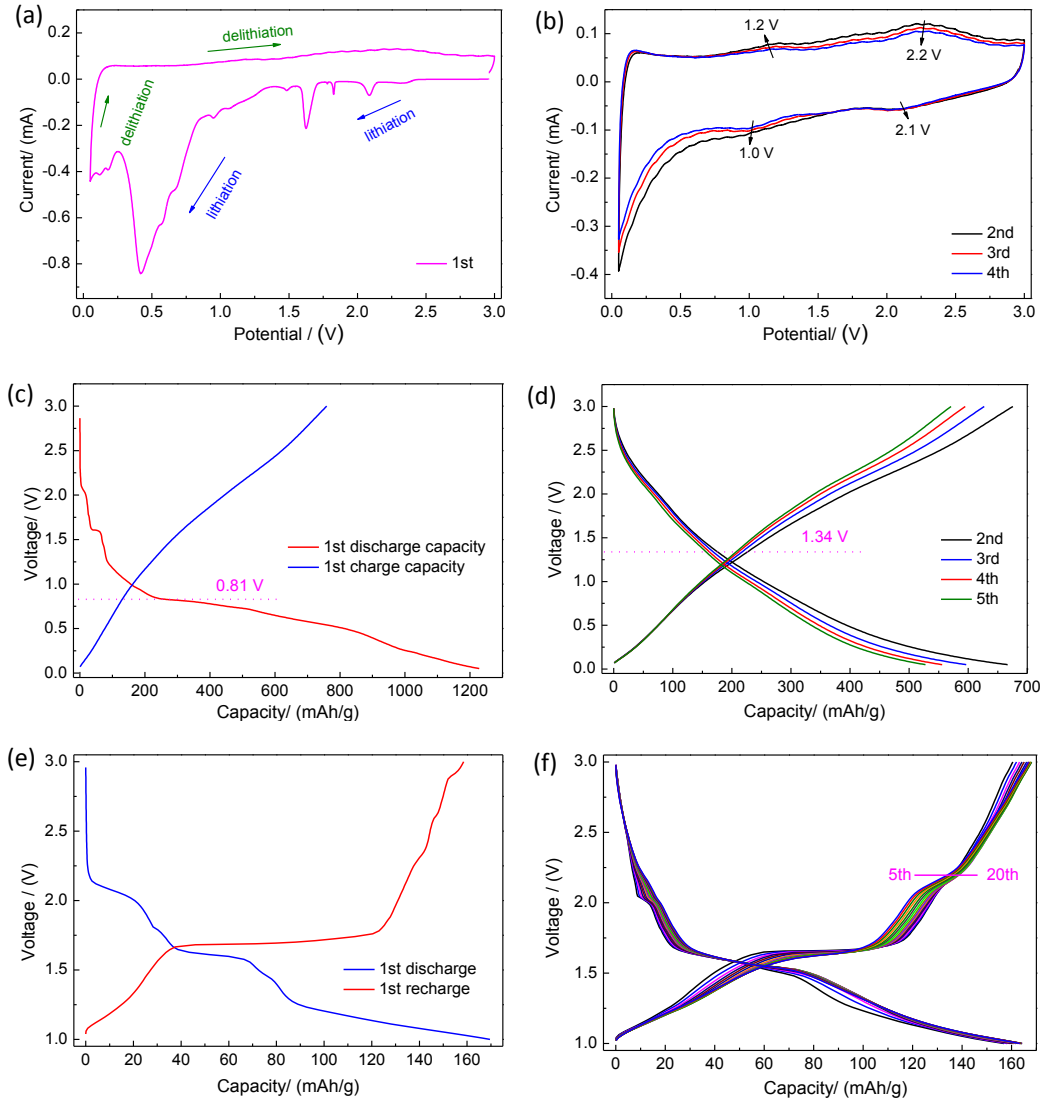

Figure 7.1: (a, b) Initial CV curves of the VOCl electrode at a scan ratio of 0.1 mV s^{-1} in a voltage range of 0.05 - 3.0 V, (c, d) Initial charge-discharge profiles of the VOCl electrode in 0.05 - 3.0 V at a current density of 100 mA g^{-1}, (e, f) Initial charge-discharge profiles of the VOCl electrode in 1.0 - 3.0 V at 100 mA g^{-1}.

A narrower voltage range of 1.0 - 3.0 V was also applied to further investigate the performance of the VOCl electrode. Two main plateaus at 2.0 V and 1.6 V with a capacity contribution of 169 mAh g^{-1} were observed at 250 mA g^{-1} in the first discharge as shown in Figure 7.1e, which is equivalent to a transfer of 0.65 e^- per formula unit. Different from that of the large change in the voltage curve after the 1st cycle in 0.05 - 3.0 V, the charge/discharge profiles of the VOCl electrode kept their peculiar shape

during cycling in the voltage range of 1.0 - 3.0 V (Figure 7.1f). This implies that the electrode reaction involved different reaction paths in 0.05 - 3.0 V and 1.0 - 3.0 V. The charge-discharge profiles of the VOCl electrode in the mentioned two different voltages range are shown in Figure 7.2. As no obvious change in the voltage curves were observed in the first and subsequent cycles in the voltage range of 1.0 - 3.0 V, which indicates that the reaction is most likely only attributed to the lithium ions intercalation/de-intercalation in the stable layered VOCl structure. In contrast, the electrochemical reaction of the VOCl electrode in the voltage range of 0.05 - 3.0 V likely involves a combination of an initial intercalation and a subsequent conversion reaction process. More detailed investigations on the phase evolution of the VOCl electrode during cycling will be discussed below.

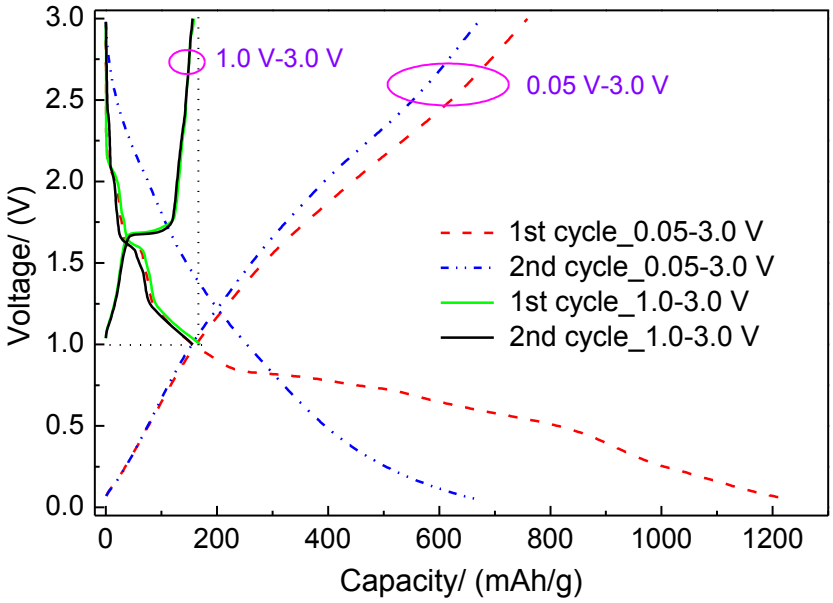

Figure 7.2: Initial charge/discharge profiles of the VOCl electrode at 100 mA g^{-1} in the voltage range of 1.0 - 3.0 V (green and black lines) and in 0.05 - 3.0 V (red and blue lines).

The cycling performance of the VOCl electrode was tested in the voltage range of 0.05 - 3.0 V at different current densities as shown in Figure 7.3a. Discharge capacities of 1204, 1179 and 1154 mAh g^{-1} with the corresponding recharge capacities of 670, 638 and 613 mAh g^{-1} were obtained in the first cycle at 260, 320 and 640 mA g^{-1},

respectively. In the 2nd cycle, the discharge capacities of 653, 625 and 608 mAh g^{-1} were obtained accordingly and the capacity faded significantly in the first 20 cycles. After 120 cycles, discharge capacities of 351, 312 and 290 mAh g^{-1} were obtained at the mentioned current densities for the VOCl electrode, respectively. Selected charge/discharge profiles (the 10th and 50th cycle) of the VOCl electrode are shown in Figures 7.3b, in which similar charge/discharge profiles were observed at different current densities during the electrochemical reaction. In addition, the potential hysteresis (polarization) of the electrode increased after 50 cycles, implying an increase of the kinetic barriers during cycling.

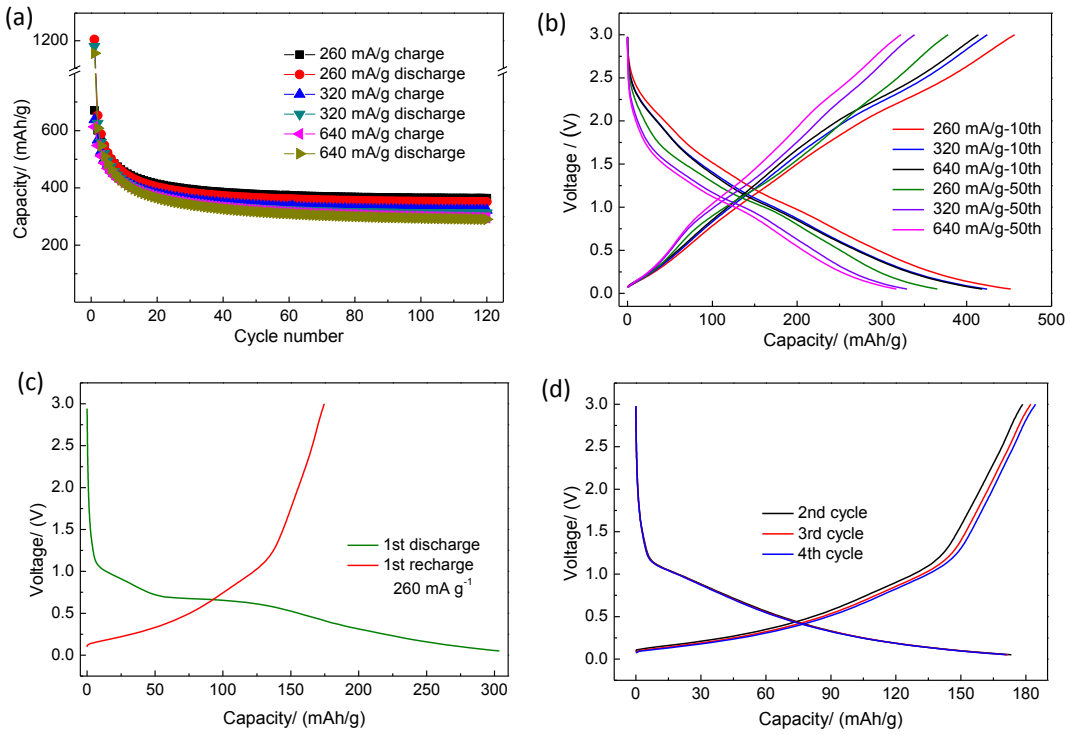

Figure 7.3: (a) Cycling performance of the VOCl electrode at various current densities in a voltage range of 0.05 - 3.0 V, (b) selected charge/discharge profiles of the VOCl electrode in the 10th and 50th cycles at 260, 320 and 640 mA g^{-1}, (c, d) Initial charge-discharge profiles of the carbon black electrode in a voltage range of 0.05 - 3.0 V at 260 mA g^{-1}.

Note that the capacity contribution from the conductive carbon black in the VOCl electrode has been deducted by testing pure carbon black as active material in the cell. The charge-discharge profiles of the carbon black electrode at 260 mA g^{-1} in the

voltage range of 0.05 - 3.0 V are shown in Figure 7.3c and d. It delivered a reversible discharge capacity of 173 mAh g^{-1} in the 2nd cycle, where capacity contributed mainly in the voltage range between 1.0 V and 0.05 V.

The reaction mechanism of the VOCl electrode was characterized by means of *ex-situ* XRD, XPS, XANES and IR measurements. Figure 7.4a shows the first charge and discharge curves in which seven different states were taken for the *ex-situ* XRD measurements. In the as-prepared state, the pattern can be assigned to the reference VOCl phase (PDF no. 01-074-1274, Figure 7.4b). After discharge to 1.2 V (state B), the (001) reflection (2θ = 11.1°) of the pristine VOCl disappeared and a new peak at 2θ = 6.9° appeared. With ongoing discharge, this peak further shifted to 2θ = 5.4° at 0.76 V (state C) and to 2θ = 3.1° at 0.4 V (state D). The continuous shift of the (001) peak can be ascribed to the intercalation of lithium ions into the VOCl interlayer in initial steps (state A → C), leading to an increase of the d-spacing. Such behavior of expansion the plane is very similar to that of analogous layered material upon intercalation of lithium ions.[192] The reflection peak at 2θ = 3.1° does not show a further shift in the following discharge and recharge processes (state D → G). Apart from this feature, a notable change in the diffraction patterns was observed between state C and D, which can be attributed to a conversion reaction, occurring at the theoretical potential (0.81 V) of the reaction $VO + 2\ Li^+ + 2\ e^- \leftrightarrow Li_2O + V$. Upon discharging to 0.05 V (state E), the intensity of the XRD pattern gradually decreased, which indicates a loss of the crystallinity of the electrode.

Li_2O, LiCl and V metallic phases, which should be formed according to the proposed reaction of $VOCl + 3\ Li^+ + 3\ e^- \leftrightarrow Li_2O + V + LiCl$, were not detected by XRD in the first cycle. This may be due to the formation of amorphous phases and/or of nanosized particles, which are found frequently in the conversion reactions - or due to a different reaction mechanism that is not reflected in the reaction equation above. LiCl and Li_2O phases, however, were further identified by IR measurement, in which the absorption

peaks related to the Li_2O and LiCl vibration (references at 452, and 498 cm^{-1}) were detected in the first discharged state (Figure 7.5a), which further confirms the conversion reaction of the VOCl electrode and giving hints for the correctness of the initial hypothesis about the reaction mechanism.

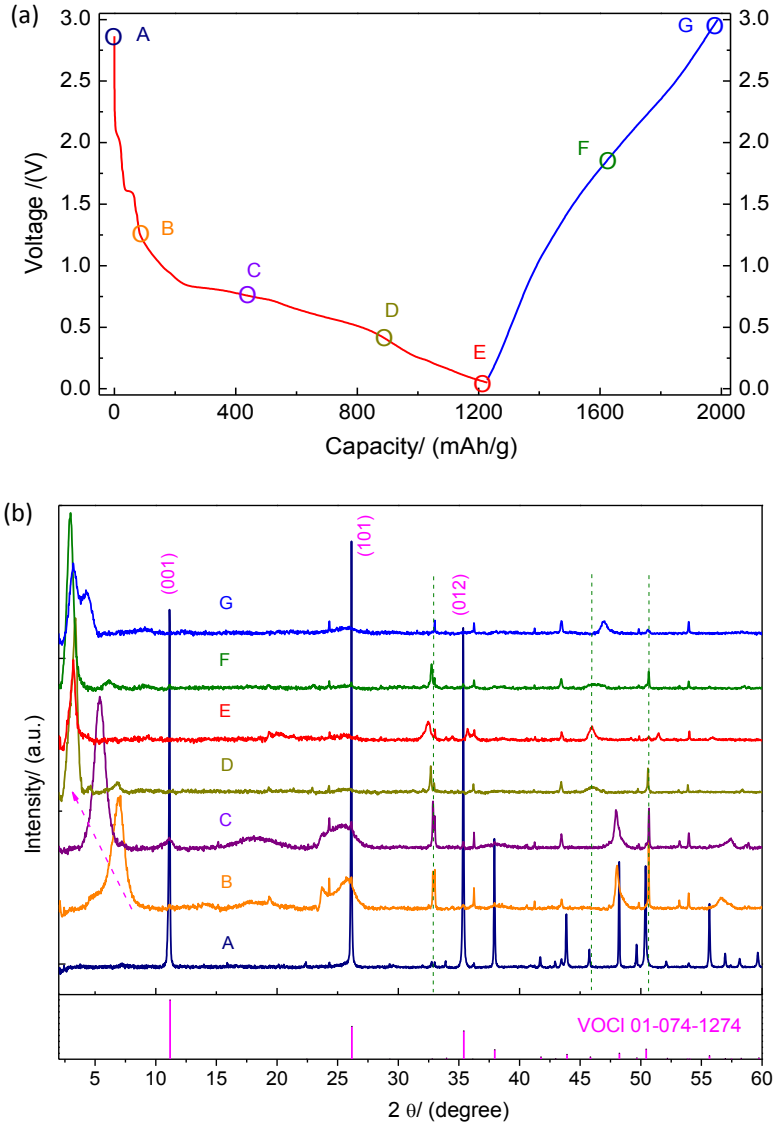

Figure 7.4: (a) Charge-discharge profile of the VOCl electrode in the first cycle where seven points were taken for the ex-situ XRD measurements, A → G denote the VOCl electrode in the as-prepared (A), discharged to 1.2 V (B), 0.76V (C), 0.4 V (D), 0.05 V (E), and recharged to 1.8 V (F) and 3.0 V states(G), (b) *ex situ* XRD patterns of the VOCl electrode at different states.

Furthermore, XRD patterns of the VOCl electrode in the 1st charged and 2nd charged

states are similar as shown in Figure 7.5b. No characteristic pattern corresponding to the as-prepared VOCl can be found in the recharged states (charged to 3.0 V). Instead, XRD pattern of the expanded VOCl electrode was observed, which suggests that some of the lithium ions remained in the VOCl during the cycling. Based on the contributed capacity in the 1st recharge and the 2nd discharge as shown in Figures 7.1c and d, the product in the charged state can reasonably be regarded as an intercalated phase of Li_xVOCl ($x \approx 0.3$).

Ex situ XPS measurement was carried out to probe the oxidation state of vanadium on the surface the VOCl electrode in different electrochemical states as shown in Figure 7.6a. In the as-prepared VOCl electrode, a single peak was detected in the $V_{2p3/2}$ spectrum at a binding energy (BE) of 516.3 eV, which is assigned to V(+III).[156] In the discharged electrode (0.05 V), the XP spectrum indicates a mixture of vanadium species with different oxidation states. The peak components at 516.2 eV, 514.7 eV and 512.3 eV are assigned to the oxidation states V(+III), V(+II) and V (0), respectively.[193,194] The observation of V (0) in the discharged state further supports the earlier conclusion that a multi-electron conversion reaction occurs during the electrochemical reaction. Therefore, the high reversible capacity of 675 mAh g^{-1} in the first recharge process at 100 mA g^{-1} can, at least in part, be attributed to the conversion reaction of $VOCl + 3\ Li^+ + 3\ e^- \leftrightarrow V + Li_2O + LiCl$. In the spectrum of the following fully recharged state (3.0 V), peaks at 516.4 eV and 514.8 eV were detected which are assigned to the oxidation states V(+III) and V(+II), respectively. This indicates that the metallic vanadium atoms in the discharged state can be reversibly oxidized in the recharge process. However, oxidation does not fully lead back to the initial state of V(+III) (of VOCl), a part of vanadium atoms remains in the oxidation state V(+II) at the surface. This result is in good agreement with the XRD observations, where showed that diffraction features observed at $2\theta = 3.1°$ in the 1st and 2nd recharged state (Figure 7.5b) were similar but different from that of the VOCl pattern in the as-prepared state,

indicating a mixture of oxidation states of vanadium in the recharged VOCl electrode.

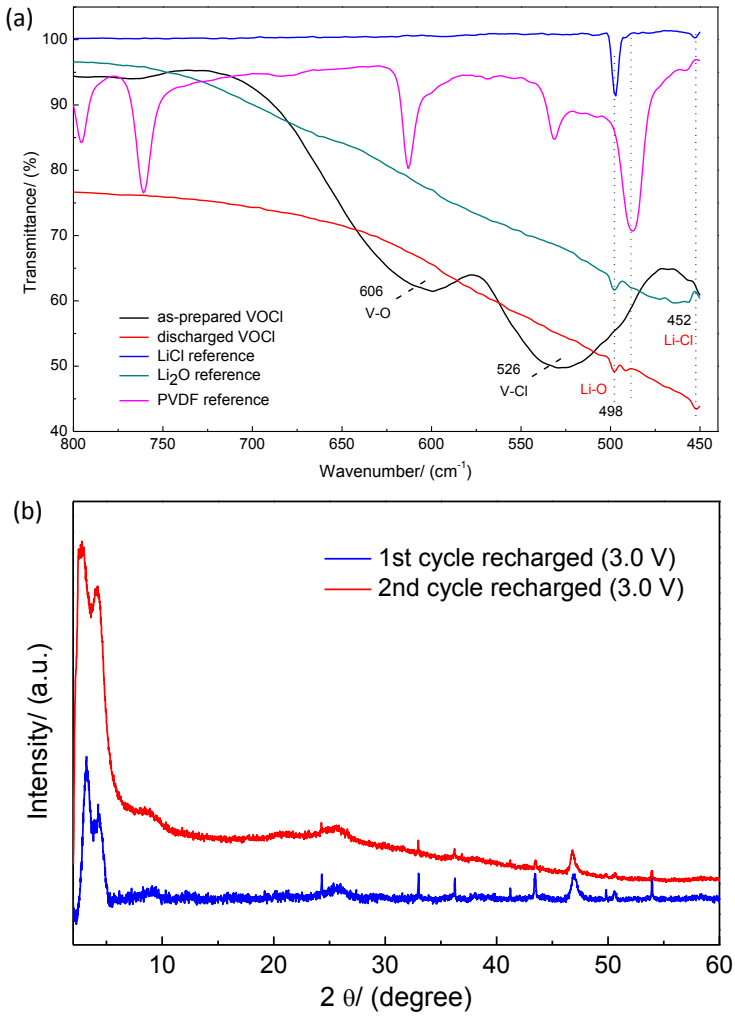

Figure 7.5: (a) IR spectra of the as-prepared and the discharged VOCl electrode (0.05 V), LiCl, Li_2O and PVDF binder were added for the reference. (b) XRD patterns of charged VOCl electrode in the 1st and the 2nd cycles.

To probe also the bulk V species for comparison, *ex-situ* vanadium K-edge XANES measurements were carried out at the VOCl electrode. Normalized V K-edge XANES spectra together spectra from a vanadium metal reference are shown in Figure 7.6b. The spectrum of the as-prepared VOCl shows that the V K-edge XANES exhibits a weak pre-edge absorption feature at a low energy (~ 5466 eV), followed by a shoulder (at 5476 eV) and the main absorption edge (at 5482 eV) at a higher energy. These features can be assigned to the forbidden 1s → 3d transition, the 1s → 4p shakedown

transition and the dipole-allowed 1s → 4p transition of the vanadium atom, respectively.[195] The pre-edge for the as-prepared VOCl sample is relatively weak, which indicates a strong forbidden transition of 1s → 3d in the octahedral VO_4Cl_2.[196] The discharged (1.0 V) electrode shows the similar spectra shape as the as-prepared VOCl electrode, which indicates that the chemical environment of the V atoms in VOCl does not change much after intercalation of lithium ions during discharging to 1.0 V.

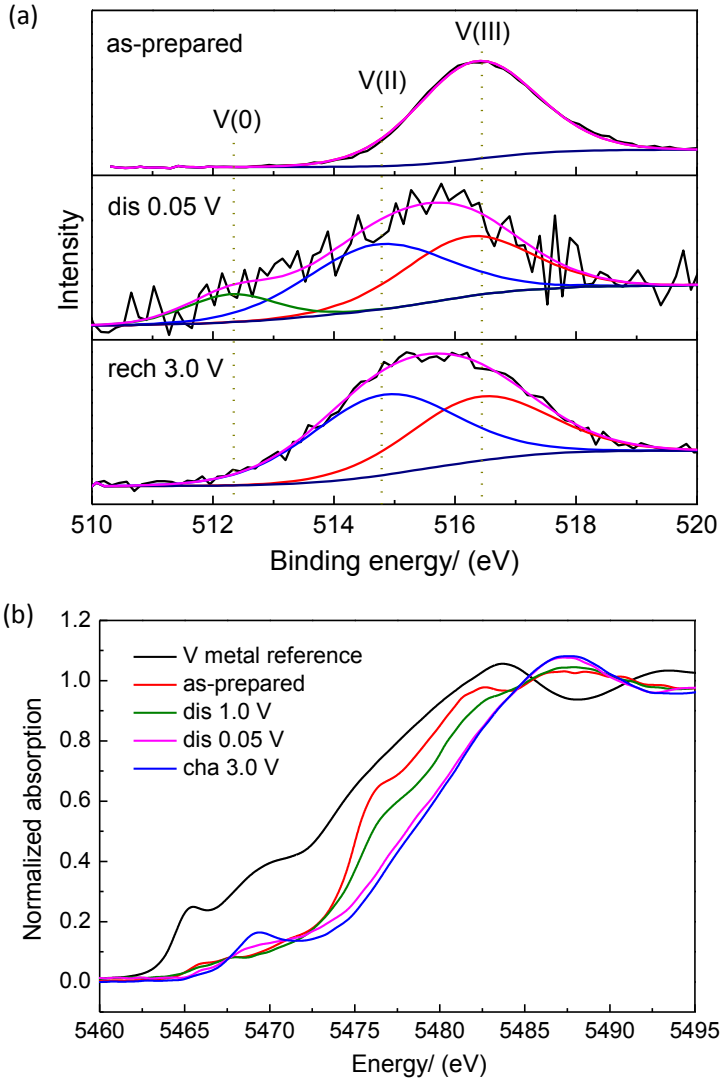

Figure 7.6: (a) $V_{2p3/2}$ region of XP spectra of the as-prepared, fully discharged (0.05 V) and recharged (3.0 V) VOCl. (b) *Ex-situ* XANES spectra of the VOCl electrode at as-prepared, discharged (1.0 V, 0.05 V), and recharged (3.0 V) states, the spectrum of vanadium metal was used as the reference.

However, after discharging to 0.05 V, the shoulder absorption peak at 5476 eV disappeared. Note that mixed oxidation states of vanadium have been found on the surface by XPS measurement in the fully discharged state (0.05 V). If this is valid for the bulk as well, the observed V K-edge absorption profiles in the discharged state (0.05 V) are an addition of scattering contributions from different vanadium species. Upon recharging to 3.0 V, an intense pre-edge peak at 5469 eV appears, indicating the weak forbidden transition of 1s $\rightarrow$ 3d. The shoulder absorption is still absent, which is different from the as-prepared VOCl sample. This finding supports the conclusions from XPS and XRD measurements, where a mixture species of vanadium was detected by XPS and the expanded VOCl phase was observed by XRD in the recharged VOCl electrode (3.0 V), respectively, showing different chemical environment of vanadium in the pristine and the recharged VOCl electrode.

The morphology of the VOCl electrode material during the electrochemical reaction was investigated by SEM as shown in Figure 7.7. The as-prepared VOCl in Figure 7.7a shows that the VOCl particles with a rod-like morphology are dispersed in carbon black particles. After discharging to 1.2 V, particle size remained similar to that of the as-prepared VOCl (Figure 7.7b). In the fully discharged state (0.05 V), many nanoparticles were observed on the surface of the VOCl material (Figures 7.7c and 7.7d), which suggests the formation of new phases through the mentioned conversion reaction. The size of the VOCl particles was reduced after 1st cycle in the recharged state (Figure 7.7e and f) and strongly reduced after 100 cycles (Figure 7.7g and h), which indicates the refinement of the particles during the conversion reaction.

The performance of the VOCl electrode during the electrochemical reaction was further investigated by electrochemical impedance spectroscopy (EIS) and cyclic voltammetry (CV) measurements. The EIS of the cell in the as-prepared, discharged to 1.2 V and discharged to 0.05 V states in the first cycle in Figure 7.8a shows that the charge transfer resistance (R_{ct}, reflected in the diameter of the semicircle[197]) of the

cell decreased with the degree of discharge. This can be due to an increase of electronic conductivity of the VOCl electrode by intercalating of lithium ions, similar to earlier reports in other analogous layered materials.[198]

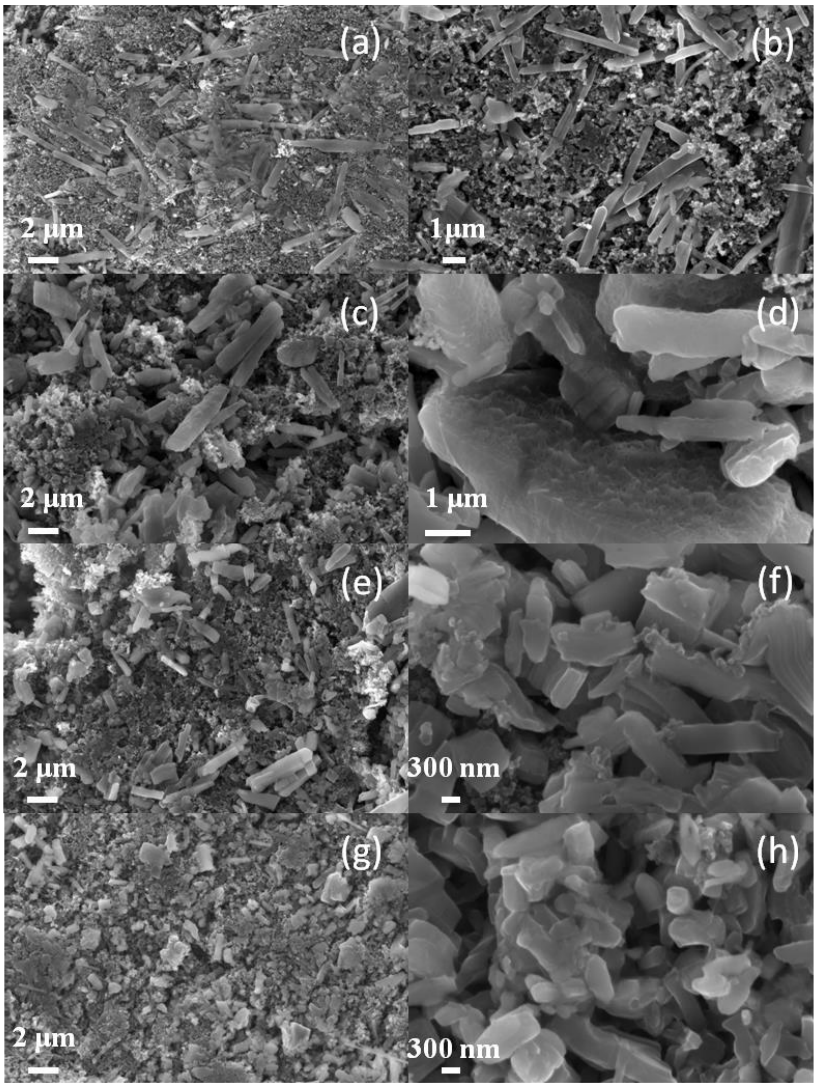

Figure 7.7: SEM images of the VOCl electrode at various states, (a) as-prepared, (b) discharged to 1.2 V, (c, d) discharged to 0.05 V, (e, f) recharged to 3.0 V in the 1st cycle, and (g, h) recharged to 3.0 V in the 100th cycle.

The charge storage in a battery through a faradaic process normally contains two parts, i.e. the diffusion controlled Li^+ insertion and contributions from surface or near-surface redox reactions (pseudocapacitance). The contribution of each part can be calculated according to the equation (7.1) and equation (7.2) by analysis of CV data taken at

various scan rates:[199–201]

$$i = a v^b \quad (7.1)$$

$$\log(i) = b \log(v) + \log(a) \quad (7.2)$$

where i is the peak current, v is the CV scan rate, and a and b are the adjustable fit parameters. When b approaches 1 or 0.5, the system is dominated by capacitance or by Li^+ insertion diffusion, respectively. Figure 7.8b shows CVs, which were obtained at different scan rates. Plots of log (i) vs. log (v) are shown in Figure 7.8c, and the inset displays the b-values which were extracted for different oxidation and reduction states. The average b value is 0.81, which indicates that the capacitance contribution cannot be neglected during the electrochemical reaction. In that case, the current response (i) at a fixed potential (V) should consist of two parts, the capacitive contribution ($k_1 v$) and the diffusion-controlled insertion ($k_2 v^{1/2}$), as shown in equation (7.3).[202]

$$i(V) = k_1 v + k_2 v^{1/2} \quad (7.3)$$

By determining k_1 and k_2, it is thus possible to calculate the fraction of the capacitive contribution and of the Li^+ insertion to the total current. Figure 7.8d shows the CV at a scan rate of 0.5 mV s^{-1} in the 3rd cycle. The shadowed region indicates the pseudocapacitance contribution to the overall current response, which was deduced from current analysis. A similar capacitance behavior has also been found for several other layered metal oxides and metal dichalcogenides.[200–204]

Based on the observed results, lithium storage in the VOCl electrode is proposed to proceed along the following mechanism as follows:

$$VOCl + x\,Li^+ + x\,e^- \leftrightarrow Li_xVOCl \quad (0 < x \leq 1) \quad (7.4)$$

$$Li_xVOCl + y\,Li^+ + y\,e^- \leftrightarrow y\,VO + y\,LiCl + Li_x(VOCl)_{1-y} \quad (0 < x + y \leq 1) \quad (7.5)$$

$$VO + 2\,Li^+ + 2\,e^- \leftrightarrow V + Li_2O \quad (7.6)$$

Overall reaction: $VOCl + 3\ Li^+ + 3\ e^- \leftrightarrow V + Li_2O + LiCl$ (7.7)

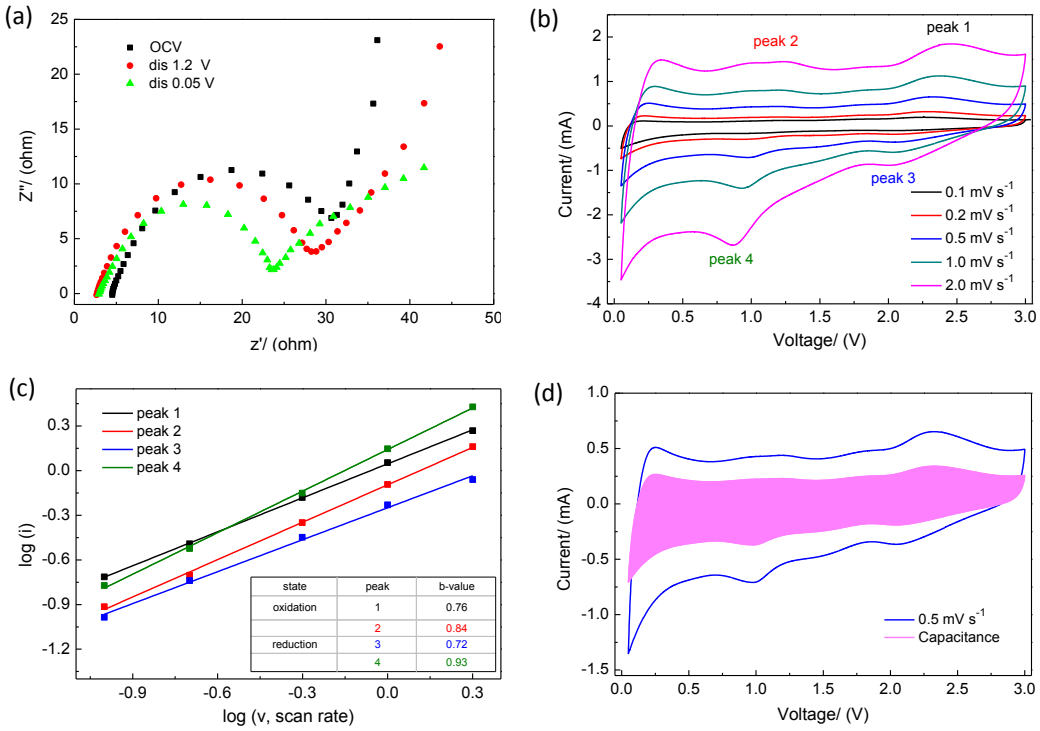

Figure 7.8: (a) Nyquist plots of the VOCl electrode at the as-prepared, discharged to 1.2 V and discharged to 0.05 V states, (b) CV curves of the VOCl electrode obtained at various scan rates after 3 cycles, (c) b-value determination of the peak cathodic and anodic currents (*i*) at scanning rate (*v*) from 0.1 to 2 mV s^{-1}, (d) CV curve at a scan rate of 0.5 mV s^{-1} with pseudocapacitive contribution (shadowed region) to the total current.

Obviously, lithium ions intercalate into the layered VOCl during the initial steps (equation 7.4 and equation 7.5, the EMF is 2.4 V), and a fraction of the formed of Li_xVOCl ($0 < x \leq 1$) is reduced to VO and LiCl. Subsequently, additional lithium ions (2 mol per formula unit, theoretical amount) can further react with VO (1 mol), leading to the formation of V and Li_2O (equation 7.6, the EMF is 0.81 V). Theoretically, 3 electrons per VOCl formula unit in total can be transferred during the electrochemical reaction leading to a theoretical capacity of 788 mAh g^{-1} with an EMF of 1.34 V for the total reaction (equation 7.7). In addition, a diffusion-controlled Li^+ insertion process and a pseudocapacitive contribution in the surface or near-surface redox reaction have been identified for the charge storage of VOCl electrode in a lithium ion rechargeable

battery.

7.3.2 VOCl electrode for sodium ion batteries

In the previous section, the layered VOCl material has been tested as electrode in LIBs, in which a high reversible capacity of 759 mAh g^{-1} has been obtained, corresponding to 2.8 Li per VOCl. Since the similar reaction mechanism for LIBs and NIBs, the VOCl material might also be used as an electrode in SIBs. Based on the observations in the previous section, the layered VOCl material can, in principle, either be as an intercalation-type electrode or as a conversion-type electrode in LIB depending on the working voltage windows, or both. To check the intercalation behavior, a narrow voltage window, i.e. 1.0 - 3.0 V, was used for the VOCl electrode in SIBs.

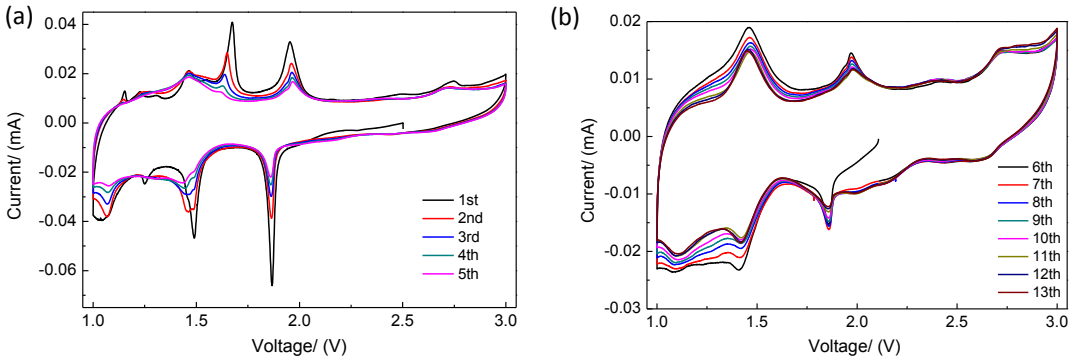

Figure 7.9: CV curves of the VOCl electrode in: (a) initial 5 cycles, (b) following cycles (6th-13th) in a voltage range of 1.0 - 3.0 V. The scanning rate was 0.1 mV s^{-1}.

The electrochemical behavior of VOCl vs. Na was investigated by CV measurements and galvanostatic charge-discharge tests. Initial CV curves of the VOCl electrode in a voltage range of 1.0 - 3.0 V are shown in Figure 7.9. Five redox couples at 2.65/2.70 V, 1.86/1.95 V, 1.48/1.67 V, 1.25/1.46 V and 1.04/1.14 V (vs. Na/Na^+) were observed in the first cycle (Figure 7.9a). After the initial cycles, three main redox peaks at 2.64/2.72 V, 1.86/1.97 V, 1.42/1.46 V remained from the 6th cycle to the 13th cycle as shown in Figure 7.9b. From the results of CV, it can be concluded that the reaction of the VOCl electrode with Na proceeds in multiple steps with different intermediate

reaction products, similar behavior has been reported in other electrode materials in SIB.[205,206]

Figure 7.10 shows the charge and discharge curves of the VOCl electrode at 0.5 C in the voltage range of 1.0 - 3.0 V for initial 10 cycles (1 C = 260 mA g^{-1}). An initial discharge capacity of 120 mAh g^{-1} was obtained, corresponding to 0.46 mol of sodium per mole VOCl. In the second cycle, the charge and discharge curves were similar to that of the first one and a coulombic efficiency of 92 % was observed. The capacity loss during the first cycle may be ascribed to an irreversible process leading to an interface layer at the surface and/or the structural changes associated with a loss of the electrical contact of a part of the active material. The features of the charge and discharge curves of the 2nd cycle to the 10th cycle were very similar, implying the similar reaction path during the charge and discharge processes.

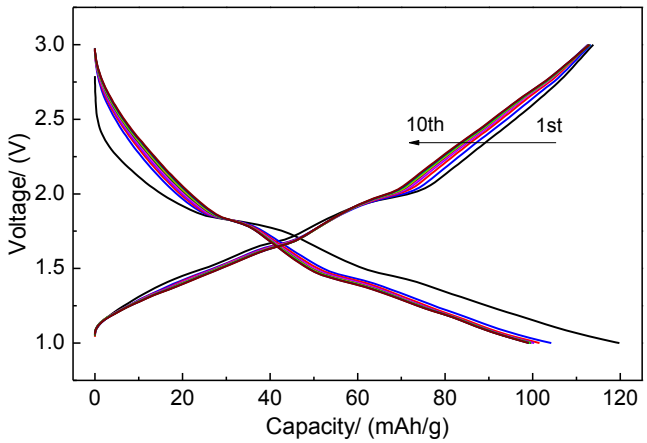

Figure 7.10: Charge-discharge curves of the VOCl electrode vs. Na/Na^+ at 0.5 C in a voltage range of 1.0 - 3.0 V for initial 10 cycles.

The cycling performance of the VOCl electrode cycled at 1 C is shown in Figure 7.11a. The electrode delivered an initial discharge capacity of 117 mAh g^{-1}. A discharge capacity of 80 mAh g^{-1} was maintained after 55 cycles, corresponding to capacity retention of 68 %. The coulombic efficiency between 92 % and 95 % indicates side reactions of the electrode, probably with the electrolyte. By coating the surface of

VOCl or confining the VOCl into conductive porous material, the cyclic stability of the electrode might be improved further. Figure 7.11b shows selected charge/discharge profiles of the VOCl-Na cell at 1 C in different cycles. It exhibited similar behavior to the one which was cycled at 0.5 C as shown in Figure 7.10. However, the polarization increased, resulting in a lower discharge potential during cycling.

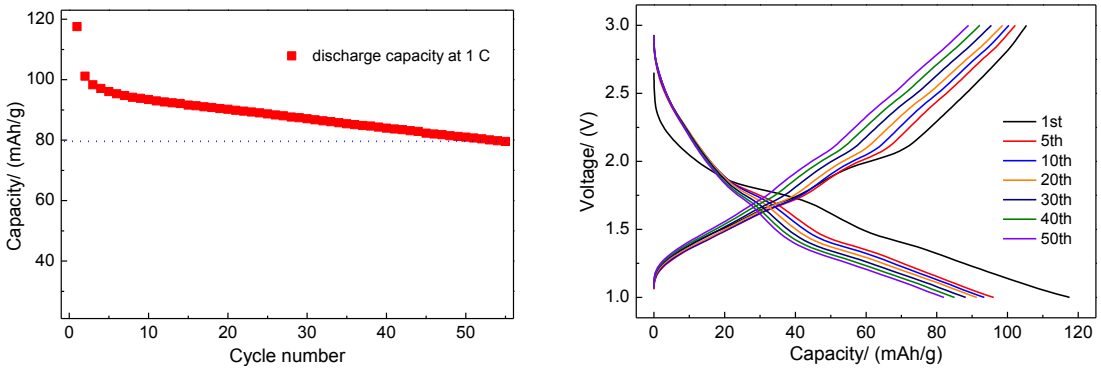

Figure 7.11: (a) Cycling performance, (b) selected charge/discharge profiles of the VOCl electrode at 1 C rate, in a voltage range of 1.0 - 3.0 V.

In order to investigate the Na-storage mechanism in the VOCl electrode, several analytical techniques were employed at various states of charge and discharge. For a first overview, *ex-situ* XRD measurements were performed on the VOCl electrode at different charged and discharged states as shown in Figure 7.12. Five points related to different states of the VOCl electrode in the first cycle shown in Figure 7.12a were taken for ex-situ XRD measurements. The reflections corresponding to the as-prepared VOCl were still present but also new diffraction peaks with high intensity appeared at low angles (2θ = 6.96°) during the discharge process. Similar behavior was also observed after lithiation of layered iron oxychloride by Aurora *et al*.[192] The observed new diffraction peak at 2θ = 6.96° corresponds to a d-spacing value of 12.68 Å. The expanded d-spacing along the c axis strongly supports the assumption of Na intercalation in the lattice of VOCl. Besides these peaks, the diffraction peaks corresponding to NaCl (PDF card no. 00-001-0994) were also observed in the discharged state which indicates that, upon sodiation, part of VOCl underwent a

conversion reaction.

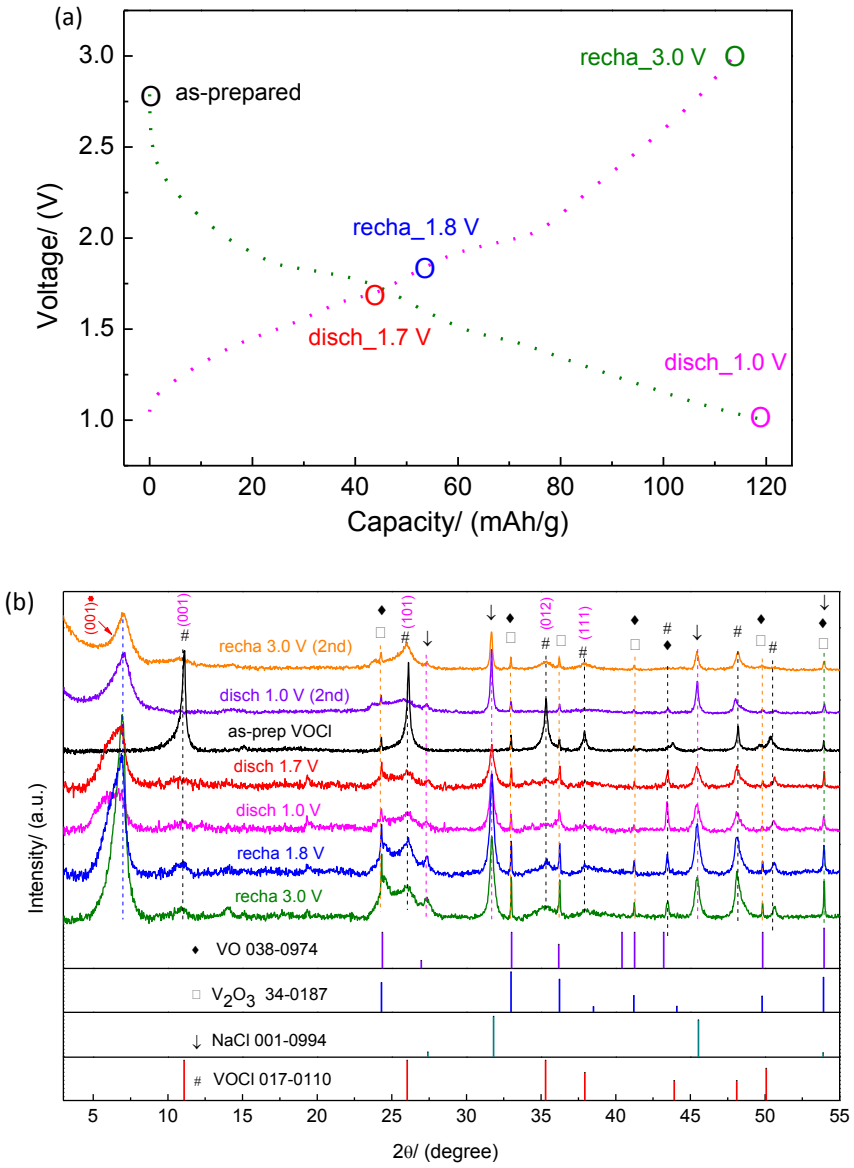

Figure 7.12: (a) Different electrochemical states of the VOCl electrode in the 1st cycle, where ex-situ XRD measurement were taken, (b) XRD patterns of the VOCl electrode at different states in the 1st cycle, discharged (1.0 V) and recharged (3.0 V) state in the 2nd cycle.

However, the detection of VO in discharged states was not possible from XRD data (Figure 7.12b), which may be attributed to the formation of nanoparticles and/or amorphous phases. The NaCl phase was still detectable in recharged states (recharged 1.8 V and 3.0 V), which suggests the partial reconversion of NaCl to VOCl during the

recharge. In addition, the patterns of the discharged and recharged VOCl in the 2nd cycle were similar to that of the 1st cycle, which demonstrate a similar path during the cycling. However, the reflection peak at 2θ = 6.96° remained in the 1st and 2nd recharged states, which indicate that the d-spacing along c-axis of the VOCl was still expanded even in the recharged state, when the material was depleted from Na.

To gain further insight in the reaction mechanism, SEM and EDX measurements were performed on the discharged VOCl electrode. Figure 7.13a and b shows SEM images of the discharged (1.0 V) VOCl electrode. Sub-micrometer sized particles can be seen on the surface of the discharged electrode which may correspond to new phases formed in the first discharge (Figure 7.13b). The elemental mapping in Figure 7.13c shows that the sodium was dispersed homogeneously in the discharged VOCl electrode. The elements V, O, Cl, F and Na were observed in the discharged state (Figure 7.13d) which provides evidence for the insertion of Na in the electrode. The high carbon content was caused by the carbonaceous substrate for the measurement and PDVF binder in the electrode. The F signal can be attributed to the fluorine content of the PVDF binder.

Summarizing the result above, we propose the sodium storage mechanism of VOCl electrode as follows:

$$VOCl + x\ Na^+ + x\ e^- \leftrightarrow Na_xVOCl \qquad (7.8)$$

$$Na_xVOCl + y\ Na^+ + y\ e^- \leftrightarrow y\ NaCl + y\ VO + Na_x(VOCl)_{1-y} \qquad (7.9)$$

During the first discharge process, *x* mol of sodium ions (per formula unit of VOCl) intercalate in the interlayers of the VOCl, leading to an expansion along the c axis ($0 < x < 1$, EMF = 2.4 V). In addition, the new phase of NaCl is formed by taking additional y mol of sodium ions in the discharge process ($0 < x + y < 1$, EMF = 2.4 V). In the recharge process, discharge product of Na_xVOCl and NaCl are partially converted into the original state. This means the sodium storage mechanism of VOCl and Na is a

combination of intercalation and conversion reaction in the voltage range between 1.0 V and 3.0 V (vs Na).

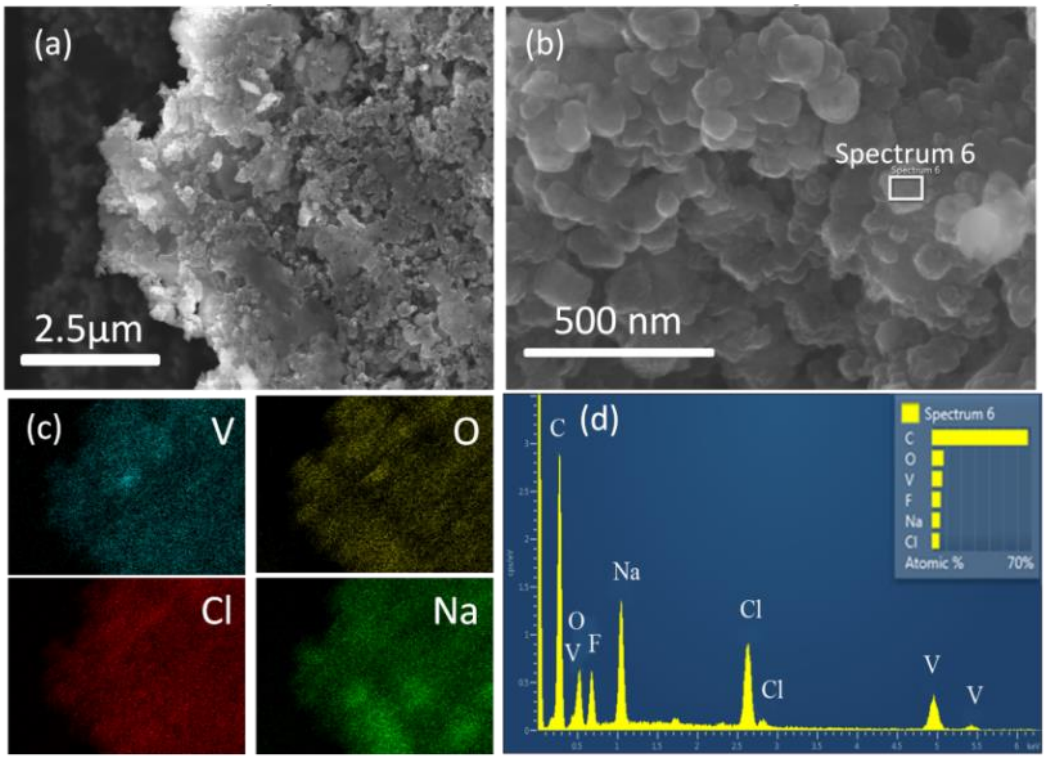

Figure 7.13: (a, b) SEM images of the discharged of the VOCl, (c) the corresponding mapping, and (d) the EDX spectrum.

In this chapter, we have investigated the layered VOCl as an electrode-active material in both Li-ion batteries and Na-ion batteries. The electrochemical performance and the reaction mechanism have been studied by various techniques, e.g. e*x-situ* XRD, XPS, XANES, FTIR and SEM. A combination of intercalation and conversion reaction has been proposed for the VOCl electrode depending on the working voltage windows.

Chapter 8 Conclusions

The introduction of renewable energy storage in our energy system raises great challenges with respect to high energy densities, long cycle lives, good safety and low-cost of electrical storage devices, rechargeable batteries in particular. In this investigation, efforts have made on developing of novel electrode materials and concepts for rechargeable batteries aiming at broadening the idea for building better energy storage devices.

Three rechargeable batteries based on anionic and/or cationic shuttles have been investigated and some promising results are documented which might help future improvements in the field of electrochemical energy storage. Two new electrode-active materials, vanadium oxychloride (VOCl) and [5,15-Bis(ethynyl)-10,20-diphenylporphinato]copper(II) (CuDEPP), have been developed for the rechargeable batteries. The electrochemical characterizations and the reaction mechanism of these electrodes have been systematically investigated.

Rechargeable chloride ion battery based on chloride ion transfer has a high theoretical energy density up to values of 2500 Wh L^{-1} depending on potential electrochemical couples, which has the potential for extending the energy storage of the lithium ion batteries. The implementation of the VOCl cathode in the chloride ion batteries was discussed in Chapter 4 and 5, in which both Li and Mg were used as anodes. 1-butyl-1-methylpiperidinium chloride dissolved in propylene carbonate and 1-butyl-1-methylpiperidinium chloride dissolved in 1-butyl-1-methylpiperidinium

bis(trifluoromethylsulfonyl)imide were tested as electrolytes. Using Li as an anode in the cell, the VOCl cathode delivered an initial discharge capacity of 189 mAh g^{-1} at a current density of 0.5 C, which corresponds to 0.72 mol of electron transferred in the reaction. A discharge capacity of 113 mAh g^{-1} was observed after 100 cycles at a current density of 2 C. The migration of chloride ions between the cathode and the anode was characterized by various techniques. XPS results indicated that the oxidation state of vanadium was partially reduced from V(III) to V(II) during the discharge, and it was oxidized to V(III) in the recharge process. The LiCl phase was detected in the Li anode after the first discharge by XRD measurement. A lattice expansion along the c axis of 5.47 Å was observed at the VOCl electrode, which is ascribed to the intercalation of PP_{14}^{+} ions during the initial discharge process. Indications for this mechanism were found by *ex-situ* XRD, IR, TEM and XPS measurements. The enlarged interlayers facilitated the Cl^{-} ions moving out/into the VOCl cathode during the discharge/recharge processes, resulting in fast charge and discharge capabilities. The good compatibility of the VOCl electrode with the liquid electrolyte could be one of reasons for the good cyclic stability. The finding in this work suggests that chloride ions can be transferred rapidly between the cathode and the anode in the chloride ion battery.

Li-free chloride ion battery cell with a Mg based anode was further investigated and discussed in Chapter 5. It was shown that the chloride ion can be dissociated from the VOCl and formed VO at the cathode in the discharge process using a composite of Mg/CB as an anode. Furthermore, the VOCl cathode was oxidized to $VOCl_2$ in the first charge process using a composite of $MgCl_2$/Mg/CB as the anode. The oxidation state of vanadium in V(II) and V(IV) were detected in the discharged and charged state, respectively. Better electrochemical performance was observed when the VOCl electrode was cycled between 2.5 V and 0.6 V with the compostite of $MgCl_2$/Mg/CB as anode. Two distinct plateaus were observed at 1.9 V and 1.3 V (vs Mg) in the discharge

process, which are related to the redox reactions of the V^{4+}/V^{3+} and V^{3+}/V^{2+}. An activation process was noticed during the initial cycles, delivering a maximum discharge capacity of 101 mAh g^{-1} in the 9th cycle and the capacity reduced to 87 mAh g^{-1} after 30 cycles. In comparison with the results of the chloride ion battery using Li as an anode, the VOCl cathode demonstrated a lower reversible capacity when the Mg based composite anode was used. Further investigation on the Mg anode is needed for better understanding the Li-free chloride ion battery. From these two chapters, it can be concluded that the chloride ion battery could have the potential to deliver highly reversible capacities depending on the electrochemical couples and the electrolytes. In addition, both Li and Mg based anodes can be used in the chloride ion batteries, which might provide new insights on building different electrochemical couples for the energy storage.

Organic rechargeable batteries have gained much attention recently due to their tunable specific energy and power density, cost-effective, environmentally friendly properties. Moreover, organic materials can facilitate and shorten the coating process during the fabrication of electrodes which is another important cost factor. However, although promising from the initial storage capacities, voltages, safety and resource situation, the cyclic stability is low of most of the published organic electrodes and new approaches seem therefore necessary. In Chapter 6, a [5,15-Bis(ethynyl)-10,20-diphenylporphinato]copper(II) (CuDEPP) has been developed as a new and much more stable electro-active material for organic rechargeable batteries. There, the organic molecule can serve both as an electron acceptor and as electrode donor during the electrochemical reaction. The CuDEPP electrode has a theoretical capacity of 188 mAh g^{-1} based on a four-electron reaction. In addition, the molecule is thermally stable up to 250 °C in air and it is insoluble in the commonly used liquid electrolyte, which is of great importance for the application in rechargeable batteries. The CuDEPP material has been tested as a cathode (cell 1), an anode (cell 2),

and in a symmetric configuration cell (cell 3) to fully evaluate its electrochemical performance.

The cell 1 cycled between 4.5 V and 1.8 V (vs Li) delivered better electrochemical performance compared to other operating voltage windows. An analogous compound of [5,10,15,20-tetraphenylporphinato]copper(II) (CuTPP) as a cathode does not have the abovementioned ethynyl groups of the CuDEPP and demonstrated poor electrochemical performance, delivering an initial discharge capacity of 17 mAh g^{-1} which was almost one order magnitude lower than that the CuDEPP electrode (198 mAh g^{-1}) using the same cell configuration. The cell 1 demonstrated both ultra-fast charge and discharge (53 C) capabilities and long-term (8100 cycles) cycling stabilities. This good electrochemical performance can be attributed to the conjugated system with two ethynyl groups in the CuDEPP molecule. The triple bonds obviously stabilize the material in the bulk configuration by coordinating the Cu in a donor-acceptor interaction and lead to a staircase-like stacking of the molecules, thus enabling good access of the charge carriers. A specific energy density of 345 Wh kg^{-1} and a specific power density of 29.5 kW kg^{-1} were achieved at a current density of 10 A g^{-1} based on the mass of the CuDEPP active material which is a world record for a battery with such a good cyclic stability. Both Li^+ and PF_6^- from the electrolyte participated in the electrochemical reaction, and migrated to the negative charge and the positive charge of the electrodes, respectively.

The CuDEPP material has also been tested as an anode in the rechargeable batteries, i.e., CuDEPP/PP_{14}TFSI/graphite. A high discharge voltage was observed using graphite as a cathode where the anions were intercalated. During the charge and discharge, PP_{14}^+ ions of the PP_{14}TFSI electrolyte migrated into/from the CuDEPP at the anode. At the same time, the $TFSI^-$ ions were intercalated/de-intercalated into/from the graphite cathode. Two electrons per CuDEPP unit were transferred between the CuDEPP and the $CuDEPP^{2-}$ species enabling a theoretical capacity of 93.5 mAh g^{-1}. The (002) plane

of the graphite expanded/shrinked during the charge/discharge processes because of the intercalation/de-intercalation of the $TFSI^-$, as was identified by XRD and EDX measurements. The cell 2 delivered an initial discharge capacity of 94 mAh g^{-1} at a current density of 1 A g^{-1} between 4.0 V and 0.0 V, which is close to the theoretical capacity. The cell 2 could endure extremely high rates of charge and discharge. A reversible discharge capacity of 32 mAh g^{-1} was observed at a current density of 106 C, and the discharge step was done in 12 seconds only.

In a symmetric cell, i.e., CuDEPP/$LiPF_6$/CuDEPP, the CuDEPP material was used as both the cathode and the anode. In this configuration, a two-electron reaction or a four-electrode reaction could be established by adjusting the operating voltage windows. The two-electron reactions occurred simultaneously at both the CuDEPP cathode and the CuDEPP anode, in which the electrons were transferred between the CuDEPP and $CuDEPP^{2+}$ species at the cathode, and between the CuDEPP and $CuDEPP^{2-}$ species at the anode in a 2.8 - 0.0 V window. The four-electron reactions process involved the electron transferring between the $CuDEPP^{2+}$ species and the $CuDEPP^{2-}$ species, which was operated between 2.6 V and (-1.8 V). The symmetric organic cell delivered discharge capacities of 72 mAh g^{-1} and 138 mAh g^{-1} in voltage ranges of 2.8 - 0.0 V and 2.6 V - (-1.8 V) at a current density of 200 mA g^{-1}, respectively.

In contrast to the comparably slow lithium insertion process in oxide host material for Li-ion batteries, high rate capability has been achieved with the CuDEPP electrode in organic batteries based on both cationic and anionic shuttles discovered in the present work. The stabilization of the redox species with highly π-conjugated structure obviously plays an important role in sustaining good battery performance. The diversity of the CuDEPP molecule as an electrode-active material in this investigation highlights a new approach for molecular design of bipolar redox organic electrode for the rechargeable batteries.

Conversion materials for rechargeable batteries offer theoretically high energy densities which have the potential as alternatives to address the challenges in traditional lithium ion batteries. In Chapter 7, the study was set out to explore high performance electrodes for rechargeable batteries based on cationic shuttle. Layered VOCl material has been initially investigated as electrode in lithium ion and sodium ion batteries. For the implementation of the VOCl electrode in Li-ion battery, it could be shown that the Li ions storage in the VOCl electrode involved an intercalation reaction in initial steps and a conversion reaction in subsequent steps. Three electrons can be transferred theoretically within a conversion reaction enabling a theoretical capacity of 788 mAh g^{-1}. A high reversible capacity of 759 mAh g^{-1} was achieved when the VOCl electrode was cycled in a voltage range of 3.0 - 0.05 V (vs Li), corresponding to 2.8 Li per VOCl formula unit. The oxidation state of V (0) was detected by XPS, and the LiCl and Li_2O were evaluated by IR on the discharged VOCl electrode, which support the hypothesis of a conversion reaction of the VOCl electrode with Li. A particle refinement was noticed in the first cycle through the conversion reaction, and this became significant after 100 cycles. In addition, a diffusion-controlled Li^+ insertion process and a pseudocapacitive contribution in the surface or near-surface redox reaction were identified for the charge storage of VOCl electrode in the Li-ion batteries.

In the second part of the Chapter 7, the study was focused on the investigation of VOCl electrode for the rechargeable Na-ion batteries between 1.0 V and 3.0 V (vs Na). The VOCl interlayers were expanded after intercalating Na ions during the first discharge. The expansion remained in the subsequent cycles, enabling fast charge and discharge capabilities. The cell delivered a reversible discharge capacity of 117 mAh g^{-1} at a current density of 1 C, which corresponds to 0.45 Na per VOCl unit, and the capacity decreased to 80 mAh g^{-1} in the 55th cycle. NaCl phase was detected in the discharged electrode by *ex-situ* XRD and it partially converted back to VOCl during the recharge

process. The Na storage mechanism in the VOCl electrode obviously involves a combination of intercalation/de-intercalation and partial conversion reaction processes in the voltage range of 3.0 - 1.0 V.

In this thesis, three rechargeable batteries based on different ions shuttles have developed. Rechargeable batteries based on chloride ion shuttling have the potential to deliver highly reversible battery performance. High power density, energy density and long-term cyclic stability of energy storage devices could be built with organic batteries based on both cationic and anionic shuttles. The functional groups in the tested molecules played an important role in the battery performance. Developing of conversion material for rechargeable batteries based on cationic shuttle provides opportunities to increase the energy storage capability for the future energy storage.

Chapter 9 Outlook

Developing new materials and batteries remains an important issue for energy storage also in the future. The new concept of chloride ion batteries is still in an early stage, there are many aspects that need to be addressed in further studies. Developing high performance electrodes (both cathode and anode), such as cathode materials of metal chloride (e.g. $FeCl_3$, $CuCl_2$ and $BiCl_3$), can be greatly important. However, these metal chlorides are easily soluble in liquid electrolytes and may migrate to the anode during the cycling, which will deteriorate the battery performance. Thus new ideas for constructing the electrodes and developing suitable chloride ion conducting electrolytes, for example solid state or gel polymer electrolytes, are desired. In addition, the interface behavior at the electrode during the electrochemical reaction needs to be further characterized.

Rechargeable batteries based on porphyrin complex electrode demonstrated excellent long-term cyclic stability and high rate capability already in this first study. The following topics related to the organic electrode may be important for the further work: 1) understanding the relationship between the battery performance, the bulk structure, and the functional groups, 2) the kinetic behavior of the organic electrode during the reaction. In addition, due to the bipolar redox-activity and air stability of the CuDEPP molecule, it may also be suitable for developing even cheaper battery systems, e.g. Na-based, Mg-based, K-based, Zn-based batteries. Moreover, not only the use of non-aqueous electrolyte, but also the development of aqueous electrolyte

for an organic battery, for example in an organic flow battery, can also be of particular interest because of its abundant resources coming from natural products.

Conversion materials for rechargeable batteries lead to a high specific capacity owing to the multi-electron reaction. Normally, these conversion electrodes can deliver high reversible capacities in initial cycles, however, the reversible capacity faded significantly in the following cycling. To understand the reason and improve the cycling stability will essential in further work.

Bibliography

[1] N.S. Lewis, Powering the Planet, MRS Bull. 32 (2007) 808–820.

[2] Achievements of applicance energy efficiency standards and labelling programs: https://www.iea.org/publications/freepublications/publication/4E_S_L_Report_180915.pdf.

[3] T.J.-M. Larcher.D, Towards greener and more sustainable batteries for electrical energy storage, Nat. Chem. 7 (2015) 19–29.

[4] M. Armand, J. Tarascon, Building better batteries, Nature 451 (2008) 652–657.

[5] R.M. Dell, Batteries: Fifty years of materials development, Solid State Ionics 134 (2000) 139–158.

[6] M. Winter, R.J. Brodd, What Are Batteries, Fuel Cells,and Supercapacitors ?, Chem.Rev. 104 (2004) 4245–4270.

[7] J.-M.M. Tarascon, M. Armand, Issues and challenges facing rechargeable lithium batteries, Nature 414 (2001) 359–367.

[8] B. Scrosati, J. Garche, Lithium batteries: Status, prospects and future, J. Power Sources 195 (2010) 2419–2430.

[9] M.S. Whittingham, Lithium batteries and cathode materials, Chem. Rev. 104 (2004) 4271–4301.

[10] V. Palomares, P. Serras, I. Villaluenga, K.B. Hueso, J. Carretero-González, T. Rojo, Na-ion batteries, recent advances and present challenges to become low cost energy storage systems, Energy Environ. Sci. 5 (2012) 5884–5901.

[11] H. Pan, Y.-S. Hu, L. Chen, Room-temperature stationary sodium-ion batteries for

large-scale electric energy storage, Energy Environ. Sci. 6 (2013) 2338–2360.

[12] B.L. Ellis, L.F. Nazar, Sodium and sodium-ion energy storage batteries, Curr. Opin. Solid State Mater. Sci. 16 (2012) 168–177.

[13] C.D. Wessells, S. V. Peddada, R.A. Huggins, Y. Cui, Nickel hexacyanoferrate nanoparticle electrodes for aqueous sodium and potassium ion batteries, Nano Lett. 11 (2011) 5421–5425.

[14] A. Eftekhari, Potassium secondary cell based on Prussian blue cathode, J. Power Sources 126 (2004) 221–228.

[15] X. Ren, Y. Wu, A low-overpotential potassium-oxygen battery based on potassium superoxide, J. Am. Chem. Soc. 135 (2013) 2923–2926.

[16] C. Kim, P.J. Phillips, B. Key, T. Yi, D. Nordlund, Y.S. Yu, et al., Direct observation of reversible magnesium ion intercalation into a spinel oxide host, Adv. Mater. 27 (2015) 3377–3384.

[17] Z. Zhao-Karger, X. Zhao, D. Wang, T. Diemant, R.J. Behm, M. Fichtner, Performance improvement of magnesium sulfur batteries with modified non-nucleophilic electrolytes, Adv. Energy Mater. 5 (2015) 1–9.

[18] Z. Zhao-Karger, X. Zhao, O. Fuhr, M. Fichtner, Bisamide based non-nucleophilic electrolytes for rechargeable magnesium batteries, RSC Adv. 3 (2013) 16330–16335.

[19] M.-C. Lin, M. Gong, B. Lu, Y. Wu, D.-Y. Wang, M. Guan, et al., An ultrafast rechargeable aluminium-ion battery, Nature 520 (2015) 324–328.

[20] A. Ponrouch, C. Frontera, F. Bardé, M.R. Palacín, Towards a calcium-based rechargeable battery, Nat. Mater. 15 (2015) 169–172.

[21] P.G. Bruce, Energy storage beyond the horizon: Rechargeable lithium batteries, Solid State Ionics 179 (2008) 752–760.

[22] J. Xu, S. Dou, H. Liu, L. Dai, Cathode materials for next generation lithium ion batteries, Nano Energy 2 (2013) 439–442.

[23] C.M. Julien, A. Mauger, K. Zaghib, H. Groult, Comparative issues of cathode materials for Li-Ion batteries, Inorganics 2 (2014) 132–154.

[24] J.B. Goodenough, K. Mizuchima, Electrochemical cell with new fast ion conductors, US patent (1980), US4302518 A.

[25] M.A. Kiani, M.F. Mousavi, M.S. Rahmanifar, Synthesis of nano- and micro-particles of $LiMn_2O_4$: Electrochemical investigation and assessment as a cathode in Li-ion battery, Int. J. Electrochem. Sci. 6 (2011) 2581–2595.

[26] T. Ohzuku, A. Ueda, Solid-state redox reactions of $LiCoO_2$ for 4 Volt secondary lithium cells, J. Electrochem. Soc. 141 (1994) 2972–2977.

[27] Y. Takahashi, S. Tode, A. Kinoshita, H. Fujimoto, I. Nakane, S. Fujitani, Development of lithium-ion batteries with a $LiCoO_2$ cathode toward high capacity by elevating charging potential, J. Electrochem. Soc. 155 (2008) A537–A541.

[28] S.T. Myung, N. Kumagai, S. Komaba, H.T. Chung, Effects of Al doping on the microstructure of $LiCoO_2$ cathode materials, Solid State Ionics 139 (2001) 47–56.

[29] P. Ghosh, S. Mahanty, R.N. Basu, Lanthanum-doped $LiCoO_2$ cathode with high rate capability, Electrochim. Acta. 54 (2009) 1654–1661.

[30] Y.-S.S. Jung, A.S. Cavanagh, A.C. Dillon, M.D. Groner, S.M. George, S.-H. Lee, Enhanced Stability of $LiCoO_2$ Cathodes in lithium-ion batteries using surface modification by atomic layer deposition, J. Electrochem. Soc. 157 (2010) A75–A81.

[31] G.Q. Liu, H.T. Kuo, R.S. Liu, C.H. Shen, D.S. Shy, X.K. Xing, et al., Study of electrochemical properties of coating ZrO_2 on $LiCoO_2$, J. Alloys Compd. 496 (2010) 512–516.

[32] K.M. Shaju, P.G. Bruce, Macroporous $Li(Ni_{1/3}Co_{1/3}Mn_{1/3})O_2$: A high-power and high-energy cathode for rechargeable lithium batteries, Adv. Mater. 18 (2006) 2330–2334.

[33] Y.-K. Sun, S.-T. Myung, B.-C. Park, J. Prakash, I. Belharouak, K. Amine, High-energy cathode material for long-life and safe lithium batteries, Nat. Mater. 8 (2009) 320–324.

[34] J.M. Tarascon, E. Wang, F.K. Shokoohi, The spinel phase of $LiMn_2O_4$ as a cathode in secondary lithium cells, J. Electrochem. Soc. 138 (1991) 2859–2864.

[35] R. Santhanam, B. Rambabu, Research progress in high voltage spinel $LiNi_{0.5}Mn_{1.5}O_4$ material, J. Power Sources 195 (2010) 5442–5451.

[36] L. Wang, H. Li, X. Huang, E. Baudrin, A comparative study of Fd-3m and $P4_332$ "$LiNi_{0.5}Mn_{1.5}O_4$", Solid State Ionics 193 (2011) 32–38.

[37] J.B. Goodenough, K.-S.S. Park, The Li-ion rechargeable battery: A perspective, J. Am. Chem. Soc. 135 (2013) 1167–1176.

[38] A.K. Padhi, K.S. Nanjundaswamy, J.B. Goodenough, Phospho-olivines as postive-electrode materials for rechargeable lithium batteries, J. Electrochem. Soc. 144 (1997) 1188–1194.

[39] W.J. Zhang, Structure and performance of $LiFePO_4$ cathode materials: A review, J. Power Sources 196 (2011) 2962–2970.

[40] C. Delacourt, L. Laffont, R. Bouchet, C. Wurm, J.-B. Leriche, M. Morcrette, et al., Toward understanding of electrical limitations (electronic, ionic) in $LiMPO_4$ (M = Fe, Mn) electrode materials, J. Electrochem. Soc. 152 (2005) A913–A921.

[41] S. Shi, C. Ouyang, Z. Xiong, L. Liu, Z. Wang, H. Li, et al., First-principles investigation of the structural, magnetic, and electronic properties of olivine $LiFePO_4$, Phys. Rev. B 71 (2005) 144404.

[42] W. Liu, P. Gao, Y. Mi, J. Chen, H. Zhou, X. Zhang, Fabrication of high tap density $LiFe_{0.6}Mn_{0.4}PO_4$/C microspheres by a double carbon coating-spray drying method for high rate lithium ion batteries, J. Mater. Chem. A 1 (2013) 2411–2417.

[43] M. Gaberscek, R. Dominko, J. Jamnik, Is small particle size more important than

carbon coating? An example study on $LiFePO_4$ cathodes, Electrochem. Commun. 9 (2007) 2778–2783.

[44] S.W. Oh, S.T. Myung, S.M. Oh, K.H. Oh, K. Amine, B. Scrosati, et al., Double carbon coating of $LiFePO_4$ as high rate electrode for rechargeable lithium batteries, Adv. Mater. 22 (2010) 4842–4845.

[45] R. Dominko, M. Bele, M. Gaberscek, M. Remskar, D. Hanzel, S. Pejovnik, et al., Impact of the carbon coating thickness on the electrochemical performance of $LiFePO_4$/C composites, J. Electrochem. Soc. 152 (2005) A607–A610.

[46] X. Ji, L.F. Nazar, Advances in Li–S Batteries, J. Mater. Chem. 20 (2010) 9821–9826.

[47] P.G. Bruce, S. A. Freunberger, L.J. Hardwick, J.-M. Tarascon, Li-O_2 and Li-S batteries with high energy storage, Nat. Mater. 11 (2011) 19–29.

[48] L. Chen, L.L. Shaw, Recent advances in lithium-sulfur batteries, J. Power Sources 267 (2014) 770–783.

[49] F. Badway, N. Pereira, F. Cosandey, G.G. Amatucci, Carbon-metal fluoride nanocomposites structure and electrochemistry of FeF_3 : C, J. Electrochem. Soc. 150 (2003) A1209–A1218.

[50] F. Wang, R. Robert, N. Chernova, N. Pereira, F. Omenya, F. Badway, et al., Conversion reaction mechanisms in lithium ion batteries: Study of the binary metal fluoride electrodes conversion reaction mechanisms in lithium ion batteries : study of the binary metal fluoride electrodes, J. Am. Chem.Soc. 133 (2011) 18828–18836.

[51] M.A. Reddy, B. Breitung, V.S.K. Chakravadhanula, C. Wall, M. Engel, C. Kuebel, et al., CF_x derived carbon-FeF_2 nanocomposites for reversible lithium storage, Adv. Energy Mater. 3 (2013) 308–313.

[52] Y.P. Wu, E. Rahm, R. Holze, Carbon anode materials for lithium ion batteries, J. Power Sources 114 (2003) 228–236.

[53] E. Peled, Improved graphite anode for lithium-ion batteries, J. Electrochem. Soc. 143 (1996) L4–L7.

[54] H.G. Jung, J. Kim, B. Scrosati, Y.K. Sun, Micron-sized, carbon-coated $Li_4Ti_5O_{12}$ as high power anode material for advanced lithium batteries, J. Power Sources 4 (2011) 1345–1351.

[55] A.R. Armstrong, G. Armstrong, J. Canales, R. García, P.G. Bruce, Lithium-ion intercalation into TiO_2-B nanowires, Adv. Mater. 17 (2005) 862–865.

[56] C.K. Chan, H.L. Peng, G. Liu, K. McIlwrath, X.F. Zhang, R.A. Huggins, et al., High-performance lithium battery anodes using silicon nanowires, Nat. Nanotechnol. 3 (2008) 31–35.

[57] S.D. Beattie, D. Larcher, M. Morcrette, B. Simon, J.-M. Tarascon, Si electrodes for Li-Ion Batteries-A new way to look at an old problem, J. Electrochem. Soc. 155 (2008) A158–A163.

[58] J. Cabana, L. Monconduit, D. Larcher, M.R. Palacín, Beyond intercalation-based Li-ion batteries: The state of the art and challenges of electrode materials reacting through conversion reactions, Adv. Mater. 22 (2010) E170–E192.

[59] S.-H. Yu, S.H. Lee, D.J. Lee, Y.-E. Sung, T. Hyeon, Conversion reaction-based oxide nanomaterials for lithium ion battery anodes, Small 16 (2015) 2146–2172.

[60] F. Gillot, S. Boyanov, L. Dupont, M.L. Doublet, M. Morcrette, L. Monconduit, et al., Electrochemical reactivity and design of NiP_2 negative electrodes for secondary Li-ion batteries, Chem. Mater. 17 (2005) 6327–6337.

[61] A.S. Nagelberg, W.L. Worrell, A thermodynamic study of sodium intercalated TaS_2 and TiS_2, J. Solid State Chem. 29 (1979) 345–354.

[62] K.M. Abraham, Intercalation positive electrodes for rechargeable sodium cells, Solid State Ionics 7 (1982) 199–212.

[63] H. Pan, Y.-S. Hu, L. Chen, Room-temperature stationary sodium-ion batteries for large-scale electric energy storage, Energy Environ. Sci. 6 (2013) 2338.

[64] R. Berthelot, D. Carlier, C. Delmas, Electrochemical investigation of the P2–Na_xCoO_2 phase diagram, Nat. Mater. 10 (2011) 74–80.

[65] F. Sauvage, L. Laffont, J.M. Tarascon, E. Baudrin, Study of the insertion/deinsertion mechanism of sodium into $Na_{0.44}MnO_2$, Inorg. Chem. 46 (2007) 3289–3294.

[66] N. Yabuuchi, M. Yano, H. Yoshida, S. Kuze, S. Komaba, Synthesis and electrode performance of O3-type $NaFeO_2$-$NaNi_{1/2}Mn_{1/2}O_2$ solid solution for rechargeable sodium batteries, J. Electrochem. Soc. 160 (2013) A3131–A3137.

[67] C.-Y. Yu, J.-S. Park, H.-G. Jung, K.-Y. Chung, D. Aurbach, Y.-K. Sun, et al., $NaCrO_2$ cathode for high-rate sodium-ion batteries, Energy Environ. Sci. 8 (2015) 2019–2026.

[68] P. Vassilaras, X. Ma, H. Chen, G. Ceder, Electrochemical properties of monoclinic $NaNiO_2$, J. Electrochem. Soc. 160 (2013) A207–A211.

[69] M. Sathiya, K. Hemalatha, K. Ramesha, J.-M. Tarascon, A.S. Prakash, Synthesis, structure, and electrochemical properties of the layered sodium insertion cathode material: $NaNi_{1/3}Mn_{1/3}Co_{1/3}O_2$, Chem. Mater. 24 (2012) 1846–1853.

[70] P. Vassilaras, A.J. Toumar, G. Ceder, Electrochemical properties of $NaNi_{1/3}Co_{1/3}Fe_{1/3}O_2$ as a cathode material for Na-ion batteries, Electrochem. Commun. 38 (2014) 79–81.

[71] W. Zhao, H. Kirie, A. Tanaka, M. Unno, S. Yamamoto, H. Noguchi, Synthesis of metal ion substituted P2-$Na_{2/3}Ni_{1/3}Mn_{2/3}O_2$ cathode material with enhanced performance for Na ion batteries, Mater. Lett. 135 (2014) 131–134.

[72] D. Buchholz, L.G. Chagas, M. Winter, S. Passerini, P2-type layered $Na_{0.45}Ni_{0.22}Co_{0.11}Mn_{0.66}O_2$ as intercalation host material for lithium and sodium batteries, Electrochim. Acta. 110 (2013) 208–213.

[73] N. Yabuuchi, M. Kajiyama, J. Iwatate, H. Nishikawa, S. Hitomi, R. Okuyama, et al., P2-type $Na_x[Fe_{1/2}Mn_{1/2}]O_2$ made from earth-abundant elements for

rechargeable Na batteries, Nat. Mater. 11 (2012) 512–517.

[74] D. Buchholz, L.G. Chagas, C. Vaalma, L. Wu, S. Passerini, Water sensitivity of layered P2/P3-$Na_xNi_{0.22}Co_{0.11}Mn_{0.66}O_2$ cathode material, J. Mater. Chem. A 2 (2014) 13415–13421.

[75] Y. Cao, L. Xiao, W. Wang, D. Choi, Z. Nie, J. Yu, et al., Reversible sodium ion insertion in single crystalline manganese oxide nanowires with long cycle life, Adv. Mater. 23 (2011) 3155–3160.

[76] K.T. Lee, T.N. Ramesh, F. Nan, G. Botton, L.F. Nazar, Topochemical synthesis of sodium metal phosphate olivines for sodium-ion batteries, Chem. Mater. 23 (2011) 3593–3600.

[77] J.M. Clark, P. Barpanda, A. Yamada, M.S. Islam, Sodium-ion battery cathodes $Na_2FeP_2O_7$ and $Na_2MnP_2O_7$: diffusion behaviour for high rate performance, J. Mater. Chem. A 2 (2014) 11807–11812.

[78] C. Zhu, K. Song, P.A. Van Aken, J. Maier, Y. Yu, Carbon-coated $Na_3V_2(PO_4)_3$ embedded in porous carbon matrix: An ultrafast Na-storage cathode with the potential of outperforming Li cathodes, Nano Lett. 14 (2014) 2175–2180.

[79] F. Sauvage, E. Quarez, J.M. Tarascon, E. Baudrin, Crystal structure and electrochemical properties vs. Na^+ of the sodium fluorophosphate $Na_{1.5}VOPO_4F_{0.5}$, Solid State Sci. 8 (2006) 1215–1221.

[80] Y. Yamada, T. Doi, I. Tanaka, S. Okada, J.I. Yamaki, Liquid-phase synthesis of highly dispersed $NaFeF_3$ particles and their electrochemical properties for sodium-ion batteries, J. Power Sources 196 (2011) 4837–4841.

[81] H.-W. Lee, R.Y. Wang, M. Pasta, S. Woo Lee, N. Liu, Y. Cui, Manganese hexacyanomanganate open framework as a high-capacity positive electrode material for sodium-ion batteries, Nat. Commun. 5 (2014) 5280.

[82] Y. Lu, L. Wang, J. Cheng, J.B. Goodenough, Prussian blue: A new framework of electrode materials for sodium batteries, Chem. Commun. 48 (2012)

6544–6546.

[83] S. Komaba, W. Murata, T. Ishikawa, N. Yabuuchi, T. Ozeki, T. Nakayama, et al., Electrochemical Na insertion and solid electrolyte interphase for hard-carbon electrodes and application to Na-ion batteries, Adv. Funct. Mater. 21 (2011) 3859–3867.

[84] W. Luo, F. Shen, C. Bommier, H. Zhu, X. Ji, L. Hu, Na-Ion battery anodes: materials and electrochemistry, Acc. Chem. Res. 49 (2016) 231–240.

[85] E. Irisarri, A. Ponrouch, M.R. Palacin, Review-hard carbon negative electrode materials for sodium-ion batteries, J. Electrochem. Soc. 162 (2015) A2476–A2482.

[86] W. Lv, F. Wen, J. Xiang, J. Zhao, L. Li, L. Wang, et al., Peanut shell derived hard carbon as ultralong cycling anodes for lithium and sodium batteries, Electrochim. Acta. 176 (2015) 533–541.

[87] P. Senguttuvan, G. Rousse, V. Seznec, J.M. Tarascon, M.R. Palacin, $Na_2Ti_3O_7$: Lowest voltage ever reported oxide insertion electrode for sodium ion batteries, Chem. Mater. 23 (2011) 4109–4111.

[88] D. Su, S. Dou, G. Wang, Anatase TiO_2: Better anode material than amorphous and rutile Phases of TiO_2 for Na-ion batteries, Chem. Mater. 27 (2015) 6022–6029.

[89] Y. Sun, L. Zhao, H. Pan, X. Lu, L. Gu, Y.-S. Hu, et al., Direct atomic-scale confirmation of three-phase storage mechanism in $Li_4Ti_5O_{12}$ anodes for room-temperature sodium-ion batteries, Nat. Commun. 4 (2013) 1870.

[90] I. Hasa, R. Verrelli, J. Hassoun, Transition metal oxide-carbon composites as conversion anodes for sodium-ion battery, Electrochim. Acta. 173 (2015) 613–618.

[91] L. David, R. Bhandavat, G. Singh, MoS_2/graphene composite paper for sodium-ion battery electrodes, ACS Nano 8 (2014) 1759–1770.

[92] J. Qian, X. Wu, Y. Cao, X. Ai, H. Yang, High capacity and rate capability of amorphous phosphorus for sodium ion batteries, Angew. Chem. Int. Ed. 52 (2013) 4633–4636.

[93] J. Duan, W. Zhang, C. Wu, Q. Fan, W. Zhang, X. Hu, et al., Self-wrapped Sb/C nanocomposite as anode material for high-performance sodium-ion batteries, Nano Energy 16 (2015) 479–487.

[94] Z. Li, J. Ding, D. Mitlin, tin and tin compounds for sodium ion battery anodes: phase transformations and Performance, Acc. Chem. Res. 48 (2015) 1657–1665.

[95] M. Anji Reddy, M. Fichtner, Batteries based on fluoride shuttle, J. Mater. Chem. 21 (2011) 17059–17062.

[96] C. Rongeat, M. Anji Reddy, R. Witter, M. Fichtner, Solid electrolytes for fluoride ion batteries: Ionic conductivity in polycrystalline tysonite-type fluorides, ACS Appl. Mater. Interfaces 6 (2014) 2103–2110.

[97] C. Rongeat, M. Anji Reddy, R. Witter, M. Fichtner, Nanostructured fluorite-type fluorides as electrolyte for fluoride ion batteries, J. Phys. Chem. C 117 (2013) 4943–4950.

[98] X. Zhao, S. Ren, M. Bruns, M. Fichtner, Chloride ion battery: A new member in the rechargeable battery family, J. Power Sources 245 (2014) 706–711.

[99] M. Li, M.J. Pietrowski, R. Souza, H. Zhang, I.M. Reaney, S.N. Cook, et al., A family of oxide ion conductors based on the ferroelectric perovskite $Na_{0.5}Bi_{0.5}TiO_3$, Nat. Mater. 13 (2014) 31–35.

[100] M. Heise, B. Rasche, A. Isaeva, A.I. Baranov, M. Ruck, K. Schaefer, et al., A metallic room-temperature oxide ion conductor, Angew. Chem. Int. Ed. 53 (2014) 7344–7348.

[101] L. Zhang, M. Anji Reddy, M. Fichtner, Development of tysonite-type fluoride conducting thin film electrolytes for fluoride ion batteries, Solid State Ionics 272 (2015) 39–44.

[102] K. Yamada, K. Isobe, E. Tsuyama, T. Okuda, Y. Furukawa, Chloride ion conductor $CH_3NH_3GeCl_3$ studied by Rietveld analysis of X-ray diffraction and ^{35}Cl NMR, Solid State Ionics 79 (1995) 152–157.

[103] G. Simkovich, The nature of point defects in solid lead chloride, J. Phys. Chem. Solids. 24 (1963) 213–216.

[104] N. Kimura, Y. Niizeki, Ionic conductivity of $SnCl_2$, Solid State Ionics 4 (1981) 385–388.

[105] C.E. Derrington, M. O'Keeffe, The solid electrolyte behavior of barium chloride and strontium bromide, Solid State Commun. 15 (1974) 1175–1177.

[106] Y. Niizeki, Ionic conductivity of polycrystalline $PbCl_2$.RbCl double salt, Solid State Ionics 66 (1993) 49–52.

[107] J. Mizusaki, K. Arai, K. Fueki, Ionic conduction of the perovskite-type halides, Solid State Ionics 11 (1983) 203–211.

[108] G.M. Hood, J.A. Morrison, Ionic conduction and diffusion in single crystals of $SrCl_2$, J. Appl. Phys. 38 (1967) 4796–4802.

[109] M. Beniere, M. Chemla, F. Beniere, Anion diffusion mechanism in strontium chloride single crystals, J. Phys. Chem. Solids 40 (1979) 729–737.

[110] M.Jacquet, Parameters thermodynamiques des defauts ponctuels dans le chlorure de strontium fur ou dope par des cations monovalents ou trivalents, J. Phys. Chem. Solids 47 (1986) 707–717.

[111] G.K. Bichile, Electrical conductivity of strontium chloride, J. Mater. Sci. Lett. 6 (1987) 459–461.

[112] N. Imanaka, K. Okamoto, G.Y. Adachi, Water-insoluble lanthanum oxychloride-based solid electrolytes with ultra-high chloride ion conductivity, Angew. Chem. Int. Ed. 41 (2002) 3890–3892.

[113] K. Ogawa, S. Hirano, T. Miyanishi, T. Yui, T. Watanabe, chloride ion conductivity in a plasticized quaternary ammonium polymer, Macromolecules 17 (1984)

975–977.

[114] P.C. Huang and K.-H. Reichert, Polymerization of diallyldimethylammonium chloride in inverse emulsion, Die Angew. Makromol. Chemie. 165 (1989) 19–34.

[115] X. Zhao, Z. Zhao-Karger, D. Wang, M. Fichtner, Metal oxychlorides as cathode materials for chloride ion batteries, Angew. Chem. Int. Ed. 52 (2013) 13621-13624.

[116] X. Zhao, Q. Li, Z. Zhao-Karger, P. Gao, K. Fink, X. Shen, et al., Magnesium anode for chloride ion batteries, ACS Appl. Mater. Interfaces 6 (2014) 10997–11000.

[117] W. Rüdorff, U. Hofmann, Über Graphitsaelze, Zeitshrift Fur Anorg. Und Allg. Chemie. 238 (1938) 1–50.

[118] M. Noel, R. Santhanam, Electrochemistry of graphite intercalation compounds, J. Power Sources 72 (1998) 53–65.

[119] T. Placke, G. Schmuelling, R. Kloepsch, P. Meister, O. Fromm, P. Hilbig, et al., In situ X-ray diffraction studies of cation and anion inter-calation into graphitic carbons for electrochemical energy storage applications, Zeitschrift Für Anorg. Und Allg. Chemie. 640 (2014) 1996–2006.

[120] P. Meister, V. Siozios, J. Reiter, S. Klamor, S. Rothermel, O. Fromm, et al., Dual-ion cells based on the electrochemical intercalation of asymmetric fluorosulfonyl-(trifluoromethanesulfonyl) imide anions into graphite, Electrochim. Acta. 130 (2014) 625–633.

[121] S. Rothermel, P. Meister, G. Schmuelling, O. Fromm, H.-W. Meyer, S. Nowak, et al., Dual graphite cells based on the reversible intercalation of bis(trifluoromethanesulfonyl)imide anions from an ionic liquid electrolyte, Energy Environ. Sci. 7 (2014) 3412–3423.

[122] T. Placke, O. Fromm, S.F. Lux, P. Bieker, S. Rothermel, H.-W. Meyer, et al., Reversible intercalation of bis(trifluoromethanesulfonyl)imide anions from an ionic liquid electrolyte into graphite for high performance dual-Ion cells, J.

Electrochem. Soc. 159 (2012) A1755–A1765.

[123] T. Placke, S. Rothermel, O. Fromm, P. Meister, S.F. Lux, J. Huesker, et al., Influence of graphite characteristics on the electrochemical intercalation of bis(trifluoromethanesulfonyl) imide anions into a graphite-based cathode, J. Electrochem. Soc. 160 (2013) A1979–A1991.

[124] R.T. Carlin, H.C. De Long, J. Fuller, P.C. Trulove, Dual intercalating molten electrolyte batteries, J. Electrochem. Soc. 141 (1994) L73–L75.

[125] Wikipedia contributors, The free Encyclopedia, https://en.wikipedia.org/w/index.php?title=Dual_carbon_battery&oldid=741373781, 27 September 2016 02:58 UTC.

[126] Y. Liang, Z. Tao, J. Chen, Organic electrode materials for rechargeable lithium batteries, Adv. Energy Mater. 2 (2012) 742–769.

[127] Z.P. Song and H.S. Zhou, Towards sustainable and versatile energy storage devices: an overview of organic electrode materials, Energy Environ. Sci. 6 (2013) 2280–2301.

[128] K. Nakahara, S. Iwasa, M. Satoh, Y. Morioka, J. Iriyama, M. Suguro, et al., Rechargeable batteries with organic radical cathodes, Chem. Phys. Lett. 359 (2002) 351–354.

[129] M. Suguro, S. Iwasa, Y. Kusachi, Y. Morioka, K. Nakahara, Cationic polymerization of poly(vinyl ether) bearing a TEMPO radical: A new cathode-active material for organic radical batteries, Macromol. Rapid Commun. 28 (2007) 1929–1933.

[130] K. Nakahara, K. Oyaizu, H. Nishide, Organic radical battery approaching practical use, Chem. Lett. 40 (2011) 222–227.

[131] K. Nakahara, J. Iriyama, S. Iwasa, M. Suguro, M. Satoh, E.J. Cairns, High-rate capable organic radical cathodes for lithium rechargeable batteries, J. Power Sources 165 (2007) 870–873.

[132] T. Nishide, H, Suga, Organic radical battery, Electrochem. Soc. Interface (2005) 32–36.

[133] T. Suga, S. Sugita, H. Ohshiro, K. Oyaizu, H. Nishide, P- and n-type bipolar redox-active radical polymer: Toward totally organic polymer-based rechargeable devices with variable configuration, Adv. Mater. 23 (2011) 751–754.

[134] Y. Waseda, E. Matsubara, K. Shinoda, X-ray diffraction crystallography, Springer Berlin Heidelberg, 2013.

[135] J. Goldstein, D. Newbury, D. Joy, C. Lyman, P. Echlin, E. Lifshin, et al., Scanning Electron Microscopy and X-Ray Microanalysis, Springer US, 2003.

[136] Wikipedia contributors, The free Encyclopedia, https://en.wikipedia.org/w/index.php?title=Scanning_electron_microscope&oldid=751845063, 28 November 2016 04:09 UTC.

[137] Wikipedia contributors, The free Encyclopedia, https://en.wikipedia.org/w/index.php?title=X-ray&oldid=751110903, 23 November 2016 12:30 UTC.

[138] Zeiss: Transmission Electron Microscope LEO 912 OMEGA Operating Manual. LEO Elektronenmikroskopie GmbH, Oberkochen (1998).

[139] Wikipedia contributors, The free Encyclopedia, https://en.wikipedia.org/w/index.php?title=X-ray_photoelectron_spectroscopy&oldid=744489171, 15 October 2016 15:26 UTC.

[140] S. Hofmann, Auger- and X-Ray Photoelectron Spectroscopy in Materials Science, Springer-Verlag Berlin Heidelberg, 2013.

[141] L.R. Faulkner, J. Bard, Electrochemical Methods: Fundamentals and Applications, Second, John Wiley & Sons, INC, 2001.

[142] H.S. and F. Wartenpfuhl, Ueber das vanadin(III)-oxydchlorid VOCl, J. Less-Common Mat. 3 (1961) 29–33.

[143] S. Glawion, M. Scholz, Y.-Z. Zhang, R. Valenti, T. Saha-Dasgupta, M. Klemm, et al., Electronic structure of the two-dimensional Heisenberg antiferromagnet VOCl: A multiorbital Mott insulator, Phys. Rev. B 80 (2009) 1551191–1551196.

[144] J.F. Bringleyt, B.A. Averill, Aromatic Hydrocarbon Intercalates: Synthesis and Characterization of Iron Oxychloride Intercalated with Perylene and Tetracene, Chem. Mater. 2 (1990) 180–186.

[145] I. Kargina, D. Richeson, Diamine Intercalates of Titanium and Vanadium Oxychloride. Evidence for the Subsequent Substitution Reactions of TiOCl with Amines, Chem. Mater. 8 (1996) 480–485.

[146] B.A. Bringley, J.F, Fabre, J-M, Averill, Intercalation of Bis(ethylenedithio)tetrathiafulvalene (ET) into Iron Oxychloride: A highly conducting low-dimentional system, J. Am. Chem. Soc. (1990) 4577–4579.

[147] S. Kikkawa, F. Kanamaru, M. Koizumi, Synthesis and some properties of $FeOOCH_3$. A new layered compound, Inorg. Chem. 15 (1976) 2195–2197.

[148] R.H. Herber, Y. Maeda, Intercalation Compounds of FeOCl: Systematics of Nitrogen-Containing Lewis Base Intercalants, Inorg. Chem. 20 (1981) 1409–1415.

[149] S.M. Kauzlarih, J.L. Stanton, J. Faber, B.A. Averill, Neutron Profile Refinement of the Structure of FeOCl and $FeOCl(TTF)_{1/8.5}$, J. Am. Chem. Soc. 108 (1986) 7946–7951.

[150] K. Song, S.M. Kauzlarich, New Intercalation Compounds of Layered Lanthanide Oxychlorides LnOCl (Ln = Ho, Er, Tm, and Yb) with Pyridine and Substituted Pyridines, Chem. Mater. 6 (1994) 386–394.

[151] J.E. Phillips, R.H. Herber, Organotin intercalation compounds of FeOCl: Synthesis, 57Fe and 119mSn Mössbauer and infrared spectroscopy, and powder X-ray diffraction studies, Inorg. Chem. 25 (1986) 3081–3088.

[152] L. Cario, S. Delagrange, F. Boucher, E. Faulques, P. Palvadeau, Synthesis and

Physical Properties of Co-intercalated Layered Lanthanide Oxychlorides Li_xTHF_yLnOCl (Ln = Y, Lu), Chem. Mater. 15 (2003) 4325–4331.

[153] M. Demeter, M. Neumann, W. Reichelt, Mixed-valence vanadium oxides studied by XPS, Surf. Sci. 454-456 (2000) 41–44.

[154] E. Hryha, E. Rutqvist, L. Nyborg, Stoichiometric vanadium oxides studied by XPS, Surf. Interface Anal. 44 (2012) 1022–1025.

[155] M. Shukla, H. Noothalapati, S. Shigeto, S. Saha, Importance of weak interactions and conformational equilibrium in N-butyl-N-methylpiperidinium bis(trifluromethanesulfonyl) imide room temperature ionic liquids: Vibrational and theoretical studies, Vib. Spectrosc. 75 (2014) 107–117.

[156] F. Werfel, U. Berg, X-ray and X-ray Photoelectron Spectra of vanadium oxides, Cryst. Res. Technol. 16 (1981) 119–126.

[157] N. Izumi, O. Hideo, S. Yoshinori, Y. Niwa, X-ray photoelectron spectroscopic study of vanadium-bearing aegirines, Mineral. J. 8 (1976) 129–134.

[158] Y. Liang, Z. Chen, Y. Jing, Y. Rong, A. Facchetti, Y. Yao, Heavily n-Dopable π-Conjugated Redox Polymers with Ultrafast Energy Storage Capability, J. Am. Chem. Soc. 137 (2015) 4956–4959.

[159] Y. Liang, P. Zhang, J. Chen, Function-oriented design of conjugated carbonyl compound electrodes for high energy lithium batteries, Chem. Sci. 4 (2013) 1330–1337.

[160] K. Sakaushi, E. Hosono, G. Nickerl, T. Gemming, H. Zhou, S. Kaskel, et al., Aromatic porous-honeycomb electrodes for a sodium-organic energy storage device, Nat. Commun. 4 (2013) 1485.

[161] C. Wang, Y. Xu, Y. Fang, M. Zhou, L. Liang, S. Singh, et al., Extended π-conjugated system for fast-charge and -discharge sodium-ion batteries, J. Am. Chem. Soc. 137 (2015) 3124–3130.

[162] K. Oyaizu, H. Nishide, Radical polymers for organic electronic devices: A radical

departure from conjugated polymers, Adv. Mater. 21 (2009) 2339–2344.

[163] W.M. Campbell, A.K. Burrell, D.L. Officer, K.W. Jolley, Porphyrins as light harvesters in the dye-sensitised TiO_2 solar cell, Coord. Chem. Rev. 248 (2004) 1363–1379.

[164] A. Yella, H.-W. Lee, H.N. Tsao, C. Yi, K.C. Chandiran, M.K. Nazerrunddin, et al., Porphyrins-sensitized solar cells with cobalt based redox electrolyte exceed 12 percent efficiency, Science 334 (2001) 629–633.

[165] W. Auwärter, D. Écija, F. Klappenberger, J. V Barth, Porphyrins at interfaces, Nat. Chem. 7 (2014) 105–20.

[166] M. Urbani, M. Graetzel, M.K. Nazeeruddin, Meso-substituted porphyrins for dye-sensitized solar cells, Chem. Rev. 114 (2014) 12330–12396.

[167] J. A. Cissell, T.P. Vaid, A.L. Rheingold, An antiaromatic porphyrin complex: tetraphenylporphyrinato(silicon)$(L)_2$ (L = THF or pyridine), J. Am. Chem. Soc. 127 (2005) 12212–12213.

[168] T. Kakui, S. Sugawara, Y. Hirata, S. Kojima, Y. Yamamoto, Anti-aromatic 16 π porphyrin-metal complexes with meso-alkyl substituents, Chem. - A Eur. J. 17 (2011) 7768–7771.

[169] H. Fliegl, F. Pichierri, D. Sundholm, Antiaromatic Character of 16 π Electron Octaethylporphyrins: Magnetically Induced Ring Currents from DFT-GIMIC Calculations, J. Phys. Chem. A 119 (2015) 2344–2350.

[170] J. A. Cissell, T.P. Vaid, G.P. Yap, Reversible oxidation state change in germanium(tetraphenylporphyrin) induced by a dative ligand: Aromatic GeII(TPP) and antiaromatic GeIV(TPP)$(pyridine)_2$, J. Am. Chem. Soc. 129 (2007) 7841–7847.

[171] C. Liu, D. Shen, Q. Chen, Synthesis and Reactions of 20 π-Electron Tetrakis(trifluoromethyl)-meso-tetraphenylporphyrins, J. Am. Chem. Soc. 129 (2007) 5814–5815.

[172] Y. Yamamoto, A. Yamamoto, S. Furuta, M. Horie, M. Kodama, W. Sato, et al., Synthesis and structure of 16 π Octaalkyltetraphenylporphyrins octaalkyltetraphenylporphyrins, J. Am. Chem. Soc. 127 (2005) 14540–14541.

[173] Y. Yamamoto, Y. Hirata, M. Kodama, T. Yamaguchi, S. Matsukawa, K.Y. Akiba, et al., Synthesis, reactions, and electronic properties of 16 π-electron octaisobutyltetraphenylporphyrin, J. Am. Chem. Soc. 132 (2010) 12627–12638.

[174] S. Prathapan, T.E. Johnson, J.S. Lindsey, Building-Block synthesis of porphyrin light-harvesting arrays, J. Am. Chem. Soc. 115 (1993) 7519–7520.

[175] R. Stranger, J.E. McGrady, D.P. Arnold, I. Lane, G. Heath, Communication between porphyrin rings in the butadiyne-bridged dimer Ni(OEP)(u-C4)Ni(OEP): a density functional study, Inorg. Chem. 35 (1996) 7791–7797.

[176] H.L. Anderson, Conjugated Porphyrin Ladders, Inorg. Chem. 33 (1994) 972–981.

[177] V.S. Lin, S.G. DiMagno, M.J. Therien, Highly conjugated, acetylenyl bridged porphyrins: new models for light-harvesting antenna systems, Science 264 (1994) 1105–1111.

[178] H.L. Anderson, S.J. Martin, D.D.C. Bradley, Synthesis and Third-Order Nonlinear Optical Properties of a Conjugated Porphyrin Polymer, Angew. Chem. Int. Ed. 33 (1994) 655–657.

[179] G. Wang, L. Zhang, J. Zhang, A review of electrode materials for electrochemical supercapacitors, Chem. Soc. Rev. 41 (2012) 797–828.

[180] C. Liu, Z. Yu, D. Neff, A. Zhamu, B.Z. Jang, Graphene-based supercapacitor with an ultrahigh energy density, Nano Lett. 10 (2010) 4863–4868.

[181] A. Jain, V. Aravindan, S. Jayaraman, P.S. Kumar, R. Balasubramanian, S. Ramakrishna, et al., Activated carbons derived from coconut shells as high energy density cathode material for Li-ion capacitors, Sci. Rep. 3 (2013) 3002.

[182] L.L. Zhang, X. Zhao, M.D. Stoller, Y. Zhu, H. Ji, S. Murali, et al., Highly conductive and porous activated reduced graphene oxide films for high-power

supercapacitors, Nano Lett. 12 (2012) 1806–1812.

[183] V. Aravindan, J. Gnanaraj, Y.-S. Lee, S. Madhavi, Insertion-Type Electrodes for Nonaqueous Li-Ion Capacitors, Chem. Rev. 14 (2014) 11619–11635.

[184] V. Aravindan, D. Mhamane, W.C. Ling, S. Ogale, S. Madhavi, Nonaqueous lithium-ion capacitors with high energy densities using trigol-reduced graphene oxide nanosheets as cathode-active material, ChemSusChem 6 (2013) 2240–2244.

[185] Y. Liang, Z. Tao, J. Chen, Organic electrode materials for rechargeable lithium batteries, Adv. Energy Mater. 2 (2012) 742–769.

[186] Y. Tang, Y. Zhang, W. Li, B. Ma, X. Chen, Rational material design for ultrafast rechargeable lithium-ion batteries, Chem. Soc. Rev. 44 (2015) 5926–5940.

[187] X. Li, B. Wei, Supercapacitors based on nanostructured carbon, Nano Energy 2 (2013) 159–173.

[188] Z. Song, H. Zhou, Towards sustainable and versatile energy storage device - an overview of organic electrode materials, Energy Environ. Sci. 6 (2013) 2280–2301.

[189] V. Etachri, R. Marom, R. Elazari, G. Salitra, D. Aurbach, Challenges in the development of advanced Li-ion batteries: A review, Energy Environ. Sci. 4 (2011) 3243–3262.

[190] M.D. Slater, D. Kim, E. Lee, C.S. Johnson, Sodium-ion batteries, Adv. Funct. Mater. 23 (2013) 947–958.

[191] B.L. Ellis, K.T. Lee, L.F. Nazar, Positive electrode materials for Li-Ion and Li-batteries, Chem. Mater. 22 (2010) 691–714.

[192] A. Sagua, E. Moran, M.A. Alario-franco, A. Rivera, J. Santamarıa, C. Leon, Lithium intercalation in FeOCl revisited, Int. J. Inorg. Mater. 3 (2001) 293–301.

[193] M.C. Biesinger, B.P. Payne, A.P. Grosvenor, L.W.M. Lau, A.R. Gerson, R.S.C. Smart, Resolving surface chemical states in XPS analysis of first row transition

metals, oxides and hydroxides: Sc, Ti, V, Cu and Zn, Appl. Surf. Sci. 257 (2010) 887–898.

[194] G. Silversmit, D. Depla, H. Poelman, G.B. Marin, R. De Gryse, Determination of the V_{2p} XPS binding energies for different vanadium oxidation states (V^{5+} to V^{0+}), J. Electron Spectros. Relat. Phenomena. 135 (2004) 167–175.

[195] J. Wong, F.W. Lytle, R.P. Messmer, D.H. Maylotte, K-edge absorption spectra of selected vanadium compounds, Phys. Rev. B 30 (1984) 5596–5610.

[196] P. Chaurand, J. Rose, V. Briois, M. Salome, O. Proux, V. Nassif, et al., New methodological approach for the vanadium K-edge X-ray absorption near-edge structure interpretation: application to the speciation of vanadium in oxide phases from steel slag, J. Phys. Chem. B 111 (2007) 5101–5110.

[197] S. Klink, E. Madej, E. Ventosa, A. Lindner, W. Schuhmann, F. La Mantia, The importance of cell geometry for electrochemical impedance spectroscopy in three-electrode lithium ion battery test cells, Electrochem. Commun. 22 (2012) 120–123.

[198] Z. Hu, L. Wang, K. Zhang, J. Wang, F. Cheng, Z. Tao, et al., MoS_2 Nanoflowers with Expanded Interlayers as High-Performance Anodes for Sodium-Ion Batteries, Angew. Chem. Int. Ed. 53 (2014) 12794–12798.

[199] I.E. Rauda, V. Augustyn, B. Dunn, S.H. Tolbert, Enhancing pseudocapacitive charge storage in polymer templated mesoporous materials, Acc. Chem. Res. 46 (2013) 1113–1124.

[200] V. Augustyn, J. Come, M. Lowe, J.W. Kim, P.-L. Taberna, S.H. Tolbert, et al., High-rate electrochemical energy storage through Li^+ intercalation pseudocapacitance, Nat. Mater. 12 (2013) 518–22.

[201] S.Y. Fu, Y.Z. Li, W. Chu, Y.M. Yang, D.G. Tong, Q. Le Zeng, Mesoporous amorphous FeOF nanococoons for high-rate and long-life rechargeable sodium-ion batteries, J. Mater. Chem. A 3 (2015) 16716–16727.

[202] T. Brezesinski, J. Wang, S.H. Tolbert, B. Dunn, Ordered mesoporous alpha-MoO_3 with iso-oriented nanocrystalline walls for thin-film pseudocapacitors, Nat. Mater. 9 (2010) 146–151.

[203] Z. Hu, Z. Zhu, F. Cheng, K. Zhang, J. Wang, C. Chen, et al., Pyrite FeS_2 for high-rate and long-life rechargeable sodium batteries, Energy Environ. Sci. 8 (2015) 1309–1316.

[204] R. Chen, M. Knapp, M. Yavuz, S. Ren, R. Witte, R. Heinzmann, et al., Nanoscale spinel $LiFeTiO_4$ for intercalation pseudocapacitive Li^+ storage, Phys. Chem. Chem. Phys. 17 (2015) 1482–1488.

[205] L. Zhao, J. Ni, H. Wang, L. Gao, $Na_{0.44}MnO_2$–CNT electrodes for non-aqueous sodium batteries, RSC Adv. 3 (2013) 6650–6655.

[206] M. Guignard, C. Didier, J. Darriet, P. Bordet, E. Elkaïm, C. Delmas, P2-Na_xVO_2 system as electrodes for batteries and electron-correlated materials, Nat. Mater. 12 (2013) 74–80.

Appendix

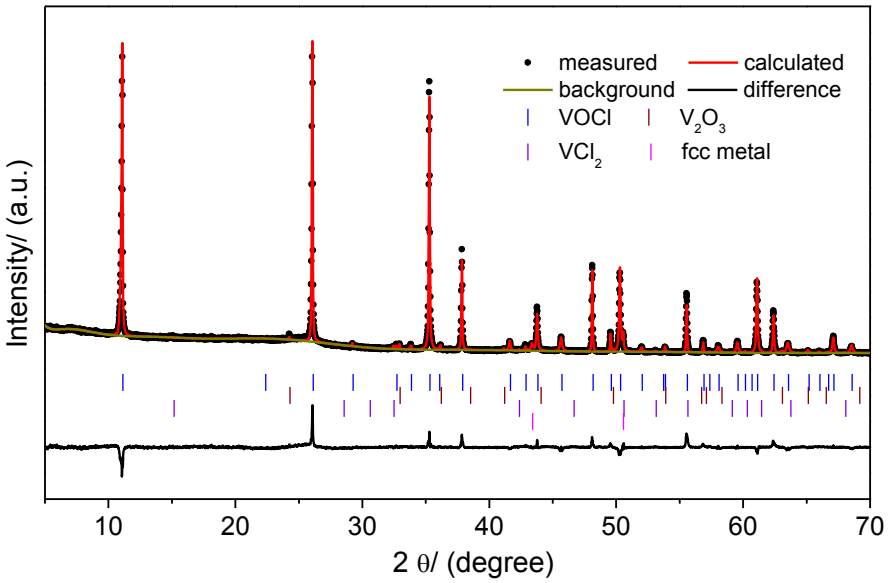

Figure A-1: Rietveld analysis of the VOCl/C composite. Small amounts of impurities of V_2O_3 (ca. 2 wt %), VCl_2 (ca. 1 wt %), and presumably an fcc metal were also found. The VOCl crystallizes in an orthorhombic structure with a space group of Pmmn, lattice parameters: a = 3.77 Å, b = 3.30 Å, c = 7.93 Å. Bragg R factor, R_{bragg} = 8.1%; Weighted R factor, R_{wp} = 8.6%; Goodness of Fit, GOF = 1.86.

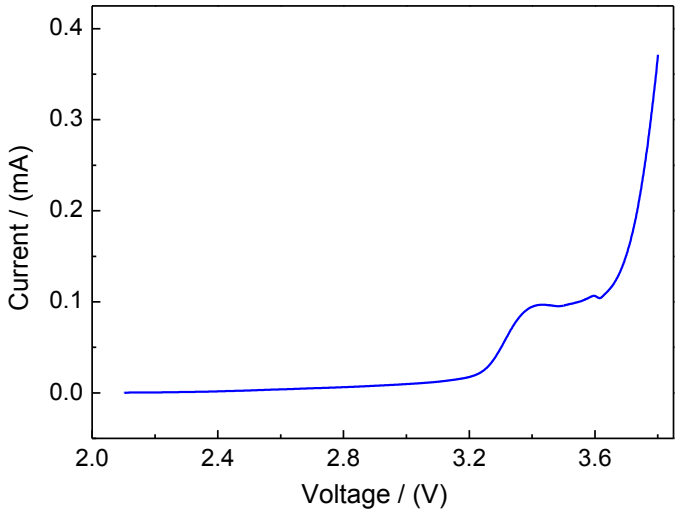

Figure A-2: Linear sweep voltammetry of the 0.5 M $PP_{14}Cl$-PC electrolyte in a cell configuration of Li/$PP_{14}Cl$-PC/stainless steel at a sweep rate of 5 mV s^{-1}.

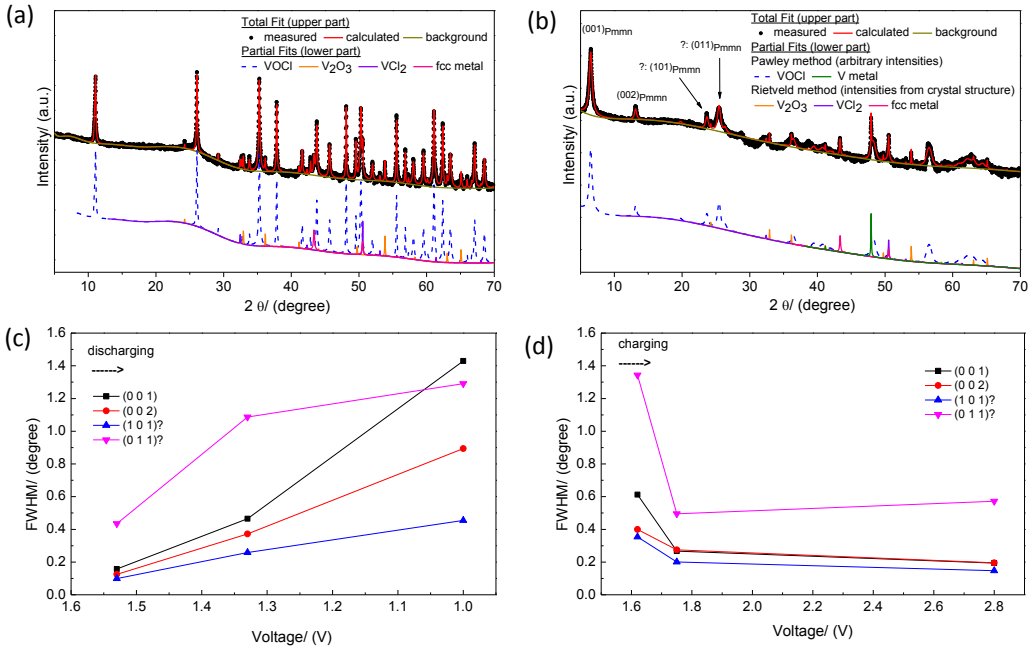

Figure A-3: (a) Rietveld analysis of the as-prepared VOCl/C electrode, (b) analysis of the recharged VOCl electrode (2.8 V) after initial discharging (Pawley type fit for the VOCl phase, Rietveld fits for other phases), dependency of the full width at half maximum (FWHM) of the first four reflections at different states of (c) discharging (1.53 V, 1.33 V, and 1.0 V), and (d) charging (1.62 V, 1.75 V, and 2.8 V). First four reflections to simple Lorentzian type functions were fitted as shown in c and d indicate that the width of all the reflections strongly increased on discharging, and decreased again on charging of the compound. R_{wp} = 10 %, GOF = 2.6 for the charged sample (b).

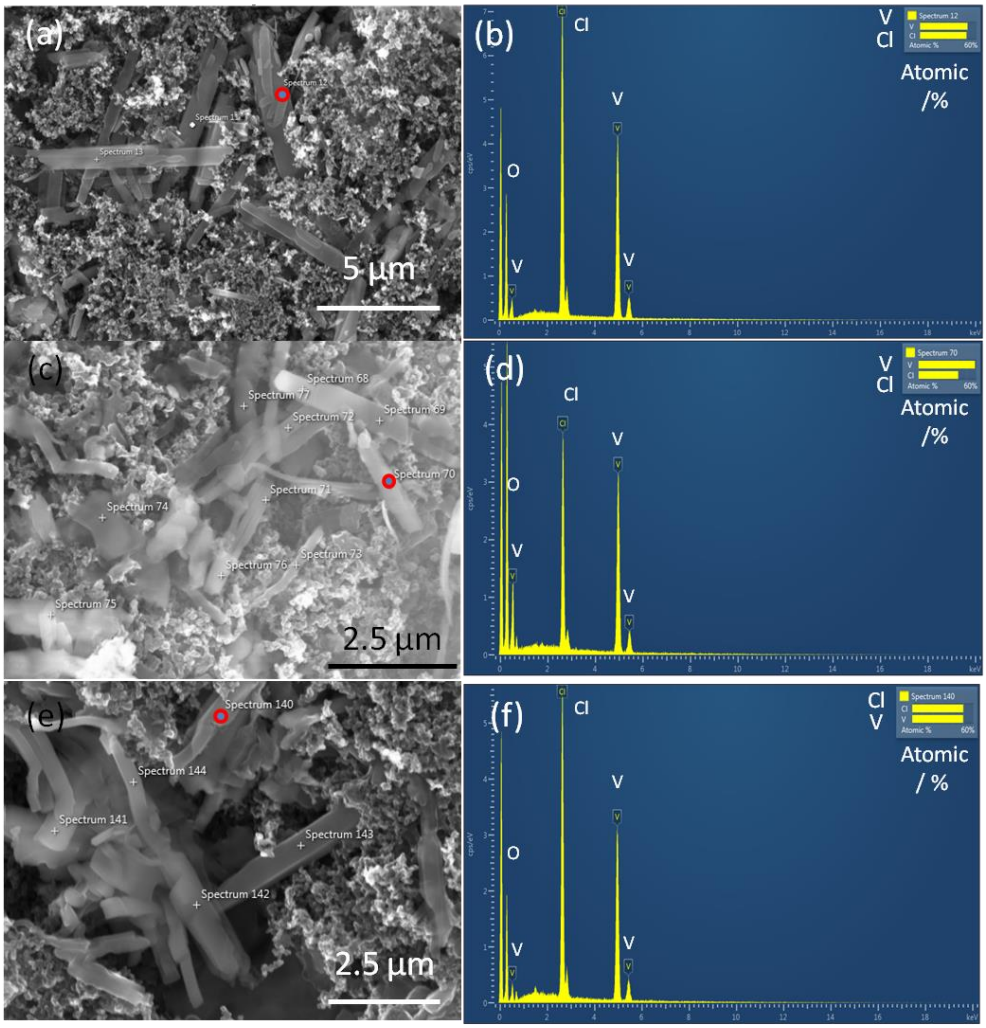

Figure A-4: SEM images and the corresponding EDX spectra of the VOCl electrode (a, b) in the as-prepared, (c, d) discharged, and (e, f) recharged states.

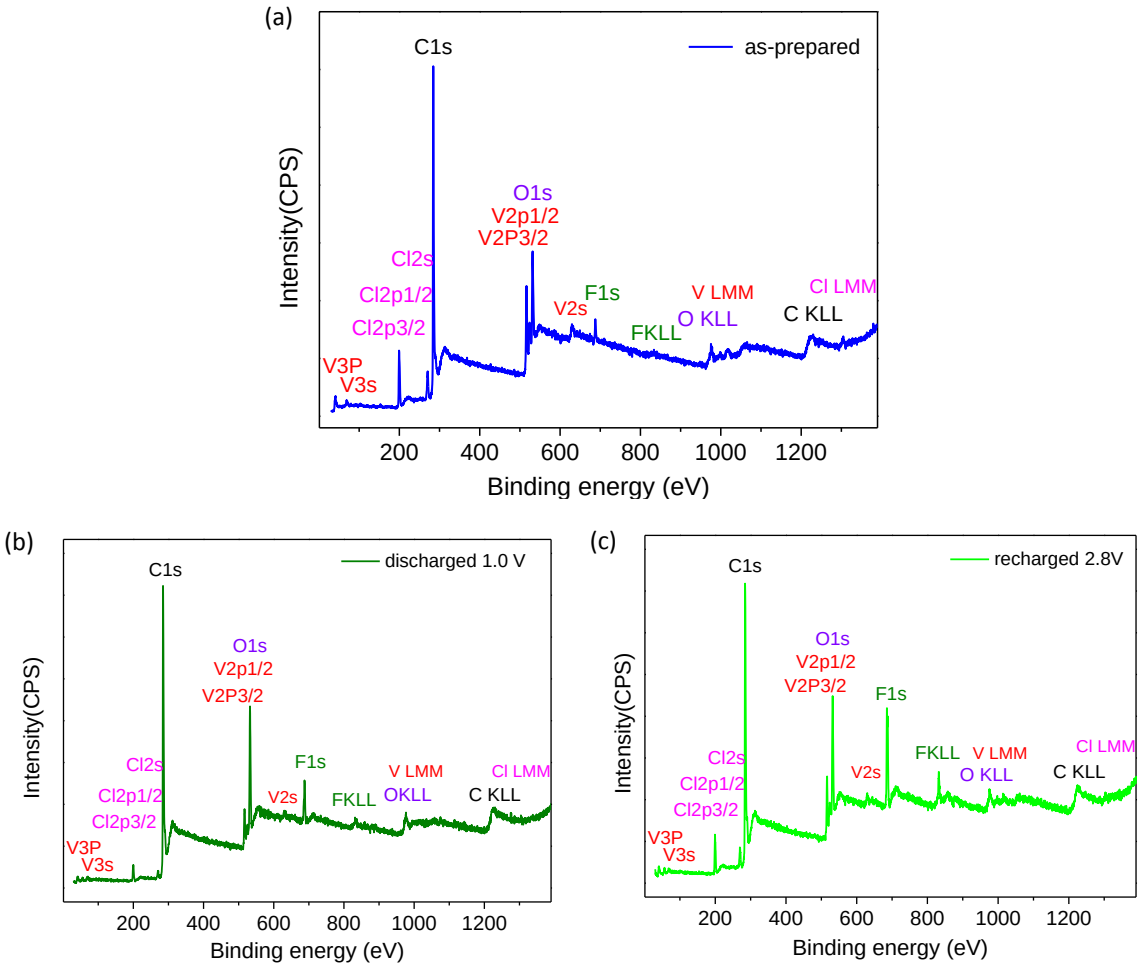

Figure A-5. XPS survey of the VOCl electrode, (a) at the as-prepared, (b) discharged (1.0 V), and (c) recharged (2.8 V) states in the first cycle.

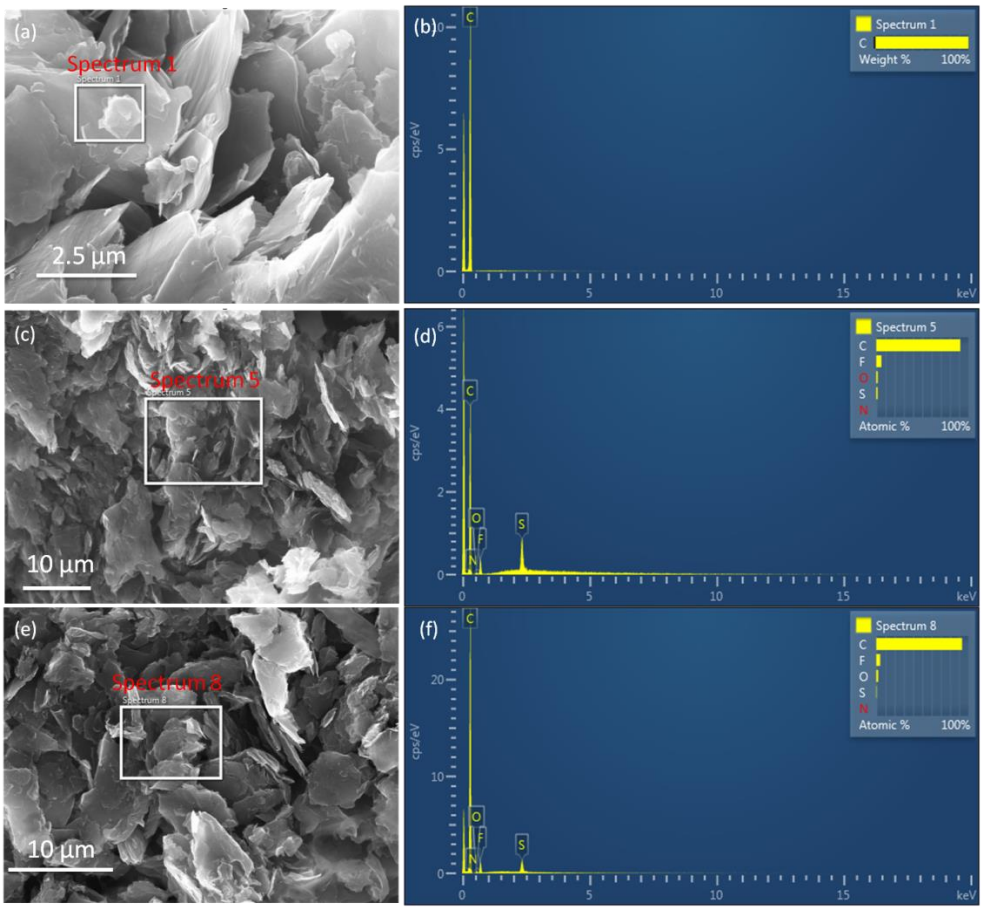

Figure A-6: SEM images of graphite cathode and their corresponding EDX spectra in the as-prepared (a, b), charged (c, d) and discharged (e, f) states.

Abbreviations

CuDEPP	[5,15-Bis(ethynyl)-10,20-diphenylporphinato]copper(II)
CuTPP	[5,10,15,20-tetraphenylporphinato]copper(II)
CB	Carbon black
CIBs	Chloride ion batteries
CV	Cyclic voltammetry
CE	Counter electrode
DMC	Dimethyl carbonate
EC	Ethylene carbonate
EDX	Energy-dispersive X-ray spectroscopy
EELS	Electron energy loss spectroscopy
EIS	Electrochemical impedance spectroscopy
EMF	Electromotive force
EV	Electric vehicle
FWHM	Full width at half maximum
FFT	Fast Fourier transformation
HAADF	High angle annular dark field
HEV	Hybrid electric vehicle
IR	Infrared spectroscopy
ICL	Irreversible capacity loss
LSV	Linear sweep voltammetry

LIBs	Lithium ion batteries
$LiPF_6$	Lithium hexafluorophosphate
MALDI	Matrix-assisted laser desorption/ionization
TOF-MS	Time-of-flight mass spectroscopy
MC	Mg/carbon black composite
MMC	$MgCl_2$/Mg/carbon black composite
NMP	N-methyl-2-pyrrolidone
NIBs	Sodium ion batteries
$NaClO_4$	Sodium perchlorate
OCV	Open circuit voltage
PVDF	Poly(vinylidene difluoride)
PC	Propylene carbonate
$PP_{14}Cl$	1-butyl-1-methylpiperidinium chloride
$PP_{14}TFSI$	1-butyl-1-methylpiperidinium bis(trifluoromethylsulfonyl)imide
PDF	Powder diffraction file
RE	Reference electrode
SEM	Scanning electron microscopy
STEM	Scanning transmission electron microscope
SAED	Selected area electron diffraction
SEI	Solid electrolyte interface
SHE	Standard hydrogen electrode
TEM	Transmission electron microscopy
TGA-DSC	Thermogravimetric differential scanning calorimetry
UV-vis	Ultraviolet-visible spectroscopy
VOCl	Vanadium oxychloride
$VOCl_2$	Vanadium oxydichloride

WE	Working electrode
XANES	X-ray absorption near edge structure
XRD	X-ray diffraction
XPS	X-ray photoelectron spectroscopy

Acknowledgements

This thesis would not have been finished without the support, and advice of many people. First of all, I would like to gratefully thank my supervisor Prof. Dr. Maximilian Fichtner for providing me the opportunity to perform this work in his research group. I thank him very much for his kind and professional guidance through this thesis. I appreciate all the freedom and opportunities to work independently in his group.

I would like to thank my thesis committee members, Prof. Dr. Maximilian Fichtner, Prof. Dr. Rolf Jürgen Behm, Prof. Dr. Werner Tillmetz, Prof. Dr. Gerhard Taubmann, and Prof. Dr. Mika Linden (chairman) for all of their guidance, valuable discussion.

I would like to acknowledge Dr. Zhirong Zhao-karger, Dr. Xiangyu Zhao, and Dr. M. Anji Reddy for all the help on my projects, teaching me some basic lab practices, and valuable scientific discussions.

I am glad to have had the opportunity to collaborate with Prof. Dr. Mario Ruben and Zhi Chen at Karlsruhe Institute of Technology on the organic battery project.

I would like to express my gratitude to Dr. Clemens Wall, Dr. Ruiyong Chen, Le Zhang, Dr. Oliver Clemens, and Dr. Xiu-Mei Lin for their helpful discussions on this work.

I would like to thank Dr. Thomas Diemant and Prof. Dr R. Jürgen Behm for the XPS measurements, data analysis, and valuable discussions.

Dr. Xiaoke Mu, and Dr. Venkata Sai Kiran Chakravadhanula, Dr. Johannes Biskupek are

acknowledged for their kind support to collect the TEM data and the discussions.

Many thanks go to Dr. Fabienne Gschwind and Dr. Alexander Pohl for the safety training and the introduction of the XRD measurement. I would like to thank Nina Laszczynski for XRD measurement of the Li anode.

I would to express my gratitude and appreciation to all other people from Prof. Fichtner's group: Dr. Shuhua Ren, Dr. Vinayan Bhaghavathi Parambath, Dr. Christian Bonatto Minella, Dr. Ulrich Ulmer, Dr. Helen Maria Joseph, Dr. Nele Schwarzburger, Dr. Bijoy Das, Musa Ali Cambaz, Pfeifer Maxim, Zijian Zhao, Daniel Sandbeck, Dominik Steinle, and Christina Danetzki, for all the good discussion about science and life.

I would like to thank Prof. Dr. Rudolf Holze, Mrs. Nora Younadam, and Mr. Tiangui You who gave me great support when I studied at the Chemnitz University of Technology. Prof. Dr. Songting Tan (Xiangtan University, China) and Prof. Dr. Henghui Zhou (Peking University, China) are greatly appreciated for their continuous support.

Finally, I would like to sincerely thank my parents (Yuee and Zeming), my brother (Wen), and my wife (Li), for their love, understanding, and support at any time.

Helmholtz Institute Ulm, 05.2016

Publications and conferences

Publications

1. Ping Gao, Zhi Chen, Zhirong Zhao-Karger, Jonathan E. Mueller, Christoph Jung, Svetlana Klyatskaya, Olaf Fuhr, Timo Jacob, Mario Ruben, and Maximilian Fichtner. A new class of organic electrodes bridging the gap between batteries and supercapacitors. 2016, ***submitted***.

2. Ping Gao, Xiu-Mei Lin, M. Anji Reddy, Le Zhang, Thomas Diemant, R. Jürgen Behm, and Maximilian Fichtner. Electrochemical behaviour of layered vanadium oxychloride in lithium ion batteries. ***J. Electrochem. Soc.,*** 2016, ***163*** (10) A2326-A2332.

3. Ping Gao, M. Anji Reddy, Xiaoke Mu, Thomas Diemant, Le Zhang, Zhirong Zhao-Karger, Venkata Sai Kiran Chakravadhanula, Oliver Clemens R. Jürgen Behm, and Maximilian Fichtner. VOCl as a cathode material for rechargeable chloride ion batteries. ***Angew. Chem. Int. Ed.***, 2016, 55, 4285-4290.

4. P. Gao, C. Wall, L. Zhang, M. A. Reddy and M. Fichtner. Vanadium oxychloride as electrode material for sodium ion batteries. ***Electrochem. Commun.,*** 2015, 60, 180-184.

5. P. Gao, X. Zhao, Z. Zhao-Karger, T. Diemant, R. J. Behm and M. Fichtner. Vanadium oxychloride/magnesium electrode systems for chloride ion batteries. ***ACS Appl. Mater. Interfaces,*** 2014, 6, 22430-22435.

6. L. Zhang, M. A. Reddy, P. Gao, M. Fichtner. Development of dense solid state thin-film electrolyte for fluoride ion batteries. ***J. Alloys Compd.,*** in press, 2016, doi: 10.1016/j.jallcom.2016.04.196.

7. X. Zhao, Q. Li, Z. Zhao-Karger, P. Gao, K. Fink, X. Shen and M. Fichtner. Magnesium anode for chloride ion batteries. ***ACS Appl. Mater. Interfaces***, 2014, 6, 10997- 10000.

Patents

1. Maximilian Fichtner, Ping Gao, Zhi Chen, Zhirong Zhao-Karger, and Mario Ruben. High performance organic electrodes for secondary batteries, ***European Patent***, No. 16000312.5.

Conferences

1. P. Gao, X. Zhao, Z. Zhao-Karger, M. Fichtner. EST 2015-Energy Science and Technology, Karlsruhe, Germany, May 20-22, 2015, ***Oral presentation***.

2. P. Gao, Z. Chen, Z. Zhao-Karger, M. Ruben, M. Fichtner. Gordon Research Conference, USA, Feb. 21-26, 2016, ***Poster***.

3. X. Zhao, P. Gao, Z. Zhao-Karger, M. Fichtner, X. Shen. 226th ECS meeting, Mexico, Oct. 05-09, 2014, ***Poster***.

Parts of this dissertation have been already published in:

Ping Gao, M. Anji Reddy, Xiaoke Mu, Thomas Diemant, Le Zhang, Zhirong Zhao-Karger, Venkata Sai Kiran Chakravadhanula, Oliver Clemens R. Jürgen Behm, and Maximilian Fichtner. VOCl as a cathode material for rechargeable chloride ion batteries. ***Angew. Chem. Int. Ed.***, 2016, 55, 4285-4290.
http://onlinelibrary.wiley.com/wol1/doi/10.1002/anie.201509564/abstract
Copyright © 2016 WILEY-VCH Verlag GmbH & Co. KGaA, Weinheim.

P. Gao, X. Zhao, Z. Zhao-Karger, T. Diemant, R. J. Behm and M. Fichtner. Vanadium oxychloride/magnesium electrode systems for chloride ion batteries. ***ACS Appl. Mater. Interfaces,*** 2014, 6, 22430-22435.
http://pubs.acs.org/doi/abs/10.1021/am5064266
Copyright © 2014 American Chemical Society.

Ping Gao, Xiu-Mei Lin, M. Anji Reddy, Le Zhang, Thomas Diemant, R. Jürgen Behm, and Maximilian Fichtner. Electrochemical behaviour of layered vanadium oxychloride in lithium ion batteries. ***J. Electrochem. Soc.,*** 2016, ***163*** (10) A2326-A2332.
http://jes.ecsdl.org/content/163/10/A2326.abstract
Copyright 2016 The Electrochemical Society.

P. Gao, C. Wall, L. Zhang, M. A. Reddy and M. Fichtner. Vanadium oxychloride as electrode material for sodium ion batteries. ***Electrochem. Commun.,*** 2015, 60, 180-184.
http://www.sciencedirect.com/science/article/pii/S1388248115002520
Copyright © 2015 Elsevier B.V.

Erklärung

Ich versichere hiermit, dass ich die Arbeit selbständig angefertigt habe und keine anderen als die angegebenen Quellen und Hilfsmittel benutzt sowie die wörtlich order inhaltlich übernommenen Stellen als solche kenntlich gemacht habe.

Ulm, den

Vorname Nachname / Unterschrift

Curriculum Vitae

Personal Data

Name:	Ping Gao
Date/Place of Birth:	Feb. 27 1987/Hunan, China
Nationality: Chinese	Gender: Male

Education

Jan. 2013 – now	PhD student in Solid State Chemistry, Ulm University, Germany
Sep. 2009 – Jul. 2012	Master in Applied Chemistry, Xiangtan University, China
Sep. 2005 – Jul. 2009	Bachelor in Chemical Engineering and Technology, Hunan City University, China

Research Experience

Mar. 2014 - now	Helmholtz Institute Um (HIU), Ulm, Germany. *Topic: Novel electrode materials for rechargeable batteries based on cationic and anionic shuttles.*
Jan. 2013 – Mar. 2014	Institute of Nanotechnology (INT), KIT, Karlsruhe, Germany. *Topic: Development of novel rechargeable batteries based on chloride ion shuttle.*
Sep. 2012 – Dec. 2012	Chemnitz University of Technology, Chemnitz, Germany. Visiting student, *topic: Li-rich cathode for lithium ion batteries*.
Jul. 2010 – Apr. 2012	Peking University, Peking, China. Master thesis, *topic: Olivine cathode material of $LiMPO_4$ (M = Fe, Mn) for lithium ion batteries.*

Language

Chinese: native	English: fluent	German: basic